PONTIFICIA UNIVERSIDAD CATÓLICA DEL PERÚ

FACULTAD DE CIENCIAS E INGENIERÍA

MANGANESE OXIDES IN THE ONSHORE FOREARC PISCO BASIN: MINERALOGY, COMPOSITION, AND ORIGIN

Tesis para obtener el título profesional de Ingeniera Geóloga

AUTORA

IVANA CARINA CARCAMO VALENCIA

ASESOR

Dr. LISARD TORRÓ I ABAT

COASESOR

Dr. JOAQUIN A. PROENZA (Universitat de Barcelona, España)

Lima, septiembre 2024

INFORME DE SIMILITUD

Yo, Lisard Torró i Abat,
docente de la Facultad de Ciencias e Ingeniería de la Pontificia Universidad Católica del Perú,
asesor de la tesis titulada “Manganese oxides in the onshore forearc Pisco Basin: Mineralogy, composition, and origin”,
de la autora Ivana Carina Carcamo Valencia
dejo constancia de lo siguiente:

- El mencionado documento tiene un índice de puntuación de similitud de 22 %. Así lo consigna el reporte de similitud emitido por el software *Turnitin* el 30/11/2024.
- He revisado con detalle dicho reporte y la Tesis y no se advierten indicios de plagio.
- Las citas a otros autores y sus respectivas referencias cumplen con las pautas académicas.

Lugar y fecha: Lima a 30 de noviembre de 2024

Apellidos y nombre del asesor: Torró i Abat, Lisard	
CE: 001833851	Firma 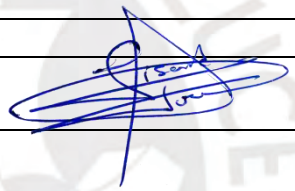
ORCID: 0000-0002-3557-8334	

Resumen

El emergente y exponencial crecimiento en el campo de las tecnologías avanzadas y "verdes" contribuye a un aumento global en la demanda de materias primas críticas de origen mineral, como lo son el manganeso y el cobalto. Los nódulos de manganeso han ganado reconocimiento recientemente como fuentes potenciales de estos elementos y otras materias críticas. Sin embargo, su presencia en los fondos marinos representa un dilema para los responsables políticos debido a su ubicación, con frecuencia más allá de las zonas económicas exclusivas de las naciones, y a las posibles amenazas de la minería submarina para los ecosistemas marinos abisales. La presente tesis tiene como objetivo realizar una caracterización estratigráfica, textural, mineralógica y composicional de los óxidos de Mn, incluidos los nódulos y concreciones, recubrimientos y venillas en la cuenca *onshore* de antearco Pisco en Perú. Los óxidos de manganeso son estratoligados y principalmente estratiformes —con la excepción de venillas discordantes—, y se concentran sobretodo a lo largo de niveles de arenisca, limolita y toba de las formaciones Chilcatay y Pisco. Es probable que capas masivas de anhidrita hayan actuado como sello para los fluidos mineralizantes y, por lo tanto, pueden también haber ejercido un control estratigráfico sobre la mineralización. Los óxidos de Mn constituyen tanto el cemento de granos detríticos angulosos, así como también reemplazan restos de organismos (diatomeas, turritelas, madera, otros) y/o el molde de los mismos en el substrato (icnofósiles). Los análisis de roca total muestran un enriquecimiento en CoO (media = 0.21 wt%; hasta 0.80 wt%). Se distinguen dos tipos mineralógicos: criptomelano/hollandita y todorokita. Los análisis de microsonda electrónica sugieren una predominancia de criptomelano sobre hollandita, y muestran contenidos medios y máximos de CoO de 0.46 wt% y 2.64 wt%, respectivamente. El control estratigráfico, las texturas de reemplazamiento biomórfico y la mineralogía concuerdan con un origen diagenético de la mineralización de óxidos de Mn. La descomposición de materia orgánica acoplada a la reducción de Mn y Fe, la consiguiente

concentración de estos elementos en el agua intersticial y la posterior circulación de fluidos ricos en Mn a lo largo de estructuras (sistemas de fracturas y chimeneas) y niveles permeables dio lugar a precipitación consecuente de los minerales antes mencionados, bajo condiciones oxigenadas, probablemente relacionadas al levantamiento tectónico durante el Plioceno tardío y la emersión consecuente de la cuenca Pisco Este. El enriquecimiento de cobalto en los óxidos de Mn sigue siendo materia de interés. Tentativamente, podría atribuirse a la circulación de fluidos originados en la zona de subducción, a través de rocas cercanas del basamento, posiblemente enriquecidas en Co, o a la ubicación del área de estudio cerca al *Nazca Drift System*, el cual influyó en la metalogénesis en los Andes. Esta tesis demuestra que los óxidos de Mn de origen diagenético pueden representar una fuente potencial de Co.

Abstract

The emerging and exponential growth of high- and green-technologies contribute to a global increase in the demand for critical raw materials of mineral origin, such as manganese and cobalt. Manganese nodules have recently gained recognition as potential sources of these and other critical commodities. However, their major occurrence in the deep seabed poses a dilemma for policy makers because of their location, often beyond nation's exclusive economic zones, and potential threats of seabed mining to abyssal marine ecosystems. The present thesis aims to perform a stratigraphic, textural, mineralogical, and compositional characterization of Mn oxides, including nodules and concretions, coatings, and veins in the onshore forearc Pisco Basin in Peru. Manganese oxides are stratabound and primarily stratiform —with the exception of discordant veins—, and concentrate along levels of sandstone, siltstone, and tuff of both the Chilcatay and Pisco formations. Massive anhydrite beds probably acted as seals for mineralizing fluids and hence may have also exerted a stratigraphic control on the mineralization. The Mn oxides constitute the cement to angular detrital grains, and also fossilize remains of organisms (e.g., diatoms, turritellas, wood) and/or their molds in the substrate (i.e., ichnofossils). In bulk analyses, data reveal an enrichment in CoO (mean = 0.21 wt%; up to 0.80 wt%). Two mineralogical types are distinguished: cryptomelane/hollandite and todorokite. Electron probe microanalysis suggests a predominance of cryptomelane over hollandite, and yield mean and maximum CoO contents of 0.46 wt% and 2.64 wt%, respectively. The stratigraphic control, biomorphic replacement textures, and mineralogy accord with a diagenetic origin of the Mn oxide mineralization. The decay of organic matter coupled to Mn and Fe reduction, ensuing concentration of these elements in porewater, and subsequent circulation of Mn-rich fluids along structures (e.g., fracture systems, chimney-like structures) and permeable levels was followed by precipitation in renewed oxygenated conditions probably connected to the late Pliocene uplift and exposure of the East Pisco Basin.

The Co enrichment in Mn oxides is still intriguing. Tentatively, it could be attributed to the circulation of subduction-water through basement rocks, possibly enriched in Co, or to the location of the study area by the Nazca Drift System, which influenced the metallogenesis in the Andes. This thesis demonstrates that Mn oxides of diagenetic origin may represent a potential source of Co.

Agradecimientos

Este proyecto de investigación está dedicado especialmente a mi madre Dora Valencia, quien ha sido mi eterno apoyo incondicional; a mi padre Luis Cárcamo, quien inculcó en mí el deseo de superación; y a mi hermano Iván Cárcamo, quien es mi mayor modelo a seguir.

Además, un agradecimiento infinito a mi asesor de tesis, Dr. Lisard Torró, por depositar tanta confianza en mí, por presentarme oportunidades desafiantes y por mostrar tanta paciencia a lo largo de la investigación. A mi co-asesor Dr. Joaquín Proenza (Universidad de Barcelona), por su apoyo intelectual y logístico para el desarrollo de esta tesis. A Xavier Llovet (Universidad de Barcelona) por su colaboración durante la obtención de datos de EPMA. Al profesor Dr. Patrice Baby y Luis Ayala por su guía en las campañas de campo y recolección de muestras, y por compartir comentarios y conocimientos útiles para la elaboración de este trabajo.

Asimismo, no puedo dejar de agradecer a mis mejores amigos Sebas, Cristian y Pacheco (*"Team Plagioclasas")* con quienes compartí momentos de gran alegría y que puedo decir que se han convertido en mi segunda familia. A Lore, Luis Benites y Luis Jerí, por su leal amistad y apoyo constante.

También, extiendo mi gratitud a Pablito, Johan y Mariana, mis jefes de práctica a quienes ahora puedo llamar buenos amigos, que siempre me ayudaron cuando lo necesité, no solo en temas relacionados a la carrera, sino también de la vida misma.

This research work was economically supported by the FAI-025-2023 project granted by the Pontifical Catholic University of Peru – PUCP and the PE501087814-2024 project granted by the Peruvian research agency PROCIENCIA, and logistically supported by the project 2021 SGR 00239 of the Agència de Gestió d'Ajuts Universitaris i de Recerca de Catalunya.

Table of contents

List of figures

List of tables

1. INTRODUCTION

1.1. Metalliferous mineralization in the seabed

Different metalliferous mineral resources (e.g., cold seeps methane barite, seafloor massive sulfides, ferromanganese crusts and nodules), each formed through distinct processes and showing different morphologies, mineralogy, and metalliferous signatures, can be found in the seabed (Seabold and Berger 2013; Lusty and Murton 2018).

Deposits of *cold seep methane barite* have been documented during the last four decades as a third mechanism of barite formation – in addition to biogenic and hydrothermal barite – related to continental margins and submarine venting of cold fluids enriched in hydrocarbons and barium (Torres et al. 2003; Canet et al. 2013, 2014). Such barite deposits are significant in size and extent (Torres et al. 2003), which indicates that barite deposition might play an important role in the global marine barium cycle (Feng and Roberts 2011). Seafloor observations have revealed the existence of up to 10-m-high barite build-ups over the seafloor along a 3.5 km track from the Sea of Okhotsk, and barite chimneys up to 10 m in height and local sites of barite deposition over 3 km along the San Clemente Fault Zone (Torres et al. 2003; Feng and Roberts 2011 and references therein).

Torres et al. (1996) suggest that the source of barium in seep-related barite is associated with accumulation of biogenic barite in organic-rich, and typically opal-rich, sediments at high productivity areas. Under these conditions, microbial degradation of organic carbon leads to methanogenesis and interstitial sulfate in sediments is consumed by oxidation of both organic carbon and

biogenic methane (Torres et al. 1996, 2003). Due to the generation of a sulfate depleted environment, barite dissolves resulting in the mobilization of barium-rich pore fluids (Torres et al. 1996, 2003). Besides, pore fluids represent a significant volume of the sediments (~50-70%) and are transported through diffuse flow or by focused flow along major fault structures in the sediments (Herzig and Hannington 2006). During fluid migration, the enhanced barium flux is coupled with a low-temperature fluid venting, commonly referred to as cold seeping, where barite precipitates when mixed with seawater sulfate (Herzig and Hannington 2006 and references therein).

Another well-known form of marine metalliferous mineralization are *seafloor massive sulfides*, which will henceforth be referred to as SMS. SMS are linked to submarine hydrothermal vents, with the majority occurring on mid-ocean ridges (65%), while a significant portion also occurs along volcanic arcs (12%) and backarc spreading centers (22%; Hannington et al. 2011). Recent studies indicate that hydrothermal vents occur every ~100 km along plate boundaries (~89,000 km). This suggests that there are approximately 900 deposits in the global neovolcanic zones, as reported by Hannington et al. (2011). SMS formation begins with the percolation of cold seawater through the seafloor and its subsequent physicochemical modification in a reaction zone situated above a magma chamber, which includes temperature increase and a decrease in pH and Eh of the fluids (Herzig and Hannington 2006). This now corrosive fluid is capable of leaching metals, namely Fe, Mn, Cu, Zn, Au, and Ag, from the surrounding rocks (Herzig and Hannington 2006; Boschen et al. 2013 and references therein). These metal-rich, hot (~350-400°C) fluids rise rapidly from the reaction zone along favorable structures like faults and fractures because of

their buoyancy and are expelled into the overlying water column through chimney vent sites (Herzig and Hannington 2006; Petersen and Hein 2013). As a consequence of mixing of this hydrothermal fluid with cold (~2°C), oxidizing seawater, sulfides precipitate creating a stockwork within the upflow zone or as massive sulfides below or at the seafloor (Herzig and Hannington 2006). SMS are commonly enriched in base metals (Fe, Zn, Cu, Pb; Boschen et al. 2013) and the mineralogy is dominated by sulfide minerals, chiefly pyrite, chalcopyrite, and sphalerite (Petersen and Hein 2013).

Another type of deep-sea mineral deposits are *ferromanganese crusts*, which recently became of great interest as potential metal resources (Lusty et al. 2018). Such Fe-Mn deposits are located at the seabed on the flank and summits of seamounts (undersea mountains with heights above 1,000 m), knolls (heights of 200-1,000 m), ridges, and plateaus onto sediment-free areas (i.e., hard-rock substrates), specially at water depths of about 400-7,000 m (Hein and Petersen 2013; Hein and Koschinsky 2014). The thickness of crusts is variable, ranging from less than 1 mm to 26 cm, with the thickest and most metal-rich crusts forming pavements at water depths of 800-2,500 m (Hein and Koschinsky 2014).

The model of formation of ferromanganese crusts is defined by a continuum between hydrothermal and hydrogenetic end-members (Lusty et al. 2018). The first one refers to precipitation of ferromanganese oxides in a late, low-temperature stage of a hydrothermal system, with temperatures of deposition between 5-20 °C (Glasby 2013). Hydrothermal crusts are composed of 10 Å (todorokite, buserite, 10 Å manganite) and/or 7 Å (birnessite, 7 Å manganite)

manganates with minor detrital minerals, and usually present high Mn/Fe ratios (>10) with low contents of Cu, Ni, Zn, Co, and Pb (<0.1 wt%; Glasby 2013). Hydrothermal Fe-Mn crusts growth rates are above 1,000 mm Myr^{-1}, which are considerably faster than the hydrogenetic ones in more than three orders of magnitude (Glasby 2013). Hydrothermal ferromanganese crusts represent less than 1% of the total Mn deposits in the global ocean (Glasby 2013) and are not economically important (Hein and Petersen 2013).

The hydrogenetic end-member implies direct precipitation of a non-crystalline iron oxyhydroxide (FeOOH) and manganese oxide (predominantly vernadite) from cold, ambient seawater (Hein and Petersen 2013; Hein and Koschinsky 2014). These two dominant mineral phases may be accompanied by minor detrital minerals (e.g., quartz, feldspars; Hein and Petersen 2013). Although accumulation of Fe oxyhydroxides and Mn oxides can occur at any water depth, it may be enhanced when an oxygen-minimum zone (i.e., a sector of the water column with the lowest oxygen saturation) is present, which is considered a great reservoir for dissolved Mn and other metals (Lusty et al. 2018). Due to very slow growth rates (~1-5 mm Myr^{-1}), metals from seawater (e.g., Co, Ni, Cu, Te, Pt, Zr, Nb, W, Bi, and rare earth elements – REE) are adsorbed onto the ferromanganese mineral surfaces (Hein and Petersen 2013). Indeed, the economic potential of ferromanganese crusts is related to significant Co (up to ~2.0 wt%) and Te (up to ~200 ppm; Lusty et al. 2018) contents. Moreover, Co-rich manganese crusts are considered to be great paleoceanographic indicators extensively used in the study of deep ocean circulation patterns based on their Nd, Pb, Be, Hf, and Os isotope signatures (Glasby 2013).

Ferromanganese crusts and nodules were not distinguished and both were called nodules until the late 1970s (Hein and Koschinsky 2014). In comparison with ferromanganese crusts, nodules contain similar metal contents, yet have a more complex mineralogy and a partly different mechanism of formation (Hein and Petersen 2013). The following section will provide further insight into the characteristics of manganese nodules.

1.2. Manganese nodules

1.2.1. Genesis

Ferromanganese nodules commonly occur on sediment-covered abyssal plains at water depths of about 4,000-6,500 m, especially where sedimentation rates are low (<10 mm kyr^{-1}; Hein and Koschinsky 2014; Hein et al. 2020). Nevertheless, shallow-water (<100 m) nodules are known to occur in a few places (e.g., Baltic Sea; Hein and Koschinsky 2014). It is noteworthy that growth rates of shallow-water nodules are higher than those of deep-sea nodules by 3-4 orders of magnitude (Hlawatsch et al. 2002; Glasby 2013).

Apart from water depth of formation (i.e., shallow vs. deep), Fe-Mn nodules have been subdivided based on their diameter size (micro, <1mm; small, <4 cm; medium, 4-8 cm; and large, >8cm; Glasby 2013), seafloor density (i.e., nodules per seafloor square meter), and shape (spheroidal, discoidal, botryoidal, or polyshape; Hein et al. 2020).

Ferromanganese nodules form via precipitation of Fe oxyhydroxides and Mn oxides around a hard nucleus (e.g., rock fragment, authigenic mineral

fragment, piece of bone, previously formed nodule) on the surface of soft sediment by two main mechanisms of formation: hydrogenetic and diagenetic (Fig. 1; Hein and Koschinsky 2014; Hein et al. 2000). Actually, there is a spectrum between the two end-members that happens to be mixed-origin Fe-Mn nodules, which are more common than either pure hydrogenetic or diagenetic nodules (Hein and Koschinsky 2014).

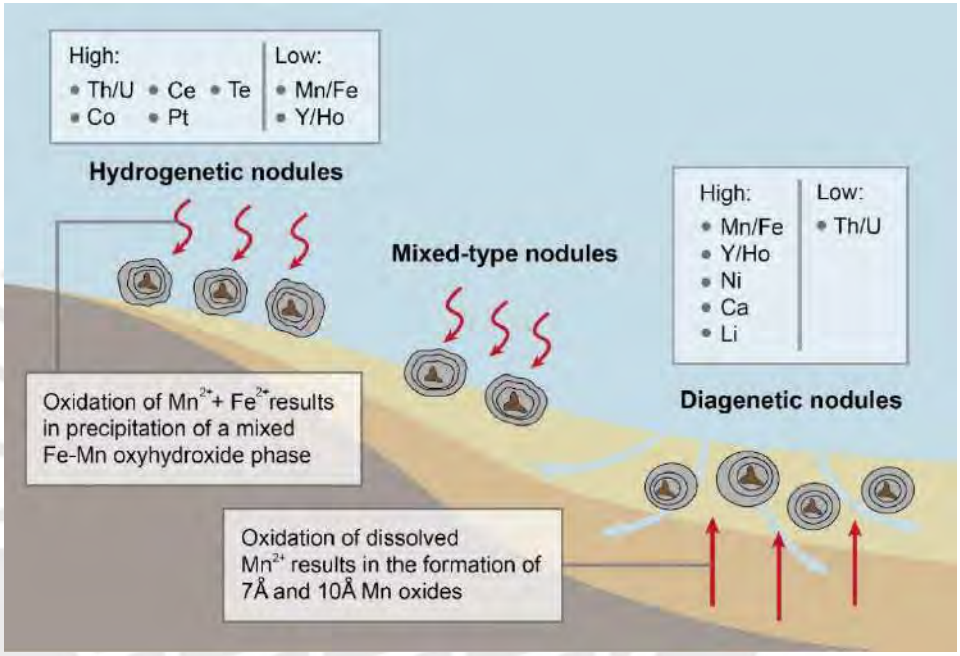

Figure 1. Formation of hydrogenetic, mixed type, and diagenetic nodules and related variations in chemistry (modified from Hein et al. 2020).

Hydrogenetic precipitation occurs directly from cold, ambient seawater (Hein et al. 2020). It consists of the oxidation of Mn^{2+} and Fe^{2+} in oxygen-rich ocean waters followed by the accretion of Mn^{4+} and Fe^{3+} oxide colloids around a hard nucleus (Hein and Koschinsky 2014). The major mineral phases in hydrogenetic nodules are Fe-rich vernadite (δ-MnO_2) and X-ray amorphous Fe oxyhydroxide (feroxyhyte, δ-FeOOH), which occur along with detrital phases such as quartz and feldspars (Hein et al. 2000). Hydrogenetic nodules commonly present similar amounts of Mn and Fe

(Mn/Fe ~1), and high contents of Co (up to 0.38 wt%), Te, Ce, and Pt (Hein and Koschinsky 2014; Hein et al. 2020). This type of nodules is characterized by slow growth rates of about 2 mm Myr^{-1} (Glasby 2013).

On the other side, diagenetic precipitation occurs from sediment porewater, which basically is chemically-modified ocean water (Hein and Koschinsky 2014). This latter process may occur under oxic or suboxic conditions, typically considering a 5 mM oxygen concentration as the lower boundary (Hein and Koschinsky 2014). Diagenetic nodules are characteristically composed of a 10 Å manganate (e.g., buserite, todorokite, asbolan) that subordinates a 7 Å manganate (i.e., birnessite), X-ray amorphous Fe oxyhydroxides (e.g., feroxyhyte, ferrihydrite, goethite), and minor detrital silicate minerals (Hein and Koschinsky 2014). Diagenetic nodules typically show high Mn/Fe ratios (>10) and high contents of Ni (up to 1.30 wt%), Cu (up to 1.07 wt%), and Li (up to 311 ppm; Hein and Koschinsky 2014; Hein et al. 2020). This type of nodule is characterized by fast growth rates of 10-100 mm Myr^{-1} (Glasby 2013).

Because of the generally slow growth of ferromanganese nodules, studies have been carried out to evaluate their potential as indicators of past oceanographic variations. For instance, Hlawatsch et al. (2002) studied ferromanganese nodules from the western Baltic Sea and determined elevated heavy metal contents since the end of the 19^{th} century, probably due to anthropogenic metal input. Also, Vineesh et al. (2009) conducted a detailed morphological study on 23,000 nodules and concluded that bottom water currents and seafloor topography may play an important role in

controlling the nodule facies along with water depths, with the smoother nodules found at shallower depths (<5,000 m). Zhang et al (2019) investigated the morphology, mineralogy, and element and isotope (Sr, Nd, and Pb) geochemistry of manganese nodules from the northern South China Sea to determine bottom water variations over the last 3.2 Myr and linked it to global cooling and Luzon arc-forearc uplift.

1.2.2. Economic importance

The economic interest in ferromanganese nodules and crusts was first developed in the 1960s, when John L. Mero predicted that they could represent an essentially endless supply of metals, such as Mn, Co, Ni, and Cu (Lusty and Murton 2018).

Manganese is used mostly in the production of alloys with iron in steel, but also with nonferrous metals, like aluminum and copper (Canon et al. 2017). Moreover, it is used during refinement of iron ore to metallic iron prior to steel fabrication (Canon et al. 2017). Noteworthy, manganese has no substitutes in the steelmaking process. Also, manganese is used in non-metallurgical industry in cell battery cathode manufacture (synthetic MnO_2), soft ferrites used in various power electronics devices (Mn-Zn ferrites), micronutrient additives included in fertilizers and animal feed ($MnSO_4$ and MnO), drinking water and wastewater treatment chemicals ($KMnO_4$ and MnO_2), and other chemicals (Canon et al. 2017).

Nowadays, manganese is considered a critical mineral commodity for various countries, such as the United States (USGS 2022), Canada

(Government of Canada 2022), and Australia (Brown et al. 2022), along with the European Union (European Commission 2023). The economic indispensability of manganese is reflected in the forecast demand from lithium-ion batteries, with the strongest predicted growth (increasing factor of 9.3) through 2030 among other elements (Fig. 2; Bloomberg NEF 2021).

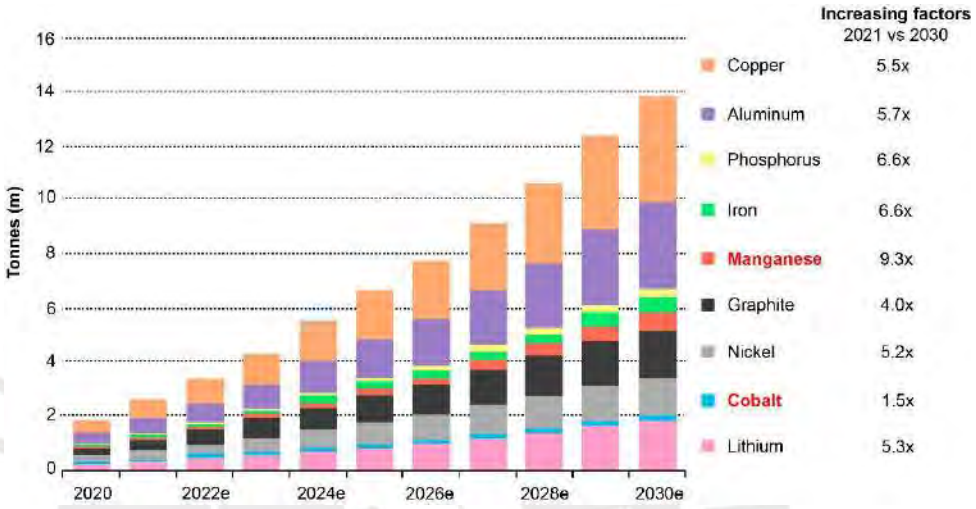

Figure 2. Metals and minerals demand from lithium-ion batteries, and respective increasing factors. Numbers starting from 2022 are forecasts (modified from Bloomberg NEF 2021).

The major sources of manganese are stratiform deposits, which are extensive layers of manganese-rich sedimentary rocks that can be classified into two types: manganiferous sediments that occur independent of iron concentrations and manganiferous sediments interlayered with ferruginous strata (e.g., banded iron formations from Kalahari, South Africa; Canon et al. 2017). Most Mn is currently mined from high-grade sectors of these deposits, including supergene enrichment zones (Canon et al. 2017). Although manganese is one of the major constituents of Fe-Mn nodules, manganese is considered of secondary economic importance in this type of deposits (Sparenberg 2019).

In contrast, manganese nodules have gained recognition as potential future resources for high- and green-tech metals (Hein et al. 2020), particularly Co. As previously stated, hydrogenetic nodules are typically enriched in Co, Te, Ce, and Pt whereas diagenetic nodules commonly exhibit high contents of Ni, Cu, and Li (Hein and Koschinsky 2014; Hein et al. 2020). Some of the aforementioned elements (Co, Ce, Pt, Li) are also considered by international organizations to be critical raw materials. For example, cobalt has been identified as a critical raw material by the United States (USGS 2022), Canada (Government of Canada 2022), Australia (Brown et al. 2022), and the European Union (European Commission 2023).

The main application of cobalt is in the manufacture of rechargeable batteries, principally lithium-ion batteries (Fig. 2; Slack et al. 2017). Further technological applications of cobalt include superalloys used in turbine engines for jet aircraft and terrestrial energy generation. In addition, cobalt is used in cemented carbides and diamond tools for the manufacturing of cutting tools employed in metalworking, mining, oil and gas drilling, and construction industries (Slack et al. 2017). Additional cobalt applications include animal feed additives, drying agents for paint, catalysts, humidity indicators, and pigments (Slack et al. 2017). Most of the global production of Co comes from primary and secondary stratiform sediment-hosted Cu-Co sulfides and oxides, secondary Ni-Co laterite deposits, and primary magmatic Ni-Cu (Co-PGE) sulfide deposits (Slack et al. 2017).

1.3. Deep-sea mining: fact or fiction

So far, the International Seabed Authority (ISA 2023) has approved 31 fifteen-year exploration contracts for areas outside of the Exclusive Economic Zone (EEZ) of any nation state (also referred to as “the Area”), with 19 exploration contracts for manganese nodules, 7 for polymetallic sulfides, and 5 for Co-rich ferromanganese crusts.

Although ISA has not introduced regulations for exploitation yet (Helmons et al. 2022), there is extensive research on potential technologies for both exploration and exploitation of deep-sea mineral deposits (Hein et al. 2020). The first extraction technologies are either available or being developed for the mining of ferromanganese nodules and SMS, but not for ferromanganese crusts, as it is considered technologically challenging to separate efficiently the Fe-Mn crusts from the substrate rock (Hein et al. 2013; Lusty et al. 2018). In the case of SMS extraction, technologies have been adapted from deep-ocean petroleum operations systems (e.g., pipeline trenching), and from offshore placer diamond mining (Hein et al. 2020).

Potential of extracting seabed mineral resources may have raised expectations with increases of mineral prices and demand, with particular interest in SMS deposits within the EEZs of Papua New Guinea and Sudan/Saudi Arabia (Boschen et al. 2013). Solwara, which is the most advanced of these projects, concerned the mining of SMS at 1,450-1,700 m water depths in Papua New Guinea, and reached as far as the development of a full Environment Impact Assessment and the production of a full-scale mining plant (Boschen et al.

2013). Nevertheless, this attempt to emerge a new marine industry failed when the project collapsed in 2019 (Boschen et al. 2013).

In the case of ferromanganese nodules, their recovery can be relatively easy by means of either mechanical or hydraulic collectors since they lie on a sediment substrate (Hein et al. 2020). At first, deep-sea exploration activities were predominantly undertaken by state agencies until 2010, when private contractors became involved and lead the establishment of nodule-mining projects (ISA 2023). A Belgium company, Global Sea Mineral Resources, developed a pre-prototype seabed nodule collector called “Patania II”. It was successfully tested in 2021 in exploration areas of Belgium and Germany in the Clarion Clipperton Zone of the Pacific Ocean, recovering more than 1,000 tons of nodules (Peacock 2023).

Nevertheless, there exist deterrents to deep-sea mining including political restrictions and, notably, potential environmental impacts (Cunningham 2022). The former involves the implementation of United Nations Convention on the Law of the Sea (UNCLOS), which confers the right to govern polymetallic nodules from “the Area” to the International Seabed Authority, and states that exploitation of marine mineral resources from “the Area” should *“be carried out for the benefit of mankind as a whole, irrespective of the geographical location of States”* (Cunningham 2022). In practice, the poor record on major cross-border issues of the United Nations encourages powerful states to ignore or even reject decisions made by UN bodies, introducing risk factors to deep-sea mining associated with geopolitics.

On the other hand, environmental issues are mostly related to the disturbance or even destruction of seabed habitats, depending on the deposit type and extraction tools (Hein et al. 2020). All types of deep-sea mining require a dewatering process, in which excess water loaded with sediment and fine-particulate ore fraction will have to be pumped back down to sea, creating a discharge plume of fine-grained material (Helmons et al. 2022). Some of the listed potentially harmful effects of discharge plumes include shading out of photosynthesizing plankton, phytoplankton blooms due to input of mineral nutrients, clogging of feeding apparatus of pelagic suspension feeders, reduced buoyancy of plankton, reduced visibility interfering with predators hunting on sight, and toxic effects of trace metals released from ore particles (Helmons et al. 2022). Eventually, the seafloor ore will be transported to land-based processing plants (Hein et al. 2020). Once the ore is transported to surface, the same potential environmental impacts that presently exist at such plants will apply to seabed-ore processing (Hein and Koschinsky 2014; Hein et al. 2020).

1.4. Previous description of Mn nodules in Peru and Chile

Potential marine resources and areas of great economic interest have been reported within the Chilean EEZ (total of 4,264,560 km^2), where offshore manganese nodules are abundant (Table 1; Fig. 3; García et al. 2020; Toro et al. 2020).

Table 1. Location, depth, and relevant metal contents of manganese nodules within the Chilean EEZ. Data from García et al. (2020) and Toro et al. (2020).

Location	**Depth** ***(m)***	**Cu+Ni** ***(wt%)***	**Comments**
Robinson Crusoe Island	3,820	-	Ni + Co + Cu grade of 0.87 wt%
Mouth of Rio Loa	4,332	1.38	-
Juan Fernandez Ridge	3,650-3,873	0.25-0.96	-
San Francisco and San Antonio Islands	3,820	0.53	Fe, Mn, and Co grades of 19.8 wt%, 14.6 wt%, 0.31 wt% Co respectively
Northern Chile	4,332	1.38	Zn grade of 0.81 wt%
Salas and Gomez Islands	2,890	0.60	Fe grade of 18.8 wt%
Southern Chile	3,767-4,007	0.30-0.57	Mn grades of 7.99-16.6 wt% and Co grades of 0.16- 0.53 wt%

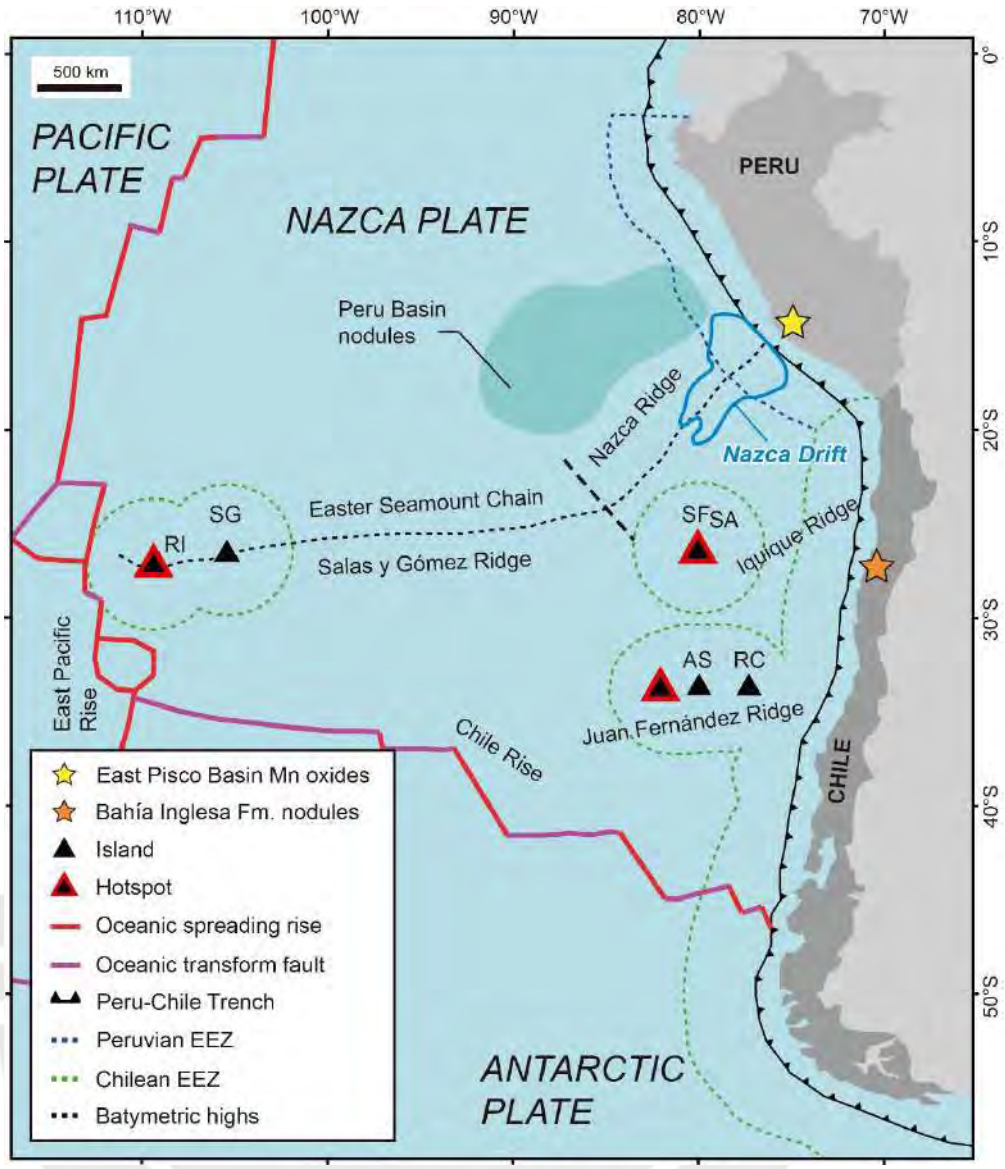

Figure 3. Locations of potential marine resources of the Chilean and Peruvian EEZ, including offshore and onshore manganese nodules. Adapted from García et al. (2020) and Toro et al. (2020). Delimitation of Nazca Ridge and Nazca Drift from Calvès et al. (2022). Abbreviations: RC = Robinson Crusoe Island; SF = San Félix Island; SA = San Ambrosio Island; RI = Rapanui Island; SG = Salas y Gómez Island; AS = Alejandro Selkirk Island.

Onshore (i.e., situated on land) manganese nodules are described within the Miocene Bahía Inglesa Formation in north-central Chile (Fig. 3; Achurra et al. 2009). This unit consists of mudrock, sandstone, and coquinas along with volumetrically minor diatomite, phosphorite, conglomerate, and breccia, and is interpreted as continental shelf to slope deposit (Achurra et al. 2009). The two

identified nodule-hosting stratigraphic units consist of silty mudstone cut by gypsum veins. Achurra et al. (2009) described basal nodules with discoidal to spherical shapes or replacing trace fossils (e.g., Ophiomorpha), and upper nodules of mainly botryoidal shape. According to these authors, manganese nodules in this locality show a nucleus composed of quartz, plagioclase, and Mn oxides, surrounded by a massive layer of silicate minerals and siliceous microorganisms (e.g., diatoms) cemented by Mn oxides, chiefly todorokite and trace amounts of cryptomelane. Achurra et al. (2009) proposed the classification of the Mn-oxide mineralization in the Bahía Inglesa Formation in a newly defined class that the authors coined *"supergene, intermediate marine (partially restricted basin) nodules"*.

Offshore manganese nodules have also been reported in the Peru Basin (Fig. 3), an oceanic basin located 3,000 km off the Peruvian coast at water depths of 3,900-4,300 m (Glasby 2013; Toro et al. 2020). They present an average seafloor density above 10 kg/m^2 reaching a maximum of 53 kg/m^2 (Glasby 2013). Manganese nodules from the Peru Basin are large (up to 190 mm in diameter), mamillated, friable, and contain fragments of fish bones or broken nodules as nucleus (Glasby 2013). Nodules in the Peru Basin are primarily diagenetic, composed of a 10 Å manganate, and yield average Mn/Fe of 4.7 (Glasby 2013). Noteworthy, they are characterized by high Ni (up to 1.30 wt%) and Li (up to 311 ppm) contents (Hein and Koschinsky 2014).

On the other hand, onshore manganese nodules have been described in the Peruvian coast, specifically in the forearc Pisco Basin (region of Ica; 14°22'S, 75°37'W). Bessler (1975) studied manganese nodules hosted in numerous

diatomite horizons within a 20-30 m stratigraphic sequence of the Pisco Formation. These authors described that the manganese nodules are friable and dendritic to irregular in shape. Their sizes range from some millimeters to 10 cm. Under the optical microscope, they are inhomogeneous and irregular and show inclusions of diatom shells. Chemical analyses on nodules within the Pisco Formation reported by Bessler (1975) yield Mn/Fe ratios between 17 and 22, and Ni, Co, and Cu contents with maximum values of 1,680, 1,950, and 440 ppm, respectively.

1.5. Conundrum

Deep-sea manganese nodules are seen as potential mineral resources for high- and green-tech metals (e.g., Hein and Koschinsky 2014; Lusty and Murton 2018; Hein et al. 2020; Garcia et al. 2020). Despite the great endeavor to develop extraction techniques (Sparenberg 2019), the recovery of manganese nodules from the seabed is still considered an environmental and social challenge (Cunningham 2022). Further, the International Seabed Authority has no defined exploitation regulations yet. Therefore, onshore manganese nodules appear as a promising alternative source for critical metals, such as Co, Ce, Pt, and Li. However, detailed studies of the aforementioned elements in on-land manganese oxides, including nodules, are limited (e.g., Achurra et al. 2009), particularly in those of the Pisco Formation in Peru (e.g., Bessler 1975).

1.6. Objectives

General objective:

- To assess the origin and economic potential for critical metals of Mn-oxide mineralization in the Pisco Formation in the onshore forearc Pisco Basin, Peru

Specific objectives:

- To contextualize the stratigraphy and geodynamic setting of manganese oxides;
- To determine the morphologies, mineralogical composition, and petrographic characteristics of manganese oxides;
- To survey major, minor, and trace element contents of manganese oxides;
- To propose a genetic model and discuss the formation conditions of Mn-oxide mineralization; and
- To evaluate the economic potential of the Mn-oxide mineralization, focusing on their critical metal contents.

1.7. Hypothesis/hypotheses

Based on previous regional mapping by the Peruvian Geological Service (León and Torres 2003), onshore manganese nodules studied in this thesis are expected to be hosted by the Mio-Pliocene Pisco Formation.

Traditional genetic models describe that manganese nodules form by precipitation of Fe oxyhydroxides and Mn oxides in deep-sea environments, generally at water depths of about 4,000-6,500 m. However, the East Pisco

Basin is considered a shallow-water embayment (Di Celma et al. 2016). Hence, manganese nodules in the Pisco Formation may have formed by processes distinct from those of deep-sea nodules.

Finally, since manganese nodules are typically enriched in elements of economic interest (e.g., Co, Te, Ce, Pt, Ni, Cu, and Li; Hein and Koschinsky 2014; Hein et al. 2020), onshore manganese nodules, and probably other Mn-oxide facies, in the Pisco Formation may present high contents of one or more of these elements.

1.8. Justification

Offshore manganese nodules have been used as paleoenvironmental indicators in a number of studies (e.g., Hlawatsch et al. 2002, Vineesh et al. 2009, Zhang et al. 2019), but have been hardly studied in onshore sites (e.g., Achurra et al. 2009). The present study aims to reduce this gap of knowledge and complement the only previous work carried out on onshore manganese nodules in Peru (i.e., Bessler 1975). Particularly, onshore manganese oxides in the Pisco Formation might have formed under distinct processes compared to deep-seabed nodules. The present study will discuss tailored genetic models for the genesis of manganese oxides in the study area.

From an economic perspective, the search for alternative sources of critical raw materials of mineral origin has been driven by the need to develop high-technology industries and green energy to support growing populations and urbanization (Hein et al. 2020). In this context, the present study will assess the potential economic interest of onshore Mn-oxide mineralizations in Peru.

Moreover, this study aims to develop exploration guidelines for onshore manganese nodule deposits, with particular focus on critical metals.

2. GEOLOGICAL SETTING

2.1. Cenozoic forearc basins of the Peruvian margin

The tectonic regime of the Peruvian margin is controlled by the oblique subduction of the Nazca/Farallon Plate underneath the South American Plate along the Peru-Chile Trench since Cretaceous times (Di Celma et al. 2017). The Nazca Ridge, a bathymetric high delineated by multiple seamounts (Casalbore 2018), is being subducted beneath the South American Plate since at least the end of middle Miocene (~11.2 Ma) and interacts with the active convergent margin enhancing tectonic erosion (Hampel 2002; Clift et al. 2003). Another important geological feature is the Nazca Drift System, which extends from the southwest of the Nazca Ridge to the Peru-Chile Trench at water depths between 2,090 and 5,330 m above the abyssal basins of Peru and Chile and stands as the largest abyssal drift system of the Pacific Ocean (Calvès et al. 2022).

Along the Peruvian continental margin, subparallel to Andean trends, two persistent structural ridges named Outer Shelf High (traced as Coastal Cordillera in onshore locations) and Upper Slope Rise controlled the geometry and distribution of Cenozoic forearc basins. These include the Talara, Sechura, Salaverry, Trujillo, Lima, East Pisco, West Pisco, Moquegua, and Mollendo basins (Fig 4; Thornburg and Kulm 1981).

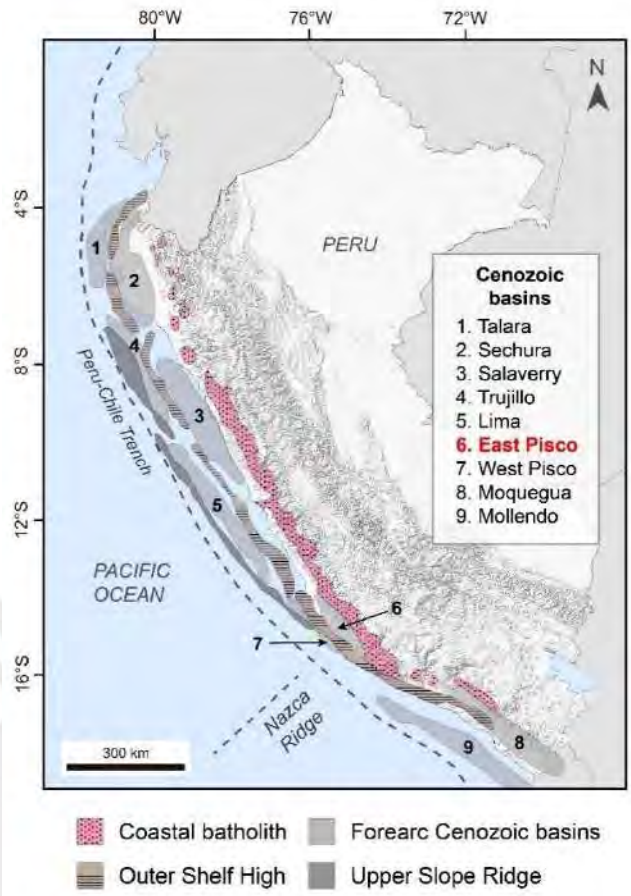

Figure 4. Major Cenozoic forearc basins along the Peruvian margin. The Coastal Cordillera is traced onto the offshore as an Outer Shelf High. Modified from Thornburg and Kulm (1981) and Ochoa et al. (2021).

The Eocene to Pliocene Pisco Basin, which extends from 13° to 15° S (León et al. 2008; Di Celma et al. 2016; Viveen and Schlunegger 2018), is part of the central and southern portions of the Peruvian forearc that were influenced by the passage of the aseismic Nazca Ridge since ~ 4-5 Ma (Macharé and Ortlieb 1992; Hampel 2002; Espurt et al. 2007; George et al. 2022). The Pisco Basin is divided into two sub-basins, West Pisco and East Pisco, which are separated by the Outer Shelf High (Fig 4; Thornburg and Kulm 1981; Quispe et al. 2018) probably since the late Oligocene (Ochoa et al. 2021).

The East Pisco Basin, where the study area is located, corresponds to the onshore portion of the basin (Fig. 4; Gioncada et al. 2018; Di Celma et al. 2022).

The sedimentary fill of the East Pisco Basin (Fig. 5) is divided in two megasequences by Di Celma et al. (2022), namely the megasequence P (Paleogene) and megasequence N (Neogene). These major sequences overlie a deformed and heterogeneous pre-Cenozoic basement, which includes Paleozoic to Mesozoic intrusive, Jurassic volcano-sedimentary series, and Proterozoic metamorphic rocks (León et al. 2008; Di Celma et al. 2017). The megasequence P consists of middle Eocene to lower Oligocene sedimentary successions, including medium- to coarse-grained sandstone with some bioclasts that pass stratigraphically upward into siltstone (Dunbar et al. 1990; León et al. 2008; Di Celma et al. 2022). In the other side, the megasequence N comprises uppermost Oligocene to Pliocene sandstone and siltstone from the Chilcatay Formation, and sandstone with minor content of fossils, and diatomaceous and tuffaceous siltstone from the Pisco formation (Dunbar et al. 1990; León et al. 2008; Di Celma et al. 2022). On top of the stratigraphic sequence, the East Pisco Basin is sealed by Quaternary conglomerates deposits of the Cañete Formation (León et al. 2008; Ochoa et al. 2021). Overall, the East Pisco Basin is interpreted as a semi-enclosed, shallow embayment (Di Celma et al. 2016).

The structural framework of the East Pisco Basin exhibits numerous, predominantly Paleogene NW–oriented normal faults and rotated blocks associated to grabens and semi-grabens (Macharé 1987; Rustichelli et al. 2016; Viveen and Schlunegger 2018). The tectonic regime under which the East Pisco Basin was formed is not totally defined yet. Some authors state alternating phases of compression and transtensional tectonics, and prolonged subsidence during the Paleogene and Neogene, with uplift and compression occurring during the Quaternary because of the arrival of the Nazca Ridge (Clift et al.

2003; Léon et al. 2008; Viveen and Schlunegger 2018; Di Celma et al. 2022). In contrast, other authors suggest a continuous compressional regime from the late Oligocene to the Quaternary associated with Andean shortening (Quispe et al. 2018; Ochoa et al. 2021).

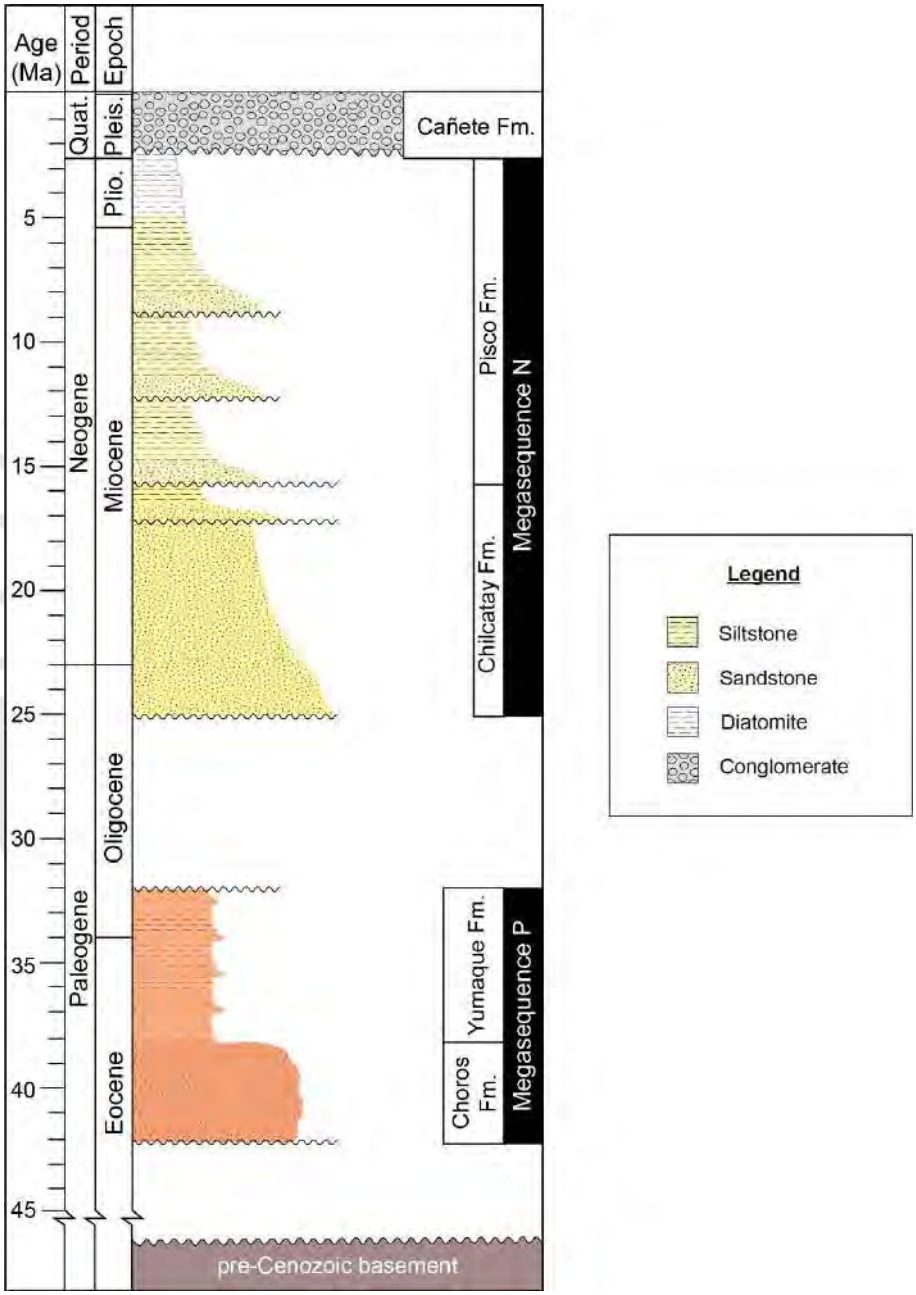

Figure 5. Regional stratigraphic column of the East Pisco Basin based on geological observations from Dunbar et al. (1990), León et al. (2008), Di Celma et al. (2016), Di Celma et al. (2017), Di Celma et al. (2018a, b), Ochoa et al. (2021), and Di Celma et al. (2022).

2.2. The Chilcatay and Pisco formations

The studied manganese oxides are hosted by the Chilcatay and Pisco formations in the East Pisco Basin. The Late Oligocene to Early Miocene Chilcatay Formation (DeVries and Jud 2018) consists predominantly of basal massive sandstone and large boulders of pre-Cenozoic basement rocks, followed by marine diatomaceous and tuffaceous sandy siltstone (Di Celma et al. 2018a). In the study area, the exposure of the Chilcatay Formation is restricted to the sides and bottom of the Rio Grande Valley and has an estimated thickness between 150 and 320 m (Fig. 6). There, it consists of minor bioturbated and fossil-bearing sandstone interbedded with coarse-grained sandstone, conglomerate, biogenic mudstone, and siltstone (León et al. 2008). The base of this sequence corresponds to a strong erosional surface related to incised valleys.

The Mio-Pliocene Pisco Formation (Ochoa et al. 2021) is one of the main lithostratigraphic units of the East Pisco Basin. It discontinuously stretches from 13.5° to 15.6° S (Dunbar et al. 1990; Léon et al. 2008; Di Celma et al. 2018b). This marine formation mainly consists of sandstone, siltstone, and diatomite, along with minor amounts of tuff and dolostone, the latter of which contains an outstanding collection of vertebrate fossil fauna (Di Celma et al. 2016; Ochoa et al. 2021). The Pisco Formation covers most of the study area in the Rio Grande Valley (Fig. 6) with an estimated thickness of 370 m. There, it unconformably overlies the Chilcatay Formation, and it is strongly eroded and covered by Quaternary deposits of the Cañete Formation in its upper part (León et al. 2008; Ochoa et al. 2021). Within the study area, the Pisco Formation mainly consists of sandstone, siltstone, and diatomite, along with minor

amounts of tuff and dolostone (Di Celma et al. 2016; Ochoa et al. 2021). Tuffaceous diatomite and tuff correspond to the Nazca volcanic event (Di Celma et al. 2016). The clastic sequence in the Pisco Formation has been interpreted as a succession of transgressive depositional sequences triggered by tectonic changes during the Miocene-Pliocene (Di Celma et al. 2018).

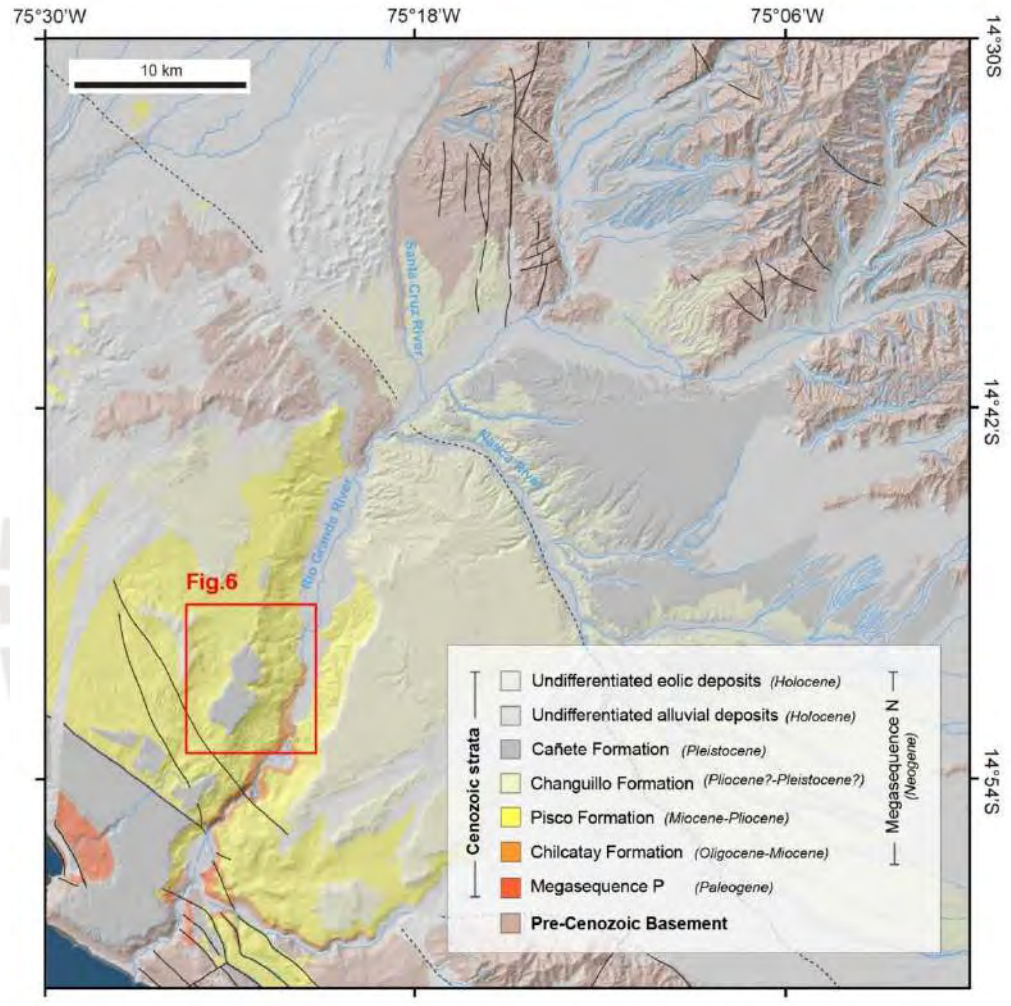

Figure 6. Regional geological map of the Rio Grande Valley (modified from León and Torres 2003). The red rectangle indicates the location of the study area. Digital Elevation Model (DEM) provided by the European Space Agency (2024).

The Rio Grande Valley is one of the least studied sites of the central Peruvian forearc despite its favored position in front of the Nazca Ridge. Since there is very limited geochronological data within this area and there are not evident

criteria to establish contacts between formations, modifications of previous works are required, as it will be shown later in this study.

3. SAMPLING AND ANALYTICAL METHODS

3.1. Sampling

This study is based on 65 representative surface samples collected from the Rio Grande Valley near the town of Palpa (Ica Region, southern Peru). A detailed list with individual hand-sample descriptions and sampling locations is provided in Appendix A. The location of the samples is shown in Figure 7.

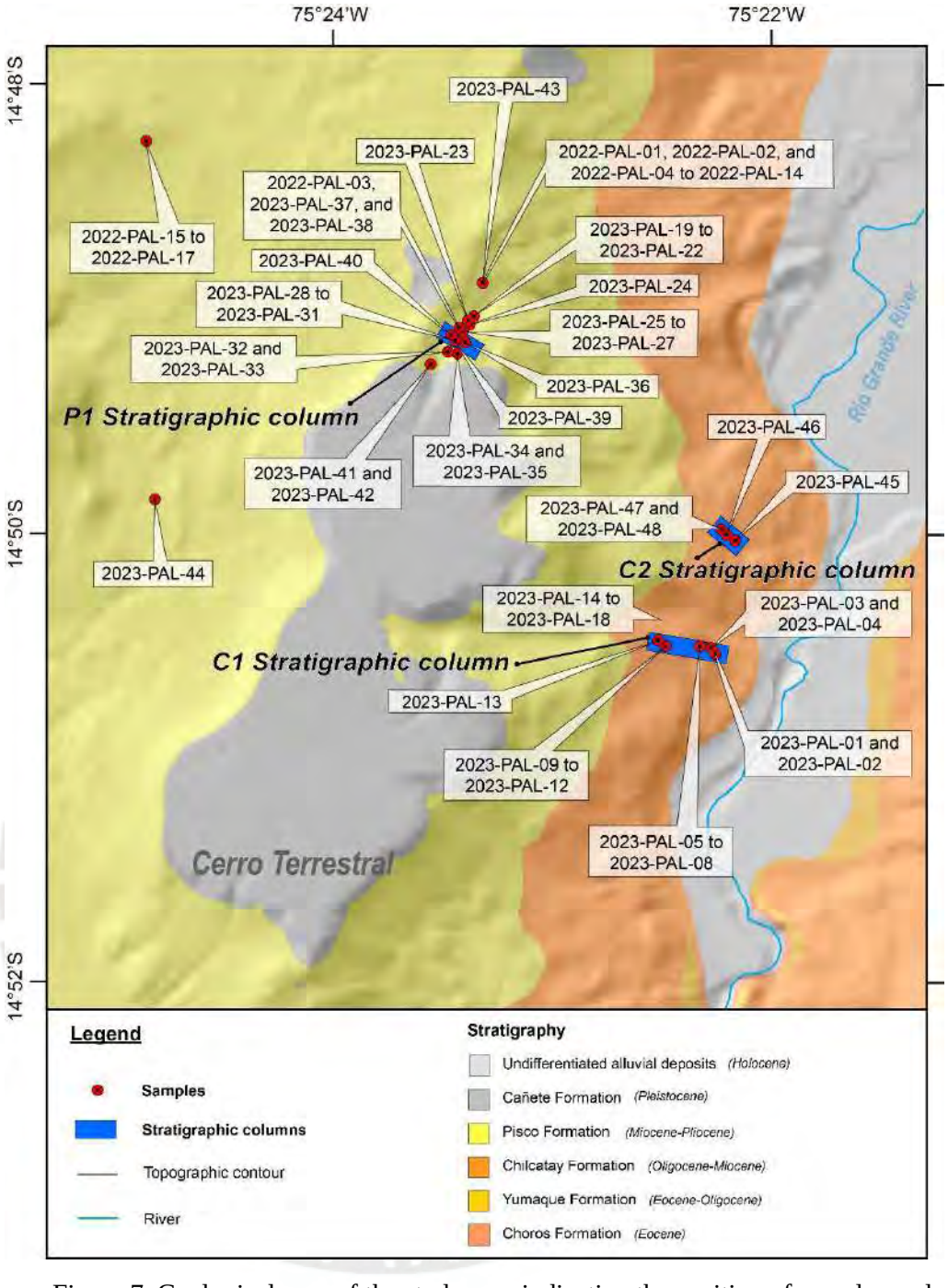

Figure 7. Geological map of the study area indicating the position of samples and stratigraphic columns. The geology base map has been modified from León and Torres (2003) according to our own field observations. Digital Elevation Model (DEM) provided by the European Space Agency (2024).

The stratigraphic position of the studied Mn oxide samples is contextualized in three stratigraphic columns produced in this thesis. The stratigraphic columns cover segments of the Chilcatay (columns C1 and C2) and Pisco (column P1)

formations in the surroundings of Cerro Terrestral (approx. coordinates: 14° 51.2'S, 75° 24.3’W) and show in detail the lithology, granulometry, and sedimentary structures. True thickness of strata was measured with a measuring tape. The dip and dip direction measurements were taken with FieldMove Clino© app (property of Petroleum Experts Limited). The stratigraphic columns are provided in the Results section.

3.2. X-Ray diffraction (XRD)

For XRD analysis, the samples were crushed with a hammer until small fragments were obtained. Rock fragments were then manually ground in an agate mortar to obtain a very fine powdered material <35 µm. The powdered material was pressed using a glass plate to obtain a flat surface in cylindrical standard sample holders of 16 mm in diameter and 2.5 mm in height. XRD data were collected with a Bruker D8 Discover diffractometer in Bragg-Brentano θ/2θ geometry of 240 mm of radius at the “Centro de Caracterización de Materiales” of PUCP (CAM-PUCP). Scanning from 4 to 80 º (2θ) was performed at a step size of 0.039° and a scan time of 4 s per step. Nickel filtered Cu Kα radiation (k = 1.5418 Å) and 40 kV–40 mA conditions were used.

The software PANalytical X’Pert Highscore 2.0.1 was used to subtract the background of the patterns, detect the peaks, and assign mineral phases to each peak. The results of the XRD analyses are provided in Appendix B.

3.3. Optical microscopy

A total of 14 thick polished sections and 3 thin sections were prepared at the QEMSCAN laboratory of PUCP and at the Servei de Làmina Prima of the

University of Barcelona respectively for their petrographic study. The petrography was performed using transmitted and reflected light in a Zeiss Primotech polarizing microscope at the Laboratory of Geology at PUCP.

Individual petrographic descriptions and photomicrographs of the studied polished and thin sections are provided in Appendix C.

3.4. Electron probe microanalysis (EPMA)

Major and minor element analyses of manganese oxide minerals were performed at the *Centres Científics i Tecnológics de la Universitat de Barcelona* (CCiTUB) using a JEOL JXA-8230 electron microprobe equipped with five wavelength-dispersive spectrometer (WDS) detectors. The accelerating voltage was set to 15 kV, with a beam current of 15 nA, and a beam diameter of 1 μm. EPMA's scanning electron microscopy (SEM) was used to acquire microphotographs with operating conditions of 15 kV accelerating voltage in backscattered electron (BSE) imaging mode.

The analyses were performed using the following natural and synthetic standards and lines: diopside (Si, Kα), kyanite (Al, Kα), wollastonite (Ca, Kα), orthoclase (K, Kα), galena (Pb, Mα), barite (Ba, Lα; S, Kα), apatite (P, Kα), periclase (Mg, Kα), albite (Na, Kα), rhodonite (Mn, Kα), hematite (Fe, Kα), metallic Co (Co, Kα), sphalerite (Zn, Kα), cuprite (Cu, Kα), bunsenite (Ni, Kα), and rutile (Ti, Kα). The detection limits (d.l.) for each element were 500 ppm Si, 350 ppm Al, 600 ppm Ca, 450 ppm K, 1,500 ppm Pb, 900 ppm S, 1,000 ppm P, 500 ppm Mg, 550 ppm Na, 800 ppm Mn, 700 ppm Fe, 650 ppm Co, 1,350 ppm Zn, 950 ppm Cu, 725 ppm Ni, 850 ppm Ti, and 1,500 ppm Ba.

Chemical compositions of analyzed minerals are reported in weight per cent (wt%) in Appendix D.

3.5. Geochemistry

A complete characterization of the chemical composition of the Mn oxides was performed at ALS Vancouver using the analytical packages ME-XRF26s and CCP-PKG01. The package ME-XRF26s is designed for chromite and manganese ores and is suitable for the determination of major and minor elements in mineralized samples that require a high dilution digest. The samples were fused with a 12:22 lithium metaborate flux and then poured into a platinum mold. The resultant fused disks were analyzed by XRF spectrometry. This method also included LOI calculation at 1000°C.

The package CCP-PKG01 comprises five methods: i) major elements by ICP-AES analysis following a combination of fusion and acid digestion plus LOI calculation by furnace or TGA; ii) trace elements by ICP-MS analysis following a combination of fusion and acid digestion; iii) total carbon and sulfur by induction furnace/IR; iv) base metals by ICP-AES analysis following a four-acid digestion; and v) volatile trace elements by ICP-MS analysis following an aqua-regia digestion.

A full dataset of whole-rock chemical compositions of the analyzed samples is available in Appendix E.

4. RESULTS

4.1. Stratigraphic position and facies of Mn nodules

4.1.1. Stratigraphic column C1

The stratigraphic column C1 (Fig. 8) covers a segment of the Chilcatay Formation in the surroundings of Cerro Terrestral in the left margin of the Rio Grande River (Fig. 7; approx. coordinates: 14° 50.5' S, 75° 22.2' W).

This 185-m-thick, upward-fining sequence is primarily composed of siltstone and silty clay, interrupted by one erosional conglomerate surface and two well-developed tuff levels. Upwards in the stratigraphic section, interbedded sandstone and siltstone are frequent, with common occurrence of slump folds and minor occurrence of bivalves and tree logs.

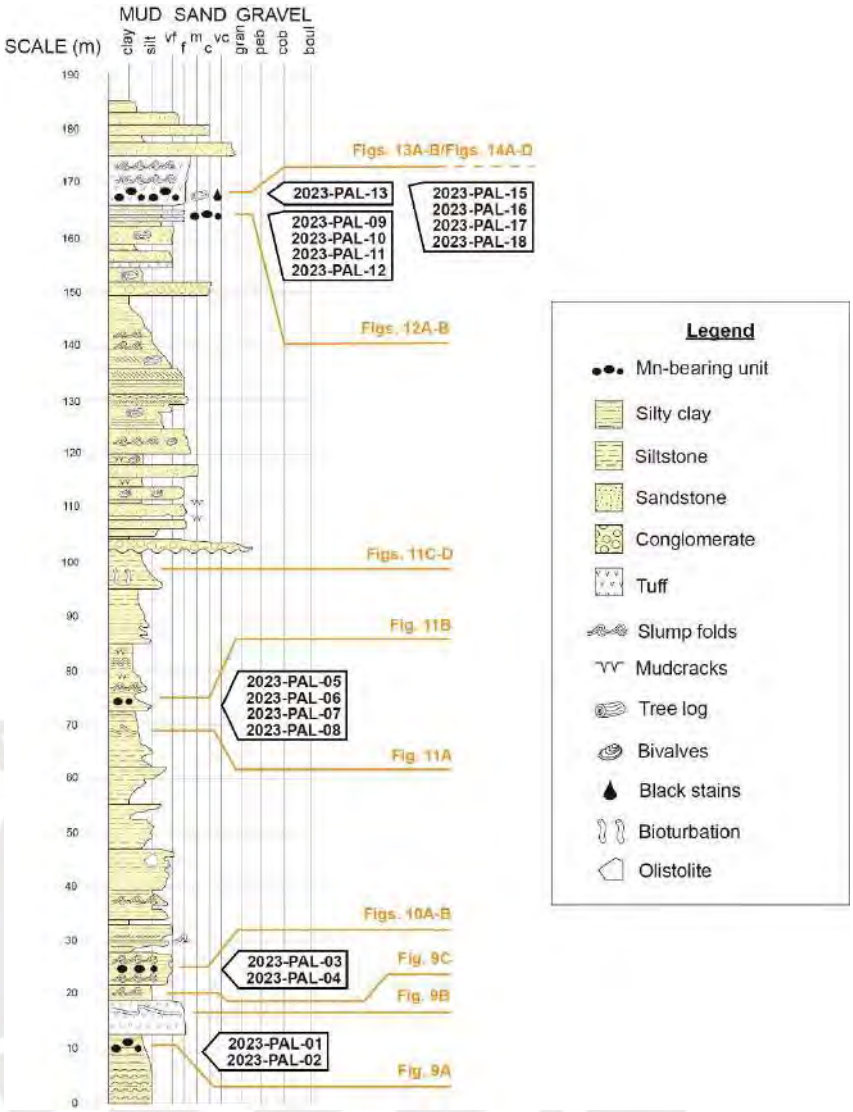

Figure 8. Stratigraphic column C1 with the position of samples and field observations illustrated in Figures 9 to 14.

The section embraces five sampling stratigraphic levels. In the first sampling level, a non-continuous Mn coating (Fig. 9A) is accreted onto a 13-m-thick siltstone level interbedded with silty clay. This unit is overlain by a 20-cm-thick brownish silty clay followed by a 6-m-thick folded tuff (Fig. 9B), which grades upward into a tuffaceous siltstone showing slump folds (Fig. 9C).

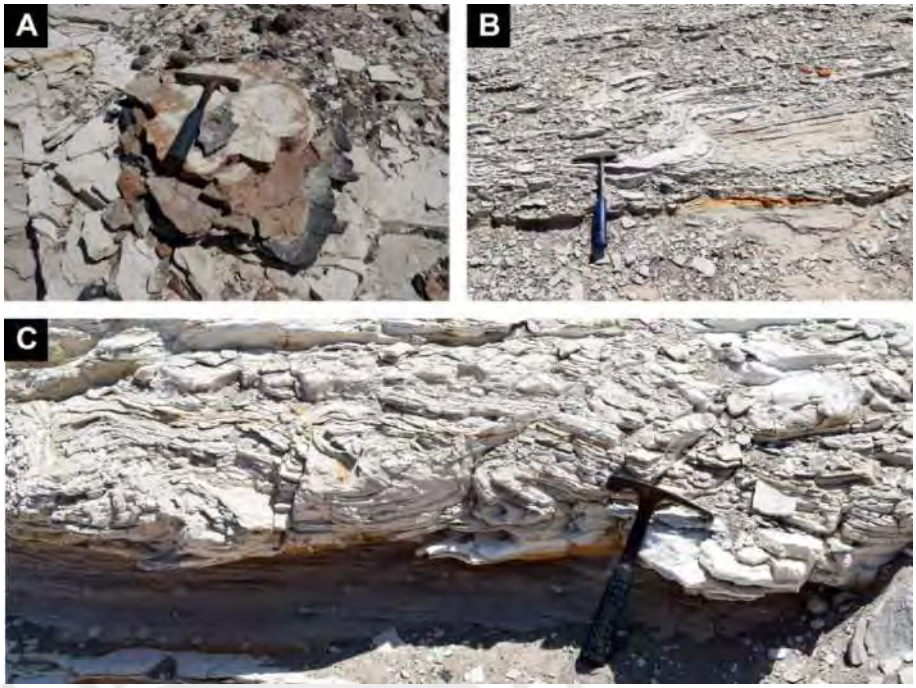

Figure 9. Sampling level 1 in stratigraphic column C1. (A) 7-mm-thick Mn coating accreted onto siltstone. The samples 2023-PAL-01 and 2023-PAL-02 were collected from this level. (B) Centimeter-scale slump folds in tuff level. (C) Decimeter-scale slump folds in tuffaceous siltstone.

The second sampling level consists also of a non-continuous Mn coating (Figs. 10A-B) accreted onto whitish, sandy siltstone. The sandy siltstone presents scarce Mn micronodules immediately below the Mn coating.

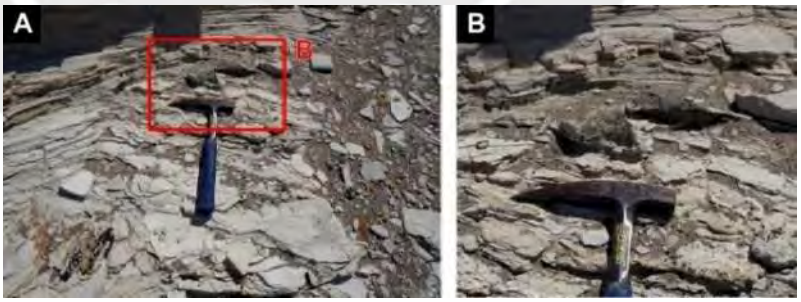

Figure 10. Sampling level 2 in stratigraphic column C1. (A) 5-mm-thick, rough Mn coating accreted onto sandy siltstone. The samples 2023-PAL-03 and 2023-PAL-04 were collected from this level. (B) Close-up view of the Mn coating.

In the third sampling level, a whitish, cross-bedded tuffaceous siltstone to silty clayey mudstone unit is topped by horizontal stratification in its

upper 4 m (Fig. 11A). Non-continuous Mn coatings are accreted onto folded tuffaceous silty clay (Fig. 11B), which grades up to horizontal stratified sandy siltstone with ichnofacies (Fig. 11C). The sandy siltstone is interrupted by a 1-m-thick, poorly-sorted conglomerate (Fig. 11D).

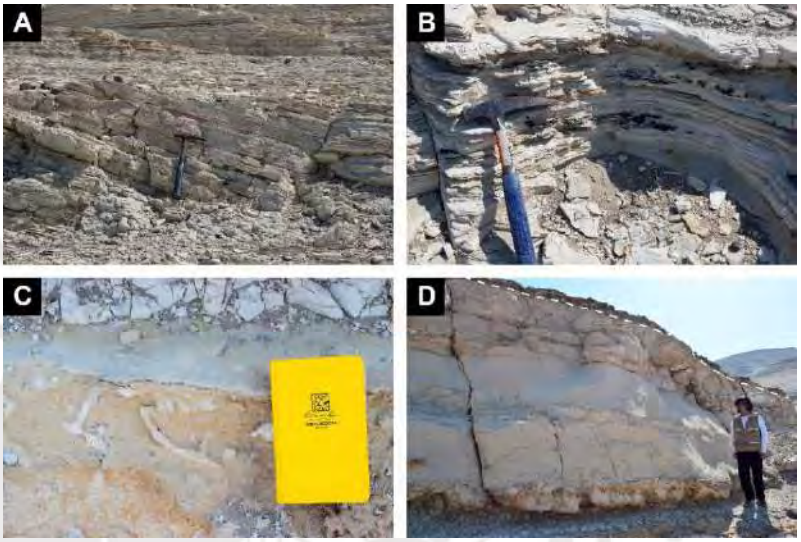

Figure 11. Sampling level 3 in stratigraphic column C1. (A) Cross-bedded tuffaceous siltstone topped by horizontal stratification. (B) Rough Mn coatings with variable thickness (8 to 15 mm) accreted onto tuffaceous silty clays. The samples 2023-PAL-05 to 2023-PAL-08 were collected from this level. (C) Ichnofossils in sandy siltstone. (D) Siltstone uncomfortably overlain by a poorly-sorted conglomerate (white dashed line).

The fourth sampling level comprises abundant Mn micronodules within a 0.30-m-thick, light-beige sandy siltstone (Figs. 12A-B). This level is overlain by a 0.50-m-thick tuff followed by 0.50 m of sandy siltstone.

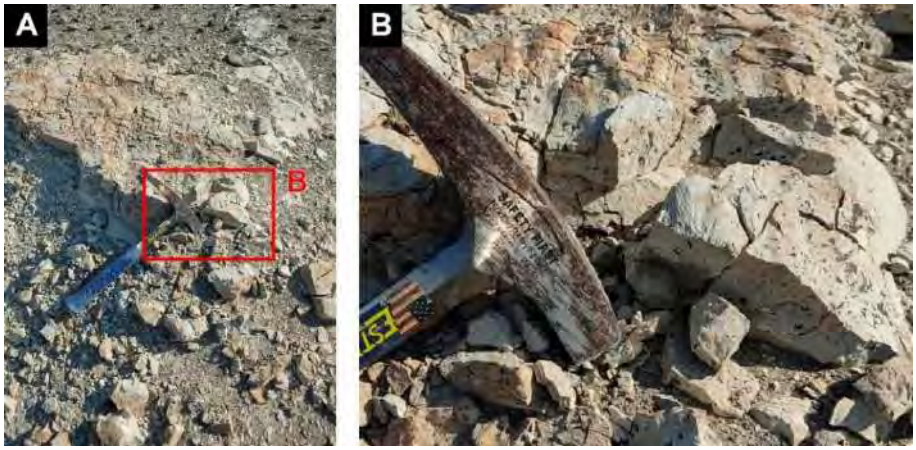

Figure 12. Sampling level 4 in stratigraphic column C1. (A) Sandy siltstone with Mn micronodules. The samples 2023-PAL-09 to 2023-PAL-12 were collected from this level. (B) Close-up view of the Mn micronodules.

Immediately above is the fifth sampling level, where large (up to 15 cm) sandy manganese nodules with rounded sandy nuclei (Figs. 13A-B) are hosted by whitish tuff. The tuff shows slump folds in its upper portion (Fig. 13A).

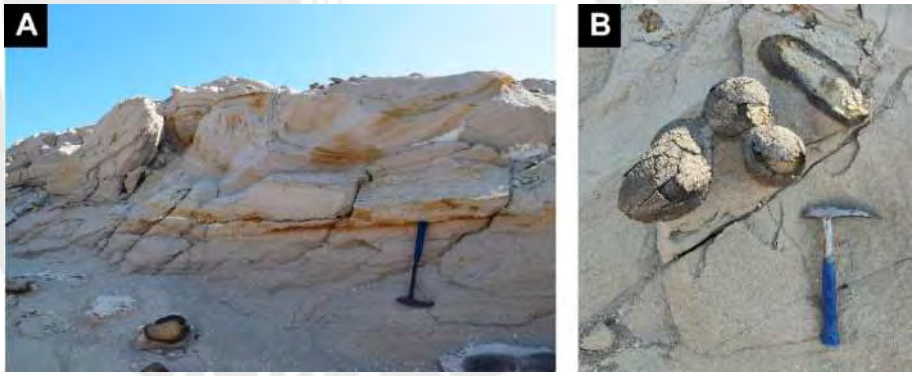

Figure 13. Sampling level 5 in stratigraphic column C1. (A) Manganese-nodules-bearing tuff with slump folds in its upper portion. The sample 2023-PAL-13 was collected from this level. (B) View of the sandy Mn nodules and their sandy nuclei.

Approximately at the same altitude (~320 m.a.s.l.) of the last two sampling levels, yet located 200 m farther N, Mn veins (i.e., fracture fillings) and nodules (Figs. 14A-B) occur in tuff intercalated with minor fine-grained sandstone. It is noteworthy that Mn-bearing tuff in this level

characteristically shows oily black stains (Fig. 14C) possibly linked to liquid hydrocarbons flow. The tuff is overlain by coarse-grained sandstone with nodular gypsum (Fig. 14D). Some nodular gypsum presents scarce Mn filling.

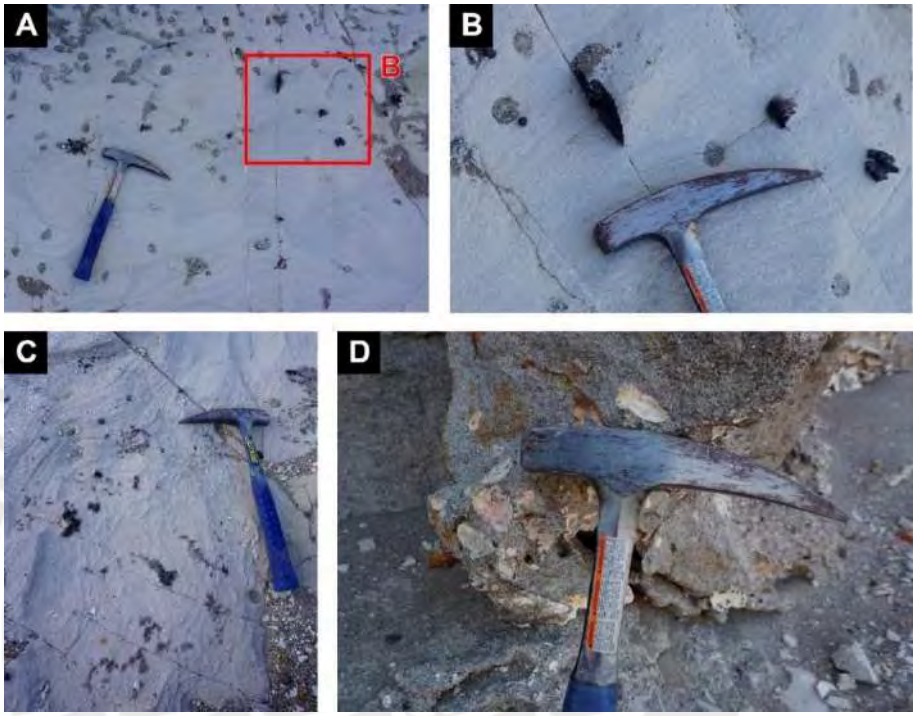

Figure 14. Sampling level 5 in stratigraphic column C1 (offset). (A) Botryoidal Mn nodules and Mn veins in tuff. The samples 2023-PAL-15 to 2023-PAL-17 were collected from this level. (B) Close-up view of the botryoidal Mn nodules and veins. (C) Oily black stains in tuff possibly associated to hydrocarbon migration. (D) View of nodular gypsum in a coarse-grained sandstone. The sample 2023-PAL-18 was collected from this level.

4.1.2. Stratigraphic column C2

The stratigraphic column C2 (Fig. 15) covers a segment of the Chilcatay Formation in the surroundings of Cerro Terrestral in the left margin of the Rio Grande River (Fig. 7; approx. coordinates: 14° 50.0' S, 75° 22.1' W). This 38-m-thick, poorly-exposed sequence is mainly composed of

silty clay and siltstone, with minor sandstone. In the upper half of this section, fibrous gypsum veins are abundant.

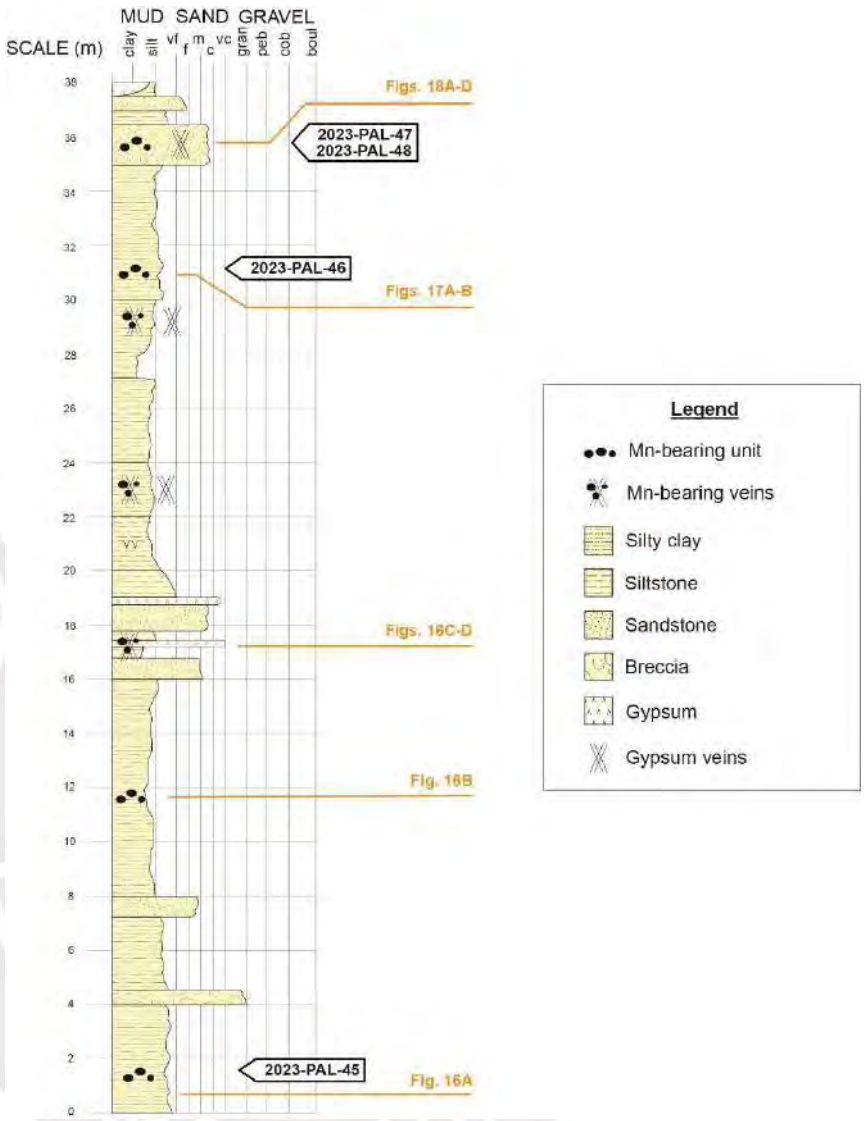

Figure 15. Stratigraphic column C2 with the position of samples and field observations illustrated in Figures 16 to 18.

The section comprises three sampling stratigraphic levels. The first sampling stratigraphic level consists of massive Mn nodules and botryoidal composite Mn concretions hosted by sandy siltstone (Fig. 16A). Close to this sampling level, abundant fragments of Mn nodules of a few centimeters in size accumulate in the stone pavement (Fig.

16B). Next, sandstone and siltstone intercalate with thin, fibrous gypsum levels (Figs. 16C-D). Above this level, Mn nodules accumulate in silty clays crossed by fibrous gypsum veins, some of which are accreted by Mn oxides.

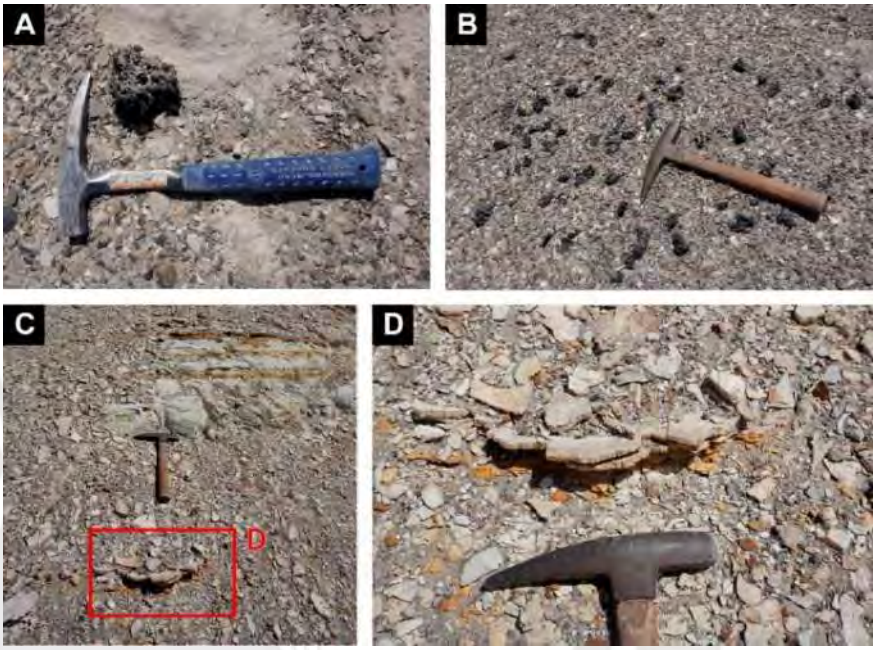

Figure 16. Sampling level 1 in stratigraphic column C2. (A) Botryoidal Mn concretions in sandy siltstones. The sample 2023-PAL-45 was collected from this level. (B) Fragmented Mn nodules in rock pavement. (C) Thin, horizontal, fibrous gypsum levels. (D) Close-up view of fibrous gypsum.

The second sampling level is a 7-cm-thick Mn coating accreted onto poorly-exposed silty clays (Figs. 17A-B). Silty clay beds are interrupted by sandstone, which hosts abundant spherical Mn nodules (Figs. 18A-C) with concentric structures (Fig. 18D) in the third sampling level.

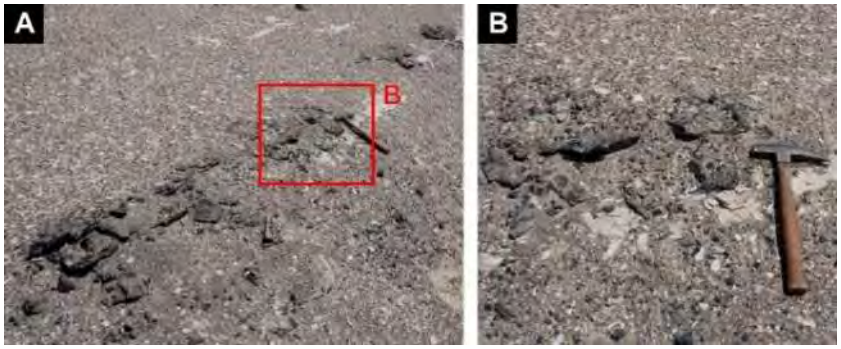

Figure 17. Sampling level 2 in stratigraphic column C2. (A) 7-cm-thick Mn coating in silty clays. The sample 2023-PAL-46 was collected from this level. (B) Close-up view of the Mn coating.

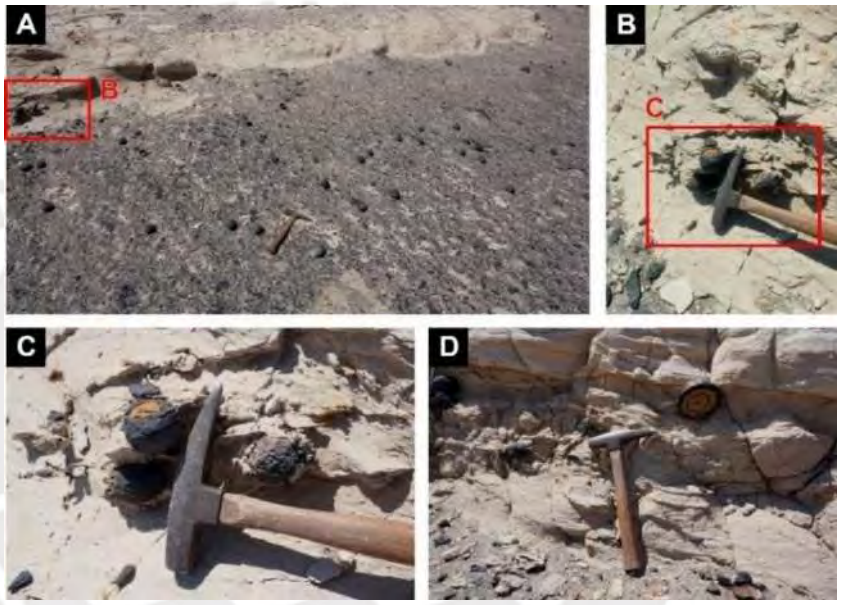

Figure 18. Sampling level 3 in stratigraphic column C2. (A) Spherical Mn nodules in sandstone. The samples 2023-PAL-47 and 2023-PAL-48 were collected from this level. (B-C) Close-up views of spherical Mn nodules. (D) Detail of a fresh cut Mn nodule hosted in sandstone showing concentrical structures.

4.1.3. Stratigraphic column P1

The stratigraphic column P1 (Fig. 19) covers a segment of the Pisco Formation in the surroundings of Cerro Terrestral in the left margin of the Rio Grande River (Fig. 7; approx. coordinates: 14° 49.1' S, 75° 23.4' W). This 47-m-thick section consists of medium-grained sandstone, intercalated with siltstone and silty clay, with abundant fibrous gypsum

veins and occasional occurrence of ichnofossils and tree logs. Some of the sandstone levels change laterally to gypsum beds. The sequence fines upward to whitish diatomite in its upper 10 m and is capped by conglomerate of the Cañete Formation.

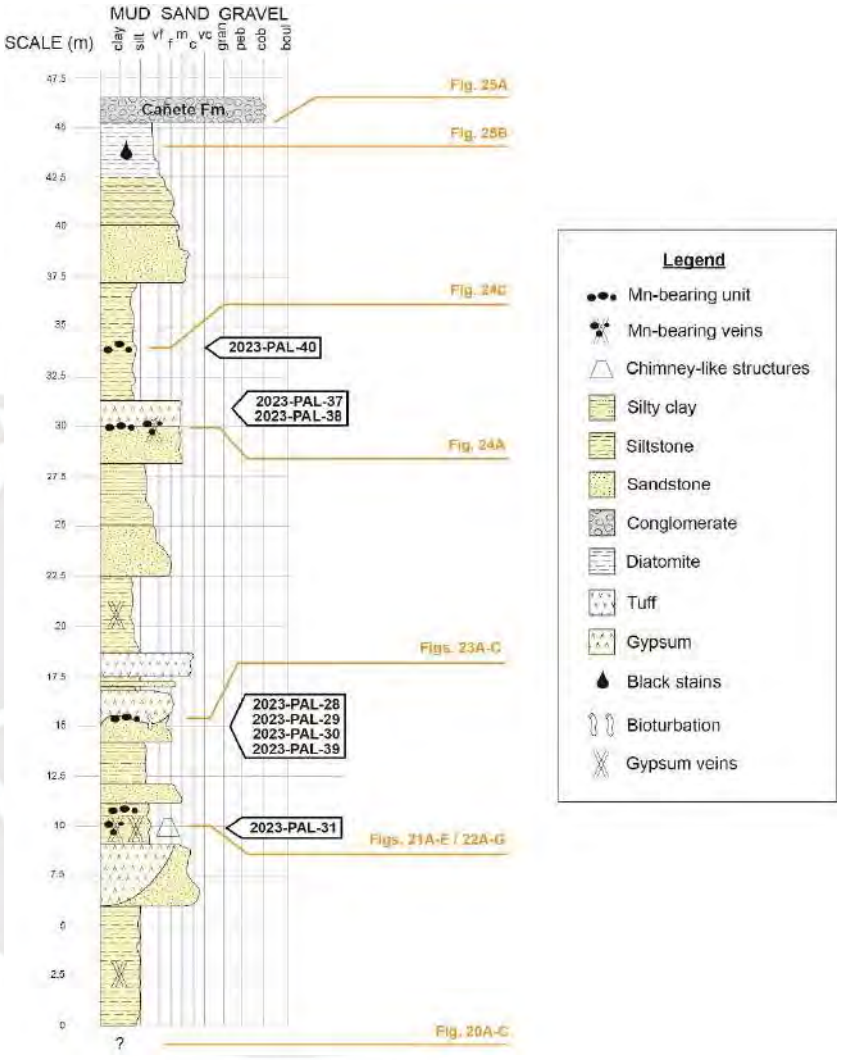

Figure 19. Stratigraphic column P1 with the position of samples and field observations illustrated in Figures 20 to 25. The pictures shown in Figure 20 were taken approx. 20-30 m below the beginning of the stratigraphic column in an area mostly covered by debris. The pictures shown in Figure 22 were taken in an outcrop located at the same stratigraphic level as that photographed in pictures shown in Figure 21, but out of trace of the stratigraphic column.

The first observed occurrence of Mn nodules in the Pisco Formation is located approximately 20-30 m below the base of the P1 stratigraphic column. This sampling level 0 is not included in the stratigraphic column due to the poor exposition of the strata, which are mostly covered by debris close to the valley bottom (Fig. 20A). In level 0, abundant Mn nodules (Fig. 20B) and nodule fragments (Fig. 20C) derived from chimney-like structures accumulate in a continuous desert pavement with a characteristic black color.

Figure 20. Sampling level 0, 20 – 30 m below the stratigraphic column P1. (A) Panoramic view of the sampling level from which the samples 2023-PAL-34 to 2023-PAL-36 were collected. Note the dark color of the valley bottom due to the accumulation of fragments of Mn nodules. (B) Close-up view of ellipsoidal Mn nodules in rock pavement. (C) Close-up view of Mn-nodules fragments accumulating in the valley bottom and constituting a dark desert pavement.

The section P1 embraces four sampling stratigraphic levels. In the first sampling level, continuous fibrous gypsum veins up to 5 cm in thickness are ubiquitous and easily identified due to linear protrusion from the siltstone bedrock (Fig. 21A). The main set of gypsum veins, which also contain Mn nodules and coatings (Figs. 21B-C), strikes NW, whereas

the associated secondary set strikes NE. Fragments of Mn nodules also accumulate around “chimney-like” structures (Figs. 21D-E).

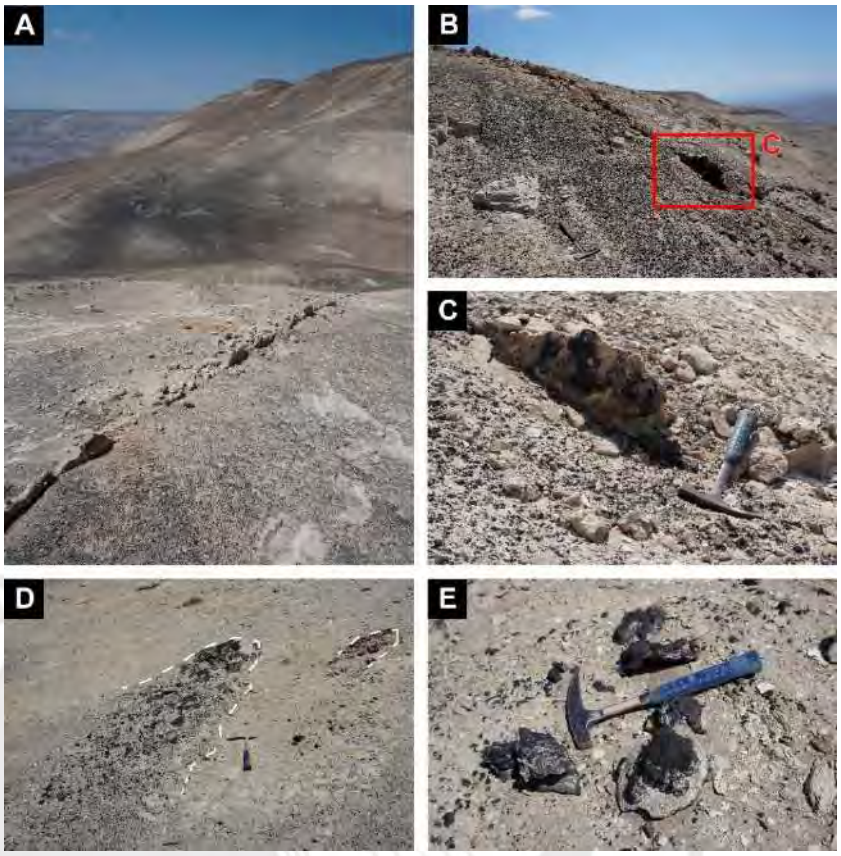

Figure 21. Sampling level 1 in stratigraphic column P1. (A) Fibrous gypsum veins protrude over the siltstone bedrock. (B) Mn nodules accreted onto fibrous gypsum veins. (C) Close-up of Mn nodule accreted onto gypsum. The sample 2023-PAL-31 was collected from this level. (D) Chimney-like structure with Mn nodules accumulations (white dashed lines). (E) Fragments of irregular Mn nodules in a chimney-like structure.

The stratigraphic level containing the nodules in the first sampling level is laterally continuous. Approximately 260 m farther NE, Mn nodules occur scattered in siltstones (Fig. 22A), in “chimney-like” structures (Fig. 22B), and accreted onto fibrous gypsum (Figs. 22C-D). About 300 m farther NE from this location, Mn veins transition abruptly to cm-scale Mn nodules (Fig. 22E). The Mn nodules are also cemented by fibrous gypsum veins (Figs. 22D, F). Manganese nodules appear either

as individual irregular, discoidal, or spherical individual specimens or as botryoidal composite concretions (Fig. 22G).

Figure 22. Sampling level 1 in stratigraphic column P1. The samples 2022-PAL-01 to 2022-PAL-13 (except for 2022-PAL-03) were collected from this level. (A) Manganese nodules scattered in siltstone. The samples 2023-PAL-19 to 2023-PAL-23 were collected from this level. (B) Chimney-like structure with irregular Mn nodules and fragments accumulations. (C-D) Botryoidal Mn composite concretions and coatings accreted onto fibrous gypsum. (E) Manganese-fibrous gypsum veins protruding from siltstone bed. (F) Spherical and discoidal Mn nodules in gypsum veins. (G) Fragment of a composite botryoidal Mn concretion.

The second sampling stratigraphic level is located above a coarse-grained sandstone (Fig. 23A). There, hanging “grape-shaped” Mn nodules and concretions (Fig. 23B) occur in the base of a sedimentary gypsum bed along with abundant ichnofacies (Fig. 23C).

Figure 23. Sampling level 2 in stratigraphic column P2. (A) General view of the outcrop at the sampling level, which consists of medium-grained sandstone overlain by a gypsum bed. “Grape-like” Mn nodules are located right in the contact between these lithologies, from which the samples 2023-PAL-28 to 2023-PAL-30 were collected. (B) Close-up view of hanging “grape-like” Mn nodules and concretions in the contact between sandstone (bottom) and gypsum (top). (C) Close-up view of cm-scale ichnofossil in sandstone.

The third sampling level is located along the contact between medium-grained sandstone and a gypsum bed. In this location, Mn mineralization consists of Mn veins (Fig. 24A). Approximately at the same altitude (~630 m.a.s.l.), yet located 120 m farther NE, Mn veins (Fig. 24B) occur in siltstone. Above the gypsum bed, in the fourth stratigraphic sampling level, trace ichnofossils in siltstone, probably burrows, are replaced by Mn oxides (Fig. 24C).

Figure 24. Sampling level 3 in stratigraphic column P1. (A) Planar to botryoidal Mn veins. The samples 2023-PAL-37 and 2023-PAL-38 were collected from this level. (B) Planar to botryoidal Mn veins concretions in siltstone (sample 2022-PAL-03). (C) Bioturbation fossilized by Mn oxides in siltstone (sample 2023-PAL-40).

The stratigraphic section ends with siltstone fining upward into diatomite, which is in turn unconformably overlain by conglomerate of the Cañete Formation (Fig. 25A). Black stains, possibly linked to liquid hydrocarbon flow, are observed in the diatomite (Fig. 25B).

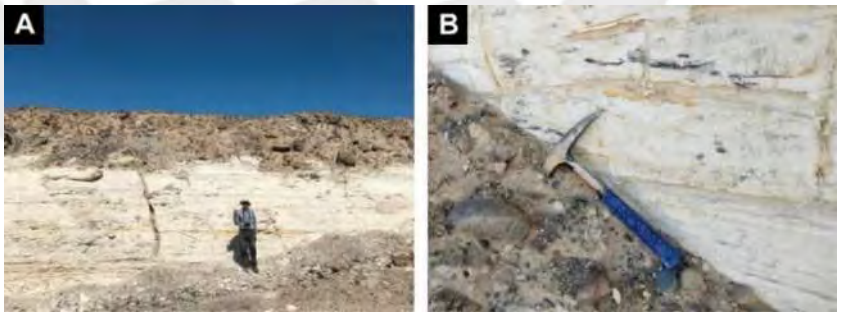

Figure 25. Sampling level 4 in stratigraphic column P1. (A) Diatomites of the Pisco Formation (bright creamy color) uncomfortably overlain by conglomerate of the Cañete Formation (brown color). (B) Oily black stains in diatomite, probably related to hydrocarbon migration. The samples 2023-PAL-41 and 2023-PAL-42 were collected from this level.

4.2. Morphology and textures of the Mn oxide mineralization

The Mn mineralization in both the Chilcatay and Pisco formations in the East Pisco Basin occurs as nodules and concretions, veins, surface coatings, and fossil replacement. Manganese nodules and concretions show a wide variety of shapes and surface textures (Fig. 26). Nodules are mostly spheroidal (Fig. 26A), discoidal (Fig. 26D), ellipsoidal (Fig. 26B) to botryoidal (Fig. 26C), and rarely irregular (Fig. 26E) in shape. Sizes range from a few millimeters, as in micronodules (Fig. 26F), to up to 15 cm. Surface textures are generally smooth (Fig. 26C), in which case the Mn nodules show a slightly shiny luster (Fig. 26D). However, some samples have a rough (Fig. 26B) or sandy (Fig. 26A), matt appearance. Occasionally, Mn nodules occur in rod- (Fig. 26G) or grape-like (Fig. 26H) aggregates or more complex composite concretions (Fig. 26C).

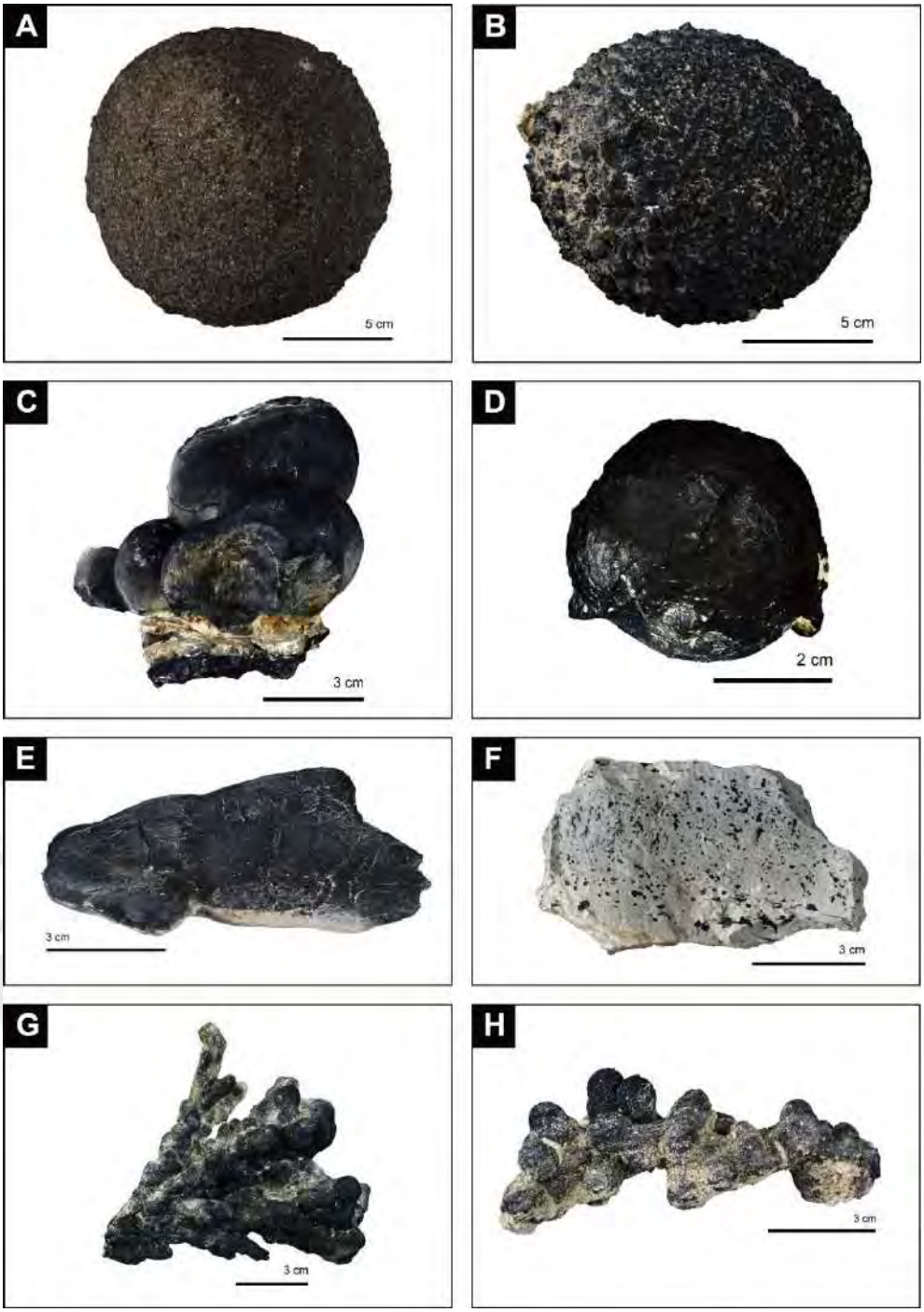

Figure 26. Morphological and textural variations of Mn oxide nodules in the East Pisco Basin. (A) Spheroidal nodule with sandy surface. (B) Ellipsoidal nodule with rough surface. (C) Composite botryoidal concretion on fibrous gypsum (white material); individual nodules show smooth surfaces. (D) Discoidal nodule with smooth, shiny surface. (E) Irregular nodule with an elongate shape. (F) Micronodules in siltstone. (G) Radiate cluster of botryoidal rods. (H) Grape-like aggregate of nodules.

A cross-sectional view of the most massive Mn oxide nodules reveals poorly defined concretional layers and septarian structures (Fig. 27A) with white material infill (Fig. 27B). Freshly cut surfaces also revealed the presence of abundant fine-grained detrital particles embedded in the Mn oxides in most of the nodular and concretional samples (Fig. 27C). Manganese oxide micronodules appear as millimetric dark specks and lenses aligned parallel to mm-scale bedding in clays with local, incipient dendritic forms in cut surfaces (Fig. 27D).

In many samples, however, the Mn oxide nodules present more complex internal structures. Sandy nodules consist of a rind concretion of a black Mn oxide cement surrounding a spherical sandstone core of ochre color (Fig. 27E). In one sample, a Mn oxide rind of black color wraps a deformed, irregular white sandstone core (Fig. 27F). In the same sample, thin veinlets of Mn oxides crosscut the sandstone core and connect diametrically opposed sides of the Mn wrapping. Two samples show a black rind concretion of Mn oxides around a dark sandstone rind of brownish color wrapping in turn a brighter, ochre sandstone core centered in the nodule (Fig. 27G) or located in its bottom center (according to the position of sampling; Fig. 27H).

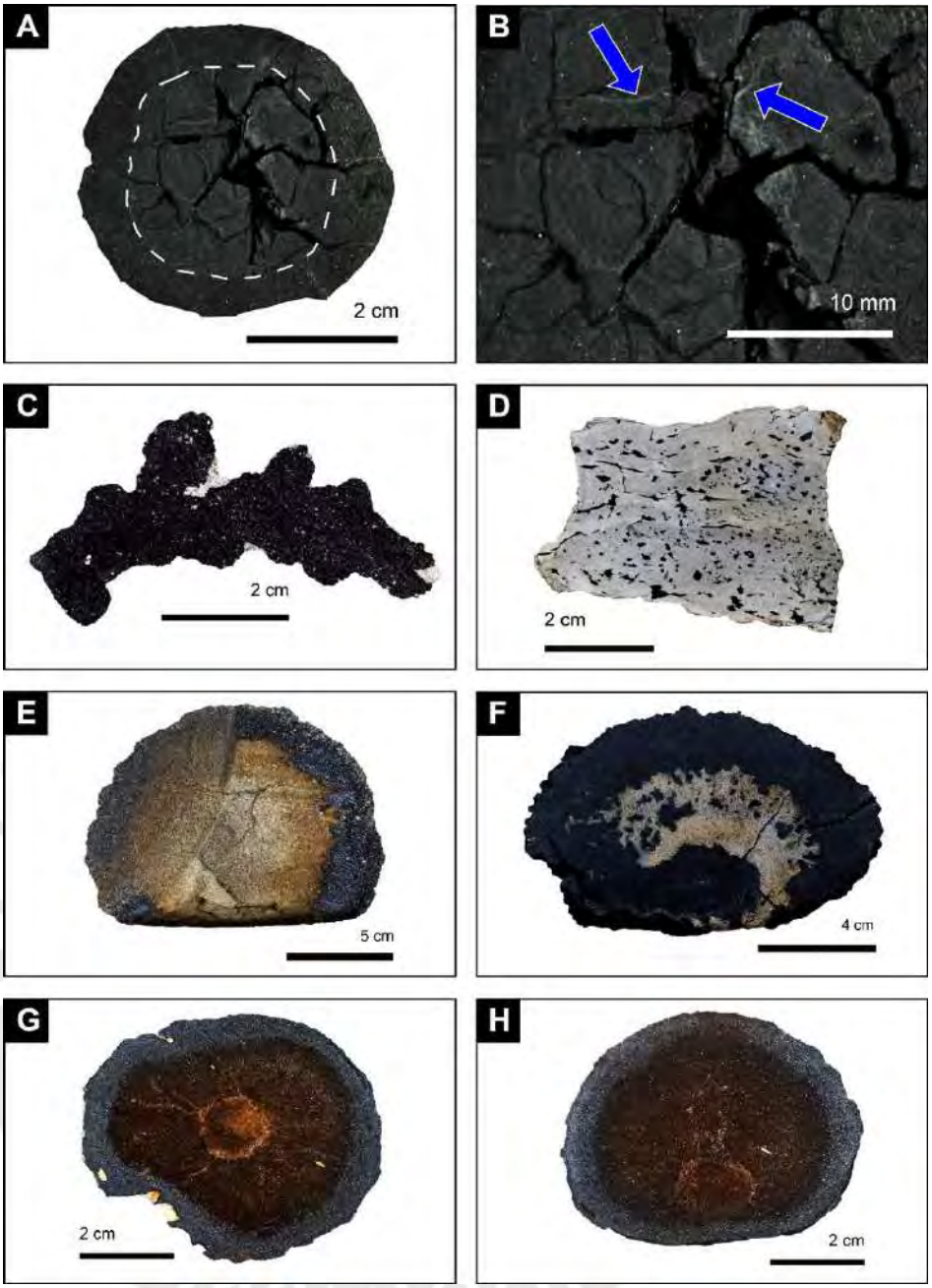

Figure 27. Cross-sections of diametrically-cut Mn oxide nodules from the East Pisco Basin. (A) Concretional rim (white dotted line) around a center with septarian cracks. (B) Detail of fine veining textures (blue arrows) in a discoidal nodule. (C) Fine-grained, bright detrital grains embedded in the Mn-oxides matrix in a botryoidal composite concretion. (D) Specks and lenses of Mn oxides with long axes aligned parallel to stratigraphic bedding. (E) Rind of black Mn oxides around sandstone of ochre color. (F) Complex wrapping of black Mn oxides around a deformed, bright-colored sandstone; note that fragments of Mn oxides appear within the sandstone core, which is crosscut by thin Mn oxide veinlets. (G-H) Rind of black Mn oxide around uncemented sandstone cores; note that the innermost cores, of bright ochre colors, may occur in the middle or bottom center of the nodules.

Manganese oxide veins (Fig. 28) may present botryoidal (Fig. 28A) or planar forms (Fig. 28B), with rough and slightly shiny surfaces. On the other hand, Mn oxide coatings occur accreted onto siltstones or silty clays (Figs. 29A-C), or onto fibrous gypsum (Fig. 29D). The thickness of the coatings varies from a few millimeters (Fig. 29D) to up to 7 cm (Fig. 29C). Surfaces of Mn oxide coatings are characterized by rough (Fig. 29A), sandy (Fig. 29B), or smooth (Fig. 29D) textures.

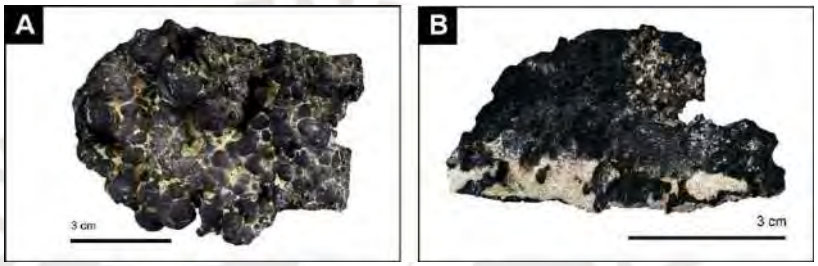

Figure 28. Morphological and textural variations of Mn oxide veins in the East Pisco Basin. (A) Manganese oxide vein with botryoidal surface. (B) Planar Mn oxide vein with rough surface.

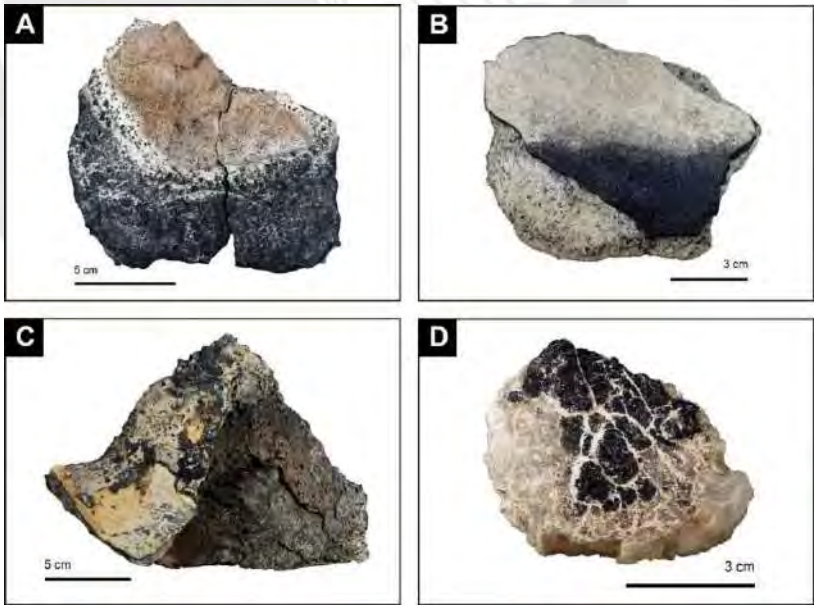

Figure 29. Morphological and textural variations of Mn oxide coatings in the East Pisco Basin. (A) Manganese oxide coating with rough, micro-botryoidal surface. (B) Manganese oxide coating with sandy surface. (C) 7-cm-thick Mn oxide coating with rough surface. (D) Thin Mn oxide coating with smooth surface accreted onto fibrous gypsum. Gypsum veinlets crosscut the Mn oxide coating.

In rare cases, Mn oxides completely replaced ichnofossils. In the example shown in Figure 30A, a bioturbation fossilized by Mn oxides consists of an 18-cm-long elliptical tunnel with small bulges at the middle (Fig. 30B) and crests at one end (Fig. 30C). The tubular shape and uniform elliptical section indicate that this bioturbation replacement corresponds to a burrow.

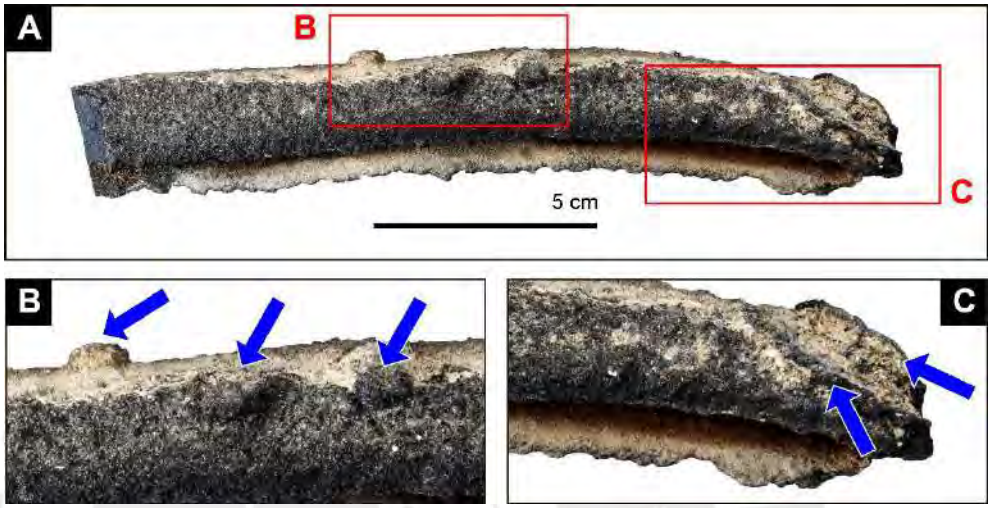

Figure 30. Bioturbation fossilized by Mn oxides in the East Pisco Basin (A) 18-cm long burrow with an ellipsoidal section, bulges, and crests. (B) Detail of small, round globe-like bulges (blue arrows). (C) Detail of small crests at one end of the burrow (blue arrows).

4.3. Major and trace element (bulk) geochemistry

Table 2 shows part of the elemental inventory of 23 Mn oxide samples. Table 3 shows a summary of the chemical compositions of Mn oxides, including minimum, maximum, geometric mean, and interquartile range values, sorted by morphological type.

All samples yield broadly similar chemical compositions, with usually high MnO contents (>34.3 wt%) except for six samples with abundant non-Mn oxide sedimentary material that yielded lower MnO contents (4.85-28.7 wt%). Fe_2O_3 contents were consistently lower (<9.73 wt%) compared to MnO, with Mn/Fe

ratios in the range of 0.62-50.2. The relatively high and variable contents of SiO_2, K_2O, P_2O_5, CaO, Na_2O, Al_2O_3, and MgO are attributed to detrital mineral components. The CoO contents are regularly high, between 0.01 and 0.80 wt% (mean = 0.21 wt%). Other metals such as Ti (<0.50 wt%), Zn (<0.17 wt%), Cu (<0.06 wt%), and Ni (<0.18 wt%) yielded much lower contents.

Table 2. Contents of selected elements in 23 samples of Mn oxides from the East Pisco Basin, expressed in wt%.

Sample	MnO	Fe_2O_3	SiO_2	K_2O	P_2O_5	Na_2O	CaO	Al_2O_3	MgO	NiO	CuO	CoO	ZnO	TiO_2
2022-PAL-02	48.54	2.19	21.15	3.25	0.58	1.72	0.70	6.05	0.82	0.02	0.06	0.56	0.03	0.24
2022-PAL-03	55.69	1.54	14.68	3.52	0.88	1.42	0.53	3.95	0.86	0.02	0.02	0.23	0.04	0.13
2022-PAL-04	47.50	1.14	21.21	4.12	0.83	1.78	0.71	5.75	0.95	0.01	0.02	0.42	0.03	0.23
2022-PAL-06	20.33	4.45	10.54	0.44	0.59	1.10	13.23	1.31	15.47	0.11	0.00	0.14	0.17	0.07
2022-PAL-11	52.23	1.41	16.28	4.13	0.63	1.41	0.95	5.34	0.84	0.02	0.05	0.80	0.05	0.21
2022-PAL-14	19.56	2.50	19.46	0.92	0.48	1.46	13.30	4.25	10.68	0.18	0.00	0.21	0.10	0.22
2023-PAL-02	25.01	1.83	34.72	2.77	0.69	2.44	7.02	7.95	0.93	0.02	0.01	0.26	0.04	0.23
2023-PAL-04	43.38	2.53	24.17	2.09	0.82	1.99	1.68	4.89	1.72	0.06	0.01	0.32	0.06	0.17
2023-PAL-08	45.72	1.39	24.12	3.14	1.19	1.98	1.04	5.04	1.03	0.03	0.01	0.38	0.07	0.19
2023-PAL-13	4.85	8.68	56.45	2.45	0.16	3.21	2.64	12.94	1.60	0.01	0.01	0.01	0.01	0.50
2023-PAL-16	34.52	1.69	33.85	2.55	0.30	2.54	1.45	7.81	1.33	0.05	0.02	0.17	0.07	0.24
2023-PAL-22	46.92	4.51	17.98	3.06	0.93	1.76	0.86	5.44	1.37	0.01	0.05	0.36	0.03	0.20
2023-PAL-25	49.62	2.01	17.95	3.35	0.95	1.91	0.93	5.75	1.04	0.01	0.06	0.34	0.04	0.24
2023-PAL-29	38.48	1.30	31.12	3.02	0.55	2.81	1.25	7.00	0.86	0.01	0.02	0.49	0.02	0.24
2023-PAL-32	48.79	3.51	20.08	3.39	0.86	1.74	0.76	5.02	0.71	0.01	0.03	0.25	0.04	0.21
2023-PAL-34	39.24	2.19	27.09	3.26	0.53	2.16	2.39	7.84	0.84	0.01	0.02	0.15	0.03	0.26
2023-PAL-35	39.85	2.27	25.44	3.26	0.90	2.14	2.24	7.14	0.99	0.01	0.03	0.21	0.03	0.23
2023-PAL-36	40.56	0.90	28.00	3.66	0.78	2.24	0.69	5.49	1.40	0.01	0.02	0.22	0.02	0.10
2023-PAL-38	37.84	2.47	29.77	2.75	0.61	2.49	1.29	7.40	0.88	0.01	0.04	0.54	0.03	0.28
2023-PAL-40	34.31	9.73	27.37	2.79	0.76	2.21	1.27	7.02	0.95	0.02	0.03	0.20	0.05	0.31
2023-PAL-45	45.82	1.01	22.35	3.87	0.49	2.15	1.34	5.48	1.03	0.01	0.01	0.05	0.03	0.20
2023-PAL-46	25.70	1.52	30.95	1.93	0.38	2.45	7.58	6.66	1.52	0.07	0.00	0.05	0.06	0.17
2023-PAL-47A	28.68	7.51	35.38	2.72	0.30	2.00	1.60	8.50	1.05	0.03	0.02	0.09	0.05	0.38

Table 3. Contents of selected elements in Mn oxides from the East Pisco Basin, sorted by morphological type. Presented data include minimum (MIN), maximum (MAX), geometric mean (GM), and inter-quartile range (IQR) values, all expressed in wt%.

	Nodule/concretion				**Vein**				**Coating**				**Bioturbation replacement**
	MIN	**MAX.**	**GM**	**IQR**	**MIN**	**MAX**	**GM.**	**IQR.**	**MIN.**	**MAX.**	**GM.**	**IQR.**	**(1 analysis)**
MnO	4.85	52.23	34.16	47.36-35.51	37.84	55.69	46.85	52.24-43.32	20.33	45.72	30.39	43.38-25.01	34.31
Fe_2O_3	0.90	8.68	2.17	2.44-1.33	1.54	3.51	2.37	2.99-2.01	1.39	4.45	2.13	2.53-1.52	9.73

	Nodule/concretion				Vein				Coating				Bioturbation replacement
SiO_2	16.28	56.45	25.20	30.34-19.88	14.68	29.77	20.63	24.93-17.38	10.54	34.72	23.12	30.95-24.12	27.37
K_2O	0.92	4.13	2.96	3.58-2.8	2.75	3.52	3.20	3.46-3.07	0.44	3.14	1.73	2.77-1.93	2.79
P_2O_5	0.16	0.95	0.54	0.82-0.48	0.61	0.88	0.77	0.87-0.74	0.38	1.19	0.69	0.82-0.59	0.76
Na_2O	1.41	3.21	2.04	2.22-1.77	1.42	2.49	1.83	2.12-1.58	1.10	2.45	1.92	2.44-1.98	2.21
CaO	0.69	13.30	1.45	2.08-0.88	0.53	1.29	0.80	1.03-0.65	1.04	13.23	4.15	7.58-1.68	1.27
Al_2O_3	4.25	12.94	6.52	7.64-5.48	3.95	7.40	5.27	6.21-4.49	1.31	7.95	4.43	6.66-4.89	7.02
MgO	0.82	10.68	1.25	1.36-0.88	0.71	0.88	0.81	0.87-0.79	0.93	15.47	2.08	1.72-1.03	0.95
NiO	0.01	0.18	0.01	0.02-0.01	0.01	0.02	0.01	0.02-0.01	0.02	0.11	0.04	0.07-0.03	0.02
CuO	0.002	0.06	0.02	0.04-0.02	0.02	0.04	0.03	0.03-0.02	0.00	0.01	0.01	0.01-0.00	0.03
CoO	0.01	0.80	0.20	0.41-0.15	0.23	0.54	0.31	0.39-0.24	0.05	0.38	0.19	0.32-0.14	0.20
ZnO	0.01	0.10	0.03	0.04-0.03	0.03	0.04	0.04	0.04-0.03	0.04	0.17	0.07	0.07-0.06	0.05
TiO_2	0.10	0.50	0.24	0.24-0.21	0.13	0.28	0.20	0.25-0.17	0.07	0.23	0.15	0.19-0.17	0.31

In the correlation plots (Fig. 31), SiO_2 tends to have a fairly positive correlation with Al_2O_3 (R^2 = 0.86; Fig. 31A) and Na_2O (R^2 = 0.80; Fig. 31B), thus suggesting the presence of aluminosilicates (e.g., plagioclase, mica, clay) probably as detrital particles. Also, SiO_2 shows a good correlation with Rb (R^2 = 0.52) and other minor and trace elements, such as Zr (R^2 = 0.36) and Ge (R^2 = 0.48; Fig. 31C). However, SiO_2 is virtually not correlated with REE (R^2 = 0.002; Fig. 31C) or K_2O (R^2 = 0.002; Fig. 31D), whereas MnO show a strong positive correlation with K_2O (R^2 = 0.51; Fig. 31E). Hence, the high values of K_2O are related to Mn oxides rather than silicates, possibly linked with K-Mn oxides (e.g., cryptomelane). Furthermore, the poor correlation between BaO and MnO (R^2 = 0.02; Fig. 31F) implies the absence of Ba-Mn oxides (e.g., hollandite). Cobalt yields a moderate positive correlation with Mn (R^2 = 0.31; Fig. 31G), and other trace metals including Pb (R^2 = 0.58), Bi (R^2 = 0.60), Te (R^2 = 0.31), and In (R^2 = 0.63; Fig. 31H).

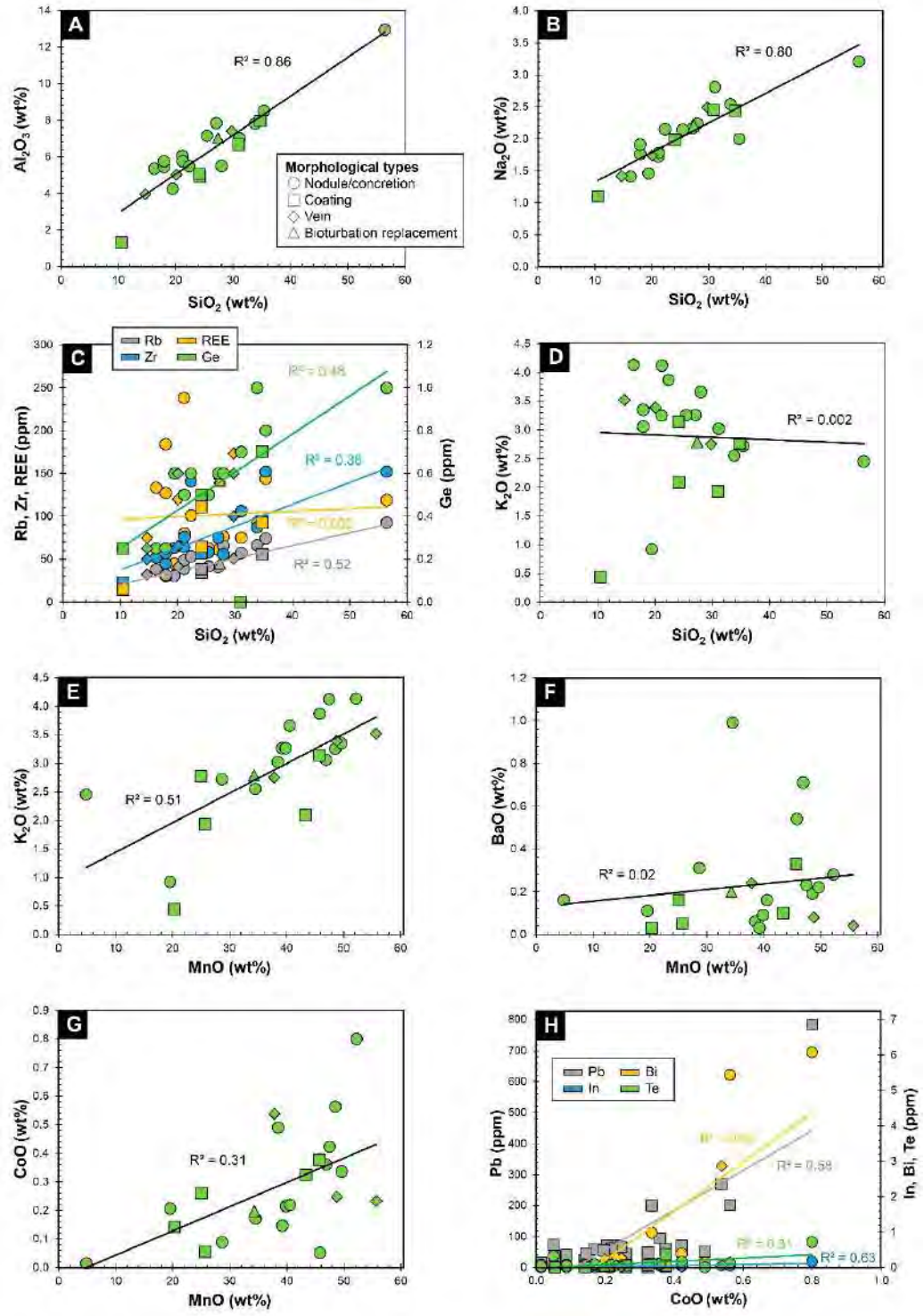

Figure 31. Correlation binary plots for selected elements in bulk samples of Mn oxide nodules, veins, and coatings. (A) SiO_2 vs. Al_2O_3 (wt%). (B) SiO_2 vs. Na_2O (wt%). (C) SiO_2 (wt%) vs. Rb, Zr, REE (ppm) in main axis, and SiO_2 (wt%) vs. Ge (ppm) in secondary axis. (D) SiO_2 vs. K_2O (wt%). (E) MnO vs. K_2O (wt%). (F) MnO vs. BaO (wt%). (G) CoO vs. BaO (wt%). (H) CoO (wt%) vs. Pb (ppm) in main axis, and CoO (wt%) vs. In, Bi, Te (ppm) in secondary axis.

4.4. Major mineralogy

The X-ray diffraction results for 47 Mn oxide samples from the Chilcatay and Pisco formations indicate predominance of Mn oxides and detrital minerals such as quartz, plagioclase, mica, and clays. Other detected phases include anhydrite, gypsum, and local dolomite which may represent chemical precipitates according to the textural observations presented above. The identified Mn oxides include either cryptomelane or hollandite, and todorokite or buserite (Table 3). Cryptomelane and hollandite, as well as todorokite and buserite, cannot be distinguished as both mineral pairs have almost equivalent X-ray diffraction patterns (e.g., Burns and Burns 1977; Pelleter et al. 2017). The results presented in the mineral geochemistry section indicate that buserite is not present.

Table 4. Mineralogical composition of Mn nodules, veins, and coatings (XRD results). Abbreviations: Cml/Hol: cryptomelane/hollandite; Tod: todorokite; Qz: quartz; Pl: plagioclase; Gp: gypsum; Mca: mica; Dol: dolomite; Anh: anhydrite; Cl: clay (undifferentiated).

N°	Sample	Mn oxides		Other minerals						
		Cml/Hol	Tod	Qz	Pl	Gp	Mca	Dol	Anh	Cl
1	2022-PAL-01	X		X	X		X			
2	2022-PAL-02	X		X	X		X			
3	2022-PAL-03	X		X	X		X			
4	2022-PAL-04	X		X	X	X	X			
5	2022-PAL-05	X		X	X		X			
6	2022-PAL-06		X				X	X		
7	2022-PAL-07	X		X	X					
8	2022-PAL-08	X		X	X		X			
9	2022-PAL-09	X		X	X					
10	2022-PAL-10	X		X	X		X			
11	2022-PAL-11	X		X	X	X	X			
12	2022-PAL-12	X		X	X		X			
13	2022-PAL-13	X		X	X		X			
14	2022-PAL-14		X	X	X	X		X		
15	2022-PAL-16/17		X	X	X	X		X		
16	2023-PAL-01	X		X	X	X	X			

N°	Sample	Mn oxides		Other minerals						
		Cml/Hol	Tod	Qz	Pl	Gp	Mca	Dol	Anh	Cl
17	2023-PAL-02	X		X	X	X	X			
18	2023-PAL-04	X		X	X	X	X			
19	2023-PAL-08	X		X	X		X			
20	2023-PAL-09/10		X	X		X	X	X		X
21	2023-PAL-13			X	X		X			
22	2023-PAL-16	X		X	X		X			
23	2023-PAL-17	X		X	X		X			
24	2023-PAL-20	X		X	X	X				
25	2023-PAL-21	X		X	X		X			
26	2023-PAL-22	X		X	X					
27	2023-PAL-25	X		X	X	X				X
28	2023-PAL-26	X		X	X		X			
29	2023-PAL-27	X		X	X					X
30	2023-PAL-29	X		X	X	X	X			
31	2023-PAL-30	X		X	X					
32	2023-PAL-32	X		X	X		X			
33	2023-PAL-33	X		X	X		X			
34	2023-PAL-34	X		X	X	X				
35	2023-PAL-35	X		X	X					X
36	2023-PAL-36	X		X	X		X			
37	2023-PAL-37	X		X	X		X			
38	2023-PAL-38	X		X	X					X
39	2023-PAL-40	X		X	X		X			
40	2023-PAL-43	X		X	X		X			
41	2023-PAL-44		X	X	X	X		X		
42	2023-PAL-45	X		X	X	X	X			
43	2023-PAL-46		X	X	X	X			X	
44	2023-PAL-47A	X		X	X		X			
45	2023-PAL-47B			X	X		X			
46	2023-PAL-48A	X		X	X		X			
47	2023-PAL-48B			X	X		X			

The obtained results allowed the classification of the 47 studied samples into two main mineralogical groups according to the dominant Mn oxide: i) cryptomelane/hollandite type, and ii) todorokite type (Fig. 32).

All Mn micronodules (samples 2022-PAL-14, 2022-PAL-16/17, 2023-PAL-09/10, and 2023-PAL-44) consistently belong to the todorokite -type group, as well as two Mn coatings (samples 2022-PAL-06 and 2023-PAL-46). The rest

of the samples yielded similar XRD patterns consistent with cryptomelane/hollandite (Fig. 32).

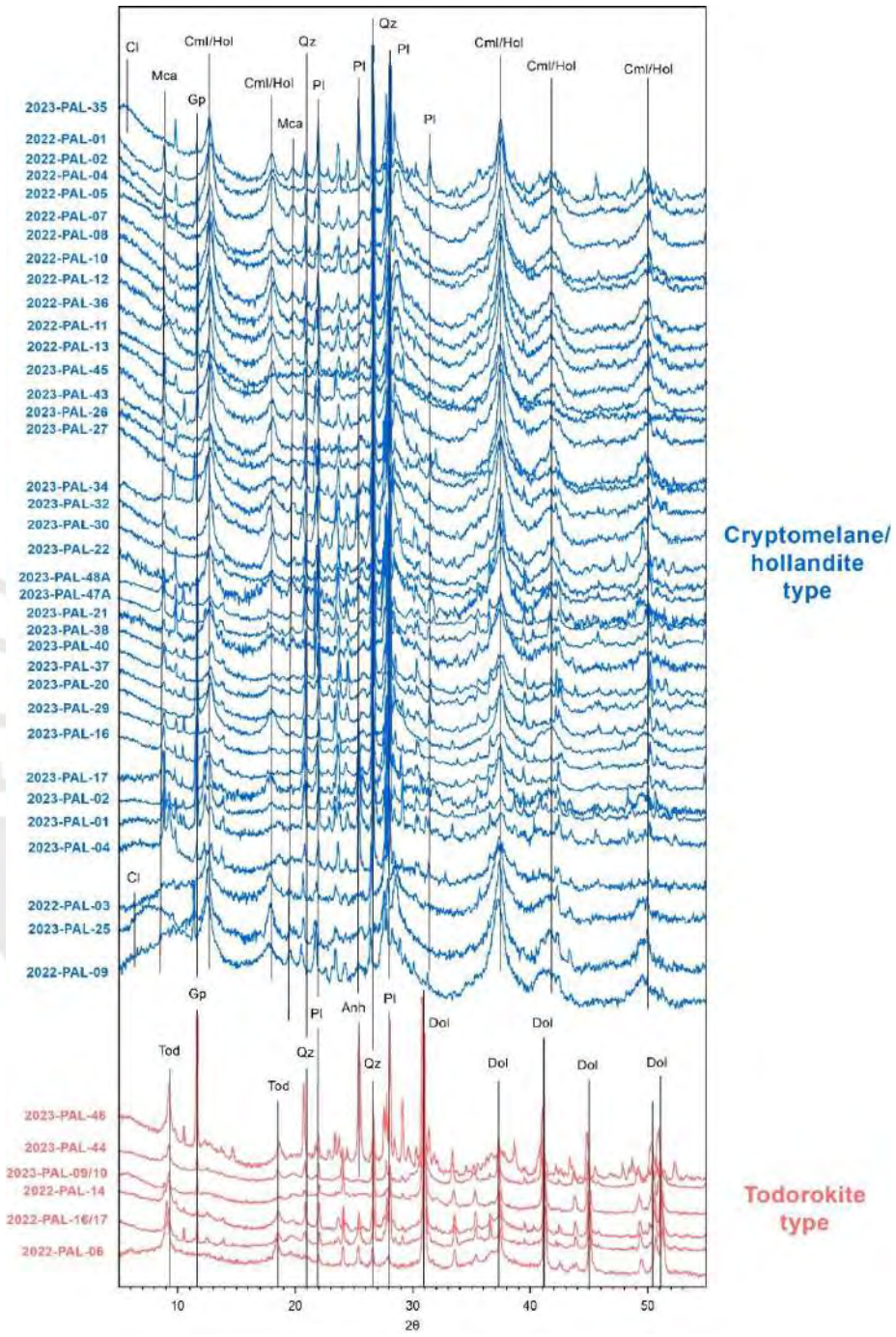

Figure 32. XRD patterns divided into mineralogical categories according to the dominant Mn-oxide. Major peaks are shown as black vertical lines with the corresponding mineral labels. Peaks at 2θ ~9.75° and ~10.50°, present in some samples, could not be correlated with any particular mineral phase. Abbreviations: cryptomelane/hollandite (Cml/Hol), todorokite (Tod); quartz (Qz), plagioclase (Pl), gypsum (Gp), mica (Mca), dolomite (Dol); anhydrite (Anh), and clay (Cl).

4.5. Microtextures of the Mn oxides

Microtextures in Mn oxides nodules, vein infills, and coatings were examined. In nodules and concretions, Mn oxides constitute the cement to detrital particles, frequently exhibiting cement-supported textures. The degree of porosity varies considerably, with Mn-oxide cement-supported fabrics exhibiting virtually no interparticle porosity (Fig. 33A) and a few samples displaying only minor Mn-oxide cement and high proportions of interparticle porosity (Fig. 33B). In the cementing material, the Mn oxides are microcrystalline to cryptocrystalline and form aggregates with a variety of internal textures including fibrous (defined by Mn oxide crystallites <10 μm in length) and microporous-spongy (Fig. 33C). The detrital grains are primarily composed of quartz, plagioclase, and minor mica (Fig. 33D). In terms of shape, the detrital grains are predominantly angular to sub-angular, with a size range of 100 to 200 μm. In tuff stratigraphic levels, grains with delicate curviplanar textures correspond to juvenile glass shards that are up to 500 μm in length (Fig. 33E). In some nodule samples, subtle concentric rims are identified under the microscope due to slight variations in brightness and coloration, which correspond to slight changes in the proportions of Mn oxides vs. detrital elements and/or porosity (Fig. 33F). Furthermore, veining is also a very common occurrence within nodules and concretions. Often, a network of very thin, usually sinuous, veinlets, less than 75 μm in thickness, cuts across the Mn-oxide cement and adapts around and locally cuts detrital particles. These veinlets are partially or entirely filled with Mn oxides that exhibit internal textures such as massive (Fig. 33G), fibrous, microporous (Fig. 33H), and/or colloidal (Fig. 33H). It is frequently observed that different generations of Mn oxide veinlets exhibit crosscutting relationships (Fig 33G).

The replacement of biomorphic remnants by Mn oxides is also ubiquitous, including the fossilization of possible diatoms (Fig. 33H-I), turritellas (Fig. 33J), and fibrous (vegetal?) microlaminae (Fig. 33A).

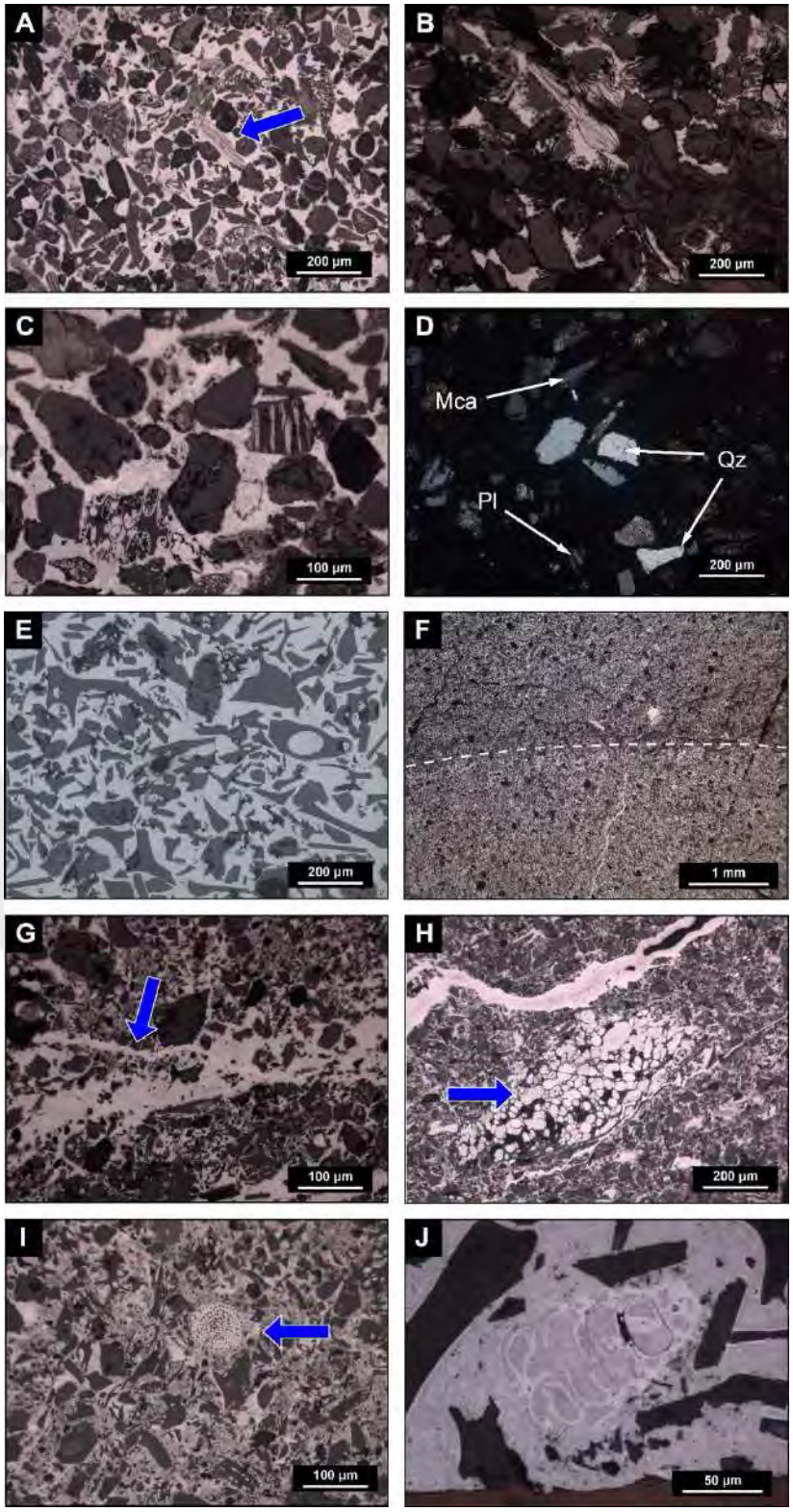

Figure 33. Reflected (A, B, C, D, F, G, H, I, J) and transmitted (E) light photomicrographs of representative microtextures in Mn oxide nodules from the East Pisco Basin. (A) Manganese oxide cement to detrital particles with low interparticle porosity. Biogenic fibrous remnant of probable vegetal origin (blue arrow) fossilized by Mn oxides. (B) Minor Mn oxide cement to detrital particles in sample with a high proportion of interparticle porosity. (C) Detail of Mn oxide cement with local microporous texture. (D) Angular detrital particles of abundant quartz (Qz), plagioclase (Pl) and minor mica (Mca) cemented by Mn oxides. (E) Juvenile glass shards with curviplanar textures cemented by Mn oxides in tuff. (F) Concentric Mn oxide cement layers (dotted lines) defined by domains with slightly different proportions of detrital grains and Mn oxide cement. (G) Porous and thin Mn oxide veinlet (blue arrow) crosscuts a more massive and thicker Mn oxide vein. (H) Porous, colloidal Mn oxide vein coating; a possible siliceous remnant of diatom is also observed (blue arrow). (I) Framboidal organic structure fossilized by Mn oxides (blue arrow); Mn oxides also occur as a cement of other detrital particles. (J) Interior view of a turritella-like organism fossilized by Mn oxides.

In Mn oxide veins, the microtextures are analogous to those described for the nodules. Consequently, in veins, the Mn oxides serve as the cement to detrital grains, variably occluding interparticle porosity (Figs. 34A-B). The detrital particles are angular to subangular in shape, and vary in size between 50 and 200 µm. Locally, irregular domains with a more massive Mn oxide mineralization alternate with domains displaying abundant microporosity, which may even exhibit spongy textures, and detrital particles (Fig. 34C). The fossilization of biomorphic remnants of possible fibrous (vegetal?) microlaminae and diatoms (Fig. 34D) is frequently observed under the microscope too.

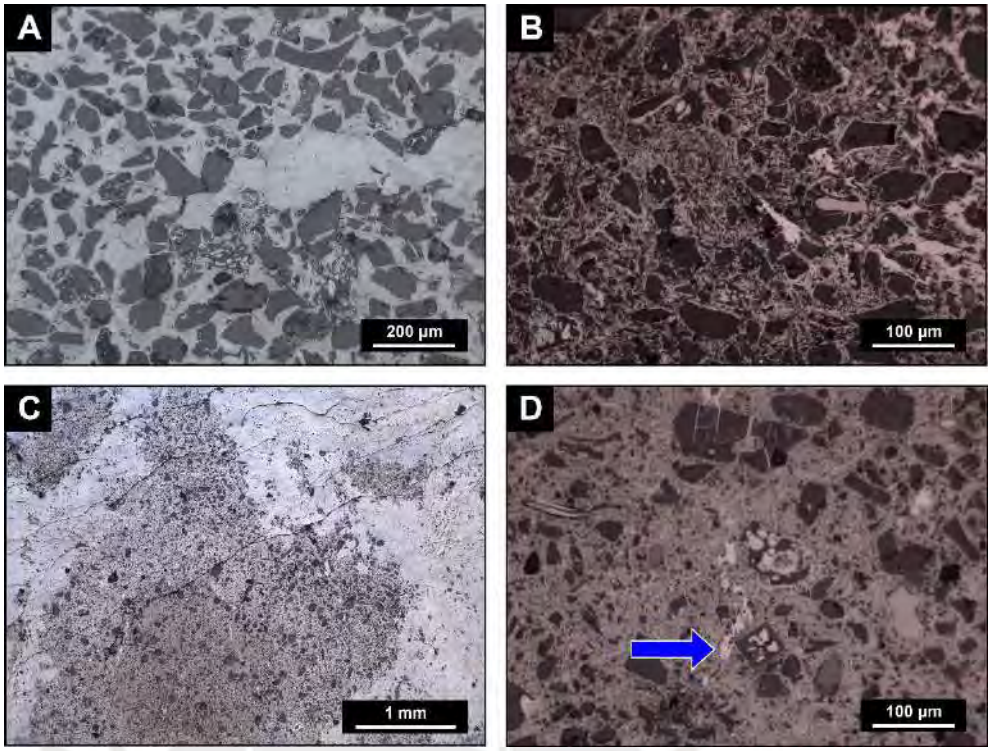

Figure 34. Reflected light photomicrographs of representative microtextures in Mn oxide veins from the East Pisco Basin. (A) Massive Mn oxide cement to detrital particles with only very local interparticle microporosity. (B) Detail of Mn oxide cement with local microporous texture. (C) Alternating domains of massive Mn oxide and zones with higher proportions of detrital grains and porosity. (D) Square organic structure fossilized by Mn oxides (blue arrow); Mn oxides also occur as a cement of other detrital particles.

In Mn oxide coatings, samples are either constituted by Mn-oxide cement to detrital particles (Figs. 35A-B) or are dominated by massive layers of Mn-oxides (Fig. 35C). In the first, the samples are characterized by grain-supported textures and high interstitial porosity, with only minor (Fig 35A) to incipient (Fig 35B) Mn-oxide cement. The Mn oxides in the cementing material are microcrystalline to cryptocrystalline and form aggregates with fibrous (defined by Mn oxide crystallites <10 µm in length), homogeneous, microporous to spongy textures. The detrital grains predominantly consist of angular to sub-angular quartz and plagioclase mostly in a range size between 50 to 150 µm

(Fig. 35D). Close to the contact with the sedimentary material, the cement consists of a clay-carbonate assemblage (Fig. 35E). Scarce biomorphic remnants of possible fibrous (vegetal?) microlaminae are fossilized by Mn oxides (Fig. 35F). In the second microtextural type, Mn oxides form massive colloidal, gel-like fabrics (Fig. 35G) that locally fill the void space between angular, detrital grains (Fig. 35H). In places, Mn oxides have partially replaced the detrital particles.

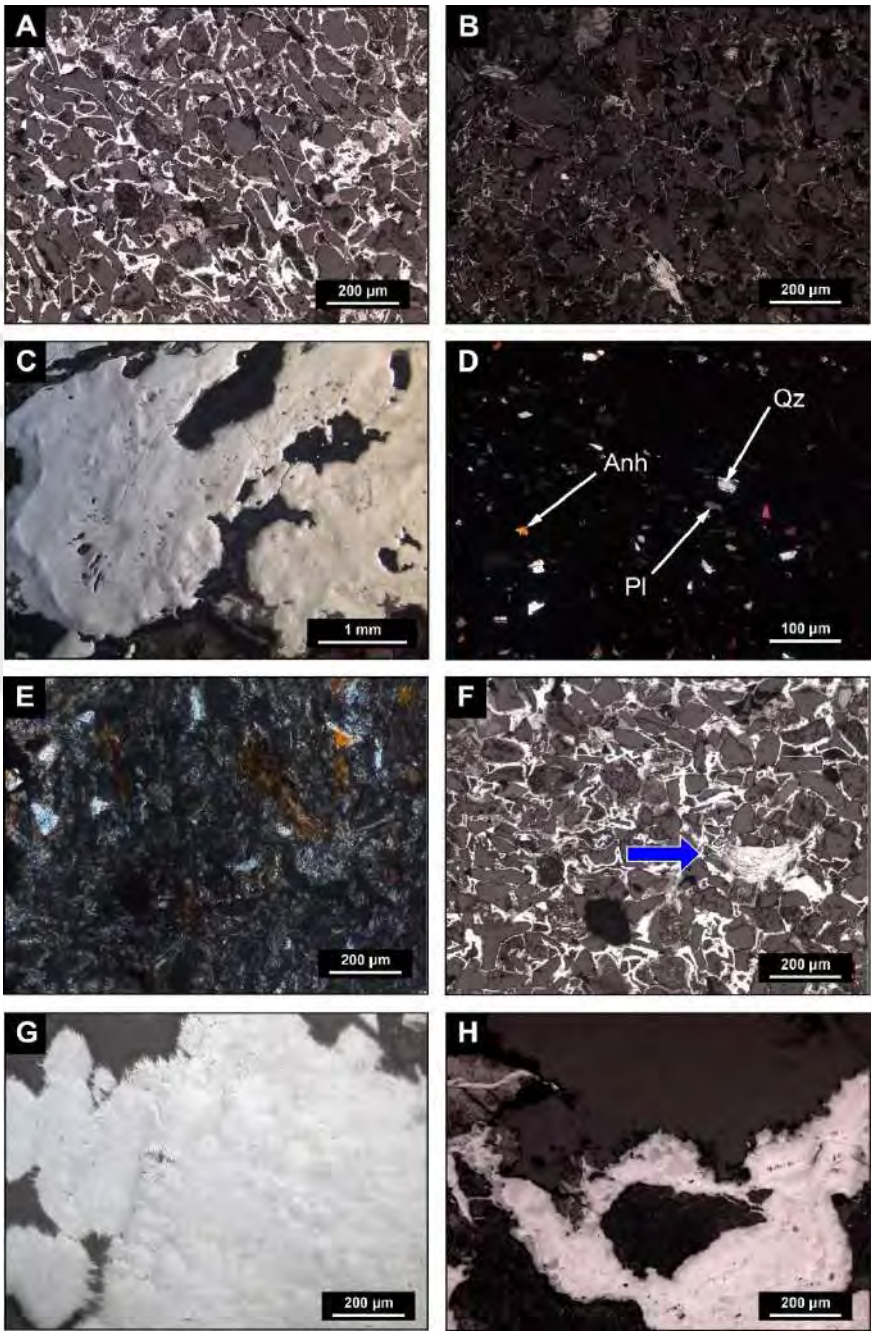

Figure 35. Reflected (A, B, C, F, G, H) and transmitted (D, E) light photomicrographs of representative microtextures in Mn oxide coatings from the East Pisco Basin. (A) Minor Mn oxide cement to detrital particles in sample with a high proportion of interparticle porosity. (B) Incipient Mn oxide cement to detrital particles in sample with a high interparticle porosity. (C) Massive, gel-like colloidal Mn oxides with only local microporosity. (D) Angular detrital particles of quartz (Qz), plagioclase (Pl), and minor anhydrite (Anh) cemented by Mn oxides. (E) Aggregates of clay and carbonate constituting the cement to detrital particles in a sector of the sample with scarce Mn mineralization. (F) Biogenic fibrous remnant of probable vegetal origin (blue arrow) fossilized by Mn oxides; Mn oxides also occur as a minor cement to other detrital particles. (G) Massive Mn oxide mineralization with internal botryoidal, gel-like texture and micro-urchin terminations. (H) Botryoidal gels of Mn oxides flooding the space between detrital particles.

4.6. Mineral geochemistry

Both the cryptomelane/hollandite and todorokite type samples were considered for EPMA. Representative results are presented in Table 4 and a summary of the chemical compositions of Mn oxides, including minimum, maximum, geometric mean, and interquartile range values, is given in Table 5.

In cryptomelane/hollandite-type samples, Mn oxide minerals are largely composed of MnO (49.0-79.5 wt%) and K_2O (1.11-6.62 wt%). Other elements that occur in high, though erratic, contents include FeO (0.09-13.2 wt%), SiO_2 (0.11-17.7 wt%), and Al_2O_3 (0.07-8.50 wt%). These erratic values may be attributed to some extent to mineral admixtures. Other elements found in lesser proportions include Na_2O (<2.57 wt%), P_2O_5 (<2.50 wt%), TiO_2 (<2.30 wt%), MgO (<1.98 wt%), NiO (<0.68 wt%), SO_3 (<0.64 wt%), CaO (<0.63 wt%), ZnO (<0.39 wt%), PbO (<0.25 wt%), and BaO (<1.17 wt%). The CoO contents range between 0.08 and 2.14 wt%, with a mean value of 0.47 wt%. The fact that most analyses returned much higher K_2O than BaO values indicate a

predominance of cryptomelane [$K(Mn^{4+},Mn^{3+})_8O_{16}$] over hollandite [$Ba(Mn^{4+},Mn^{3+})_8O_{16}$].

In todorokite -type samples, the Mn oxide materials chiefly consist of MnO (45.8-65.5 wt%) and MgO (3.48-5.01 wt%). Other elements in minor amounts include Al_2O_3 (0.07-3.90 wt%), CaO (1.18-1.70 wt%), Na_2O (0.78-1.49 wt%), BaO (0.34-1.37 wt%), and K_2O (0.81-1.07 wt%). The highest values of SiO_2 (0.30-19.6 wt%) are attributed to mineral admixtures. Other elements that are present in lesser proportions include P_2O_5 (<0.27 wt%), TiO_2 (<0.41 wt%), NiO (<0.21 wt%), and FeO (<1.88 wt%). The CoO contents are in the range between 0.10 and 2.64 wt%, with a mean value of 0.35 wt%.

Table 5. Representative EMPA results of Mn oxides. Data in wt%. Abbreviations: <d.l., below detection limit; C/H, cryptomelane/hollandite type; T, todorokite type.

Sample	SiO_2	Al_2O_3	CaO	K_2O	PbO	SO_3	P_2O_5	MgO	Na_2O	MnO	FeO	CoO	ZnO	CuO	NiO	TiO_2	BaO	Total
2023-PAL-19 (C/H)	<d.l.	<d.l.	0.27	5.15	<d.l.	<d.l.	1.52	0.27	0.54	74.31	<d.l.	0.20	<d.l.	<d.l.	<d.l.	<d.l.	<d.l.	82.26
	<d.l.	0.66	0.10	4.78	<d.l.	<d.l.	1.96	0.33	0.62	70.41	<d.l.	0.30	<d.l.	<d.l.	<d.l.	<d.l.	0.24	79.39
	<d.l.	<d.l.	0.15	5.15	<d.l.	<d.l.	1.46	0.16	0.40	72.65	<d.l.	0.20	<d.l.	<d.l.	<d.l.	<d.l.	<d.l.	80.17
2023-PAL-40 (C/H)	0.13	0.19	0.22	1.69	<d.l.	<d.l.	0.81	1.84	2.11	68.74	<d.l.	0.44	<d.l.	<d.l.	<d.l.	<d.l.	<d.l.	76.16
	0.13	0.49	0.11	3.41	<d.l.	<d.l.	0.99	0.62	1.36	71.10	<d.l.	0.48	<d.l.	<d.l.	<d.l.	<d.l.	0.18	78.87
	0.14	0.50	0.13	3.38	<d.l.	<d.l.	1.04	0.66	1.31	71.49	<d.l.	0.42	<d.l.	<d.l.	<d.l.	<d.l.	0.52	79.59
2023-PAL-35 (C/H)	0.16	1.07	0.14	3.80	<d.l.	<d.l.	2.03	0.44	1.83	70.84	<d.l.	0.45	<d.l.	<d.l.	<d.l.	<d.l.	<d.l.	80.77
	0.14	1.04	0.21	3.20	<d.l.	<d.l.	1.53	0.63	2.27	70.65	<d.l.	0.54	<d.l.	<d.l.	<d.l.	<d.l.	<d.l.	80.20
	0.62	1.07	0.13	3.75	<d.l.	0.23	1.66	0.47	1.60	70.45	<d.l.	0.37	<d.l.	<d.l.	<d.l.	<d.l.	<d.l.	80.37
2023-PAL-34 (C/H)	0.13	0.11	0.12	2.84	<d.l.	<d.l.	0.37	0.78	1.98	73.41	<d.l.	0.10	<d.l.	<d.l.	<d.l.	<d.l.	<d.l.	79.84
2022-PAL-03 (C/H)	0.14	1.04	0.14	4.38	<d.l.	<d.l.	1.72	0.33	0.99	70.31	0.19	0.29	<d.l.	<d.l.	<d.l.	<d.l.	<d.l.	79.54
	0.17	1.60	0.26	4.68	<d.l.	<d.l.	2.21	0.34	0.94	69.73	0.13	0.26	<d.l.	<d.l.	<d.l.	<d.l.	<d.l.	80.32
	<d.l.	0.93	0.11	4.17	<d.l.	<d.l.	1.66	0.67	0.87	69.61	0.16	0.33	<d.l.	<d.l.	<d.l.	<d.l.	<d.l.	78.51
2023-PAL-27 (C/H)	0.11	0.60	0.19	2.11	<d.l.	<d.l.	1.10	1.01	1.95	70.81	0.25	0.55	<d.l.	<d.l.	<d.l.	<d.l.	0.57	79.23
	0.56	0.60	0.17	2.32	<d.l.	<d.l.	0.97	0.82	1.55	71.04	0.56	0.73	<d.l.	<d.l.	<d.l.	<d.l.	0.94	80.27
	<d.l.	0.61	0.19	2.11	<d.l.	<d.l.	1.36	1.04	2.28	71.27	0.09	0.61	0.21	0.16	<d.l.	<d.l.	0.46	80.39
2023-PAL-48A (C/H)	0.32	1.41	0.44	2.19	<d.l.	<d.l.	0.41	1.71	1.85	66.46	1.73	0.24	<d.l.	<d.l.	0.11	<d.l.	0.58	77.46
	0.35	3.68	0.44	2.55	<d.l.	<d.l.	0.43	1.42	1.93	65.33	1.82	0.26	<d.l.	<d.l.	0.20	<d.l.	0.62	79.03
	0.50	0.49	0.63	1.65	<d.l.	<d.l.	0.48	1.98	2.30	63.93	3.86	0.30	<d.l.	<d.l.	<d.l.	0.57	0.68	77.37
2023-PAL-29 (C/H)	<d.l.	0.29	0.11	2.44	<d.l.	0.38	0.71	0.99	2.41	69.57	0.30	0.69	<d.l.	<d.l.	<d.l.	<d.l.	<d.l.	77.89
	<d.l.	0.23	0.17	2.38	<d.l.	0.33	0.79	1.02	1.88	68.04	0.13	0.68	<d.l.	<d.l.	<d.l.	<d.l.	<d.l.	75.65
	0.12	0.17	0.22	2.66	<d.l.	0.46	0.62	1.10	2.19	75.82	0.12	0.78	<d.l.	<d.l.	<d.l.	<d.l.	<d.l.	84.26

Sample	SiO_2	Al_2O_3	CaO	K_2O	PbO	SO_3	P_2O_5	MgO	Na_2O	MnO	FeO	CoO	ZnO	CuO	NiO	TiO_2	BaO	Total
2023-PAL-43 (C/H)	0.11	0.18	0.36	2.47	<d.l.	0.30	0.64	1.42	2.12	70.13	0.16	1.14	<d.l.	<d.l.	<d.l.	<d.l.	<d.l.	79.04
	<d.l.	0.17	0.29	2.34	<d.l.	0.30	0.69	1.64	2.11	69.24	0.11	1.34	<d.l.	<d.l.	<d.l.	<d.l.	<d.l.	78.24
	<d.l.	0.17	0.24	2.41	<d.l.	0.37	0.77	1.29	2.52	69.68	0.10	1.26	<d.l.	<d.l.	<d.l.	<d.l.	<d.l.	78.81
2023-PAL-38 (C/H)	0.13	<d.l.	0.09	5.06	<d.l.	<d.l.	0.43	0.17	0.76	73.46	0.23	0.96	<d.l.	<d.l.	<d.l.	<d.l.	<d.l.	81.29
	<d.l.	<d.l.	0.11	5.83	<d.l.	<d.l.	0.65	0.09	0.44	75.11	0.27	0.65	<d.l.	<d.l.	<d.l.	<d.l.	<d.l.	83.15
	0.54	0.22	<d.l.	5.40	<d.l.	<d.l.	0.53	0.12	0.55	74.74	0.52	0.54	<d.l.	<d.l.	<d.l.	<d.l.	0.24	83.39
2022-PAL-04 (C/H)	0.15	0.45	<d.l.	6.33	<d.l.	<d.l.	1.33	0.26	0.67	70.96	0.14	0.77	<d.l.	<d.l.	<d.l.	<d.l.	<d.l.	81.07
	0.18	0.22	0.21	2.70	<d.l.	0.33	0.73	1.47	1.12	67.18	0.14	0.94	<d.l.	<d.l.	<d.l.	<d.l.	0.38	75.60
	0.16	0.23	0.21	2.47	<d.l.	0.32	0.58	1.39	1.30	66.90	0.13	1.11	<d.l.	<d.l.	<d.l.	<d.l.	0.22	75.03
2022-PAL-10 (C/H)	0.24	0.52	<d.l.	5.52	<d.l.	<d.l.	0.83	0.11	0.58	75.11	0.17	0.47	<d.l.	0.13	<d.l.	<d.l.	<d.l.	83.68
	<d.l.	0.19	0.14	2.12	<d.l.	0.30	0.89	1.10	1.54	69.16	0.11	1.42	<d.l.	<d.l.	<d.l.	<d.l.	0.26	77.23
	0.29	0.81	0.10	4.80	<d.l.	<d.l.	0.93	0.17	1.03	74.30	0.13	0.59	<d.l.	0.14	<d.l.	<d.l.	<d.l.	83.29
2023-PAL-09 (T)	<d.l.	<d.l.	1.29	0.90	<d.l.	<d.l.	<d.l.	4.33	1.49	65.47	0.20	0.15	0.18	<d.l.	0.18	<d.l.	0.46	74.65
	<d.l.	<d.l.	1.26	0.89	<d.l.	<d.l.	<d.l.	4.54	1.46	65.47	0.14	0.10	0.25	<d.l.	0.18	<d.l.	0.56	74.85
	0.30	0.07	1.70	0.86	<d.l.	<d.l.	<d.l.	4.40	1.47	63.13	0.21	0.26	<d.l.	<d.l.	0.21	<d.l.	0.34	72.96

Table 6. Summary of the EPMA results of Mn oxides, including minimum (MIN), maximum (MAX), geometric mean (GM), and inter-quartile range (IQR) values expressed in wt%. Abbreviation: <d.l., below detection limit.

	All analyses				Cryptomelane/hollandite type				Todorokite type			
	MIN	MAX	GM	IQR	MIN	MAX	GM	IQR	MIN	MAX	GM	IQR
SiO_2	0.11	19.61	0.57	2.5-0.1	0.11	17.67	0.52	1.8-0.1	0.30	19.61	3.66	11.5-1.2
Al_2O_3	0.07	8.50	0.51	1-0.2	0.07	8.50	0.49	1-0.2	0.07	3.90	0.98	3.3-0.4
CaO	0.09	1.70	0.20	0.2-0.1	0.09	0.63	0.18	0.2-0.1	1.18	1.70	1.41	1.5-1.3
K_2O	0.81	6.62	3.01	4.7-2.2	1.11	6.62	3.15	4.7-2.3	0.81	1.07	0.90	1-0.8
PbO	0.17	0.25	0.20	0.2-0.2	0.17	0.25	0.20	0.2-0.2	<d.l.	<d.l.	-	-
SO_3	0.23	1.54	0.31	0.4-0.3	0.23	0.64	0.30	0.4-0.3	<d.l.	<d.l.	-	-
P_2O_5	0.23	2.50	0.83	1.2-0.6	0.24	2.50	0.82	1.1-0.6	0.23	0.27	0.25	0.3-0.2
MgO	0.08	5.01	0.72	1.2-0.5	0.08	1.98	0.68	1.1-0.5	3.48	5.01	4.21	4.5-3.9
Na_2O	0.23	2.57	1.24	1.9-0.8	0.23	2.57	1.27	2-0.9	0.78	1.49	1.17	1.4-1
MnO	45.77	79.46	68.99	72.6-67.6	48.95	79.46	69.48	73-68.5	45.77	65.47	58.00	64.1-53
FeO	0.09	13.19	0.33	0.8-0.1	0.09	13.19	0.32	0.6-0.1	0.14	1.88	0.54	1.4-0.2
CoO	0.08	2.64	0.46	0.8-0.3	0.08	2.14	0.47	0.8-0.3	0.10	2.64	0.35	0.8-0.2
ZnO	0.17	0.39	0.22	0.2-0.2	0.17	0.39	0.22	0.2-0.2	0.17	0.25	0.21	0.2-0.2
CuO	0.12	0.17	0.14	0.1-0.1	0.12	0.17	0.14	0.1-0.1	<d.l.	<d.l.	-	-
NiO	0.09	0.68	0.16	0.2-0.1	0.09	0.68	0.17	0.2-0.1	0.12	0.21	0.16	0.2-0.1
TiO_2	0.14	2.30	0.27	0.4-0.2	0.16	2.30	0.28	0.4-0.2	0.14	0.41	0.21	0.3-0.2
BaO	0.17	1.37	0.46	0.7-0.3	0.17	1.17	0.44	0.7-0.3	0.34	1.37	0.67	0.9-0.4

5. DISCUSSION

5.1. Origin of the Mn oxide mineralization: stratigraphic, textural, and mineralogical evidence

Manganese oxides in the East Pisco Basin, including nodules and concretions, veins, and coatings, concentrate along different stratigraphic levels of sandstone, siltstone, and, to a lesser extent, tuff of the Chilcatay and Pisco formations (Figs. 8, 15, 19). Manganese oxides are mostly stratiform, except for the discordant Mn-veins system (Figs. 14A-C, 21A-C, 24A). The stratabound and partly stratiform distribution of Mn oxides and the occurrence of gypsum – Mn-oxide veins (Figs. 21A-C, 22C-G) and Mn coatings (Figs. 9A, 10, 11B, 17, 29) evidence mobilization of Mn-rich fluids to different sedimentary levels and rules out a diffuse precipitation and, ultimately, a hydrogenetic origin of the Mn nodules (e.g., Hein and Koschinsky 2014; Hein et al. 2020). The shallow water environment (Di Celma et al. 2016) and high rates of sedimentation (Gariboldi et al. 2017) recorded in the East Pisco Basin are not consistent with the typical environments of hydrogenetic precipitation of Mn oxides either (Hein and Koschinsky 2014; Hein et al. 2020). Instead, Mn-oxide vein mineralization is consistent with a focused circulation of Mn-rich fluids along fractures across the stratigraphy of the East Pisco Basin. The facts that in places Mn nodules accumulate on base of gypsum – Mn oxide veins (e.g., Fig. 17) or around "chimney-like" structures (Figs. 21D, 22B) strongly suggest that veins and other structures associated to the circulation of fluids represent feeders for the precipitation of nodules and concretions in discharge zones along more permeable sedimentary levels. In nodules and concretions, the Mn oxide

mineralization occurs as a cement to (bio)clastic elements (Figs. 33H-J, 34D, 34F) and formed by precipitation within primary interparticle porosity (Fig. 35A) stressing its secondary origin. That concretional sandy Mn nodules preserve the primary bedding is indisputable evidence of the secondary nature of the Mn mineralization relative to sedimentation (Chan 2022). In cases in which permeable layers are “sealed” by overlying massive gypsum beds, Mn oxide may form “grape-like” composite concretions that hang from the gypsum base (Fig. 17) further stressing the stratigraphic control on the mobilization and precipitation of Mn oxides in the East Pisco Basin.

The fossilization of bioturbation (Fig. 30) and organic structures (e.g., diatoms, turritellas; Figs. 33H-J, 34D, 35F) by Mn oxides is typical of mineralization of diagenetic origin (Achurra et al. 2009; Chan 2022). Moreover, the main Mn mineral identified in Mn oxide nodules, veins, and coatings is cryptomelane, which can be of diagenetic origin (Vodyanitskii et al. 2004) and has been identified in onshore diagenetic nodules from the Bahía Inglesa Formation in Chile (Achurra et al. 2009). Todorokite, which is restricted to Mn micronodules and two Mn coatings in the studied samples, is also consistent with a diagenetic origin of the Mn oxide mineralization (Hein and Koschinsky 2014).

Different processes have been proposed to explain the genesis of diagenetic Mn oxides in general and of Mn nodules and concretions in particular. In general, in these models, reductive dissolution of Mn, as well as other metals (e.g., Ni, Cu, Zn), takes place in the upper part of the sediment column during the decomposition of organic matter during early diagenesis (Koschinsky et al. 2010). Then, dissolved Mn in porewater reprecipitates under oxidizing

conditions in the uppermost sediment layer. (Koschinsky et al. 2010). However, this model alone fails to explain the significant vertical distribution (e.g., 185 m in stratigraphic column C1; Fig. 8) of the Mn oxide mineralization found in the East Pisco Basin.

In Jurassic sandstone from Utah, Chan et al. (2000) describe the occurrence of Mn oxides, including pyrolusite, manganite, and cryptomelane-hollandite, either as a cement to quartz sand grains or filling fractures that parallel a major structure, the Moab Fault. Chan et al. (2000) propose that faulting and salt tectonism caused the dissolution of a salt-cored anticline by interacting with meteoric water. The resulting saline brines acquired a reducing character as a result of a reaction with hydrocarbons, organic acids, or hydrogen sulfide. This saline, reduced fluid flowed up through the Moab Fault and adjacent permeable red sandstone, and lixiviated the Fe and Mn from them. The Fe- and Mn-charged fluid entered in a dynamic flow system in the aquifers of the area, where mixing with shallow, oxygenated groundwater resulted in the precipitation of Fe and Mn oxides along the porous and permeable sandstone bed.

In the Bahía Inglesa Formation in Chile (Fig. 3), Achurra et al. (2009) identified two onshore stratigraphic units consisting of silty mudstone that host Mn nodules and are cut by gypsum veins. In the lower unit, diagenetic Mn-nodules occur with discoidal to spherical shapes and replacing trace fossils (e.g., Ophiomorpha), whereas in the upper unit the nodules are mainly botryoidal. The Mn nodules are composed of todorokite and trace amounts of cryptomelane, which constitute a cement to silicate minerals and siliceous microorganisms (e.g., diatoms). Achurra et al. (2009) argue, based on the analysis of a literature-

derived geochemical dataset, that Mn nodules from the Bahía Inglesa Formation formed in an environment with intermediate-depth marine characteristics (i.e., continental slope to outer shelf) with partly restricted conditions because of topographic highs forming partial barriers to ocean circulation. However, these authors do not provide a model of precipitation for the Mn oxides.

In our particular study case in the East Pisco Basin, Gioncada et al. (2018) describe scarce Fe and Mn oxides accompanying dolomite within and around fossils in the Pisco Formation. These authors propose that the decay of organic matter at the bottom of the shallow marine basin, coupled to Mn and Fe reduction, may have increased the concentration of these elements in sediment porewater. As a consequence of the involvement of porewater sulfate acting as an oxidizing agent for organic matter, Fe sulfides formed, which is evidenced by common occurrence of ghost framboidal pyrite. Then, high-Mn/Fe Mn oxides precipitated in renewed oxygenated conditions due to the increase in alkalinity attributed to sulfate reduction, or to the renewed interaction with oxygenated seawater at sea bottom after the depletion of organic matter.

Onshore Mn oxides from the Chilcatay and Pisco formations could be linked to decomposition of organic matter at the bottom of the shallow marine East Pisco basin as explained by Gioncada et al. (2018). The oily black stains observed in rocks from the East Pisco Basin (Figs. 14C, 25B) would attest to the circulation of liquid hydrocarbons derived from the decomposition of organic matter. The reduced, organic matter-rich sediment porewater flowed up through permeable beds and structures similarly to the proposed model by Chan et al. (2000) for Mn oxides in the Jurassic sandstone from Utah. Some of the permeable beds are

occasionally “sealed” by overlying massive gypsum beds, which acted as a stratigraphic trap for the fluids. Furthermore, since Mn oxides are distributed from siltstone of the Chilcatay Formation to siltstone topping the Pisco Formation—considered Pliocene in age (Ochoa et al. 2021)—, Mn oxide precipitation should be Pliocene or younger. In this line of thought, the rapid uplift of the East Pisco Basin during the late Pliocene related to the oblique subduction of the aseismic Nazca Ridge underneath the South American Plate (Di Celma et al. 2016) since ca. 4-5 Ma (Macharé and Ortlieb 1992; Hampel 2002) could have promoted brine expulsion through compactive dewatering or seismic pumping (cf. Eisenlohr et al. 1994). A subsequent mixing with either shallow, oxygenated seawater (Gioncada et al. 2018) or groundwater (Chan et al. 2000) controlled the precipitation of Mn oxides.

5.2. Assessment of geochemical discrimination diagrams

Different geochemical genetic discrimination plots for Mn oxide mineralization have been proposed in the literature (e.g., Bonatti et al. 1972; Josso et al. 2017; Zawadzki et al. 2022). EPMA and bulk chemical analyses in this study are plotted in some of such diagrams together with previous analyses of Mn nodules from a different site within the Pisco Formation by Bessler (1975) (Figs. 36-37). In the Fe-Mn-(Cu + Co + Ni)*10 diagram, the data plot in the overlapping area of the hydrothermal and early diagenetic fields (Fig. 36A). Likewise, in the (Fe + Mn)/4-(Ni + Cu)*15-(Zr + Y + Ce)*100 diagram, the data plot in the area of hydrothermal and suboxic diagenesis origins (Fig. 36B). In the Ce/Ce* vs. Y_N/Ho_{CN} diagram, most of the samples fall between the hydrogenetic and hydrothermal fields, with a remarkable dispersion (Fig. 37).

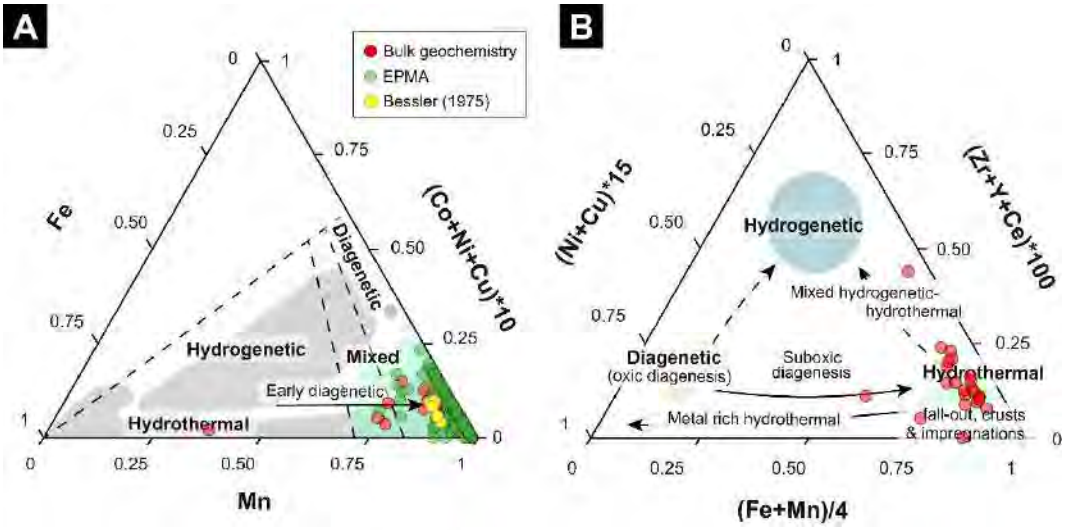

Figure 36. Ternary genetic discrimination plots for Mn-oxides of the East Pisco Basin. (A) Ternary Fe - Mn - (Co + Ni + Cu) × 10 plot with compositional fields after Bonatti et al. (1972) and Zawadzki et al. (2022). (B) Ternary (Ni + Cu) × 15 - (Fe + Mn)/4 - (Zr + Y + Ce) × 100 plot with compositional fields after Josso et al. (2017). EPMA (this study) and bulk geochemistry data (this study) are plotted along with data by Bessler (1975) for comparison.

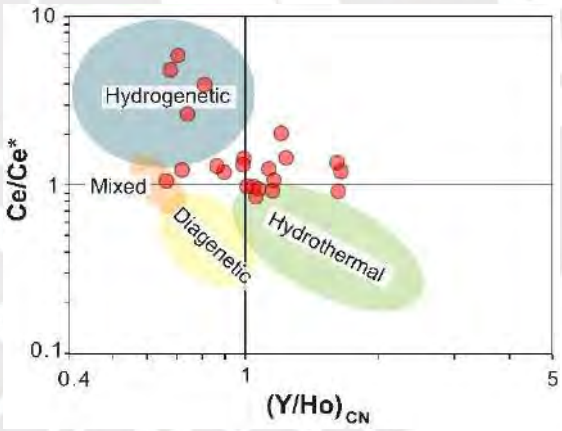

Figure 37. Binary Ce/Ce* vs. $(Y/Ho)_{CN}$ genetic discrimination plot for Mn oxides of the East Pisco Basin (bulk geochemistry; this study). $Ce/Ce^*=Ce_{CN}/(0.5*La_{CN}+0.5*Pr_{CN})$, where CN refers to normalization to C1 chondrite using values of Sun and McDonough (1989). Compositional fields are after Bau et al. (2014).

The representation of our data in the Fe-Mn-(Cu + Co + Ni)*10 discrimination diagram (Fig. 36A; Bonatti et al. 1972; Zawadzki et al. 2022) concurs with the proposed diagenetic origin of the Mn oxides in the East Pisco Basin, probably

transitional to a hydrothermal environment. This classification is broadly equivalent to the suboxic diagenetic and/or hydrothermal origin(s) deduced from the (Fe + Mn)/4-(Ni + Cu)*15-(Zr + Y + Ce)*100 diagram (Fig. 36B; Josso et al. 2017). Finally, the Ce/Ce* vs. Y_N/Ho_{CN} plot does not contribute clear conclusions as to the origin of the Mn mineralization, mostly due to the large data dispersion, and suggests contradictory results (hydrogenetic vs. hydrothermal). Although hydrogenetic nodules characteristically possess positive Ce anomalies (Ce/Ce* = 1.10–4.61), Ce can migrate simultaneously to Mn remobilization, to be later incorporated into Mn oxides during the reoxidation and precipitation of Mn at oxic-anoxic interfaces (Zhang et al. 2023).

These results indicate that origin discrimination diagrams based on the chemical composition of Mn oxides may give rise to contradictory conclusions. Therefore, they should be used with caution and complemented with field and mineralogical data when possible.

5.3. Metalliferous potential

Although Mn oxides in the East Pisco Basin are irregularly distributed along different stratigraphic levels of the Chilcatay and Pisco formations (Figs. 8, 15, 19), Mn-bearing beds are laterally continuous, such that in some cases they have been followed for more than 300 m along strike (Figs. 20-22). Moreover, the accumulation of Mn-oxide fragments in rock pavement is so extensive that it sets a dark color to valley bottoms (Fig. 20A).

In addition to high Mn (mean value of 34.71 wt%), Mn oxides from the East Pisco Basin yield significant CoO contents, which are up to 0.80 wt% with a mean value of 0.21 wt% in bulk analyses (Table 2) and up to 2.64 wt% with a mean value of 0.46 wt% in EPMA data (Tables 4-5). These values are similar to those in hydrogenetic Mn nodules from the Cook Islands-Penrhyn Basin (mean value of 0.48 wt% CoO) and those in mixed-type Mn nodule deposits from the Clarion Clipperton Zone and other abyssal plains (mean value of 0.31 wt% CoO; Hein et al. 1997). In comparison, Mn oxides from the East Pisco Basin yield CoO contents generally higher than those in mixed-type Mn nodule deposits from the Central Indian Ocean Basin (mean value of 0.14 wt% CoO) and diagenetic Mn nodules from the Peru Basin (mean value of 0.06 wt% CoO) according to data compiled by Hein et al. (2020). Noteworthy, this finding contrasts with the typically low Co contents of diagenetic nodules (<0.1 wt%; Hein and Koschinsky 2014).

The reason for the Co enrichment, and ultimately its origin, in the Mn oxide mineralization in the East Pisco Basin are unknown. Cobalt enrichment is particularly intriguing when compared to Mn oxide nodules from the nearby Bahía Inglesa Formation in Chile (<0.06 wt% CoO; Achurra et al. 2009), with which the mineralization studied in this thesis shares many similarities: i) Mn oxides, including nodules, of diagenetic origin which are ii) hosted in Miocene marine sediments deposited in a restricted environment that are iii) crosscut by abundant networks of gypsum/anhydrite veins near a iv) subducting ridge. Such contrast in Co contents could be explained in terms of distance of deposition of continental-shelf seafloor sediments to river-dominated continental margins and/or the abundance of organic matter thereof (cf. Lenstra et al. 2022).

Alternatively, the circulation of deeper fluids (e.g., subduction-water) throughout the sedimentary pile and basement rocks could have also contributed to the Co endowment, particularly of those rocks of mafic composition in the Coastal Basal Complex underlying the Cenozoic sedimentary rocks in the East Pisco Basin (Ochoa et al. 2021). A conspicuous geographic feature of the study area is its location on top of the subducting Nazca ridge and by the Nazca Drift System (Fig. 3). Calvès et al. (2022) suggest that the large volumes of accumulated sediments and polymetallic material as well as the excess porosity water in the Nazca Drift System could have impacted the orogenesis and metallogenesis in the Andes since the middle-late Miocene. At this stage, a purely suboxic diagenetic vs. a hydrothermal imprint in the origin of the Mn-oxide mineralization in the Chilcatay and Pisco formations cannot be discriminated using available data (e.g., geochemical discrimination diagrams in Figs. 36A-B). Further work is needed to elucidate the origin of metals and mineralizing fluids associated to the Mn-oxide mineralization in the East Pisco Basin.

Despite this, the exposed observations do suggest that diagenetic Mn oxides from the East Pisco Basin might represent a novel, previously overlooked mineralization style for cobalt and that Mn oxides of diagenetic origin may also be prospective for this metal. Moreover, the onshore exposure of Co-rich Mn oxides represents an attractive alternative to the controversial deep-sea mining of Mn nodules, which is still in question due to political restrictions and potential environmental threats (Cunningham 2022).

5.4. Exploration guidelines

This study demonstrates that Mn oxide mineralization of diagenetic origin (± hydrothermal imprint) can be enriched not only in Mn, but also in other critical metals such as Co. A key factor to the genesis of Mn oxide mineralization in the onshore East Pisco Basin is a high interstitial porosity. The presence of juvenile, poorly-consolidated, poorly-lithified sediments which, at the time of mineralization, allows Mn-rich fluids circulation and Mn oxide deposition as cement. Another key factor is the availability of fault structures. As Chan et al. (2000) propose for Mn mineralization in Jurassic sandstone from Utah, permeable beds and structures allow Fe- and Mn- rich fluids to enter in an extensive dynamic flow system. Otherwise, the vertical distribution of Mn oxides in the East Pisco Basin cannot be explained. In addition, rock formations which contain stratigraphic beds that could act as seals (e.g., anhydrite and gypsum beds) come up as prospective sequences.

As Mn-oxide nodules tend to grow in vast horizontal fields, a primary exploration focus for onshore exposition can be based on satellite imagery. Through this technic, prospective locations for Mn oxide mineralization would be identified by a much darker color in comparison with the surrounding areas. Specifically, eroded zones would favor the accumulation of Mn-oxide fragments as rock pavement in lower levels, such as valley bottoms (Fig. 20A).

6. CONCLUSIONS

The present study documents the morphological, mineralogical, and compositional variations of Mn oxides in the Chilcatay and Pisco formations exposed in the onshore forearc East Pisco Basin in Peru. The main conclusions are the following:

- Manganese oxides appear as nodules and concretions, veins, and surface coatings that concentrate along particular sandstone, siltstone, and tuff levels. The lithological and stratigraphic control of the mineralization, the evidence of focused circulation of Mn-bearing fluids through fractures, occurrence of Mn-oxides cementing bioclastic components, fossilization of bioelements by Mn oxides, and the crystallization as cryptomelane/hollandite and todorokite are clear evidence of a diagenetic origin of Mn oxide mineralization.

- Traditional discrimination diagrams are, by themselves, unreliable to determine the genetic type of Mn nodules and must be properly complemented by field observations and mineralogical data.

- The Mn-oxide mineralization could be related to decay of organic matter at the bottom of the shallow marine East Pisco basin. The reduced sediment porewater flowed up through permeable beds, some of which are “sealed” by overlying massive gypsum beds. The rapid uplift of the East Pisco Basin during late Pliocene linked to the oblique subduction of the aseismic Nazca Ridge may have induced fluid circulation and renewed oxygenated conditions that lead to the precipitation of Mn oxides.

- An efficient Mn-oxide mineralization of diagenetic origin was enhanced by high interstitial porosity and the availability of sub-vertical structures connecting different stratigraphic levels and enabling the circulation of Mn-rich fluids within an extensive and dynamic flow system.

- Manganese oxides from the East Pisco Basin stand among the richest in Co globally (up to 2.64 wt% CoO with a mean value of 0.46 wt% in point analyses,

and up to 0.80 wt% CoO with a mean value of 0.21 wt% in bulk analyses). The onshore exposure of Co-rich Mn oxides represents an unexplored metalliferous potential for critical elements.

7. REFERENCES

Achurra LE, Lacassie JP, Le Roux JP, Marquardt C, Belmar M, Ruiz-del-Solar J, Ishman SE (2009) Manganese nodules in the Miocene Bahía Inglesa Formation, north-central Chile: Petrography, geochemistry, genesis and palaeoceanographic significance. Sediment Geol 217:128-139

Bau M, Schmidt K, Koschinsky A, Hein JR, Kuhn T, Usui A (2014) Discriminating between different genetic types of marine ferro-manganese crusts and nodules based on rare earth elements and yttrium. Chem Geol 60:1709-1725

Bessler E (1975) Sobre la existencia de los nódulos de manganeso en la Formación Pisco. Boletín SGP 50:10-34

Bloomberg NEF (2021) 1H 2021 Battery metals outlook. Bloomberg, London

Bonatti E, Kraemer T, Rydell H (1972) Classification and genesis of submarine iron-manganese deposits. Ferromanganese deposits on the ocean floor, pp 149-166

Boschen RE, Rowden AA, Clark MR, Gardner JPA (2013) Mining of deep-sea seafloor massive sulfides: A review of the deposits, their benthic communities, impacts from mining, regulatory frameworks and management strategies. Ocean Coastal Manag 84:54-67

Brown T, Duuring P, Morin-Ka S, Strong CA (2022) Manganese: A mineral systems analysis, record 2022/5. Geological Survey of Western Australia

Burns RG, Burns VM (1977) Chapter 7 Mineralogy. In: Glasby GP (ed) Marine Manganese Deposits. Elsevier Oceanography Series, Elsevier, Wellington, pp. 185-248

Calvès G, Mix A, Giosan L, Clift PD, Brusset S, Baby P, Vega M (2022) The Nazca Drift System – Palaeoceanographic significance of a giant sleeping on the SE Pacific Ocean floor. Geol Mag 159:322-336

Canet C, Anadón P, Alfonso P, Prol-Ledesma RM, Villanueva-Estrada RE, García-Vallès M (2013) Gas-seep related carbonate and barite authigenic mineralization in the Northern Gulf of California. Mar Pet Geol 43:147-165

Canet C, Anadón P, González-Partida E, Alfonso P, Rajabi A, Pérez-Segura E, Alba-Aldave LA (2014) Paleozoic bedded barite deposits from Sonora (NW Mexico): Evidence for a hydrocarbon seep environment of formation. Ore Geol Rev 56:292-300

Canon WF, Kimball BE, Corathers LA (2017) Manganese. In: Schulz KJ, DeYoung JH, Jr. Seal II RR, Bradley DC (eds) Critical mineral resources of the United States—Economic and environmental geology and prospects for future supply. US Geological Survey, Virginia

Casalbore D (2018) Volcanic Islands and Seamounts. In: Micallef A, Krastel S, Savini A (eds) Submarine Geomorphology. Springer, Berlin, pp 333-347

Chan M (2022) A perspective on concretions: Deciphering diagenesis from Earth to Mars. J Geol Soc Japan 128:445-464

Chan M, Parry W, Bowman J (2000) Diagenetic hematite and manganese oxides and fault-related fluid flow in Jurassic sandstones, Southeastern Utah. AAPG Bulletin 84:1281-1310

Clift PD, Pecher I, Kukowski N, Hampel A (2003) Tectonic erosion of the Peruvian forearc, Lima basin, by subduction and Nazca ridge collision. Tectonics 22:1023

Cunningham A (2022) Assessing the feasibility of deep-seabed mining of polymetallic nodules in the Area of seabed and ocean floor beyond the limits of national jurisdiction, as a method of alleviating supply-side issues for cobalt to US markets. Miner Econ 37:1-20

DeVries TJ, Jud NA (2018) Lithofacies patterns and paleogeography of the Miocene Chilcatay and lower Pisco depositional sequences (East Pisco Basin, Peru). Boletín SGP 8:124–167

Di Celma C, Malinverno E, Gariboldi K, Gioncada A, Rustichelli A, Pierantoni PP, Landini W, Bosio G, Tinelli C, Bianucci G (2016) Stratigraphic framework of the late Miocene to Pliocene Pisco Formation at Cerro Colorado (Ica Desert, Peru) J Maps 12:515-529

Di Celma C, Malinverno E, Bosio G, Collareta A, Gariboldi K, Gioncada, A, Molli G, Basso D, Varas-Malca R, Pierantoni P, Villa I, Lambert O, Landini W, Sarti G, Cantalamessa G, Urbina-Schmitt M, Bianucci G (2017) Sequence stratigraphy and paleontology of the Upper Miocene Pisco Formation along the western side of the lower Ica valley (Ica desert, Peru). Riv Ital 123:255-273

Di Celma C, Malinverno E, Bosio G, Gariboldi K, Collareta A, Gioncada A, Landini W, Pierantoni P, Bianucci G (2018a) Intraformational unconformities as a record of late Miocene eustatic falls of sea level in the Pisco Formation (southern Peru). J Maps 14:607-619

Di Celma C, Malinverno E, Collareta A, Bosio G, Gariboldi K, Lambert O, Landini W, Pierantoni PP, Gioncada A, Villa IM, Coletti G, De Muizon C, Urbina M,

Bianucci G (2018b) Facies analysis, stratigraphy and marine vertebrate assemblage of the lower Miocene Chilcatay Formation at Ullujaya (Pisco basin, Peru). J Maps 14:257-268

Di Celma C, Pierantoni P, Volatili T, Molli, G, Mazzoli S, Sarti G, Ciattoni S, Bosio G, Malinverno E, Collareta A, Gariboldi K, Gioncada A, Jablonska D, Landini W, Urbina M, Bianucci G (2022) Towards deciphering the Cenozoic evolution of the East Pisco Basin (southern Peru). J Maps 18:1-16

Dunbar RB, Marty RC, Baker PA (1990) Cenozoic marine sedimentation in the Sechura and Pisco basins, Peru. Palaeogeogr Palaeoclimatol Palaeoecol 77: 235-261

Eisenlohr BN, Tompkins LA, Cathles LM, Barley M, Groves D (1994) Mississippi Valley-type deposits: products of brine expulsion by eustatically induced hydrocarbon generation? An example from northwestern Australia. Geology 22:315-318

Espurt N, Baby P, Brusset S, Roddaz M, Hermoza W, Regard V, Antoine P-O, Salas-Gismondi R, Bolaños R (2007) How does the Nazca Ridge subduction influence the modern Amazonian foreland basin? Geology 35:515–518

European Commission (2023) Study on the EU's list of Critical Raw Materials (final report). European Commission, Brussels, pp 1–157

European Space Agency (2024) Copernicus global digital elevation model. Distributed by OpenTopography. https://doi.org/10.5069/G9028PQB. Accessed 29 August 2024

Feng D, Roberts HH (2011) Geochemical characteristics of the barite deposits at cold seeps from the northern Gulf of Mexico continental slope. Earth Planet Sci Lett 309:89-99

García M, Correa J, Maksaev V, Townley B (2020) Potential mineral resources of the Chilean offshore: An overview. Andean Geol 47:1-13

Gariboldi K, Bosio G, Malinverno E, Gioncada A, Di Celma C, Villa I, Urbina M, Bianucci G (2017). Biostratigraphy, geochronology and sedimentation rates of the upper Miocene Pisco Formation at two important marine vertebrate fossil-bearing sites of southern Peru. Newsl Stratigr 50:417-444

George SWM, Perez ND, Struble W, Ellis Curry M, Horton BK (2022) Aseismic ridge subduction focused late Cenozoic exhumation above the Peruvian flat slab. Earth Planet Sc Lett 600:117754

Gioncada A, Petrini R, Bosio G, Gariboldi K, Collareta A, Malinverno E, Bonaccorsi E, Di Celma C, Pasero M, Urbina M, Bianucci G (2018) Insights into the diagenetic environment of fossil marine vertebrates of the Pisco Formation (late Miocene, Peru) from mineralogical and Sr-isotope data. J S Am Earth Sci 81:141-152

Glasby GP (2013) Manganese: Predominant role of nodules and crusts. In: Schulz and Zabel (eds) Marine geochemistry, 2nd edn. Springer, Berlin, pp 371–427

Government of Canada (2022) The Canadian critical minerals strategy, from exploration to recycling: powering the green and digital economy for Canada and the world. Natural Resources Canada, Ottawa

Hampel A (2002) The migration history of the Nazca Ridge along the Peruvian active margin: A re-evaluation. Earth Planet Sci Lett 203:665–679

Hannington M, Jamieson J, Monecke T, Petersen S, Beaulieu S (2011) The abundance of seafloor massive sulfide deposits. Geology 39:1155–1158

Hein JR, Koschinsky A (2014) Deep ocean ferromanganese crusts and nodules. In: Holland and Turekian (eds) Earth systems and environmental sciences, treatise in geochemistry, 2nd edn. Elsevier, Amsterdam, pp 273–291

Hein JR, Koschinsky A, Halbach P, Manheim FT, Bau M, Kang JK, Lubick N (1997) Iron and manganese oxide mineralization in the Pacific. Geol Soc Lond Spec Publ 119:123–138

Hein JR, Koschinsky A, Bau M, Manheim FT, Kang J-K, Roberts L (2000) Cobalt-rich ferromanganese crusts in the Pacific. In: Cronan DS (ed) Handbook of marine mineral deposits. CRC Press, Florida, pp 239-279

Hein JR, Petersen S (2013) The geology of cobalt–rich ferromanganese crusts. In: Baker E and Beaudoin Y (eds) Deep sea minerals: seafloor massive sulphides, a physical, biological, environmental, and technical review. Secretariat of the Pacific Community, pp 7–14

Hein JR, Mizell K, Koschinsky A, Conrad TA (2013) Deep-ocean mineral deposits as a source of critical metals for high- and green-technology applications: Comparison with land-based resources. Ore Geol Rev 51:1-14

Hein JR, Koschinsky A, Kuhn T (2020) Deep-ocean polymetallic nodules as a resource for critical materials. Nat Rev Earth Environ 1:158–169

Helmons R, de Wit L, de Stigter H, Spearman J (2022) Dispersion of benthic plumes in deep-sea mining: What lessons can be learned from dredging? Front Earth Sci 10:868701

Herzig PM, Hannington MD (2006) Input from the deep: Hot vents and cold seeps. In: Schulz and Zabel (eds) Marine Geochemistry, 2nd edn. Springer, Berlin, pp 457–479

Hlawatsch S, Neumann T, van den Berg CMG, Kersten M, Harff J, Suess E (2002) Fast-growing, shallow-water ferro-manganese nodules from the western Baltic Sea: origin and modes of trace element incorporation. Mar Geol 182:373–387

International Seabed Authority (2023) Exploration Contracts. https://www.isa.org.jm/exploration-contracts/. Accessed 3 June 2023

Josso P, Pelleter E, Pourret O, Fouquet Y, Etoubleau J, Cheron S, Bollinger C (2017) A new discrimination scheme for oceanic ferromanganese deposits using high field strength and rare earth elements. Ore Geol Rev 87:3–15

Koschinsky A, Hein J, Schmidt K, Alexander B, Bau M (2010) Rare and valuable metals for high-tech applications in marine ferromanganese nodules and crusts: Relationships to genetic endmembers. In: Toward the sustainable development of marine minerals: Geological, technological and economic aspects. UMI, Gelendzhik, pp 1-13

León WR, Torres V (2003) Memoria descriptiva de la revisión y actualización de los cuadrángulos de Punta Grande (29-k), Ica (29-1), Lomitas (30-1), Palpa (30-m), San Juan (31-m), Acari (31-n) y Yauca (32-n) Escala 1:1 00 000. INGEMMET, Lima

León WR, Rosell W, Alemán AM, Torres VR, De la Cruz MO (2008) Estratigrafía, sedimentología y evolución tectónica de la cuenca Pisco Oriental. Boletín INGEMMET 27:1-154

Lenstra W, van Helmond N, Zygadlowska O, Zummeren R, Witbaard R, Slomp CP (2022) Sediments as a source of iron, manganese, cobalt and nickel to continental shelf waters (Louisiana, Gulf of Mexico). Front Mar Sci 9:811953

Lusty P, Hein JR, Josso P (2018) Formation and occurrence of ferromanganese crusts: Earth's storehouse for critical metals. Elements 14:313–318

Lusty P, Murton B (2018) Deep-ocean mineral deposits: Metal resources and windows into Earth processes. Elements 14:301–306

Macharé J (1987) La Marge Continentale du Pérou: régimes tectoniques et sédimentaires Cénozoiques de L'avant-Arc des Andes Centrales. PhD Thesis, Université de Paris Sud, Paris, France

Macharé J, Ortlieb L (1992) Plio-Quarternary vertical motions and the subduction of the Nazca Ridge, central coast of Peru. Tectonophysics 205:97-108

Ochoa D, Salas-Gismondi R, DeVries T, Baby P, de Muizon C, Sierra A, Barbosa A, Foster D, Quispe K, Cardich J, Gutiérrez D, Perez A, Valqui J, Urbina M, Carré M (2021) Late Neogene evolution of the Peruvian margin and its ecosystems: A synthesis from the Sacaco record. Int J Earth Sci (Geol Rundsch) 110:995–1025

Peacock T (2023) The GSR Patania II expedition: Technical achievements and scientific learning. Global Sea Mineral Resources. Internal report.

Pelleter E, Fouquet Y, Etoubleau J, Cheron S, Labanieh S, Josso P, Bollinger C, Langlade J 796 (2017) Ni-Cu-Co-rich hydrothermal manganese mineralization in the Wallis and 797 Futuna back-arc environment (SW Pacific). Ore Geol Rev 87:126-146

Petersen S, Hein JR (2013) The geology of seafloor massive sulphides. In: Baker E, Beaudoin Y (eds) Deep sea minerals: seafloor massive sulphides, a physical, biological, environmental, and technical review. Secretariat of the Pacific Community, pp 7-18

Quispe K, Baby P, Calderón Y, Hurtado C, Ramírez L (2018) La Cuenca Pisco: nuevo modelo estructural para una cuenca de antearco peruana, evidencias de contexto

compresivo, desarrollo de la Cordillera de la Costa, XIX Congreso Peruano de Geología. SGP, Lima

Rustichelli A, Di Celma C, Tondi E, Bianucci G (2016) Deformation within the Pisco Basin sedimentary record (southern Peru): Stratabound orthogonal vein sets and their impact on fault development. J S Am Earth Sci 65:79–100

Seabold E, Berger W (2013) The sea floor: An introduction to marine geology. Springer, Heidelberg

Slack JF, Kimball BE, Sheed KB (2017) Cobalt. In: Schulz KJ, DeYoung JH, Jr. Seal II RR, Bradley DC (eds) Critical mineral resources of the United States—Economic and environmental geology and prospects for future supply. US Geological Survey, Virginia

Sparenberg O (2019) A historical perspective on deep-sea mining for manganese nodules, 1965–2019. Extr Ind Soc 6:842-854

Sun SS, McDonough WF (1989) Chemical and isotopic systematics of oceanic basalts: implications for mantle composition and processes. In: Saunders AD, Norry MJ (eds) Magmatism in the Ocean Basins. Geol Soc Spec Publ 42:313-345

Thornburg TM, Kulm LD (1981) Sedimentary basins of the Peru continental margin: Structure, stratigraphy, and Cenozoic tectonics from 6°S to 16°S latitude. In: Kulm LD, Dymond J, Dasch EJ, Hussong DM (eds) Nazca plate: crustal formation and Andean convergence. Geol Soc America Mem 154:393-422

Toro N, Jeldres RI, Órdenes JA, Robles P, Navarra A (2020) Manganese nodules in Chile, an alternative for the production of Co and Mn in the future— A review. Minerals 10:674

Torres ME, Brumsack HJ, Bohrmann G, Emeis KC (1996) Barite fronts in continental margin sediments: A new look at barium remobilization in the zone of sulfate

reduction and formation of heavy barites in diagenetic fronts. Chem Geol 127:125–139

Torres ME, Bohrmann G, Dubé TE, Poole FG (2003) Formation of modern and Paleozoic stratiform barite at cold methane seeps on continental margins. Geology 31:897–900

US Geological Survey (2022) 2022 Final list of critical minerals. https://www.usgs.gov/news/national-news-release/us-geological-survey-releases-2022-list-critical-minerals. Accessed 3 June 2023

Vineesh TC, Nagender B, Banerjee R, Jaisankar S, Lekshmi V (2009) Manganese nodule morphology as indicators for oceanic processes in the Central Indian Basin. Int Geol Rev 51:27–44

Viveen W, Schlunegger F (2018) Prolonged extension and subsidence of the Peruvian forearc during the Cenozoic. Tectonophysics 730:48-62

Vodyanitskii YN, Vasilév AA, Lesovaya SN, Sataev EF, Sivtsov AV (2004) Formation of manganese oxides in soil. Eurasian Soil Sci 37:572–584

Zawadzki D, Maciąg Ł, Blasco I, González FJ, Wernette B, Marino E, Kozub-Budzyń GA, Piestrzyński A, Wróbel RJ, McCartney K (2022) Geochemistry and mineralogy of ferromanganese crusts from the Western Cocos-Nazca spreading centre, Pacific. Minerals 12:538

Zhang H, Zhou J, Yuan P, Dong Y, Fan W, Yu X, Lu J (2023) Implication from mineralogical and geochemical characteristics of authigenic micronodules in the Haima cold seeps for understanding the manganese geochemistry in active seepage. J Geophys Res Oceans 128:1-21

Zhong Yi, Liu Q, Chen Z, González FJ, Hein JR, Zhang Ji, Zhong L (2019) Tectonic and paleoceanographic conditions during the formation of ferromanganese

nodules from the northern South China Sea based on the high-resolution geochemistry, mineralogy and isotopes. Mar Geol 410:146–163

APPENDICES

Appendix A: Sampling location and macroscopic description of the studied samples

Sample	Sampling location		Macroscopic description
	Latitude	Longitude	
2022-PAL-01	14° 48.876'S	75° 23.314'W	Botryoidal, massive, intraformational manganese nodule with a smooth, slightly shiny surface.
2022-PAL-02	14° 48.876'S	75° 23.314'W	Discoidal, massive, intraformational manganese nodule with a rough, slightly shiny surface.
2022-PAL-03	14° 48.876'S	75° 23.314'W	Botryoidal, manganese veins with a smooth, matt surface.
2022-PAL-04	14° 48.876'S	75° 23.314'W	Botryoidal, massive manganese intraformational nodule with a smooth, matt surface. Associated with fibrous gypsum and a rough bottom manganese-oxides layer.
2022-PAL-05	14° 48.876'S	75° 23.314'W	Botryoidal, massive, intraformational manganese nodule with a smooth, matt surface.
2022-PAL-06	14° 48.876'S	75° 23.314'W	Black, thin manganese coating accreted onto a silty clay with manganese micronodules (<1mm).
2022-PAL-07	14° 48.876'S	75° 23.314'W	Botryoidal, massive manganese intraformational nodule with a smooth, slightly shiny surface.
2022-PAL-08	14° 48.876'S	75° 23.314'W	Discoidal, massive, intraformational manganese nodule with a rough, slightly shiny surface.
2022-PAL-09	14° 48.876'S	75° 23.314'W	Sub-rounded, massive, intraformational manganese nodule with a rough, matt surface. Associated with fibrous gypsum.
2022-PAL-10	14° 48.876'S	75° 23.314'W	Discoidal, massive, intraformational manganese nodule with a rough, slightly shiny surface.
2022-PAL-11	14° 48.876'S	75° 23.314'W	Sub-rounded, massive, intraformational manganese nodule with a rough, matt surface. Associated with fibrous gypsum and a rough bottom manganese-oxides layer.
2022-PAL-12	14° 48.876'S	75° 23.314'W	Discoidal, massive, intraformational manganese nodule with a rough, matt surface.
2022-PAL-13	14° 48.876'S	75° 23.314'W	Discoidal, massive, intraformational manganese nodule with a rough, slightly shiny surface.

Sample	Sampling location		Macroscopic description
	Latitude	Longitude	
2022-PAL-14	14° 48.254'S	75° 24.325’W	Spherical and elongated, massive, intraformational manganese nodules (sizes ranging from 1 mm to 1,9 cm) with a rough, matt surface hosted by a layered whitish fine-grained sandstone.
2022-PAL-15	14° 48.254'S	75° 24.325’W	Scarce, irregular manganese micronodules hosted by a beige, fine-grained sandstone.
2022-PAL-16	14° 48.254'S	75° 24.325’W	Elongated to spherical manganese micronodules with a matt surface hosted by a light-beige silty clay
2022-PAL-17	14° 48.254'S	75° 24.325’W	Elongated to spherical manganese micronodules with a matt surface hosted by a light-beige silty clay
2023-PAL-01	14° 50.543'S	75° 22.238’W	Black, thin manganese coating with a rough, matt surface accreted onto a brownish silty clay.
2023-PAL-02	14° 50.543'S	75° 22.238’W	Black, sandy manganese coating with a rough, matt surface accreted onto a light-beige fine-grained sandstone.
2023-PAL-03	14° 50.526'S	75° 22.256’W	Black, thin manganese coating with a rough, matt surface accreted onto a light-beige fine-grained sandstone with small manganese nodules (<5mm).
2023-PAL-04	14° 50.526'S	75° 22.256’W	Black, thin manganese coating with a rough, matt surface accreted onto a light-beige fine-grained sandstone.
2023-PAL-05	14° 50.506'S	75° 22.308’W	Globular manganese coating with a rough, matt surface accreted onto a whitish silty clay.
2023-PAL-06	14° 50.506'S	75° 22.308’W	Black, thin manganese coating with a rough, matt surface accreted onto a whitish silty clay.
2023-PAL-07	14° 50.506'S	75° 22.308’W	Black, irregular manganese coating with a rough, matt surface accreted onto a whitish silty clay.
2023-PAL-08	14° 50.506'S	75° 22.308’W	Black, sandy manganese coating with a rough, matt surface accreted onto a whitish silty clay.
2023-PAL-09	14° 50.501'S	75° 22.473’W	Elongated to spherical manganese micronodules with a matt surface hosted by a light-beige silty mudstone
2023-PAL-10	14° 50.501'S	75° 22.473’W	Elongated to spherical manganese micronodules with a matt surface hosted by a light-beige silty mudstone
2023-PAL-11	14° 50.501'S	75° 22.473’W	Elongated to spherical manganese micronodules with a matt surface hosted by a light-beige silty mudstone.
2023-PAL-12	14° 50.501'S	75° 22.473’W	Elongated to spherical manganese micronodules with a matt surface hosted by a light-beige silty mudstone.

Sample	Sampling location		Macroscopic description
	Latitude	Longitude	
2023-PAL-13	14° 50.481'S	75° 22.499’W	Black, spherical, medium-grained sandy manganese nodule with a beige, sandy nucleus
2023-PAL-14	14° 50.397'S	75° 22.491’W	White, medium-grained, biotite-rich tuff
2023-PAL-15	14° 50.397'S	75° 22.491’W	Globular, clast-covered, manganese nodule accreted onto a whitish medium-grained sandstone.
2023-PAL-16	14° 50.397'S	75° 22.491’W	Globular, clast-covered, manganese nodule accreted onto a whitish medium-grained sandstone.
2023-PAL-17	14° 50.397'S	75° 22.491’W	Botryoidal, manganese veins with a rough, matt surface.
2023-PAL-18	14° 50.397'S	75° 22.491’W	Pale beige, fine gypsum nodules in a gray granular matrix. Note that one gypsum nodule is scarcely filled with black manganese oxides.
2023-PAL-19	14° 49.027'S	75° 23.358’W	Black, manganese coating with a rough, slightly shiny surface accreted onto whitish to translucent, fibrous gypsum
2023-PAL-20	14° 49.027'S	75° 23.358’W	Black, manganese coating with a rough, slightly shiny surface accreted onto whitish, fibrous gypsum
2023-PAL-21	14° 49.027'S	75° 23.358’W	Black, mammillary manganese nodule with a rough, matt surface.
2023-PAL-22	14° 49.027'S	75° 23.358’W	Black, massive, irregular manganese oxides with a rough, matt surface.
2023-PAL-23	14° 49.063'S	75° 23.384’W	Whitish, fine-grained gypsum nodule.
2023-PAL-24	14° 49.068'S	75° 23.378’W	White, fine-grained gypsum.
2023-PAL-25	14° 49.102'S	75° 23.408’W	Black, elongated manganese nodules with a rough, matt surface accreted onto a whitish to translucent fibrous gypsum vein.
2023-PAL-26	14° 49.102'S	75° 23.408’W	Black, globular manganese nodule with a rough, matt surface.
2023-PAL-27	14° 49.102'S	75° 23.408’W	Black, irregular manganese nodule with a rough, matt surface.
2023-PAL-28	14° 49.139'S	75° 23.446’W	Black, botryoidal, "grape-shaped" manganese nodules hanging on medium-grained sand bed.
2023-PAL-29	14° 49.139'S	75° 23.446’W	Black, botryoidal, "grape-shaped" manganese nodules hanging on medium-grained sand bed.

Sample	Sampling location		Macroscopic description
	Latitude	Longitude	
2023-PAL-30	14° 49.139'S	75° 23.446’W	Black, botryoidal, "grape-shaped" manganese nodules hanging on medium-grained sand bed.
2023-PAL-31	14° 49.139'S	75° 23.446’W	Manganese coating with a smooth, shiny surface and spherical manganese nodules with a rough, matt surface accreted onto a whitish to translucent fibrous gypsum vein.
2023-PAL-32	14° 49.182'S	75° 23.473’W	Globular, manganese vein with a rough, matt surface.
2023-PAL-33	14° 49.182'S	75° 23.473’W	Globular, manganese vein with a rough, matt surface.
2023-PAL-34	14° 49.187'S	75° 23.438’W	Black, spherical, globular manganese nodule with a rough, slightly shiny surface.
2023-PAL-35	14° 49.187'S	75° 23.438’W	Black, ellipsoidal, massive manganese nodule with a smooth, matt surface.
2023-PAL-36	14° 49.143'S	75° 23.399’W	Black, "root-shaped", globular manganese nodules with a rough, matt surface.
2023-PAL-37	14° 49.094'S	75° 23.423’W	Botryoidal, manganese veins with a rough, matt surface.
2023-PAL-38	14° 49.094'S	75° 23.423’W	Botryoidal, manganese veins with a rough, matt surface.
2023-PAL-39	14° 49.137'S	75° 23.447’W	Tuffaceous coarse-grained sandstone replacing a tubular-shaped bioturbation.
2023-PAL-40	14° 49.122'S	75° 23.463’W	Black, elongated, massive, sandy manganese oxides replacing a tubular-shaped bioturbation.
2023-PAL-41	14° 49.243'S	75° 23.558’W	White, fine-grained diatomite with black, greasy stains.
2023-PAL-42	14° 49.243'S	75° 23.558’W	White, fine-grained diatomite crossed by fine gypsum veinlets.
2023-PAL-43	14° 48.876'S	75° 23.314’W	Botryoidal, massive manganese intraformational nodule with a smooth, slightly shiny surface.
2023-PAL-44	14° 49.867'S	75° 24.787’W	Irregular to subrounded manganese micronodules with a matt surface hosted by a light-beige silty mudstone.
2023-PAL-45	14° 50.024'S	75° 22.139’W	Black, botryoidal, "grape-shaped" manganese nodules covered by medium-grained sand.
2023-PAL-46	14° 50.000'S	75° 22.184’W	Black, thick manganese coating with a rough, matt surface accreted onto a light-beige silty clay.

Sample	Sampling location		Macroscopic description
	Latitude	Longitude	
2023-PAL-47	14° 49.985'S	75° 22.211’W	Black, spherical manganese nodule with a rough, slightly shiny surface.
2023-PAL-48	14° 49.985'S	75° 22.211’W	Black, spherical manganese nodule with a rough, slightly shiny surface accreted onto a medium-grained sandstone.

Appendix C: Petrographic descriptions and photomicrographs - Polished and thin sections

2022-PAL-03

Type of sample: vein

Manganese oxide cement-supported matrix embedding angular detrital grains. Homogeneous, irregular layers of more massive Mn oxides frequently alternate with zones of fibrous, spongy Mn oxides. Biomorphic remnants of possible diatoms are fossilized by Mn oxides.

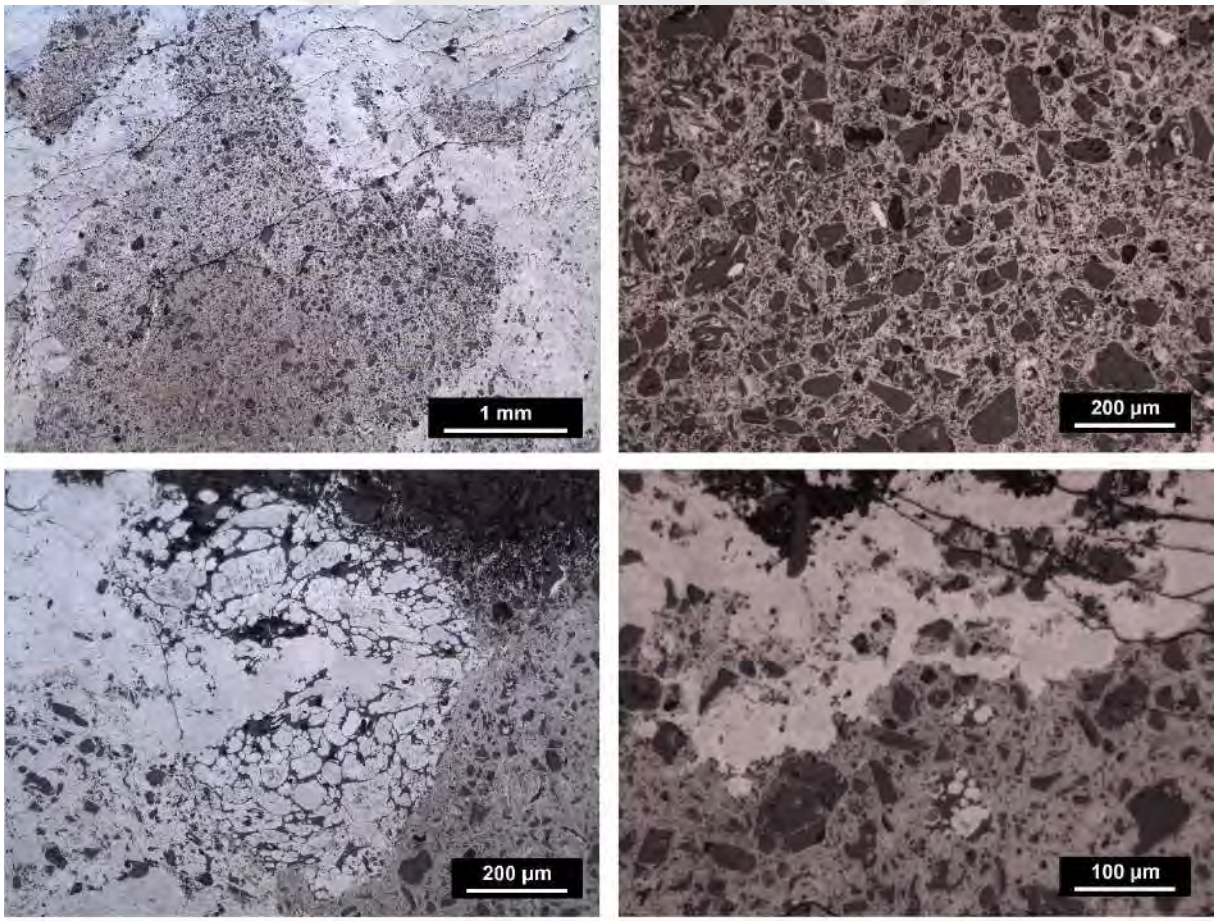

2022-PAL-04

Type of sample: nodule

Nodule sample with at least two concentrical rims with patchy textures of Mn oxides. Microcrystalline Mn oxides with fibrous and spongy textures cement angular detrital grains. Biomorphic remnants of possible diatoms are replaced by Mn oxides. Thin, irregular and sinuous fractures are totally or partially filled with Mn oxides with internal porous, colloidal, or homogeneous textures.

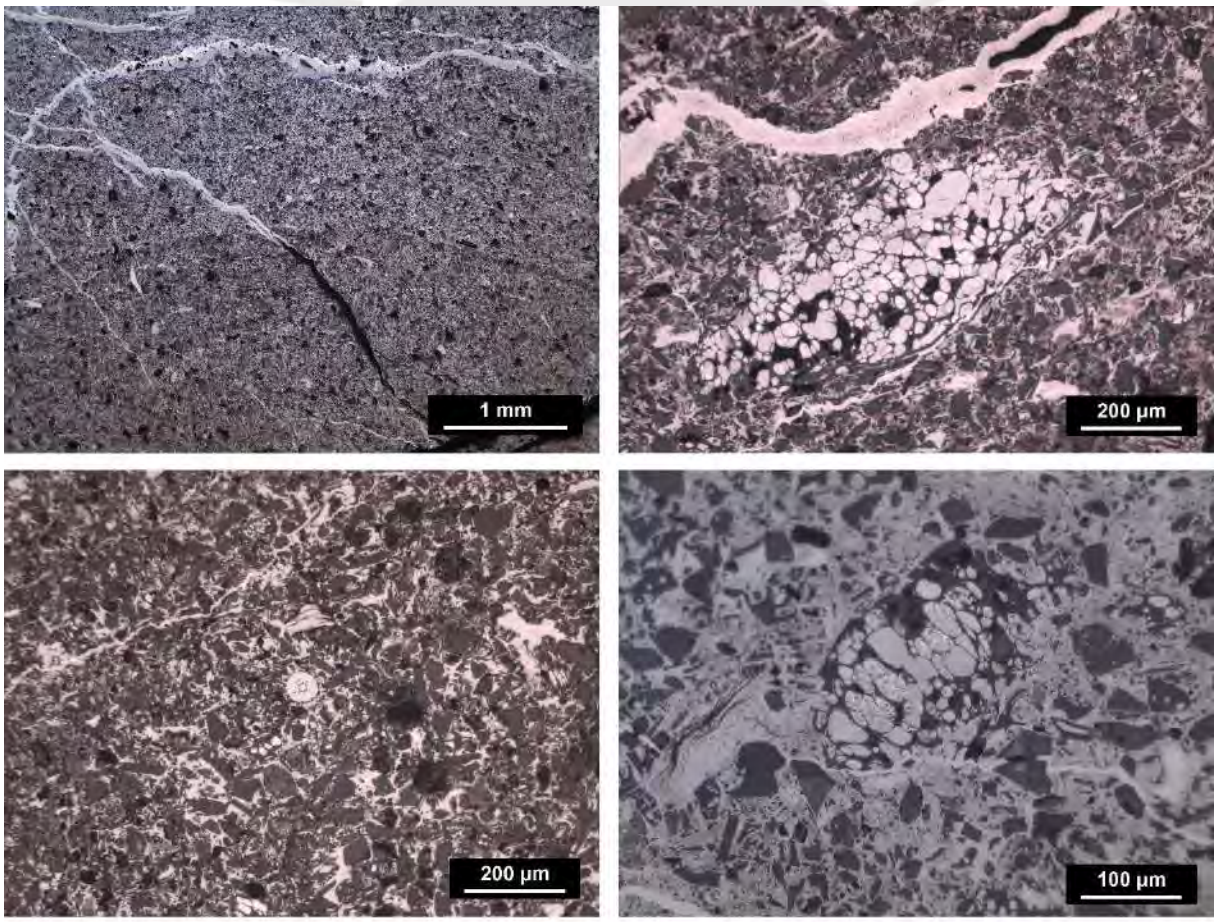

2022-PAL-10

Type of sample: nodule

Nodule sample with at least two concentrical rims with patchy textures of Mn oxides cut by a network of thin veinlets. Microcrystalline, fibrous Mn oxides cement angular detrital grains. The veinlets are filled with Mn oxides with internal porous, colloidal, or massive homogeneous textures. Biomorphic remnants of possible diatoms are fossilized by Mn oxides.

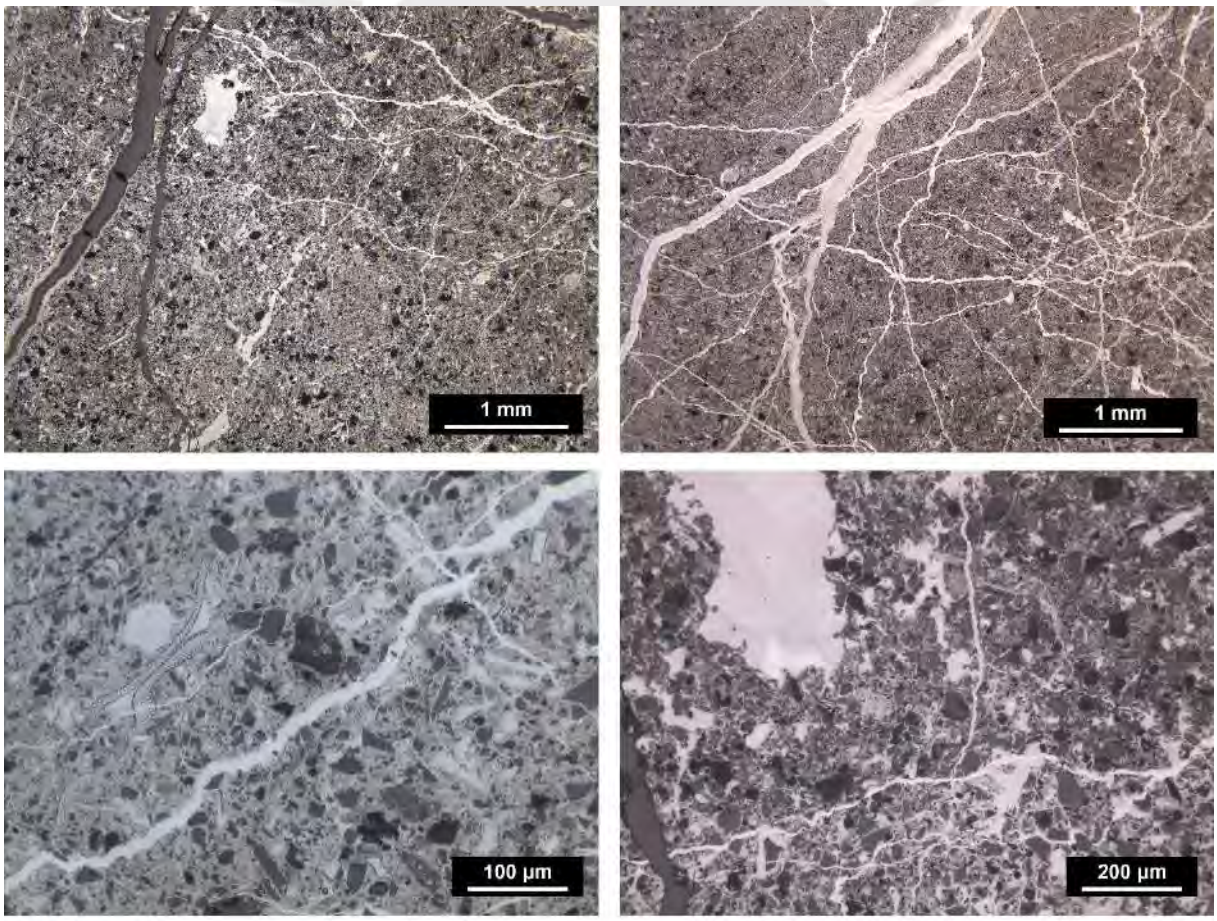

2023-PAL-02

Type of sample: coating

Rock with high interstitial porosity only filled with a minor to incipient Mn-oxide cement to angular detrital grains of quartz, plagioclase and minor anhydrite (?). The proportion of Mn-oxide abruptly decrease towards the contact with the sedimentary material, where the cement turns to a clay and carbonate assemblage. Some grains are partially replaced by Mn oxides. Scarce biomorphic remnants are fossilized by Mn oxides with internal homogeneous textures.

Abbreviations: RL = reflected light; TL = transmitted light; PPL = plane polarized light; XPL = cross polarized light

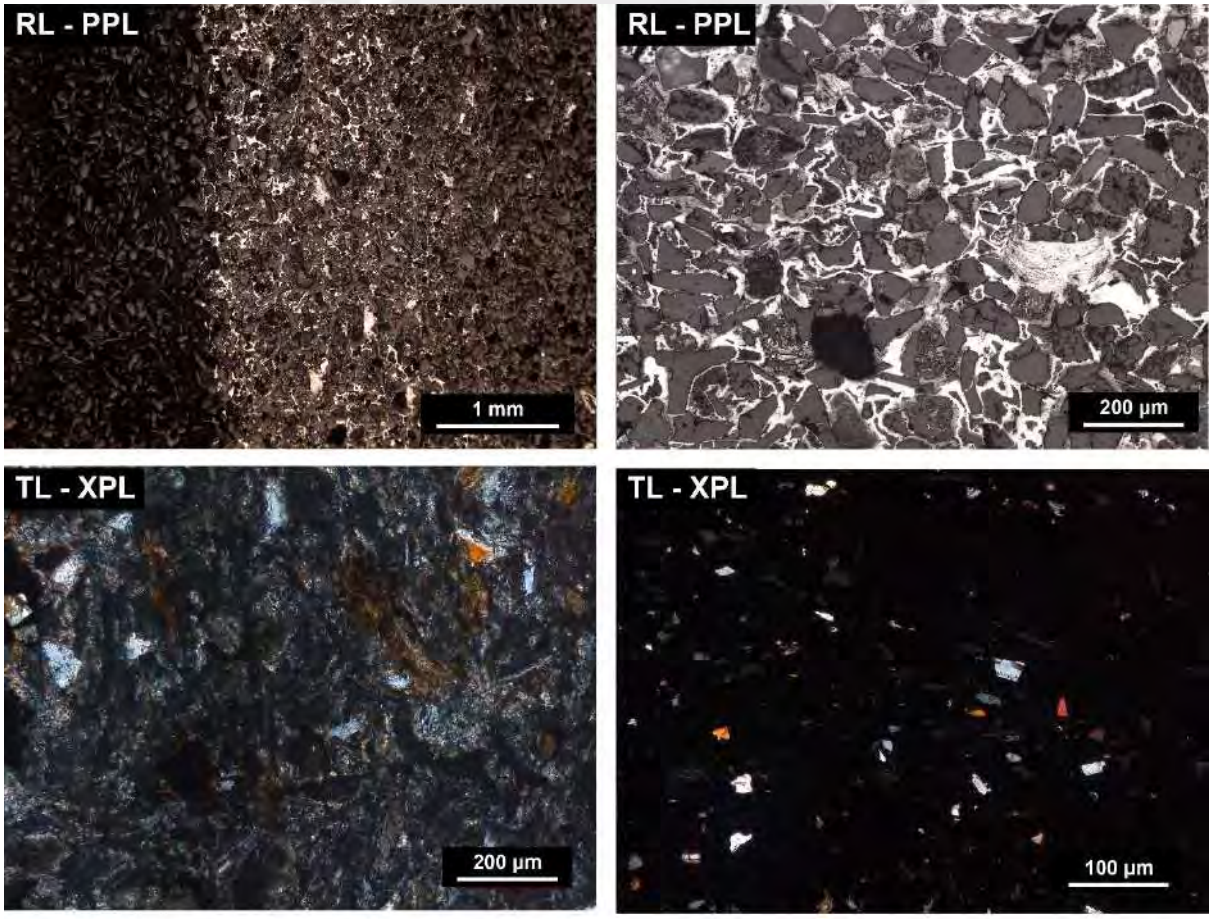

2023-PAL-09

Type of sample: micronodule

Manganese oxide mineralization forming micronodules and partly replacing some grains. Micronodules are between 25 and 100 µm in size and their internal textures is restricted to anhedral aggregates.

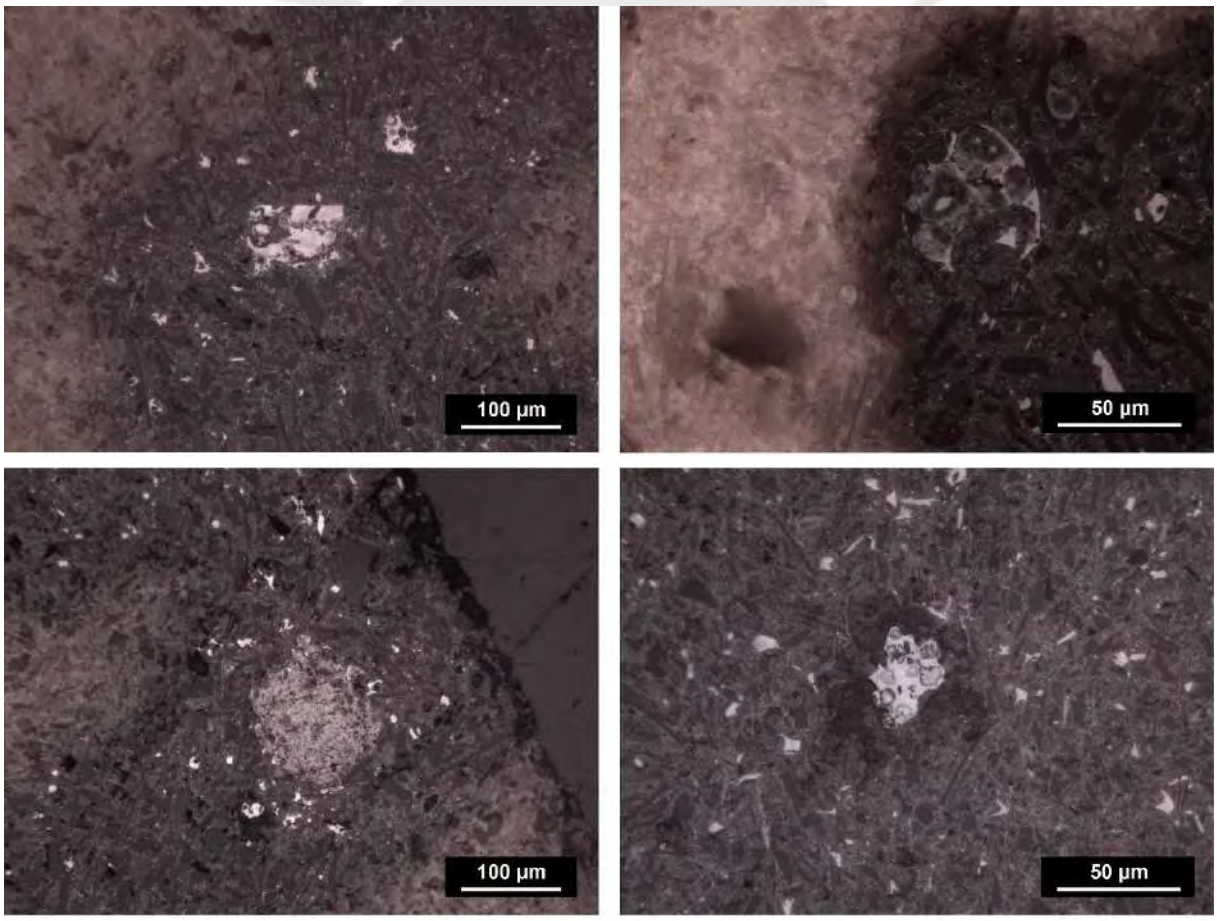

2023-PAL-19

Type of sample: coating

The sample is dominated by massive to slightly micro-porous or fibrous layers of manganese oxides with ubiquitous colloidal textures. In places, the colloidal Mn oxide floods the space between angular, detrital grains. Locally, Mn oxides have replaced detrital elements of the sample.

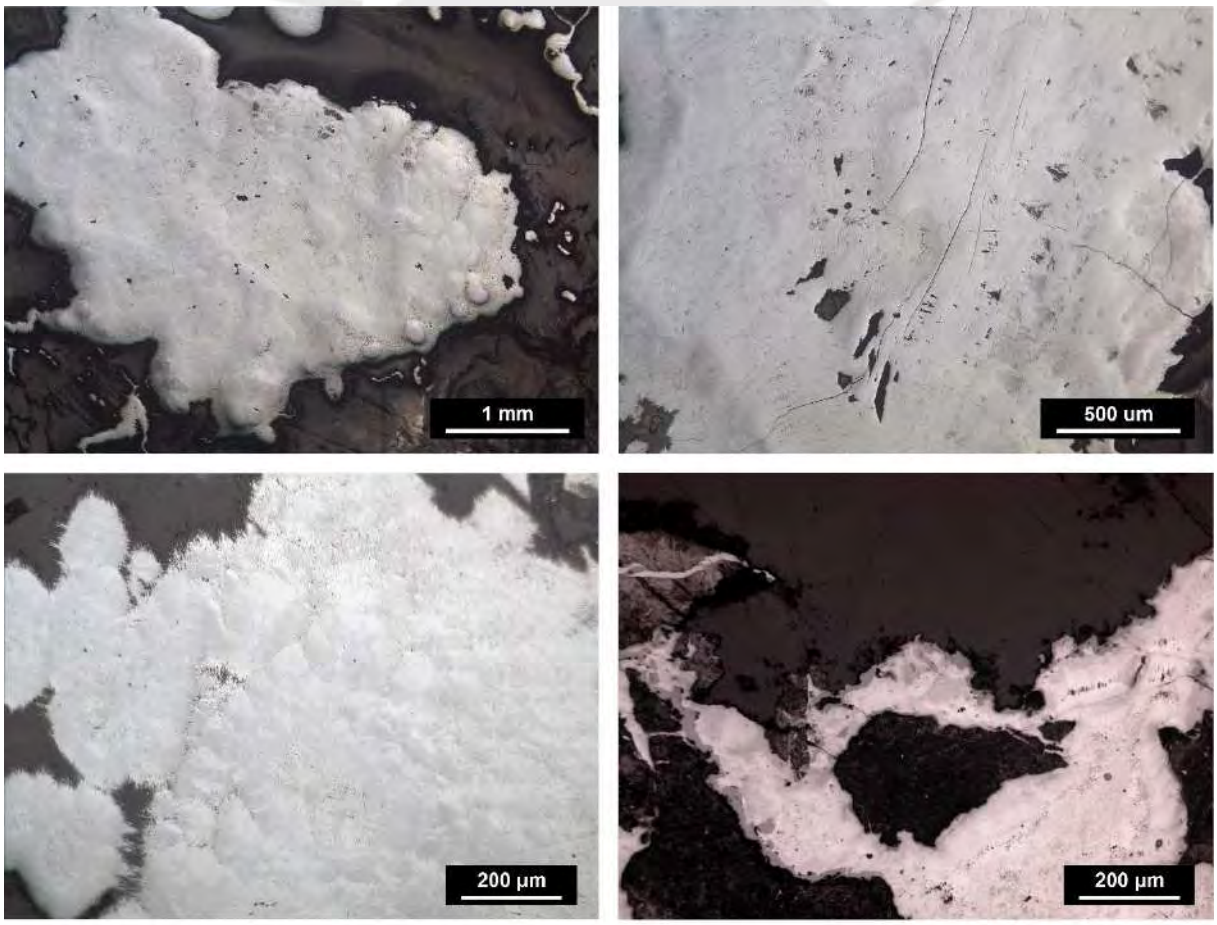

2023-PAL-27

Type of sample: nodule

Manganese oxide cement-supported matrix with patchy textures embedding angular detrital grains cut by a network of thin veinlets. The veinlets are filled with Mn oxides with internal porous, or massive homogeneous textures. Void-filling textures of massive Mn-oxides are present. Biomorphic remnants of possible diatoms are fossilized by Mn oxides.

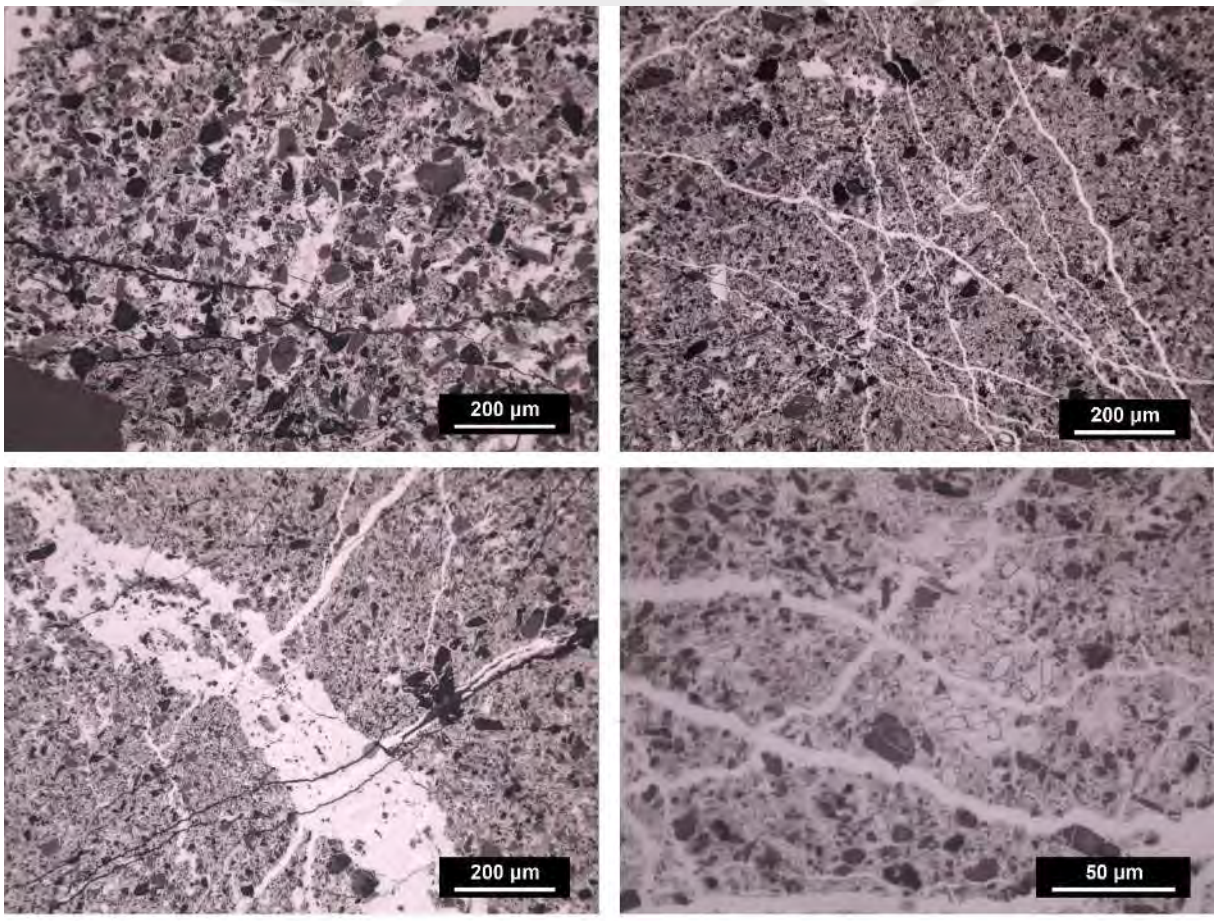

2023-PAL-29

Type of sample: nodule

Manganese oxide cement-supported with patchy to homogeneous textures embedding angular grains. Some of the grains show delicate curvioplanar textures that are typical of juvenile volcanic features such as glass shards. Void-filling textures of homogeneous Mn oxides are present. Biomorphic remnants of possible diatoms are fossilized by Mn oxides.

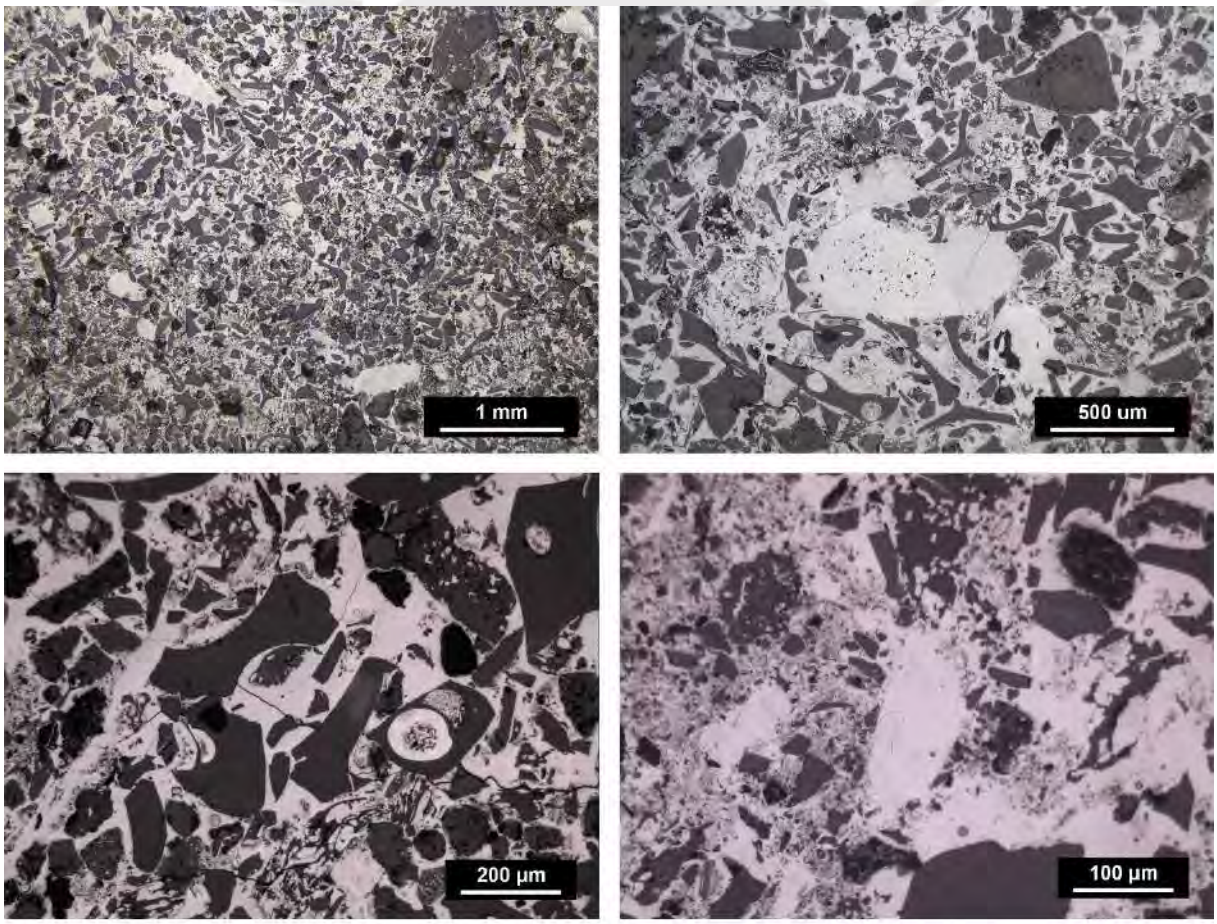

2023-PAL-34

Type of sample: nodule

Manganese oxide cement-supported embedding angular detrital grains. In certain zones, Mn mineralization is restricted to scarce replacement of some grains. A main vein filled with massive Mn oxides cuts the sample. Biomorphic remnants of possible diatoms are fossilized by Mn oxides.

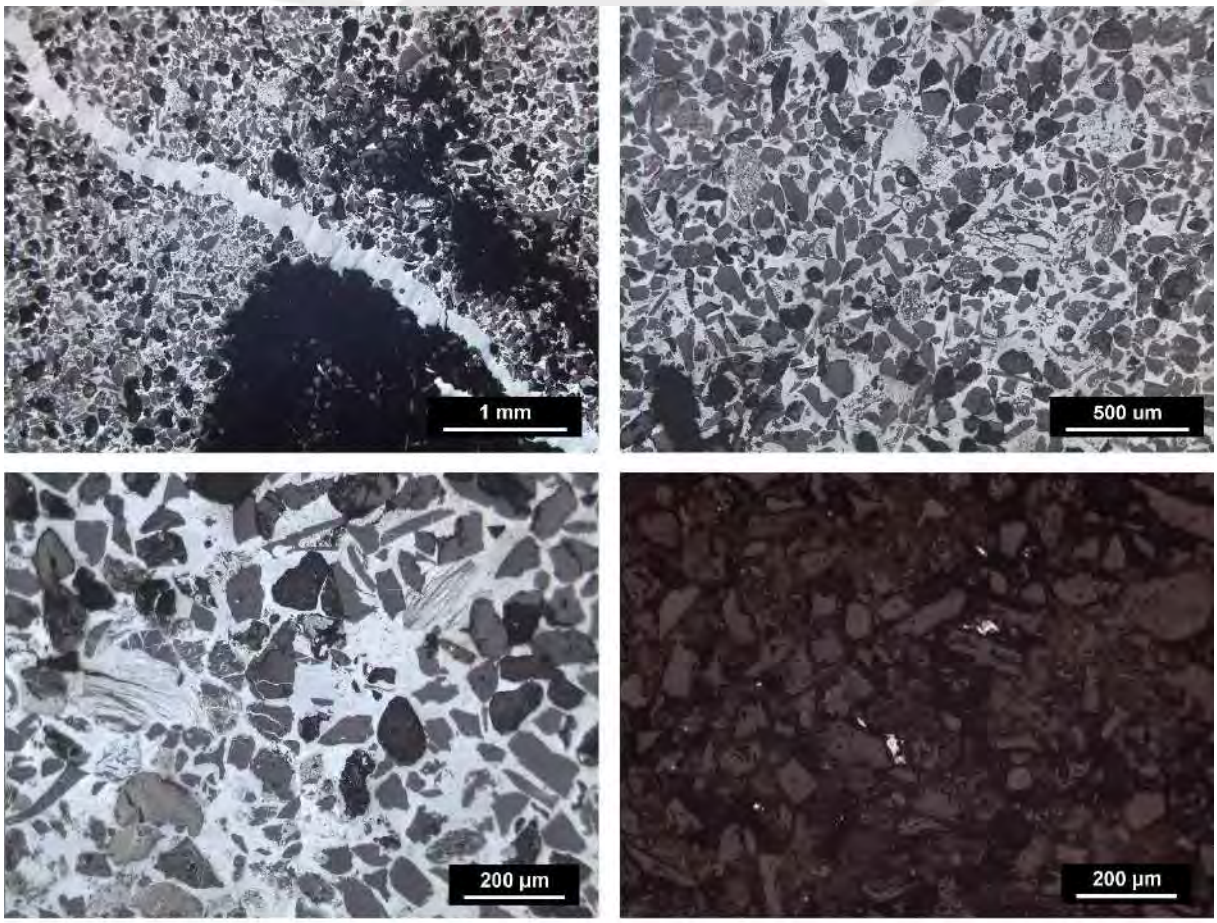

2023-PAL-35

Type of sample: nodule

Manganese oxide cement-supported with patchy to homogeneous textures. Microcrystalline Mn oxides with fibrous and spongy textures cement angular grains. Some of the grains show delicate curvioplanar textures that are typical of juvenile volcanic features such as glass shards. Biomorphic remnants of possible diatoms are fossilized by Mn oxides.

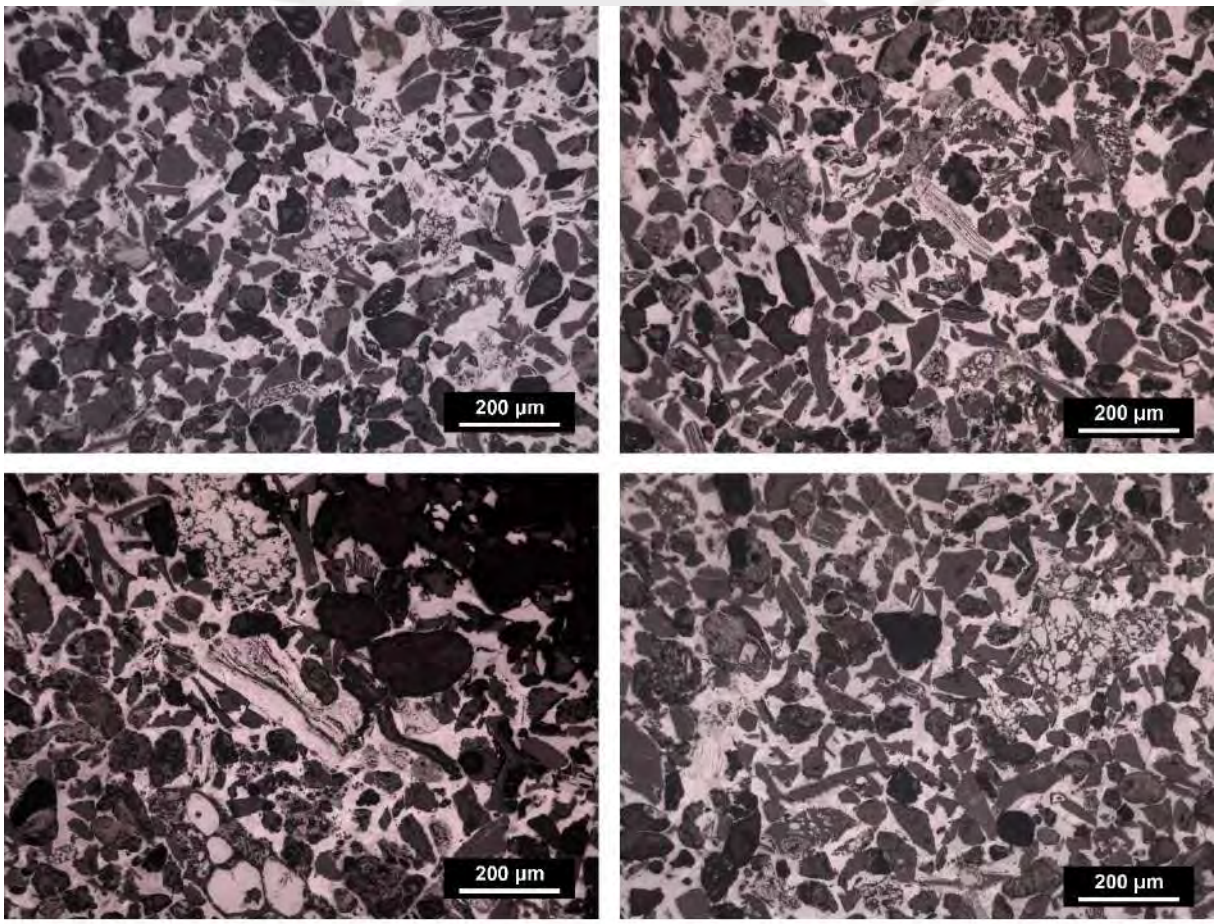

2023-PAL-36

Type of sample: nodule

Manganese oxide cement-supported matrix with patchy to homogeneous textures embedding angular grains. Some of the grains show delicate curviplanar textures that are typical of juvenile volcanic features such as glass shards. Biomorphic remnants of possible diatoms and turritellas are fossilized by Mn oxides.

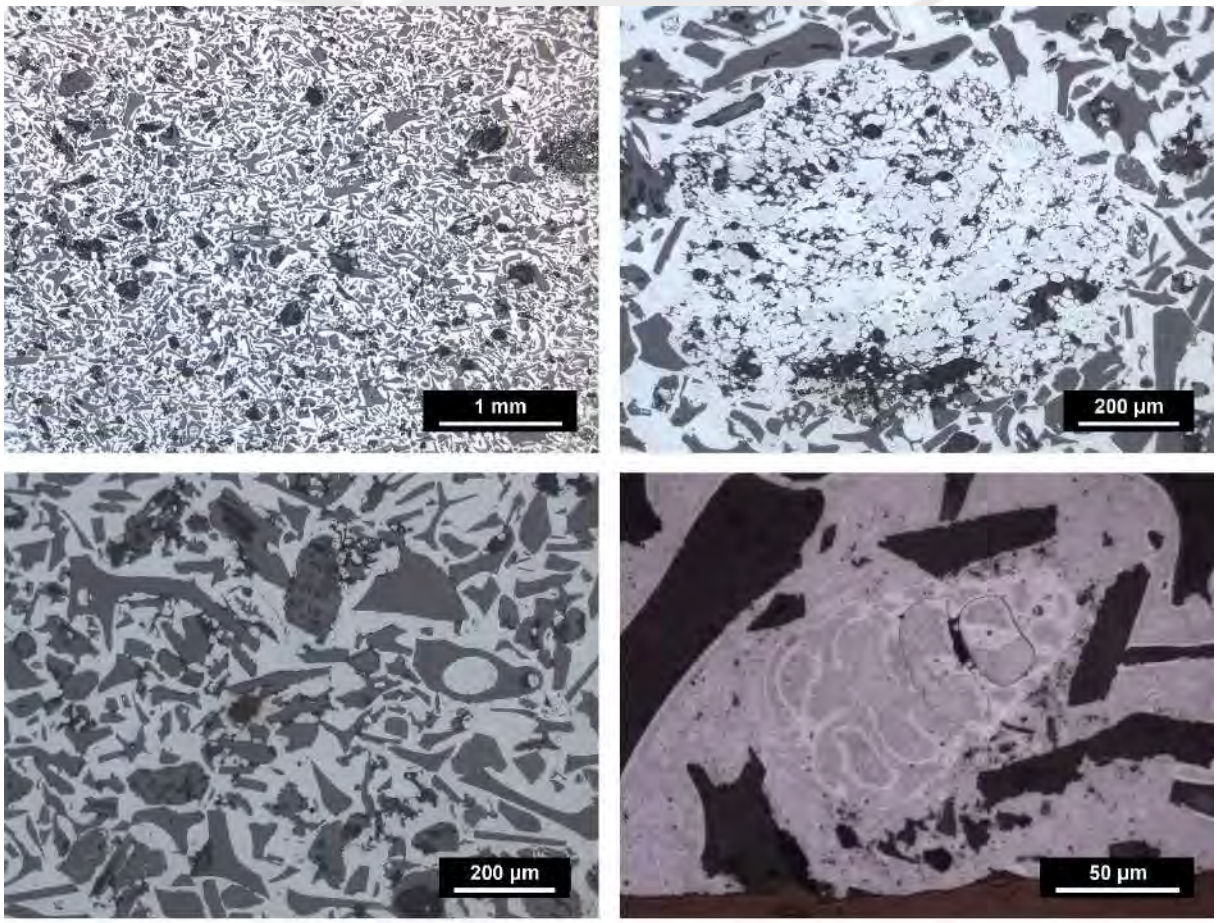

2023-PAL-38

Type of sample: vein

Manganese oxide cement-supported with patchy to homogeneous textures. Microcrystalline Mn oxides with fibrous and spongy textures cement angular grains. Biomorphic remnants of possible diatoms are fossilized by porous to homogeneous Mn oxides.

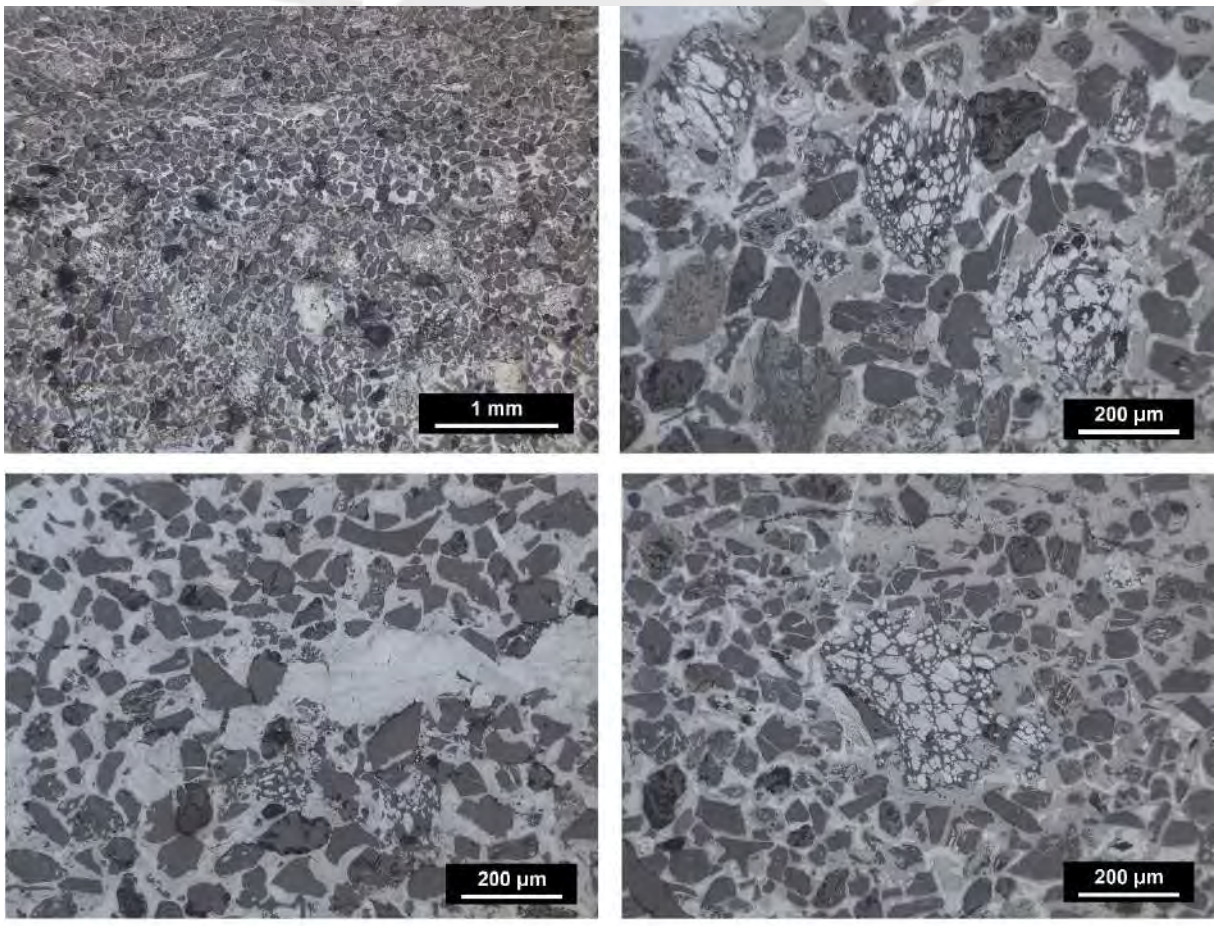

2023-PAL-40

Type of sample: bioturbation replacement

Manganese oxide cement-supported with patchy to homogeneous textures. Microcrystalline Mn oxides with fibrous and spongy textures cement angular grains. Biomorphic remnants of possible diatoms are filled with porous to homogeneous Mn oxides.

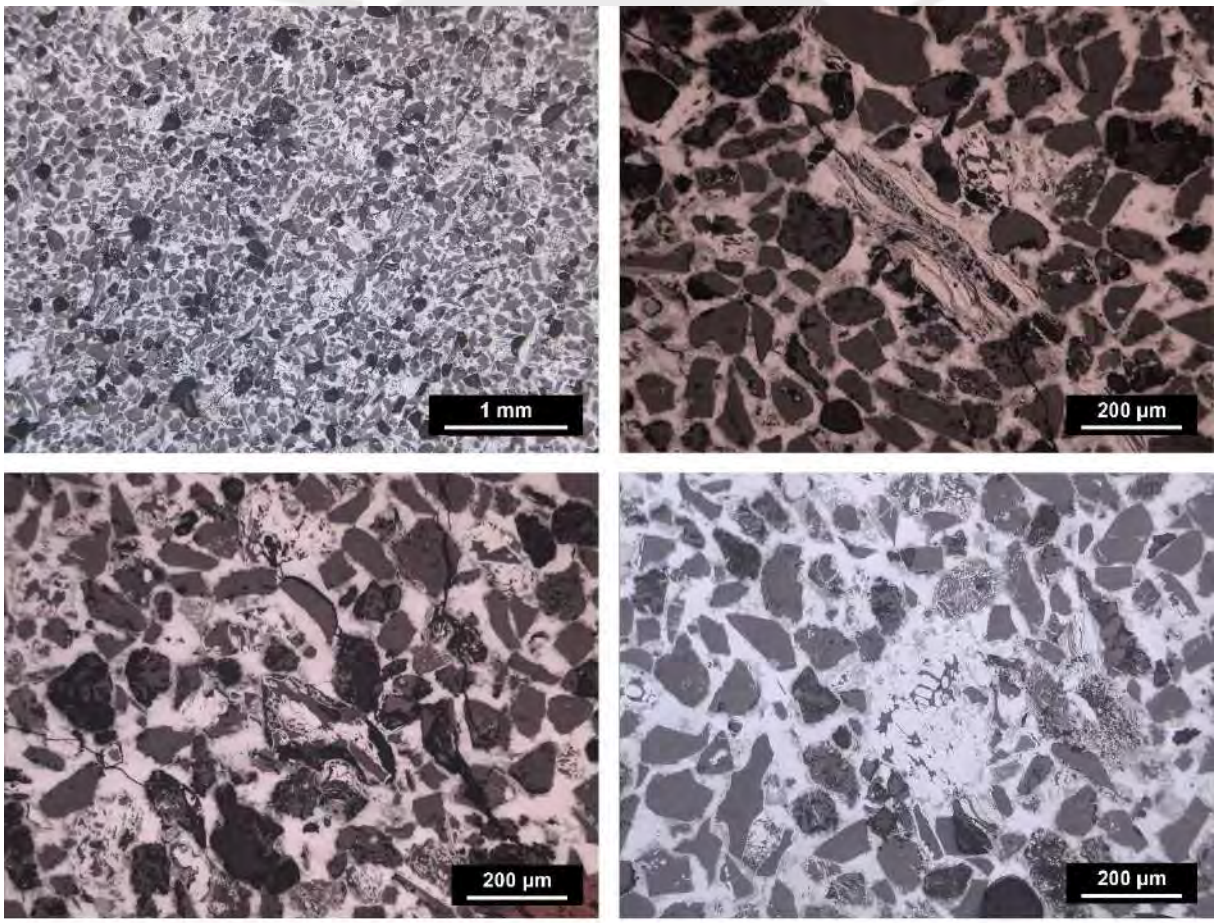

2023-PAL-43

Type of sample: nodule

Nodule sample with at least three concentrical rims with patchy textures of Mn oxides. Microcrystalline Mn oxides with fibrous and spongy textures cement angular detrital grains. Thin, irregular and sinuous fractures are totally or partially filled with Mn oxides with internal porous, or homogeneous textures. Biomorphic remnants of possible diatoms are replaced by Mn oxides.

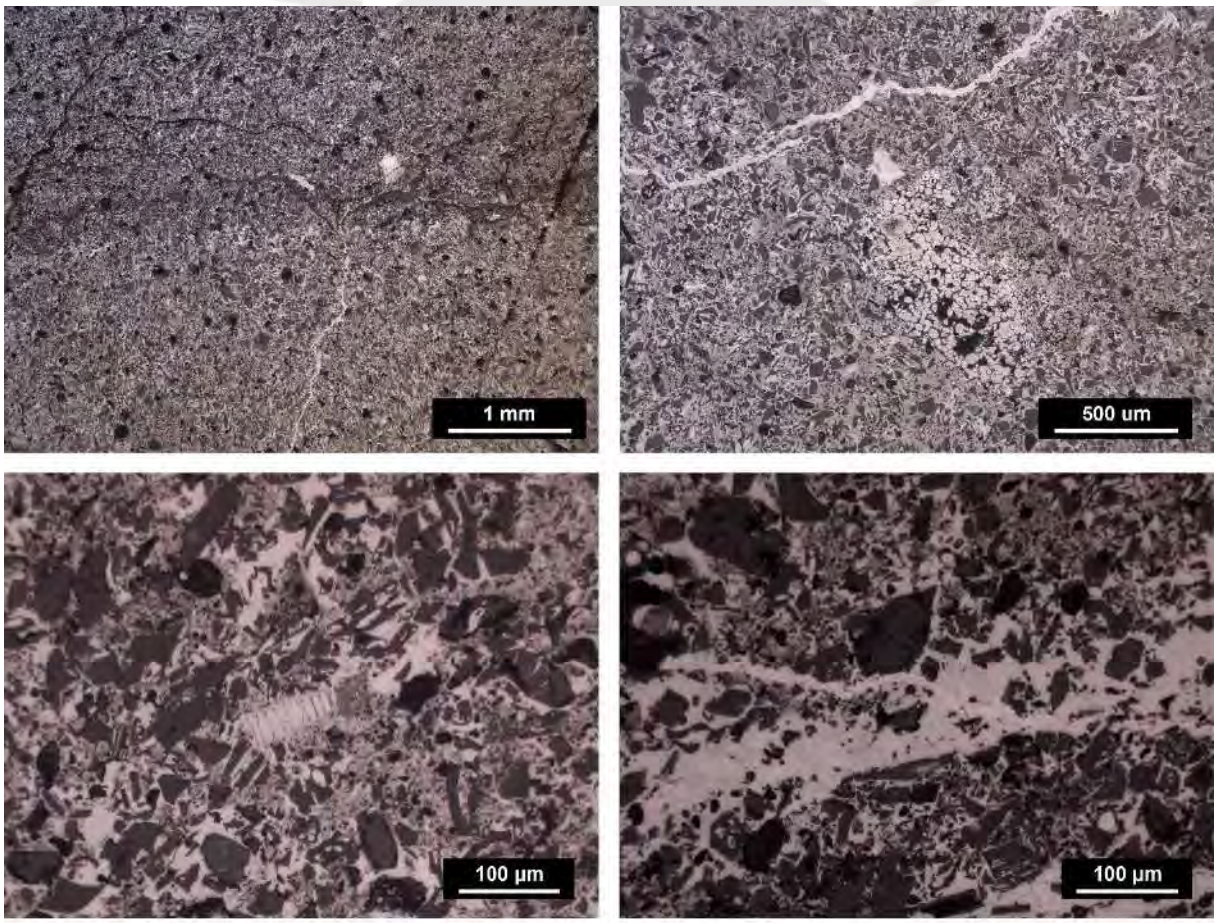

2023-PAL-47

Type of sample: nodule

Manganese oxide cement-supported with patchy to homogeneous textures embedding angular detrital grains. The detrital grains predominantly consist in quartz and plagioclase. In certain zones, Mn mineralization is restricted to scarce replacement of some grains or incipient cement. In places with minor or absent Mn-cement, carbonates and Fe oxides fill the space between detrital grains.

Abbreviations: RL = reflected light; TL = transmitted light; PPL = plane polarized light; XPL = cross polarized light

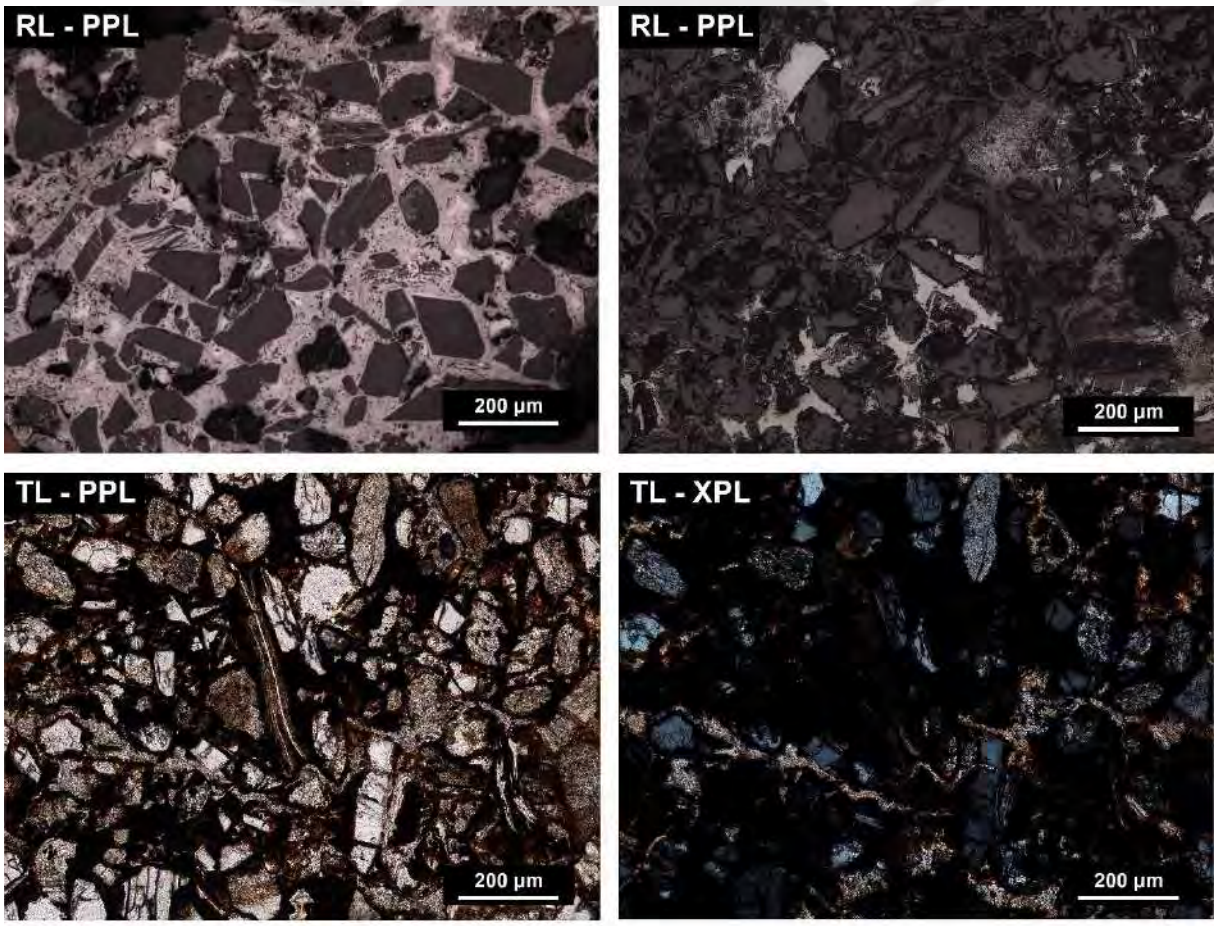

2023-PAL-48A

Type of sample: nodule

Incipient patchy Mn-oxide cement to detrital grains. Some grains are scarcely replaced by Mn oxides.

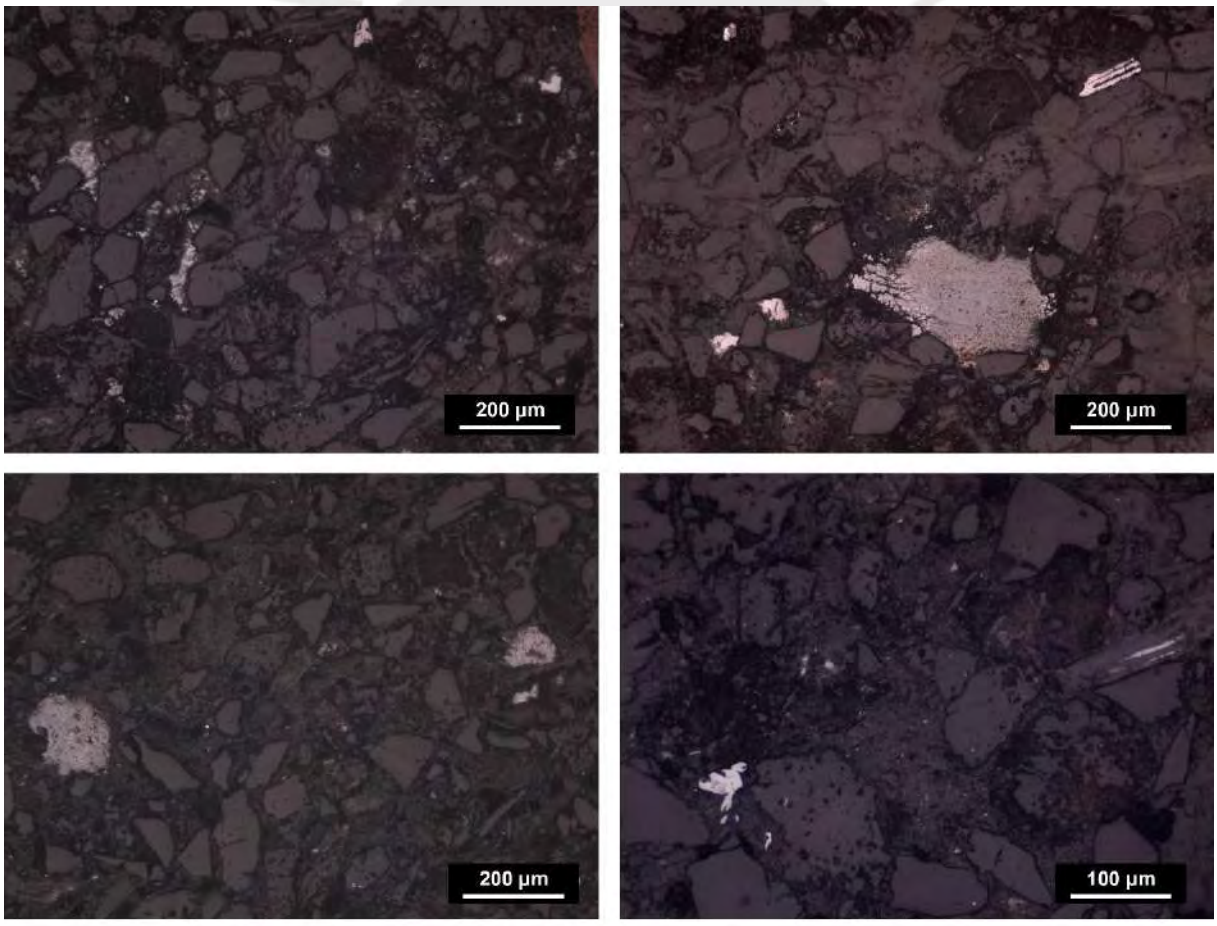

2023-PAL-48B

Type of sample: nodule

Manganese oxide cement-supported sample with patchy to homogeneous textures embedding angular detrital grains of quartz, plagioclase and minor mica. In certain zones, Mn mineralization is restricted to scarce replacement of some grains or incipient cement and accompanied by Fe oxides. Thin, irregular and sinuous fractures are totally or partially filled with Mn oxides with internal porous, or homogeneous textures.

Abbreviations: RL = reflected light; TL = transmitted light; PPL = plane polarized light; XPL = cross polarized light

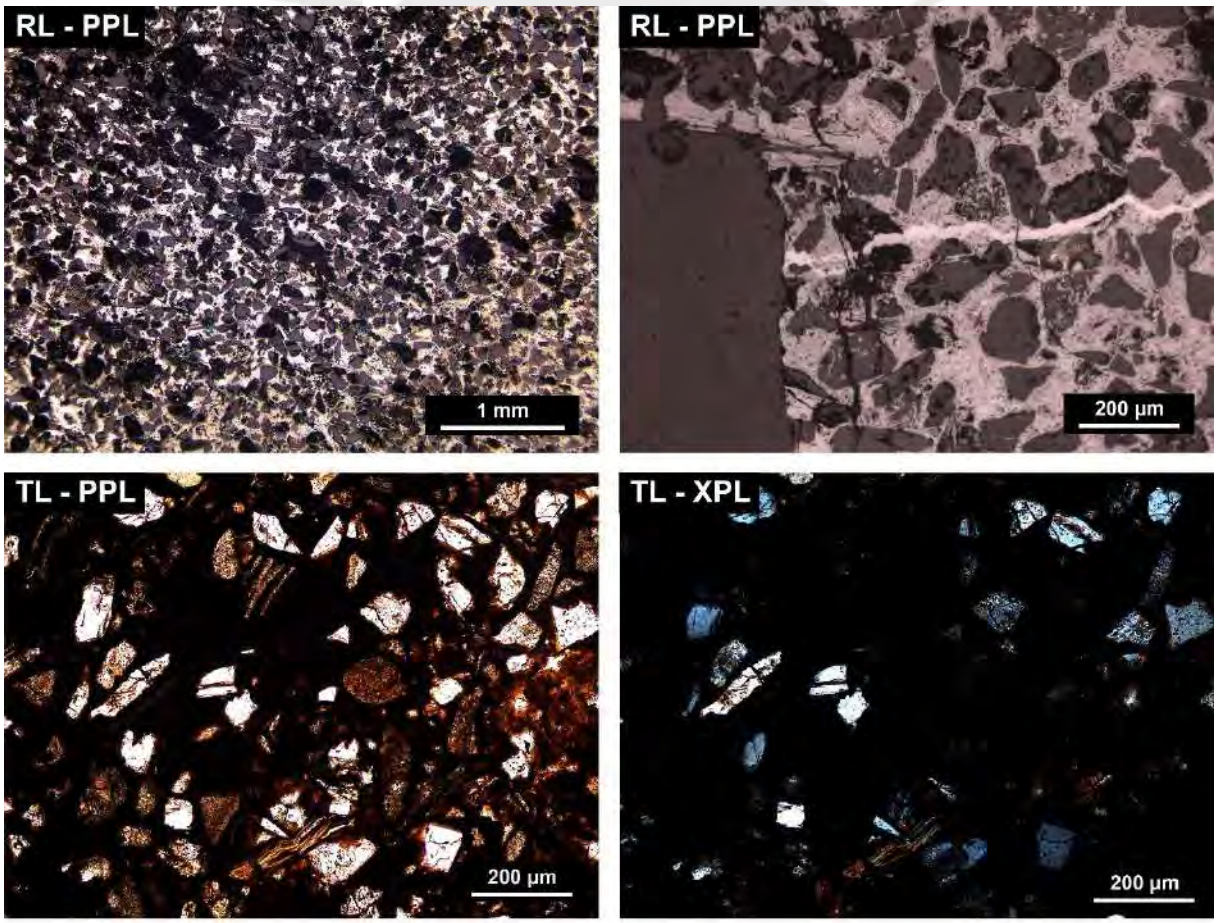

Appendix B: XRD results

2022-PAL-01

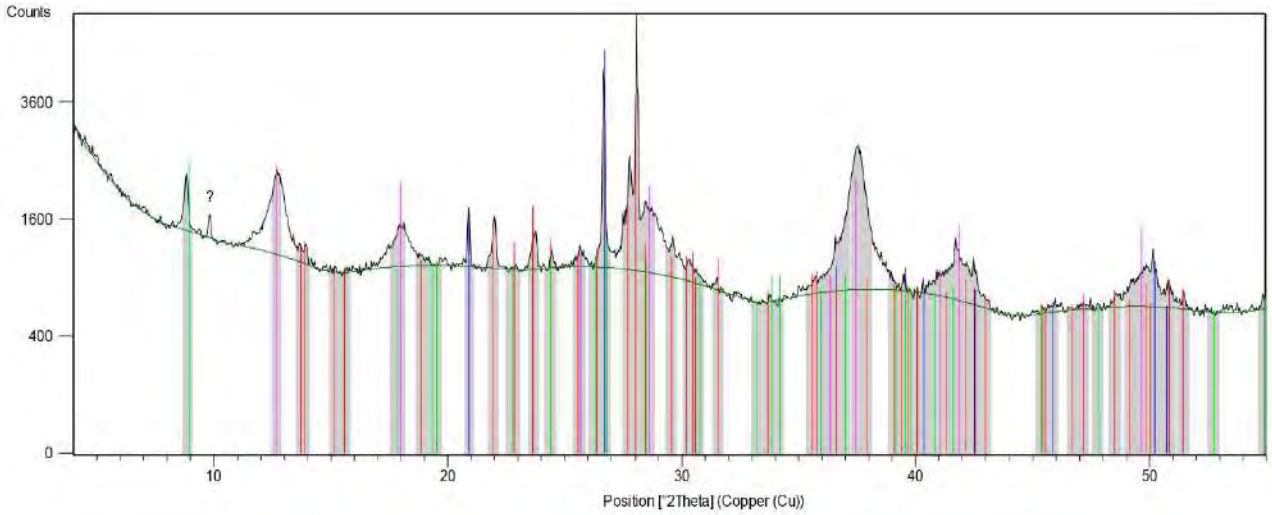

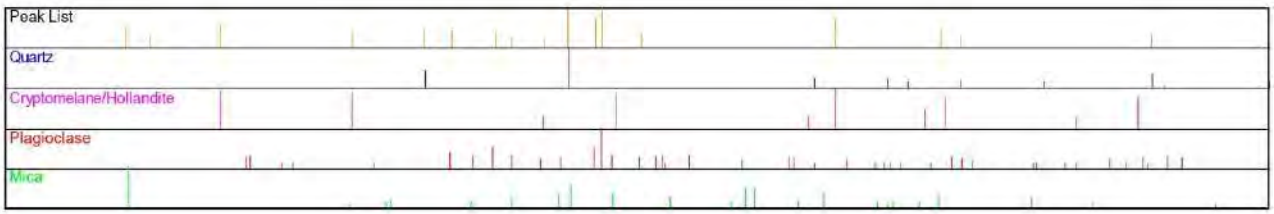

2022-PAL-02

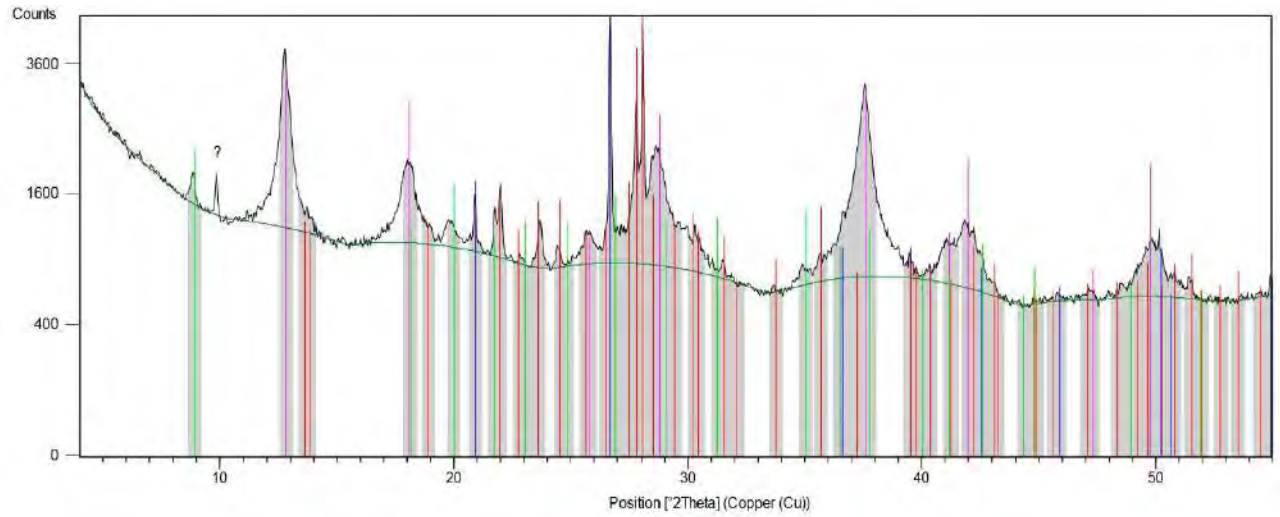
Counts
3600
1600
400
0
?
10
20
30
40
50
Position [°2Theta] (Copper (Cu))

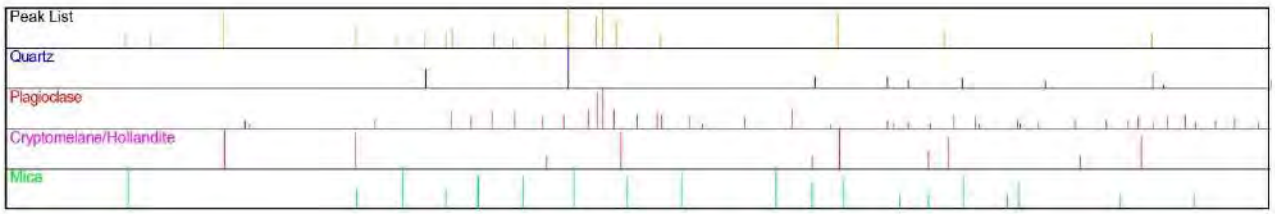
Peak List
Quartz
Plagioclase
Cryptomelane/Hollandite
Mica

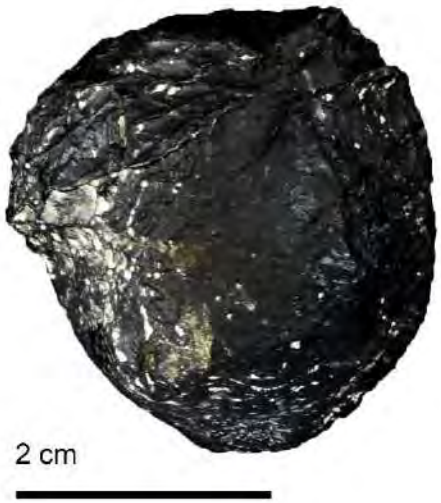
2 cm

2022-PAL-03

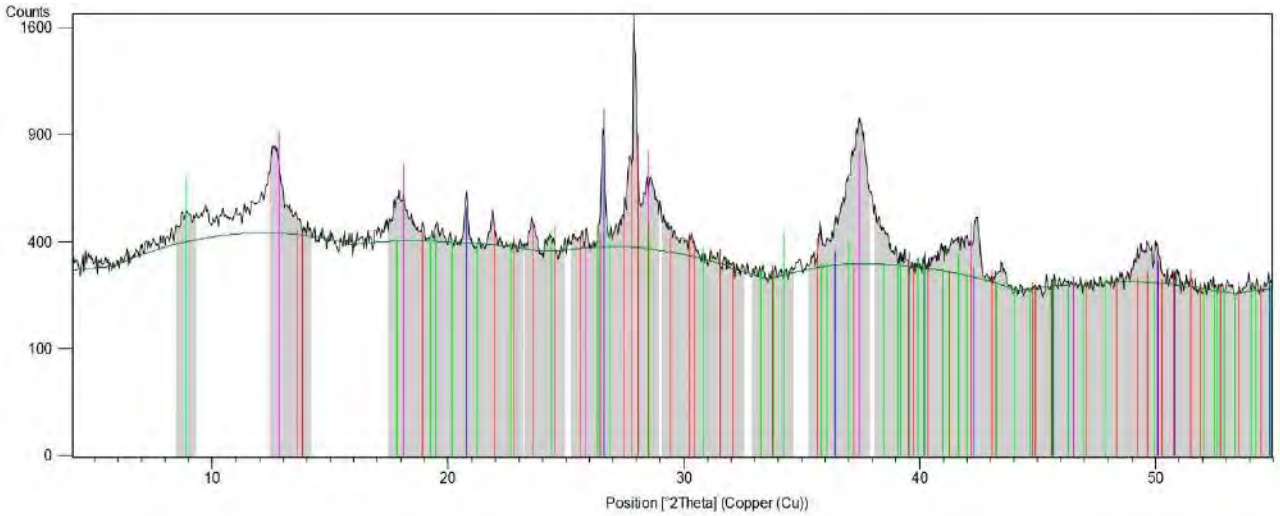
Counts
1600
900
400
100
0
10
20
30
40
50
Position [°2Theta] (Copper (Cu))

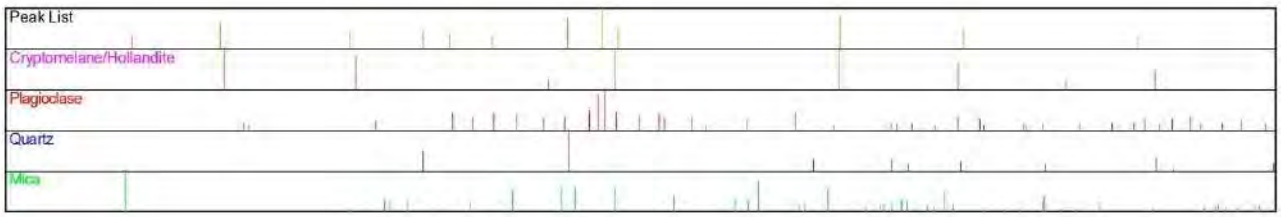
Peak List
Cryptomelane/Hollandite
Plagioclase
Quartz
Mica


3 cm

2022-PAL-04

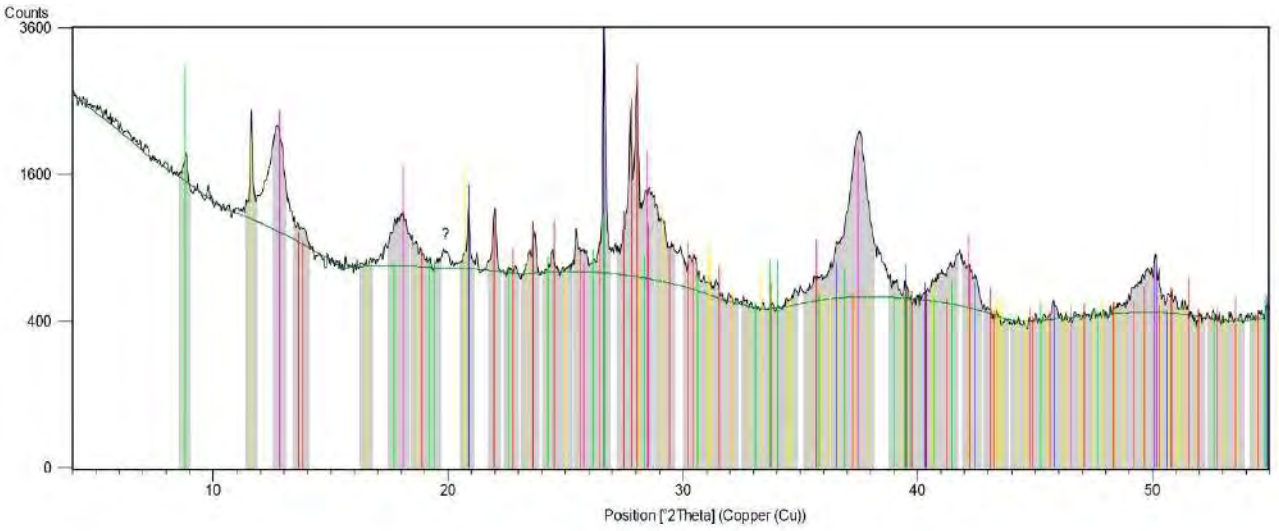
Counts
3600
1600
400
0
?
10
20
30
40
50
Position [°2Theta] (Copper (Cu))

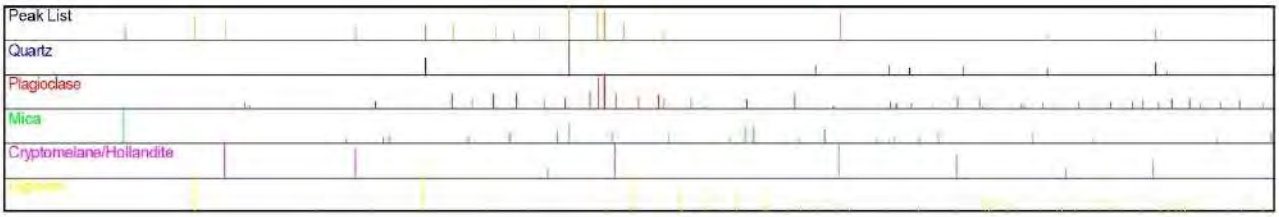
Peak List
Quartz
Plagioclase
Mica
Cryptomelane/Hollandite


3 cm

2022-PAL-05

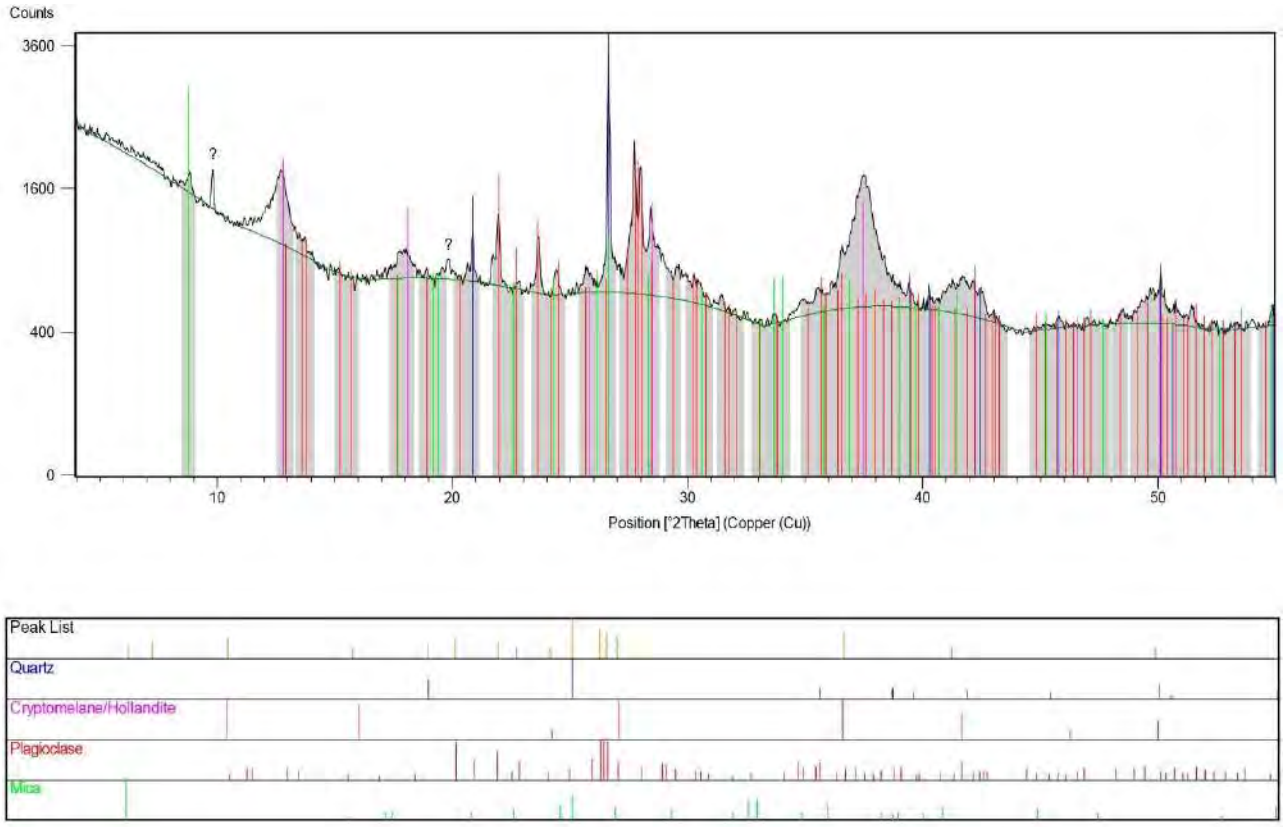
Counts
3600
1600
400
0
?
?
10
20
30
40
50
Position [°2Theta] (Copper (Cu))
Peak List
Quartz
Cryptomelane/Hollandite
Plagioclase
Mica


2 cm

2022-PAL-06

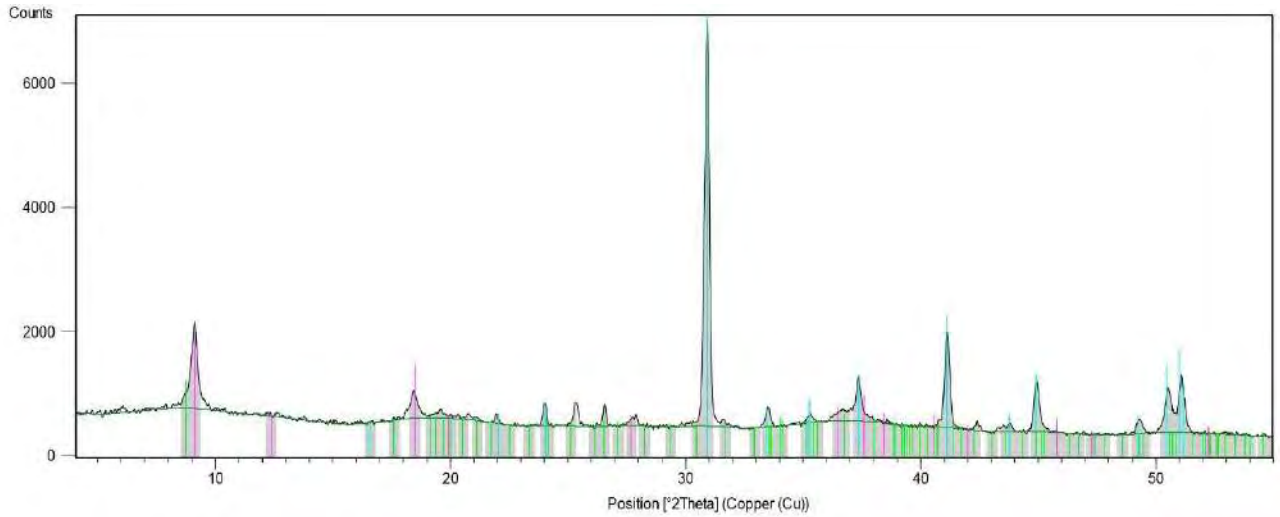
Counts
6000
4000
2000
0
10
20
30
40
50
Position [°2Theta] (Copper (Cu))
Peak List
Dolomite
Mica
Todorokite


3 cm

2022-PAL-07

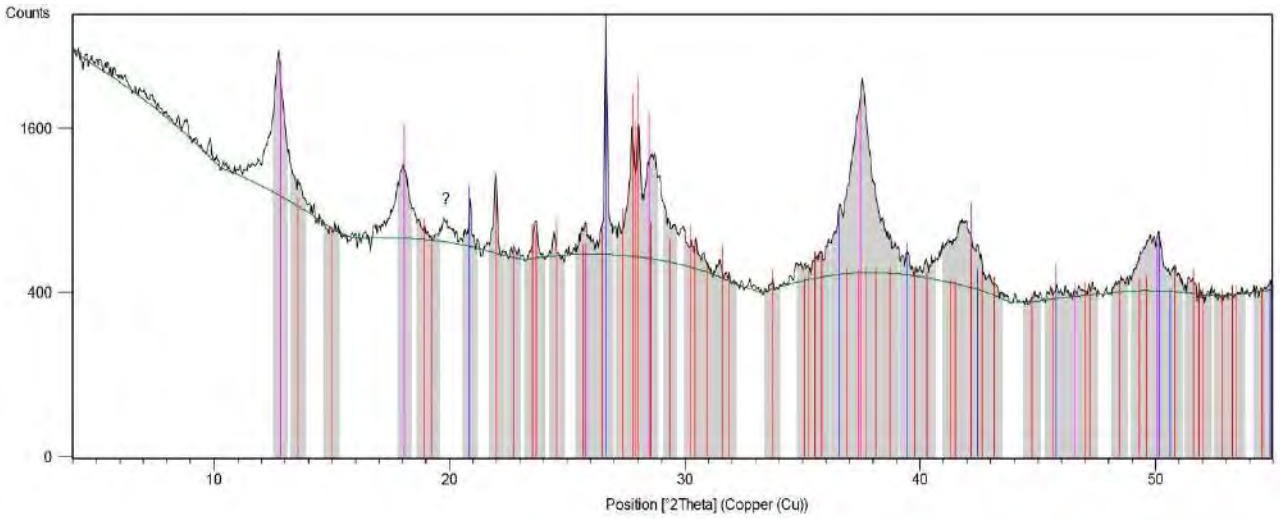
Counts
1600
400
0
?
10
20
30
40
50
Position [°2Theta] (Copper (Cu))
Peak List
Cryptomelane/Hollandite
Quartz
Plagioclase


3 cm

2022-PAL-08

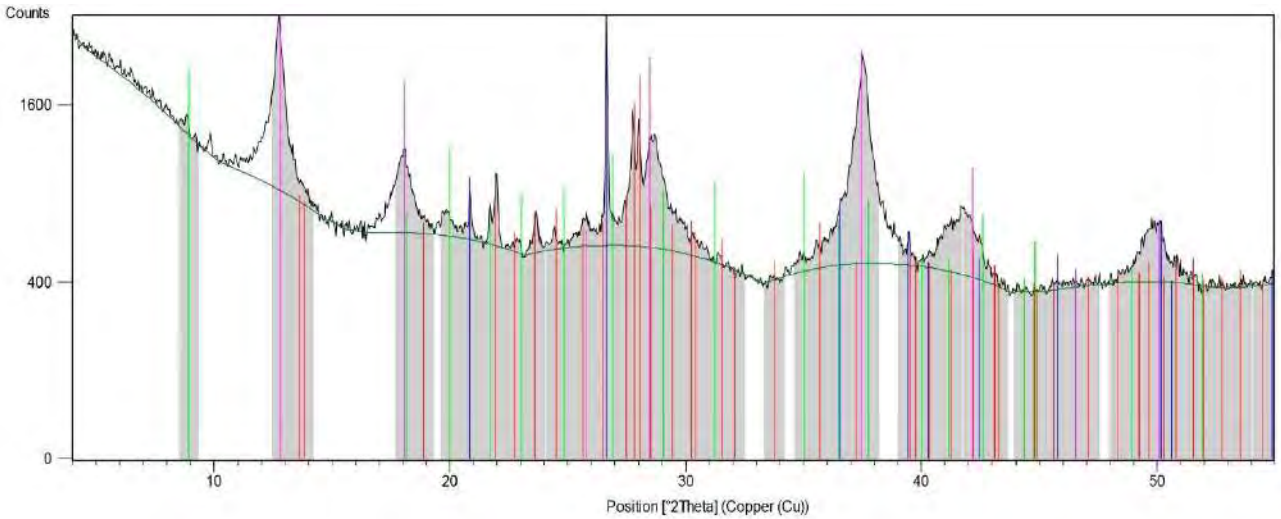
Counts
1600
400
0
10
20
30
40
50
Position [°2Theta] (Copper (Cu))
Peak List
Cryptomelane/Hollandite
Quartz
Mica
Plagiodase


2 cm

2022-PAL-09

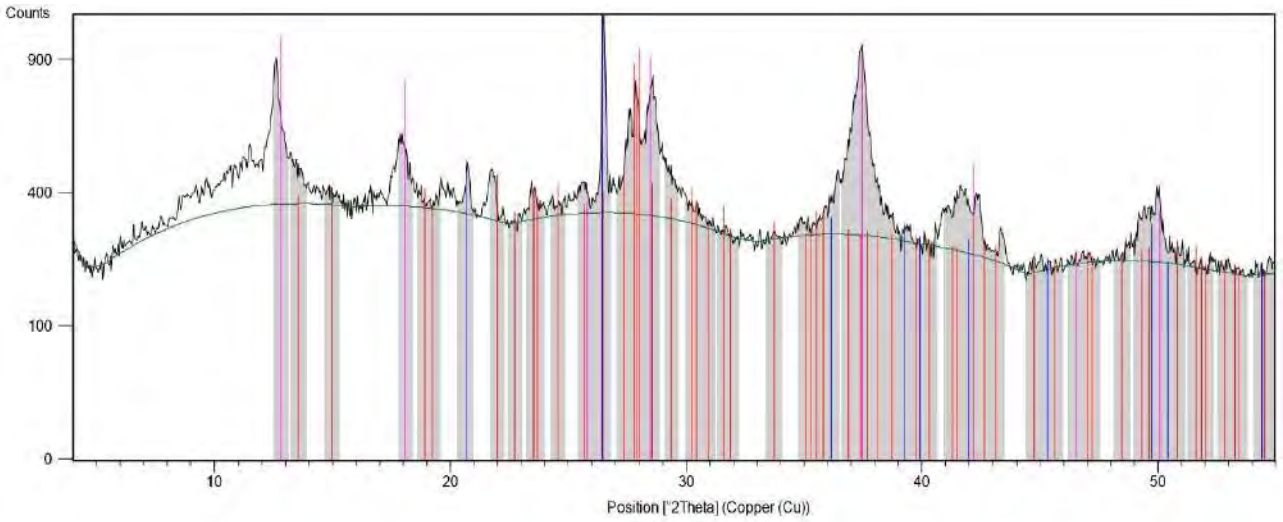
Counts
900
400
100
0
10
20
30
40
50
Position [°2Theta] (Copper (Cu))
Peak List
Cryptomelane/Hollandite
Quartz
Plagioclase


3 cm

2022-PAL-10

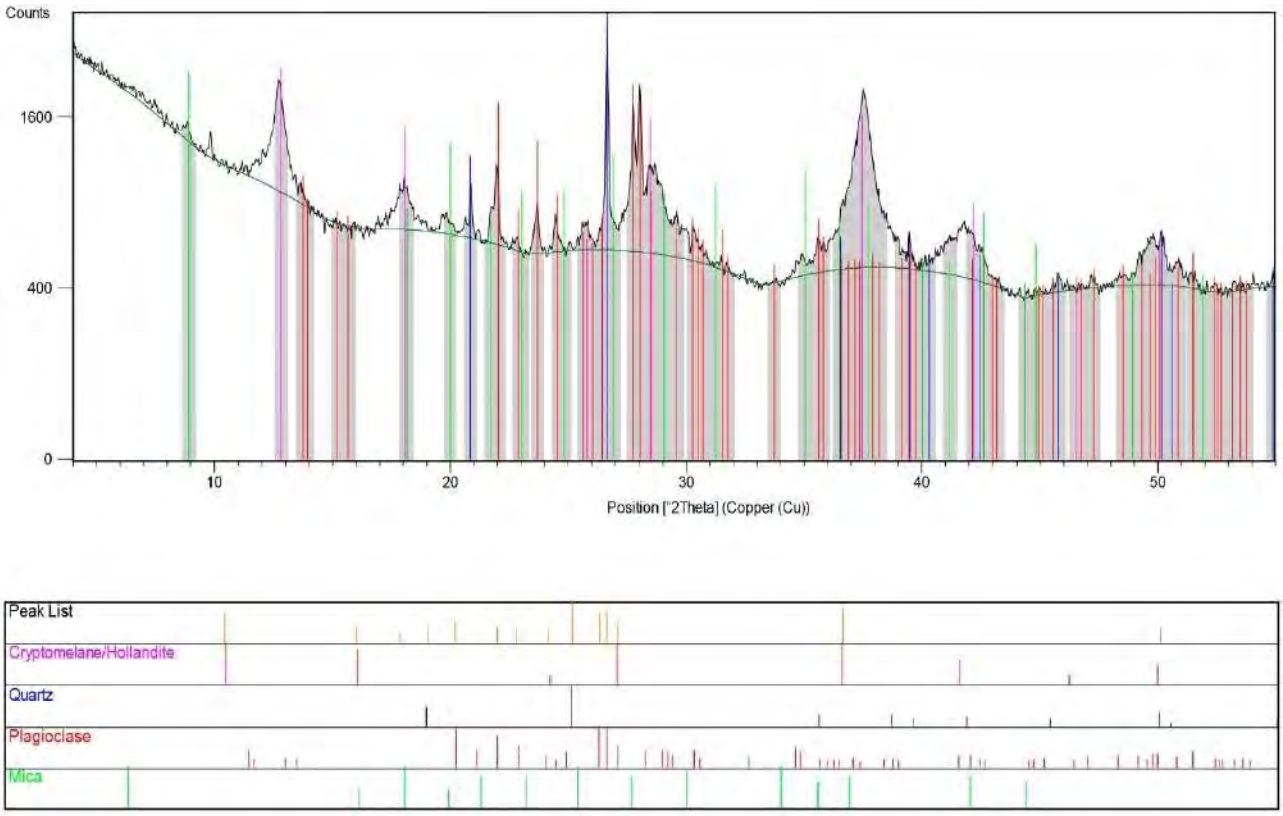
Counts
1600
400
0
10
20
30
40
50
Position [°2Theta] (Copper (Cu))
Peak List
Cryptomelane/Hollandite
Quartz
Plagioclase
Mica


2 cm

2022-PAL-11

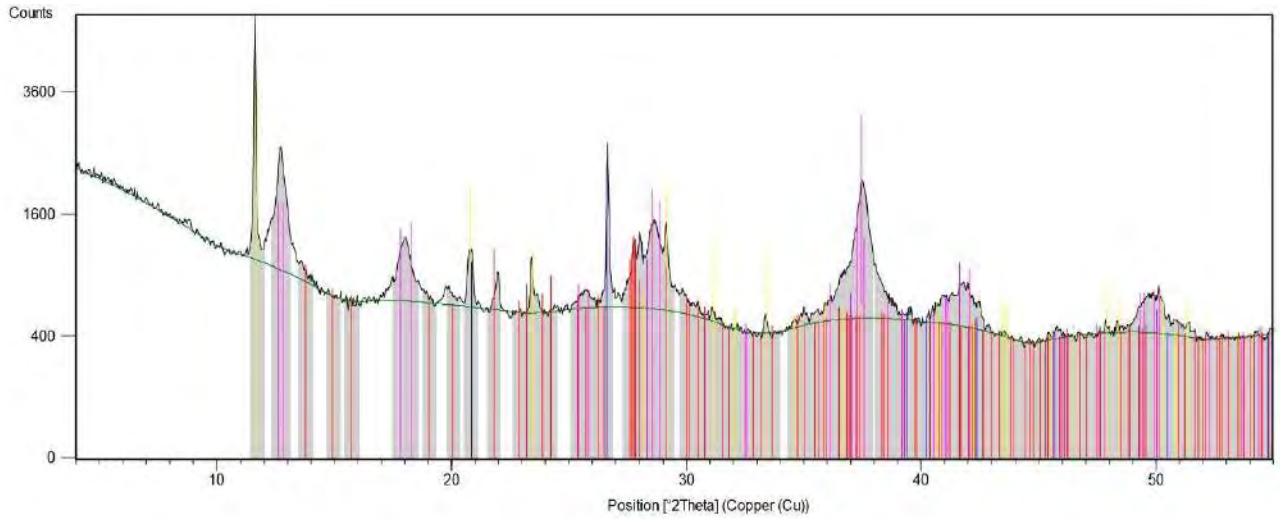
Counts
3600
1600
400
0
10
20
30
40
50
Position [°2Theta] (Copper (Cu))
Peak List
Cryptomelane/Hollandite
Quartz
Plagioclase


3 cm

2022-PAL-12

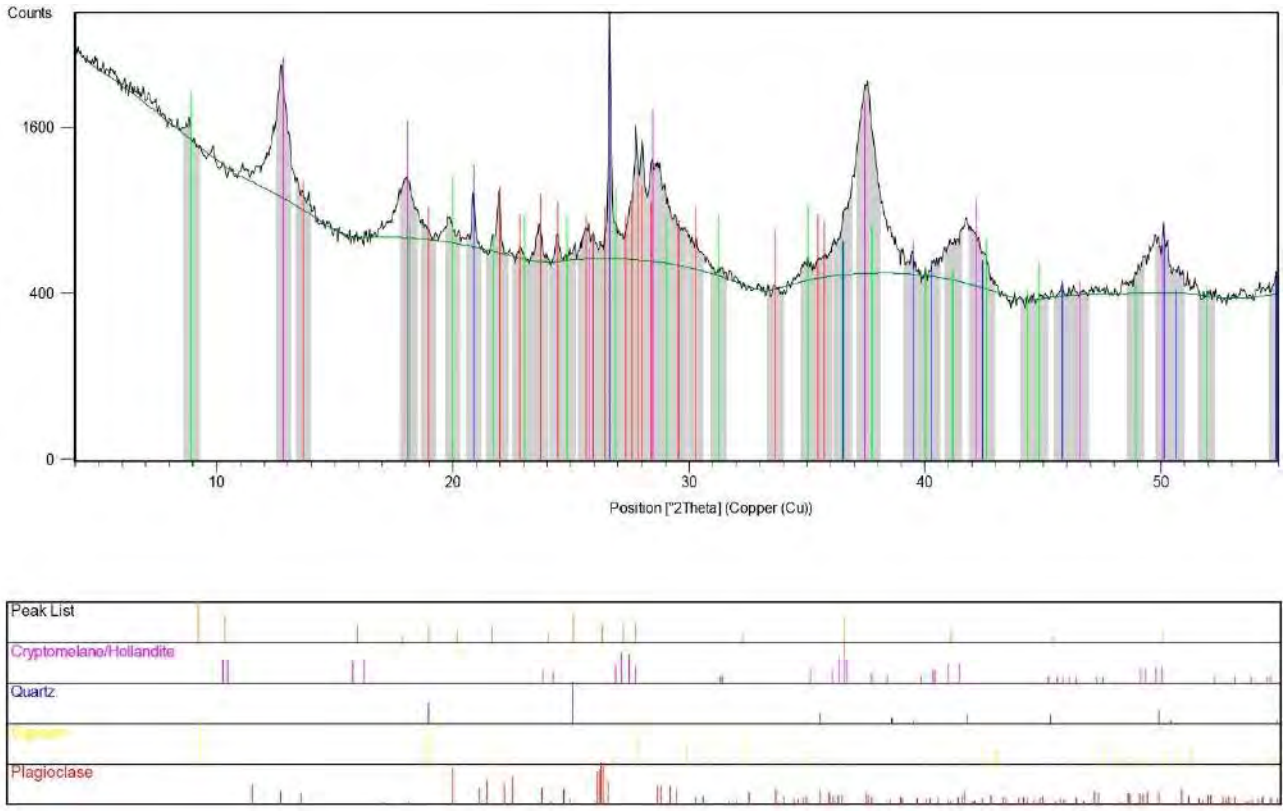
Counts
1600
400
0
10
20
30
40
50
Position [°2Theta] (Copper (Cu))
Peak List
Cryptomelane/Hollandite
Quartz
Plagioclase


3 cm

2022-PAL-13

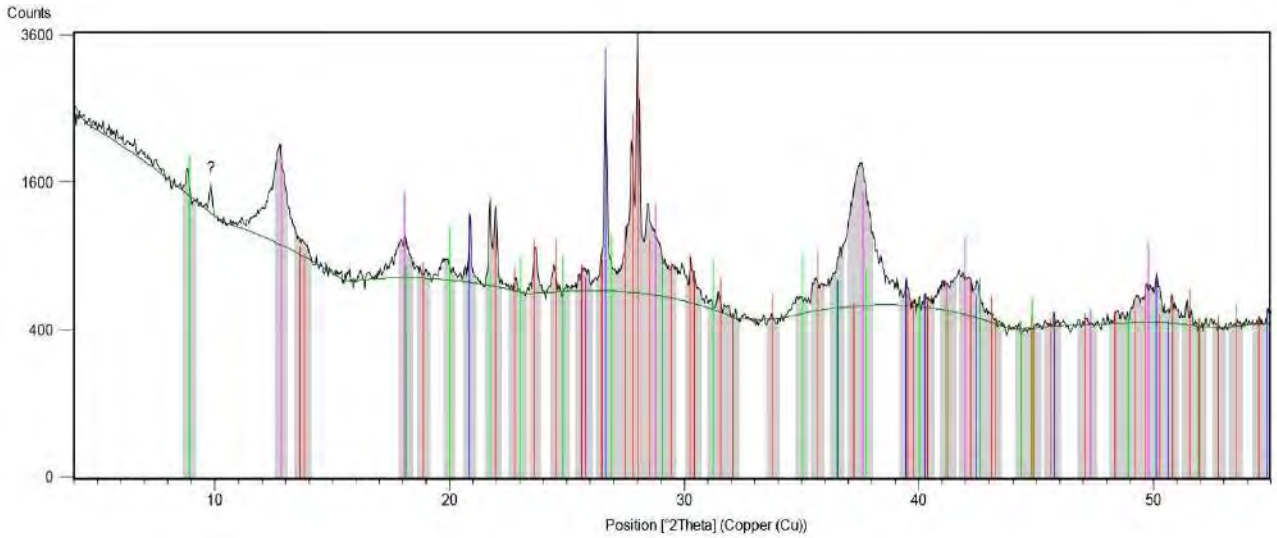
Counts
3600
1600
400
0
?
10
20
30
40
50
Position [°2Theta] (Copper (Cu))
Peak List
Quartz
Plagioclase
Cryptomelane/Hollandite
Mica


2 cm

2022-PAL-14

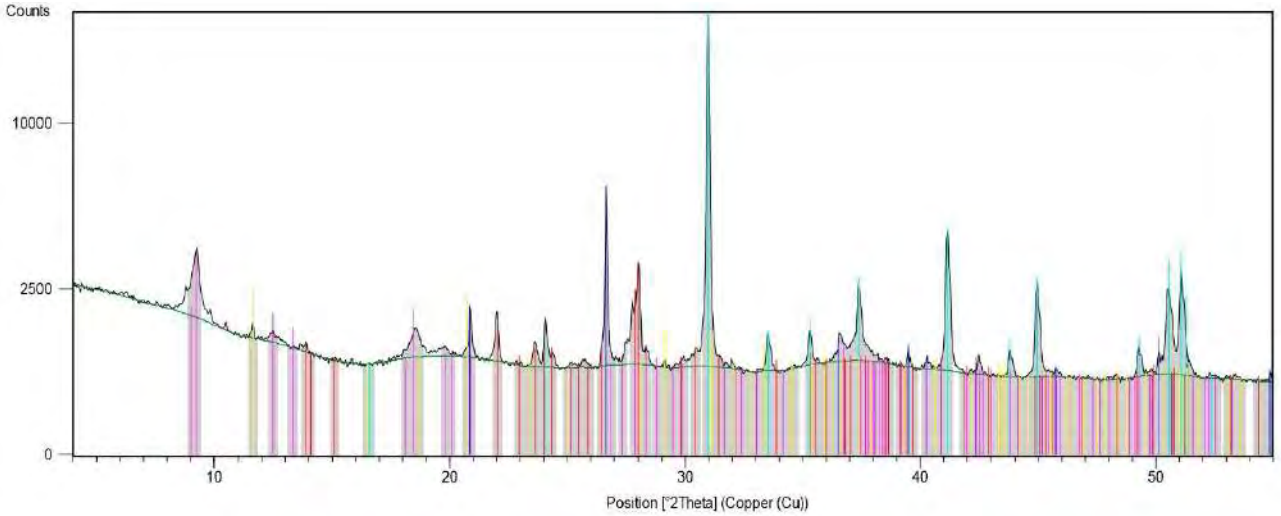
Counts
10000
2500
0
10
20
30
40
50
Position [°2Theta] (Copper (Cu))

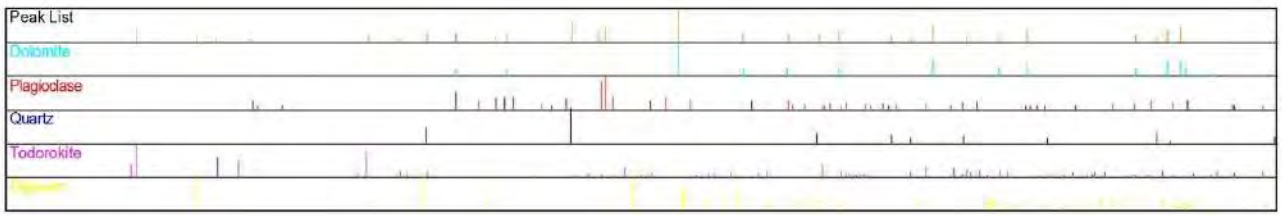
Peak List
Dolomite
Plagioclase
Quartz
Todorokite


5 cm

2022-PAL-16/17

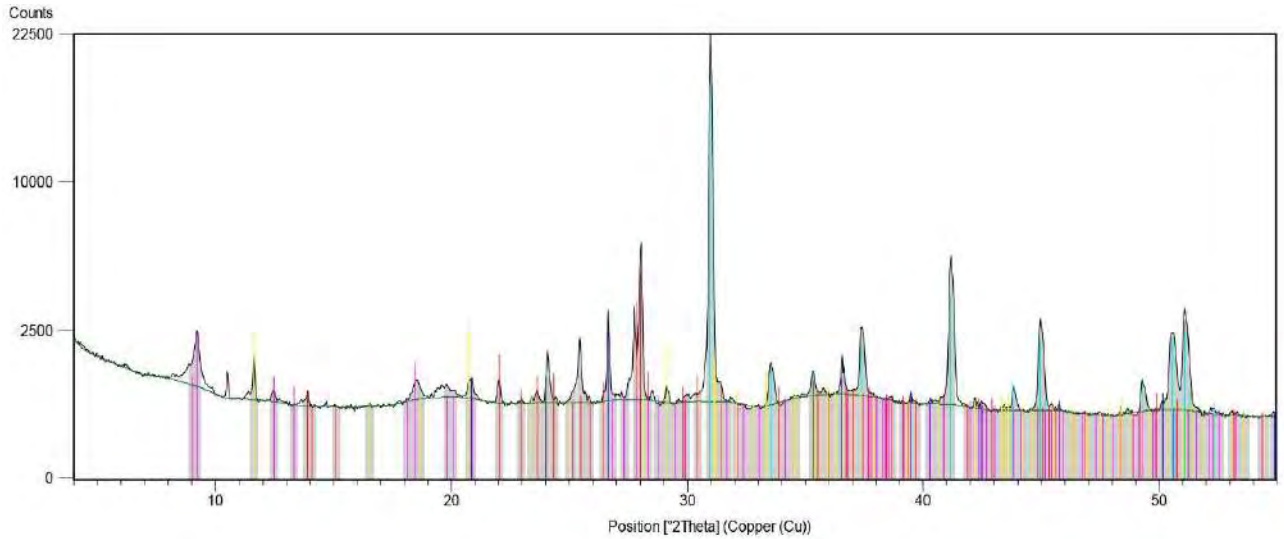

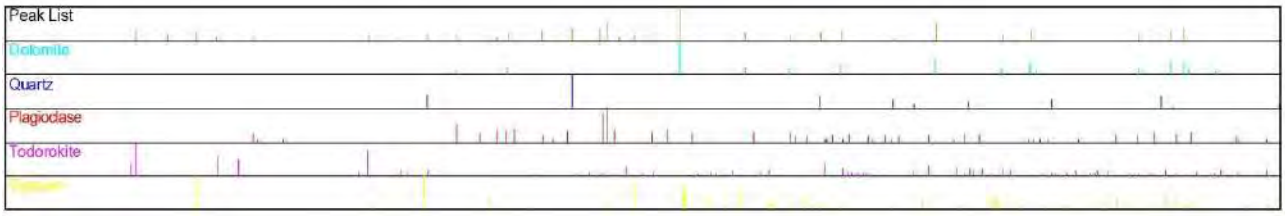

2023-PAL-01

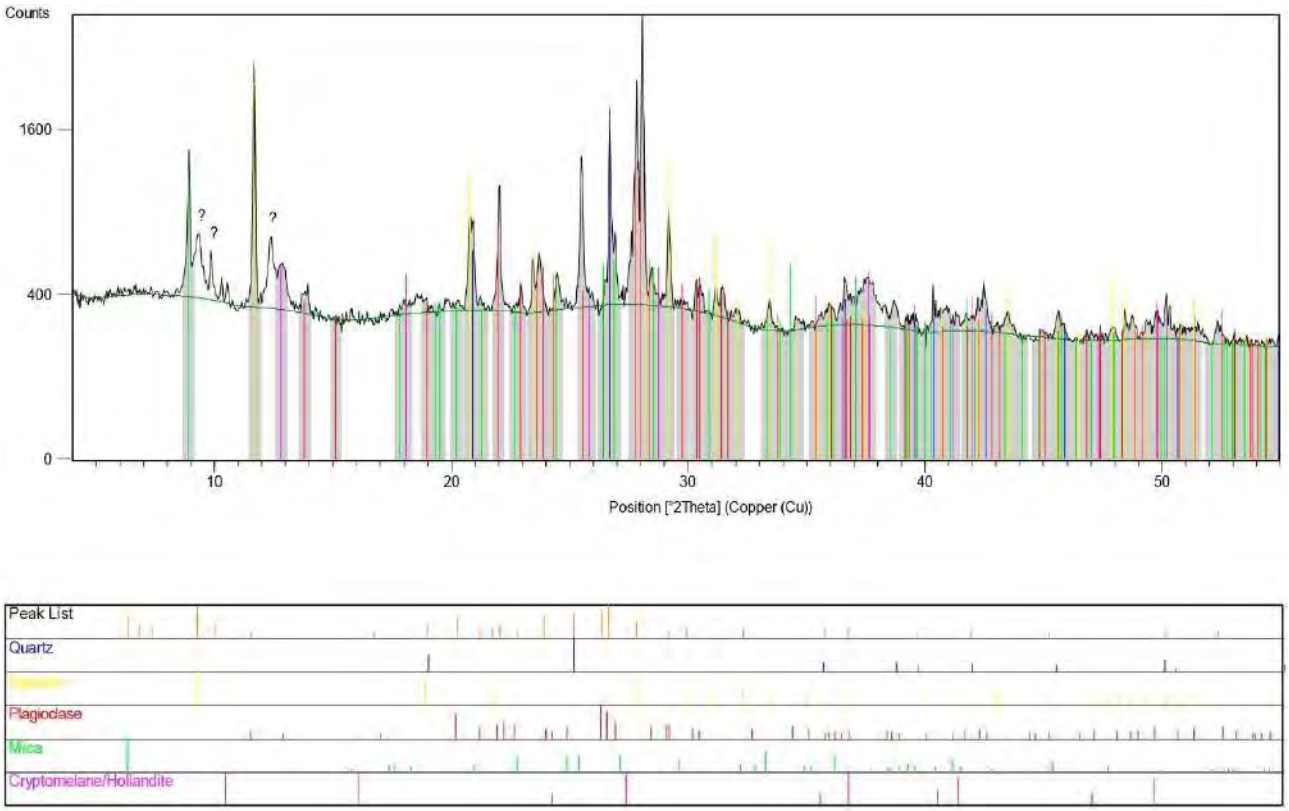
Counts
1600
400
0
?
?
?
10
20
30
40
50
Position [°2Theta] (Copper (Cu))
Peak List
Quartz
Plagioclase
Mica
Cryptomelane/Hollandite


5 cm

2023-PAL-02

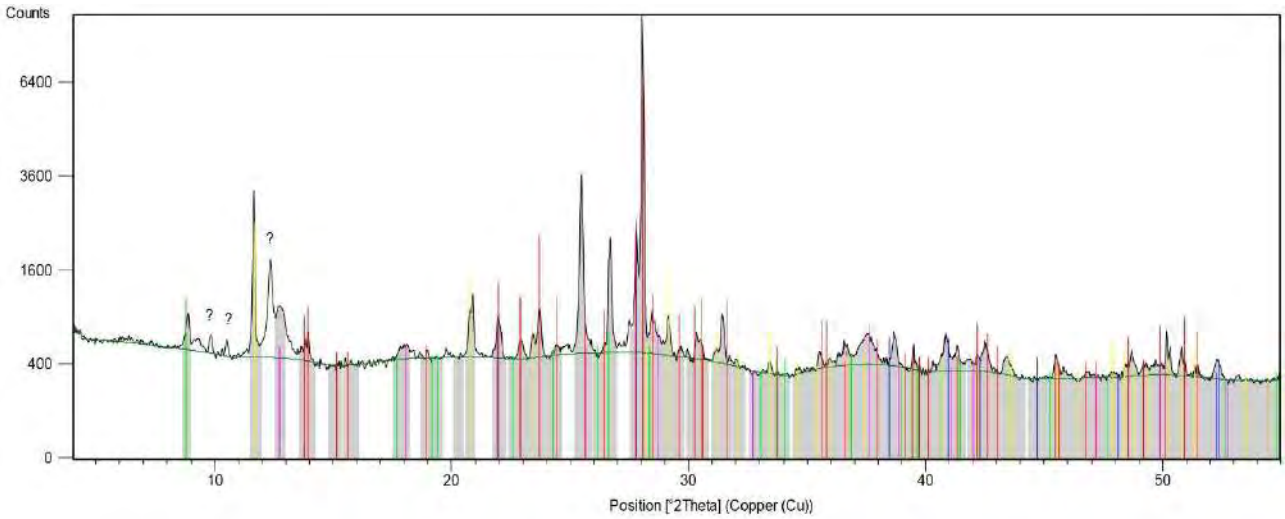
Counts
6400
3600
1600
400
0
10
20
30
40
50
Position [°2Theta] (Copper (Cu))
? ? ?

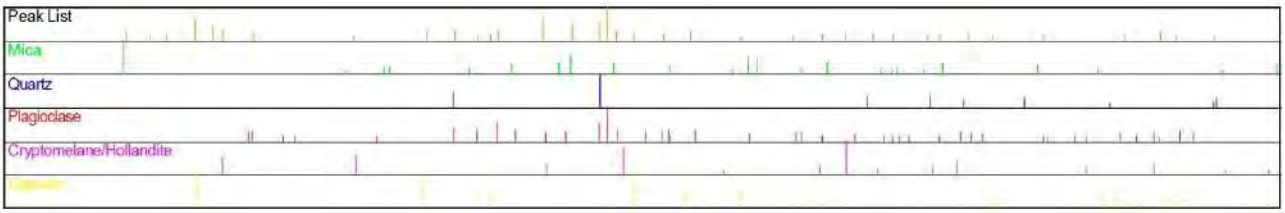
Peak List
Mica
Quartz
Plagioclase
Cryptomelane/Hollandite


3 cm

2023-PAL-04

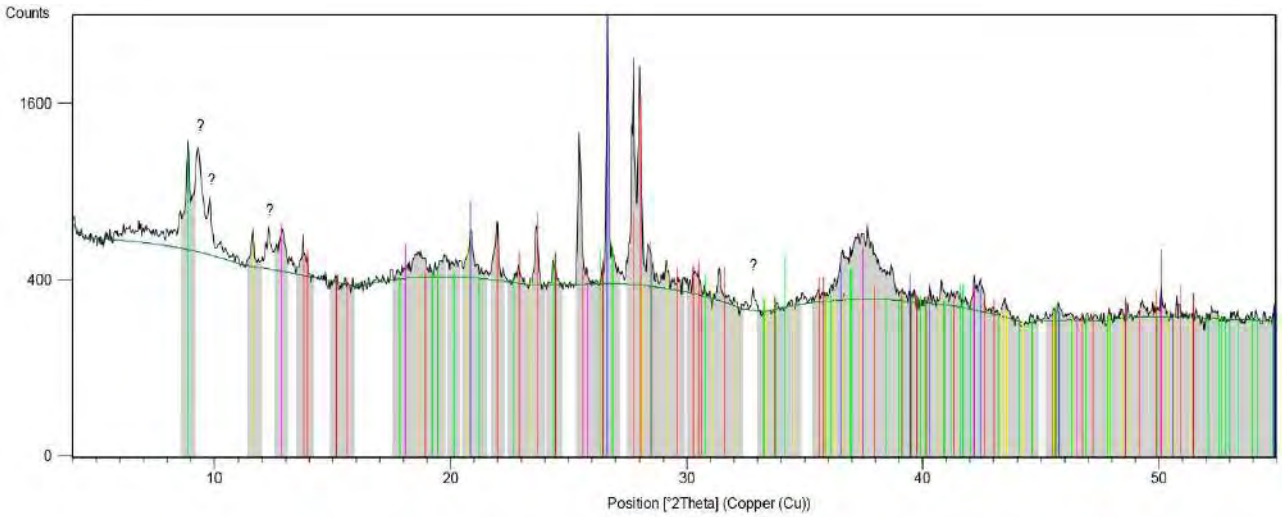
Counts
1600
400
0
?
?
?
?
10
20
30
40
50
Position [°2Theta] (Copper (Cu))

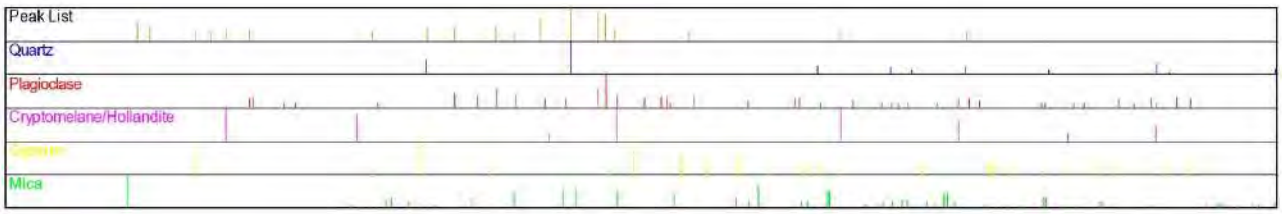
Peak List
Quartz
Plagioclase
Cryptomelane/Hollandite
Mica


3 cm

2023-PAL-08

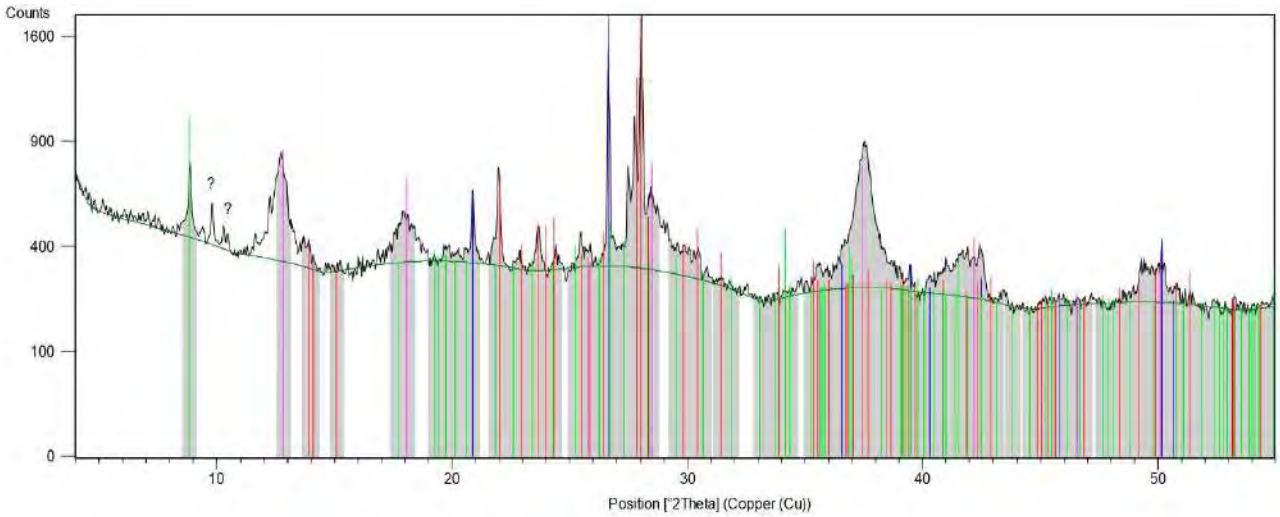
Counts
1600
900
400
100
0
?
?
10
20
30
40
50
Position [°2Theta] (Copper (Cu))

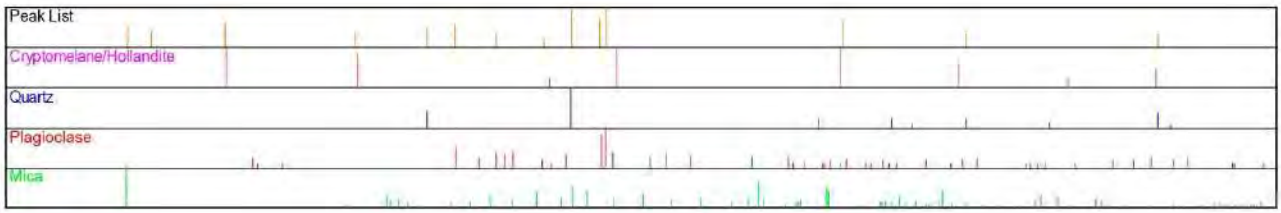
Peak List
Cryptomelane/Hollandite
Quartz
Plagioclase
Mica


2 cm

2023-PAL-09/10

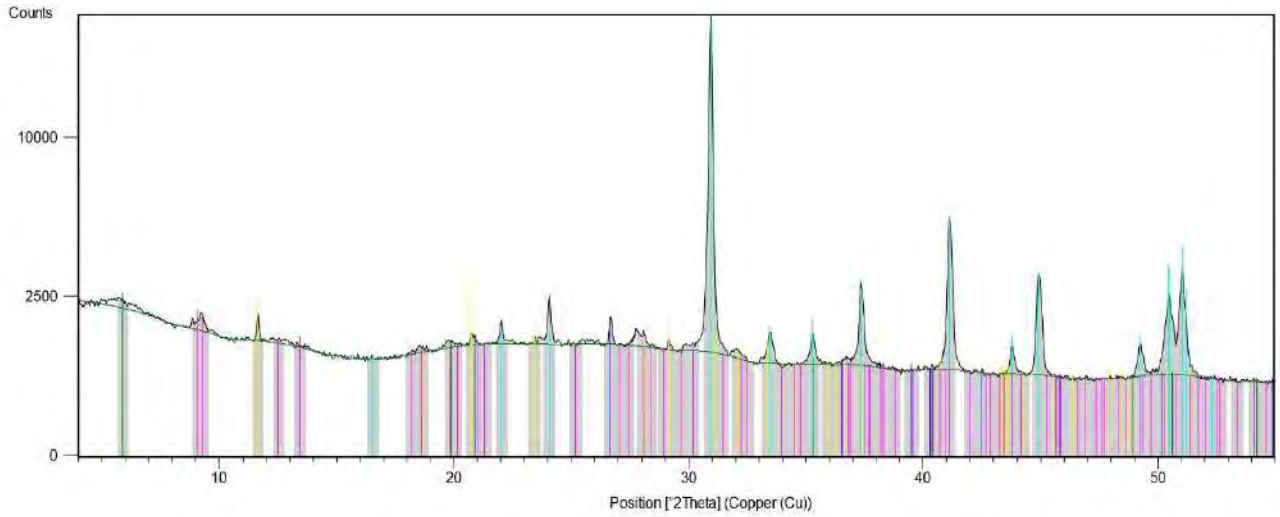

2023-PAL-13

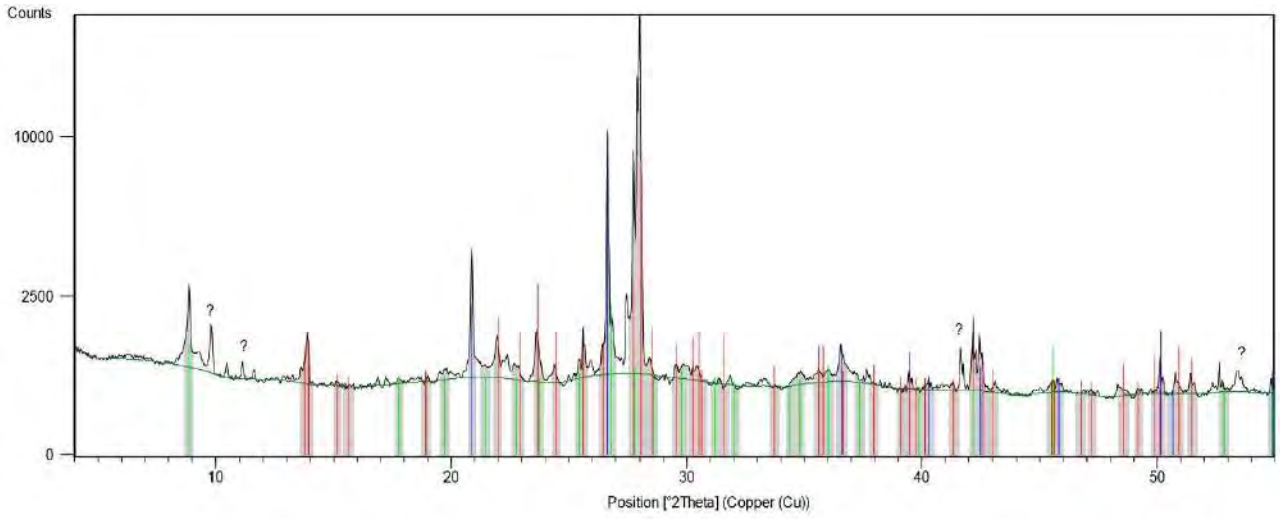
Counts
10000
2500
0
?
?
?
?
10
20
30
40
50
Position [°2Theta] (Copper (Cu))

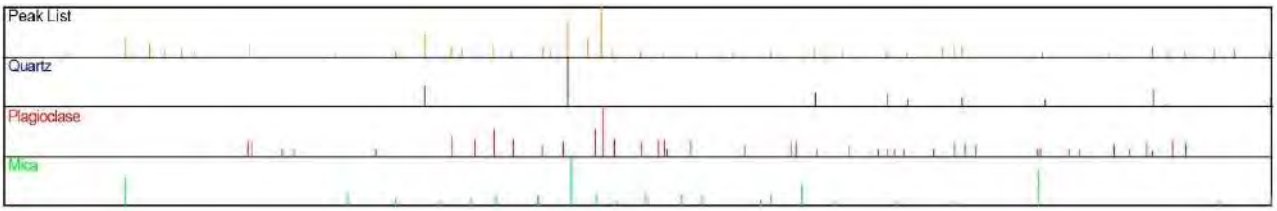
Peak List
Quartz
Plagioclase
Mica


5 cm

2023-PAL-16

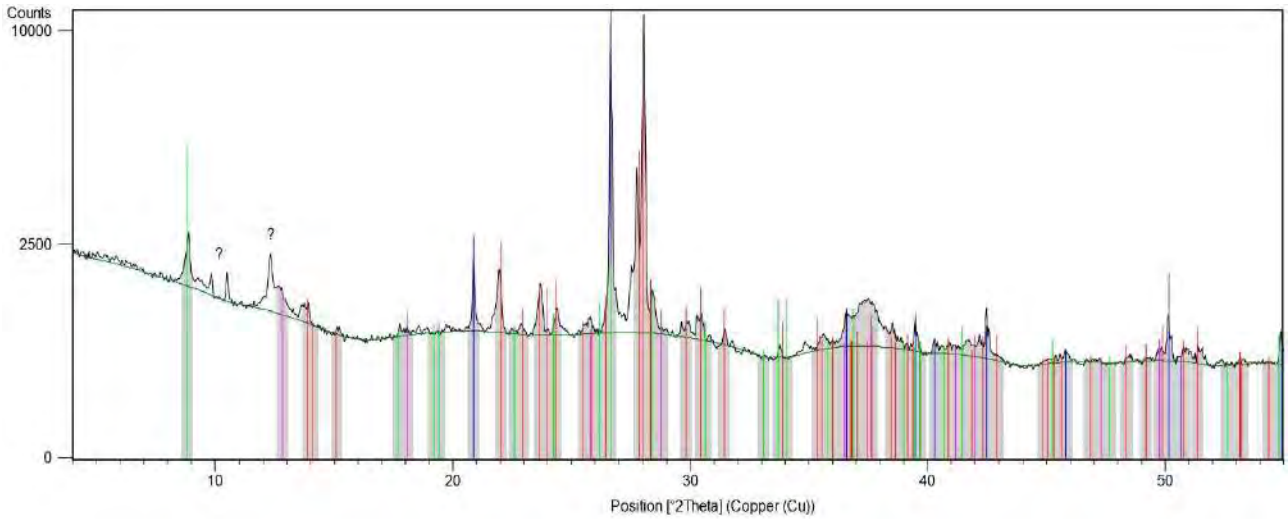
Counts
10000
2500
0
?
?
10
20
30
40
50
Position [°2Theta] (Copper (Cu))

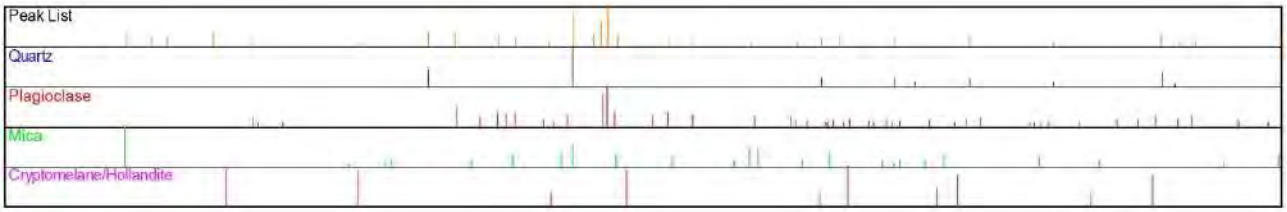
Peak List
Quartz
Plagioclase
Mica
Cryptomelane/Hollandite


2 cm

2023-PAL-17

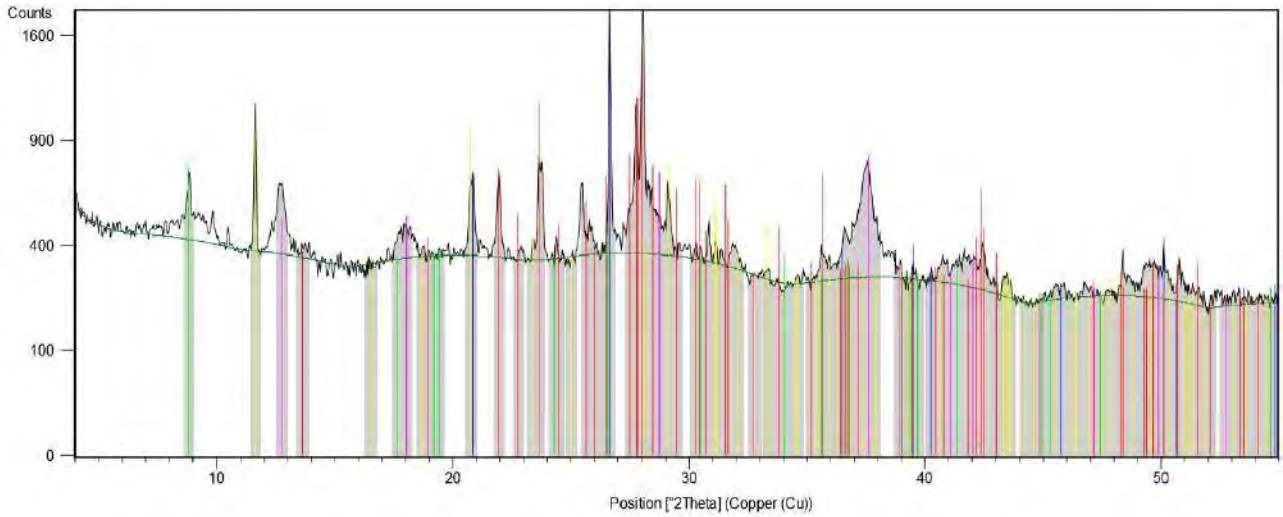
Counts
1600
900
400
100
0
10
20
30
40
50
Position [°2Theta] (Copper (Cu))
Peak List
Quartz
Cryptomelane/Hollandite
Mica
Plagioclase


3 cm

2023-PAL-20

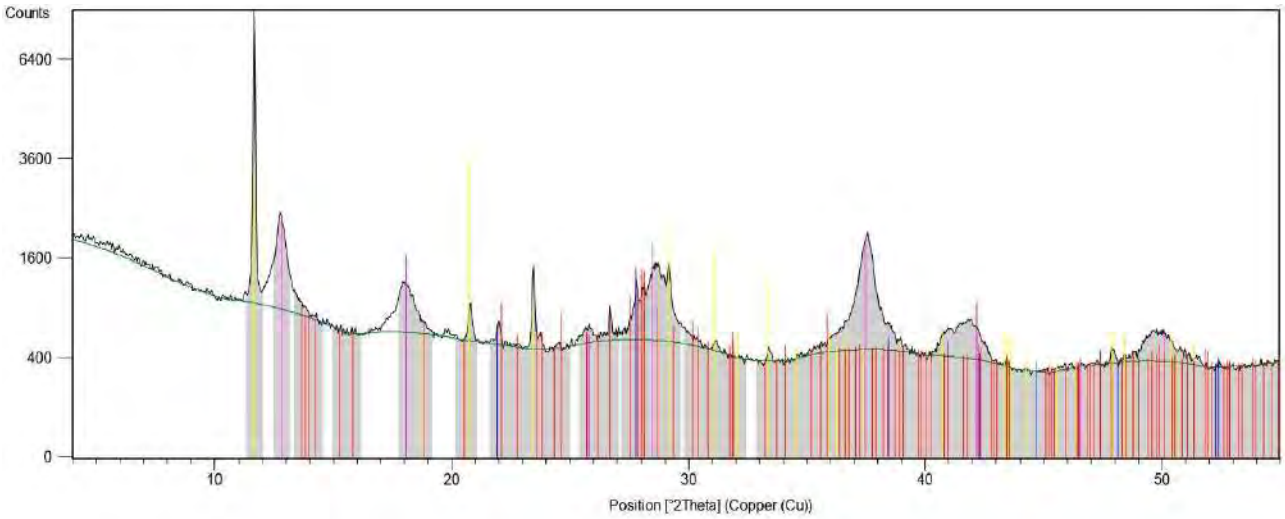
Counts
6400
3600
1600
400
0
10
20
30
40
50
Position [°2Theta] (Copper (Cu))

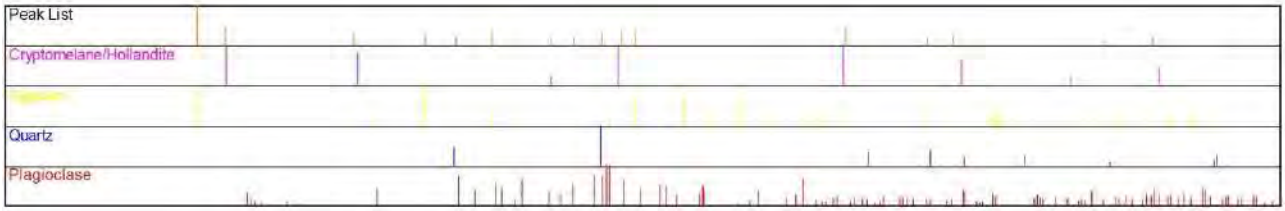
Peak List
Cryptomelane/Hollandite
Quartz
Plagioclase


5 cm

2023-PAL-21

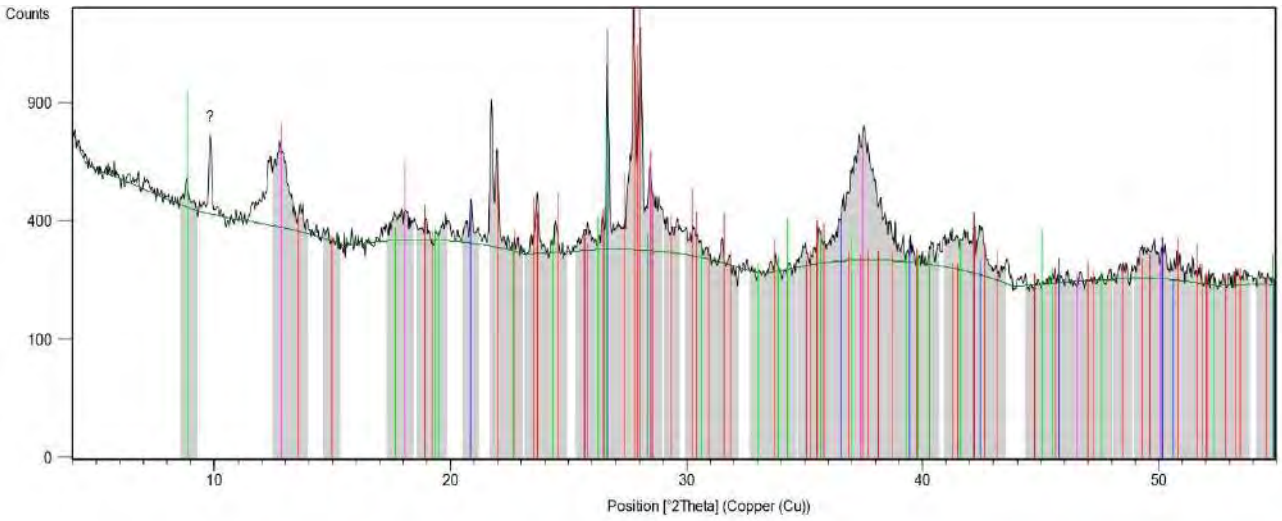
Counts
900
400
100
0
?
10
20
30
40
50
Position [°2Theta] (Copper (Cu))

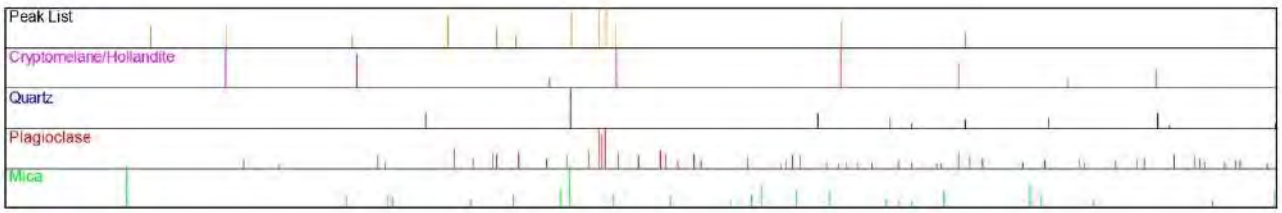
Peak List
Cryptomelane/Hollandite
Quartz
Plagioclase
Mica


5 cm

2023-PAL-22

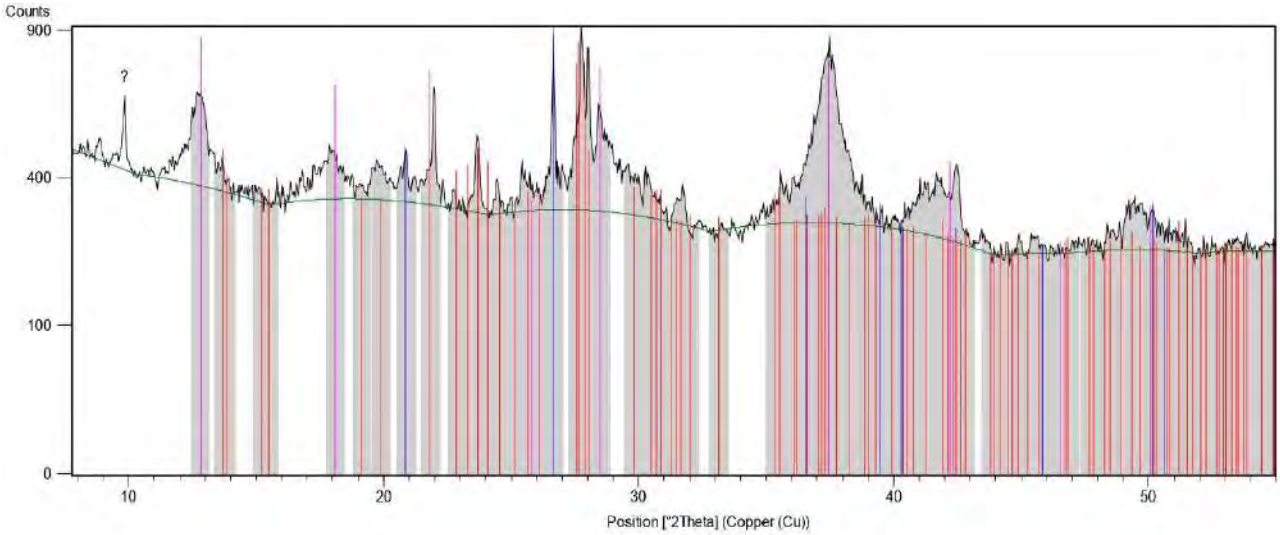
Counts
900
400
100
0
?
10
20
30
40
50
Position [°2Theta] (Copper (Cu))

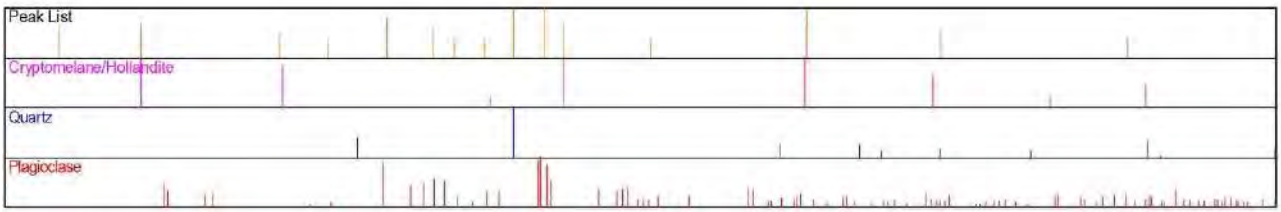
Peak List
Cryptomelane/Hollandite
Quartz
Plagioclase


3 cm

2023-PAL-25

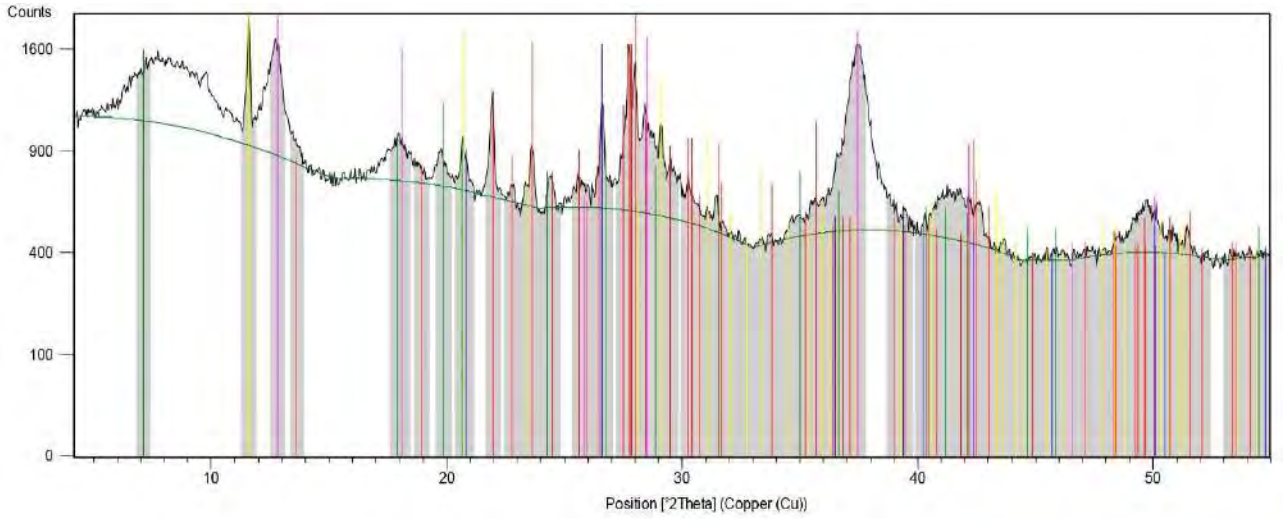
Counts
1600
900
400
100
0
10
20
30
40
50
Position [°2Theta] (Copper (Cu))

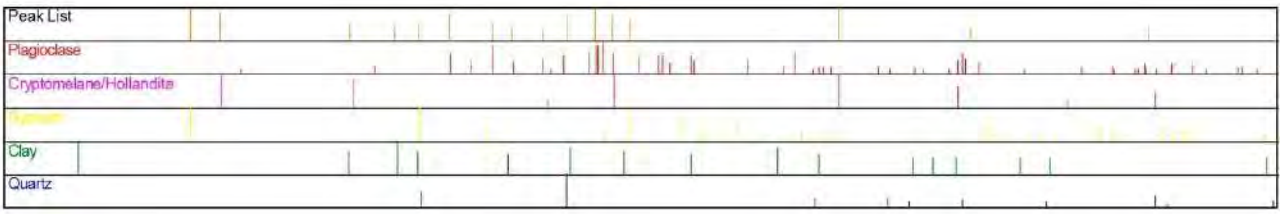
Peak List
Plagioclase
Cryptomelane/Hollandite
Clay
Quartz


5 cm

2023-PAL-26

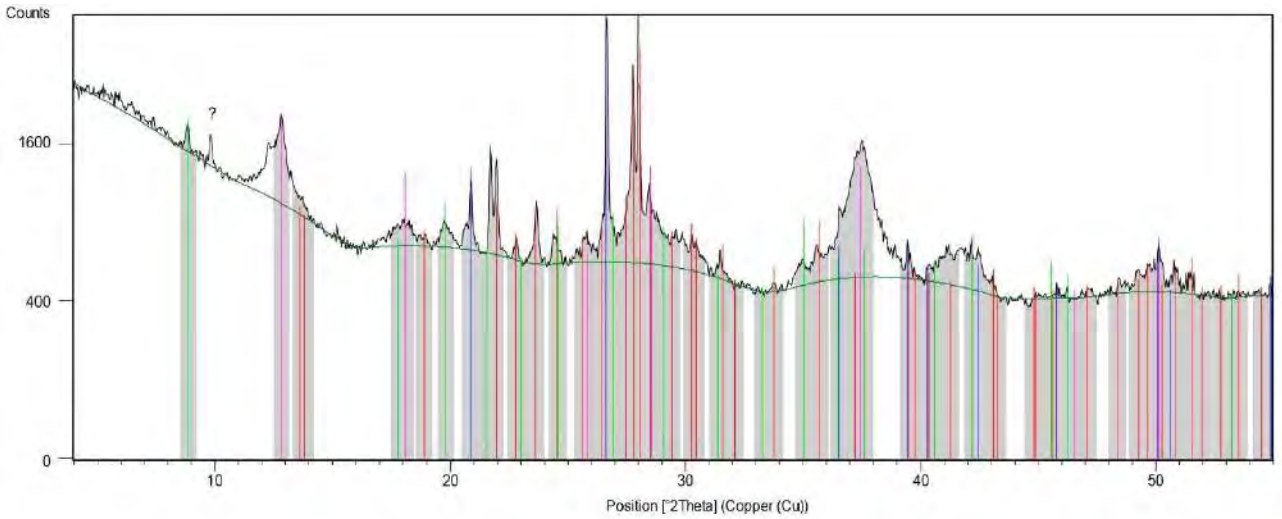
Counts
1600
400
0
?
10
20
30
40
50
Position [°2Theta] (Copper (Cu))
Peak List
Quartz
Plagioclase
Cryptomelane/Hollandite
Mica


3 cm

2023-PAL-27

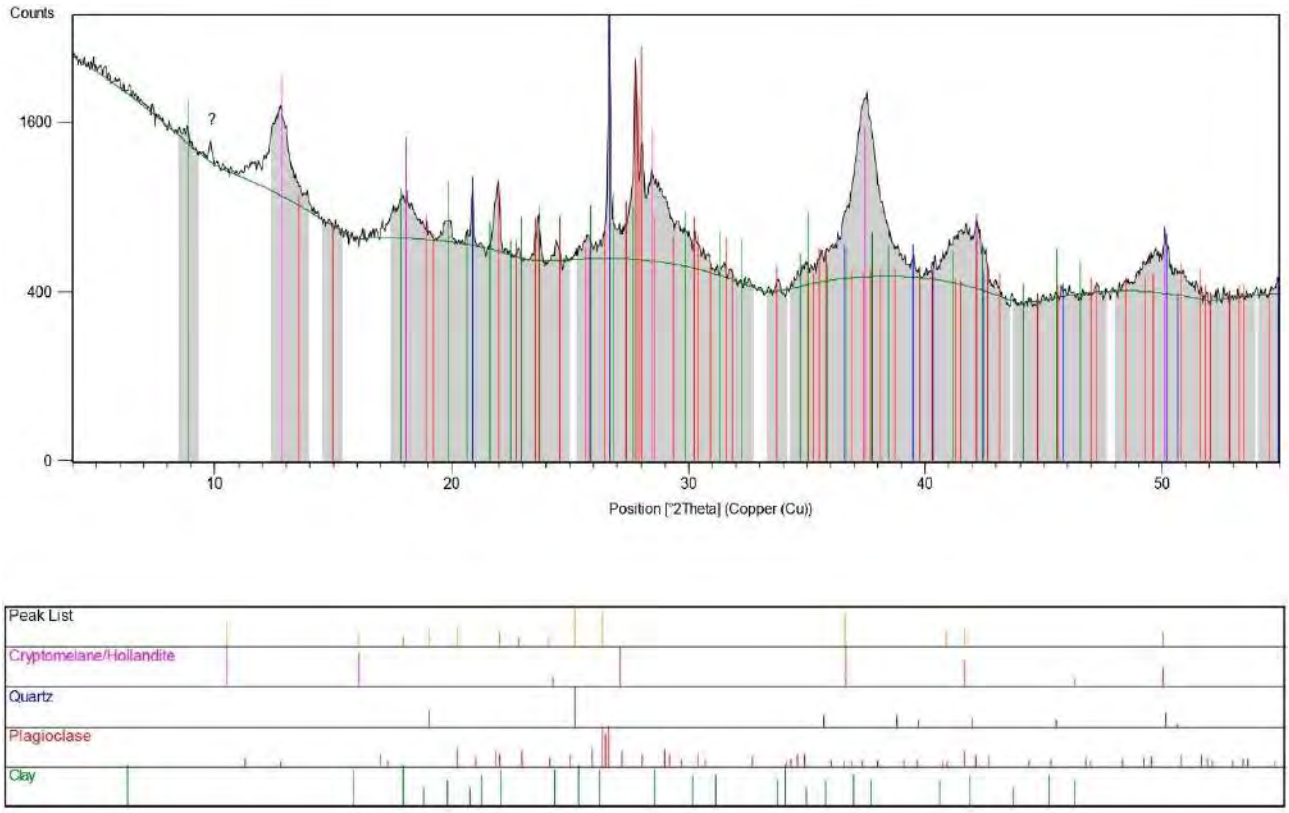
Counts
1600
400
0
?
10
20
30
40
50
Position [°2Theta] (Copper (Cu))
Peak List
Cryptomelane/Hollandite
Quartz
Plagioclase
Clay


3 cm

2023-PAL-29

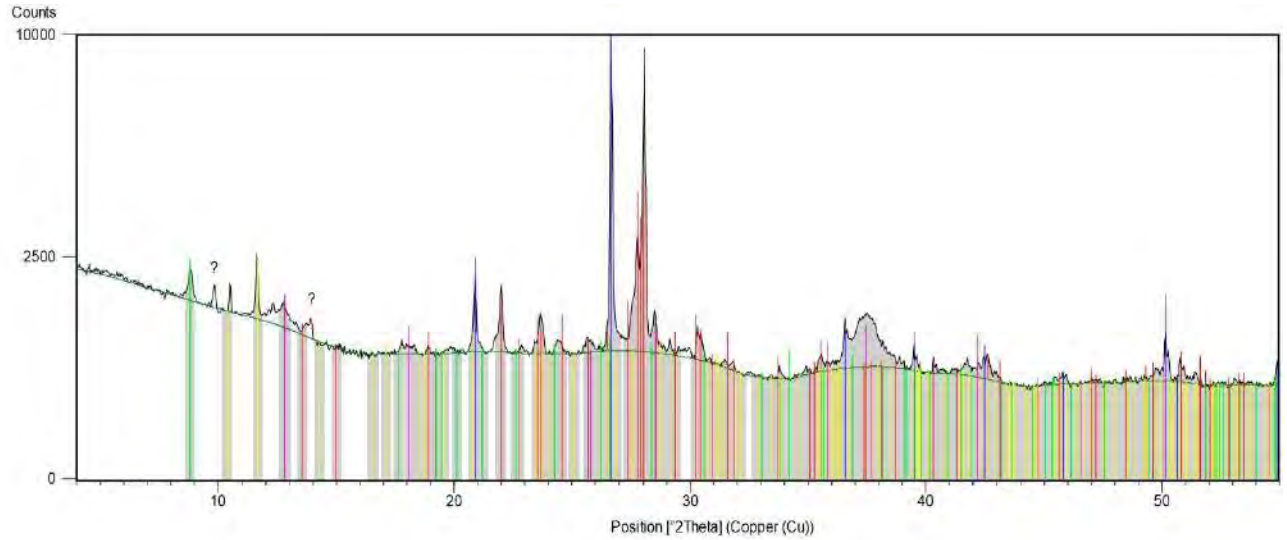
Counts
10000
2500
0
?
?
10
20
30
40
50
Position [°2Theta] (Copper (Cu))

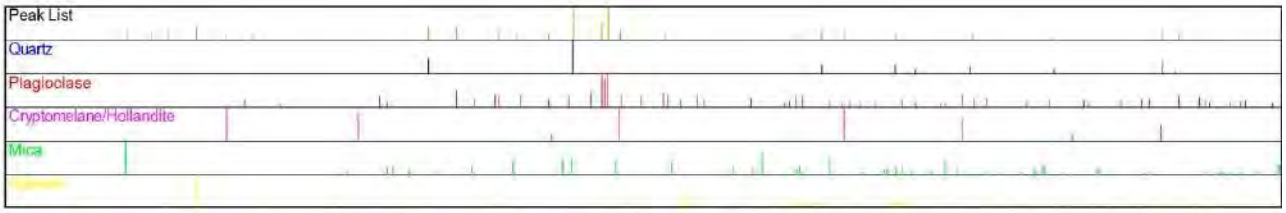
Peak List
Quartz
Plagioclase
Cryptomelane/Hollandite
Mica


3 cm

2023-PAL-30

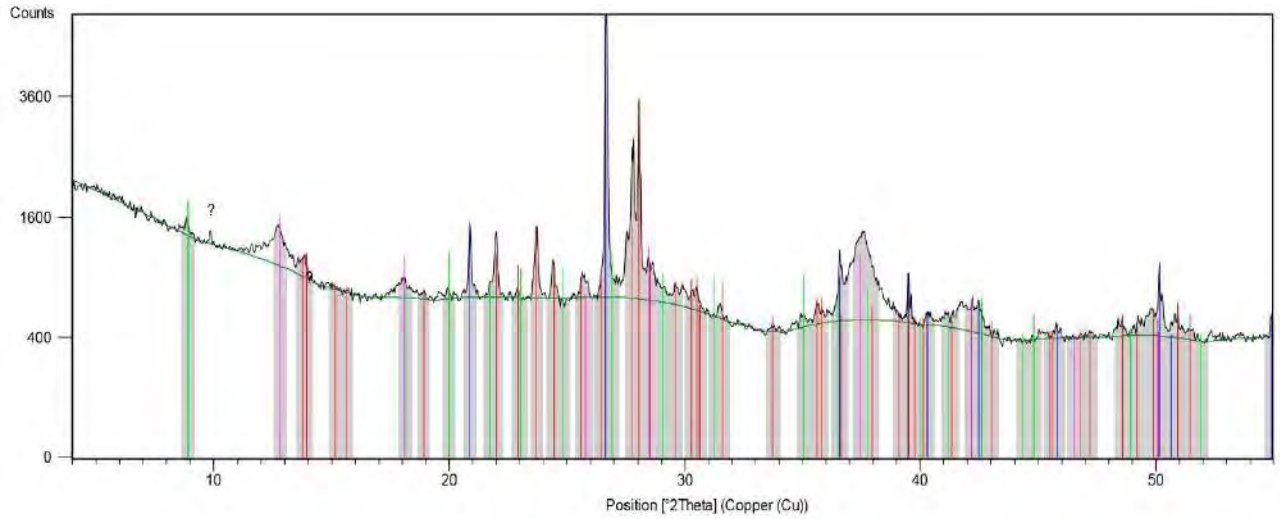
Counts
3600
1600
400
0
?
10
20
30
40
50
Position [°2Theta] (Copper (Cu))
Peak List
Quartz
Plagioclase
Cryptomelane/Hollandite
Mica


3 cm

2023-PAL-32

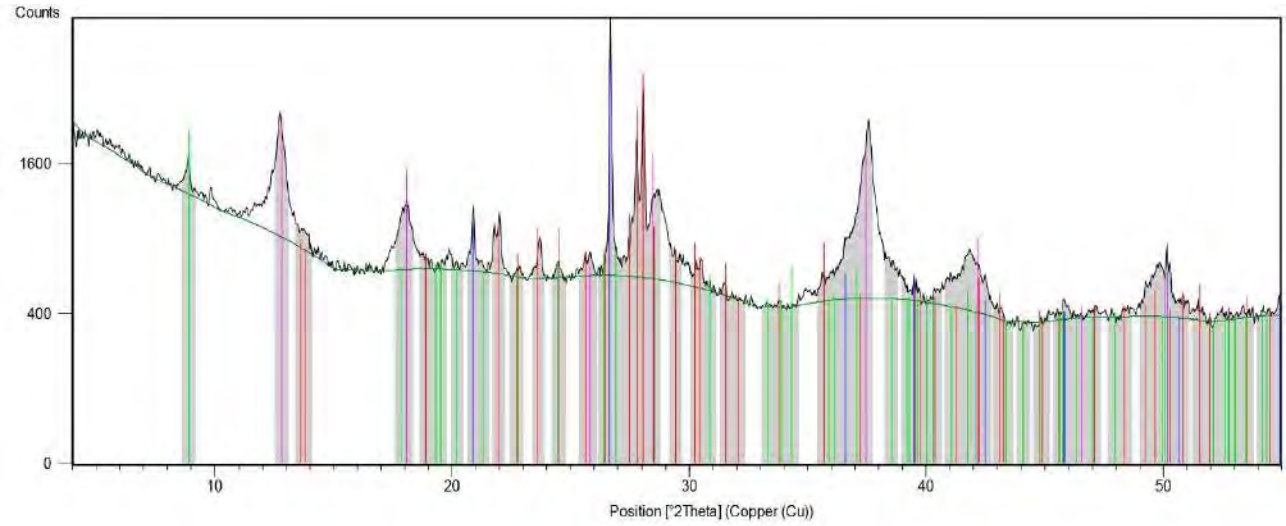
Counts
1600
400
0
10
20
30
40
50
Position [°2Theta] (Copper (Cu))

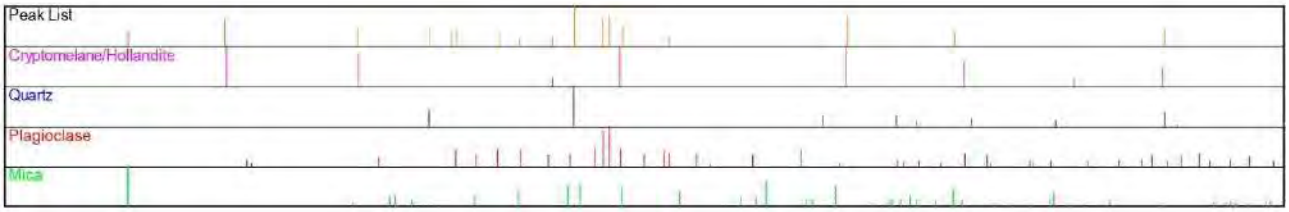
Peak List
Cryptomelane/Hollandite
Quartz
Plagioclase
Mica


5 cm

2023-PAL-33

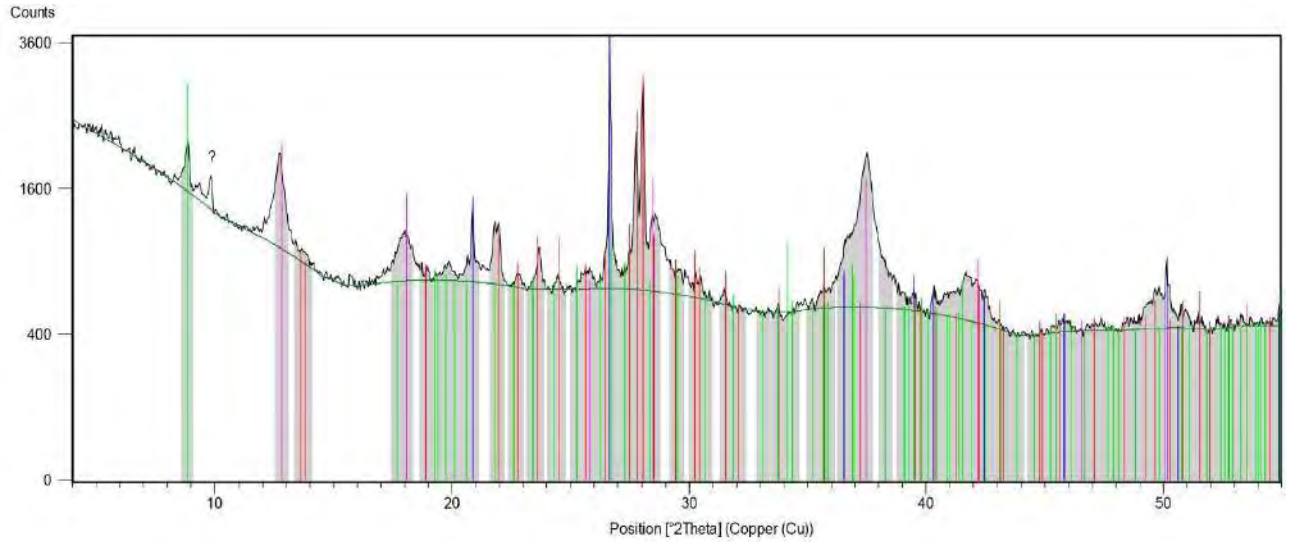
Counts
3600
1600
400
0
?
10
20
30
40
50
Position [°2Theta] (Copper (Cu))

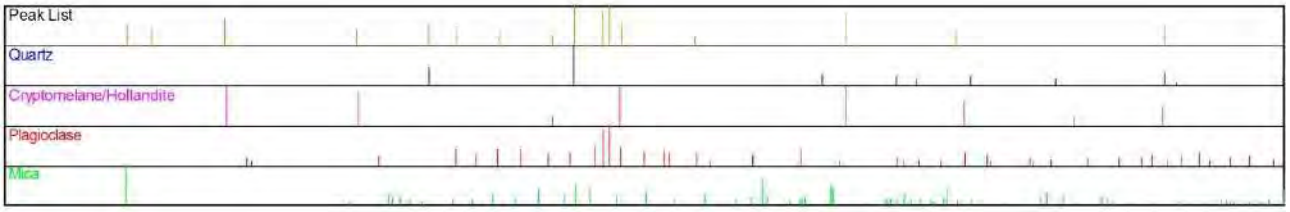
Peak List
Quartz
Cryptomelane/Hollandite
Plagioclase
Mica


3 cm

2023-PAL-34

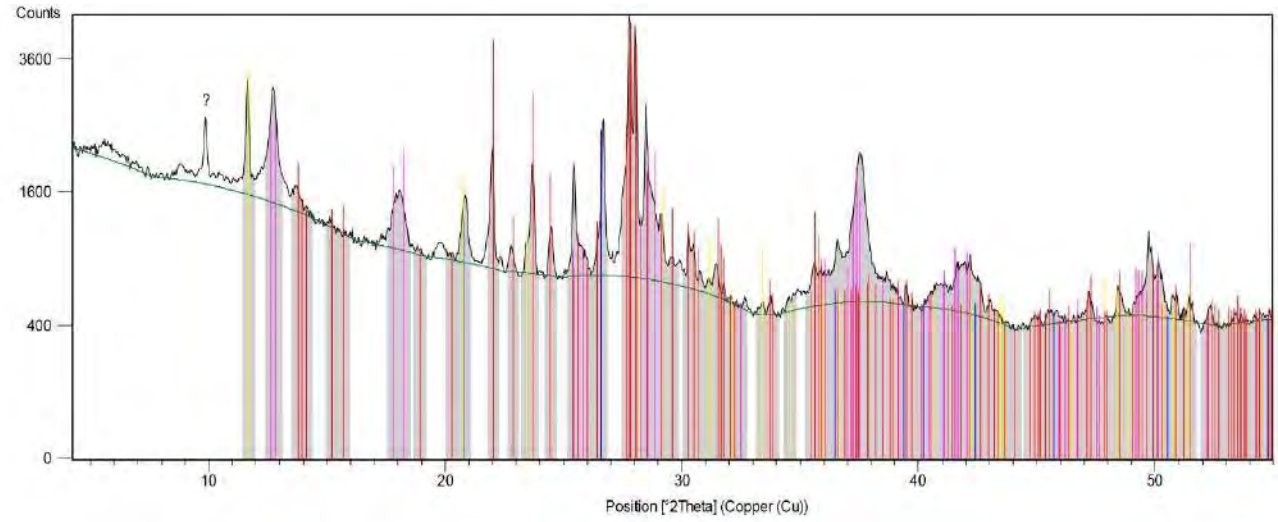
Counts
3600
1600
400
0
?
10
20
30
40
50
Position [°2Theta] (Copper (Cu))

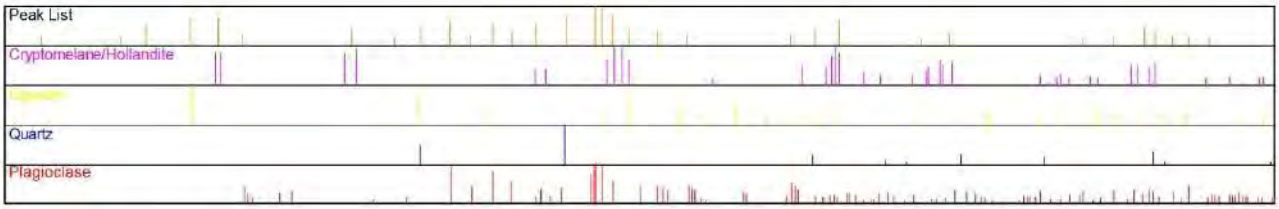
Peak List
Cryptomelane/Hollandite
Quartz
Plagioclase


5 cm

2023-PAL-35

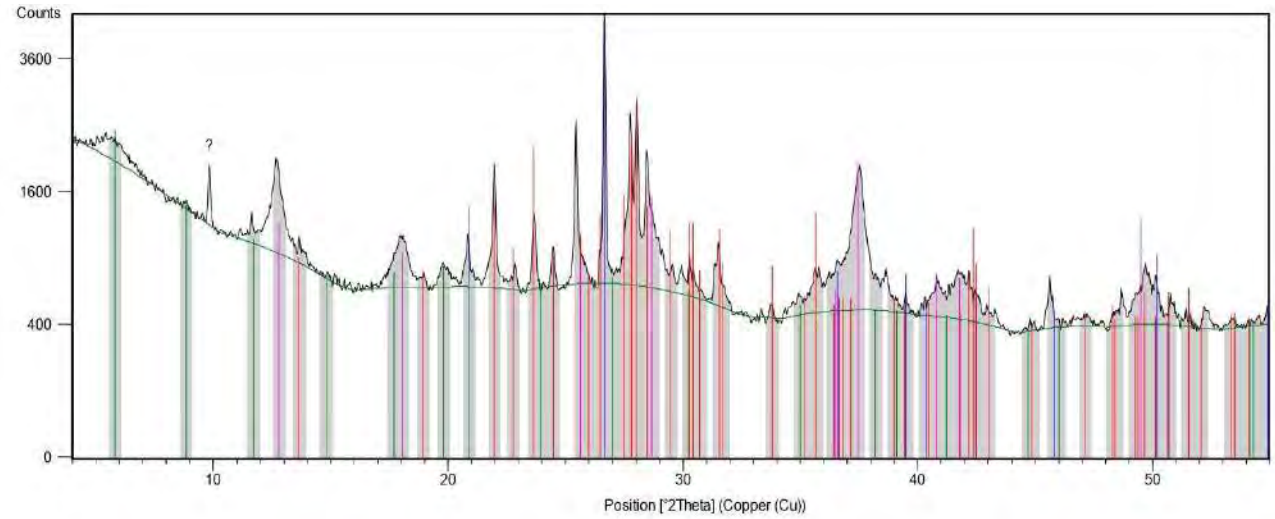
Counts
3600
1600
400
0
?
10
20
30
40
50
Position [°2Theta] (Copper (Cu))

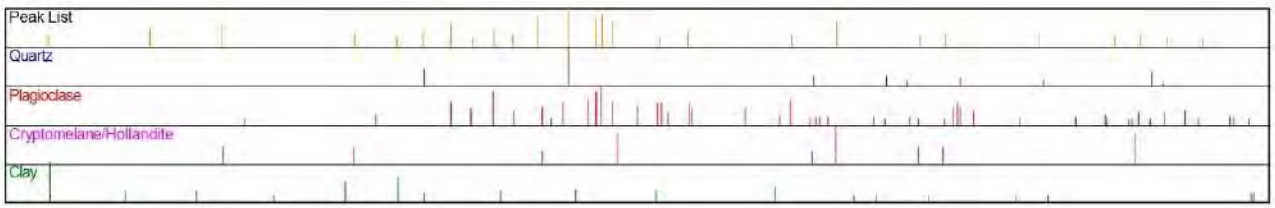
Peak List
Quartz
Plagioclase
Cryptomelane/Hollandite
Clay


3 cm

2023-PAL-36

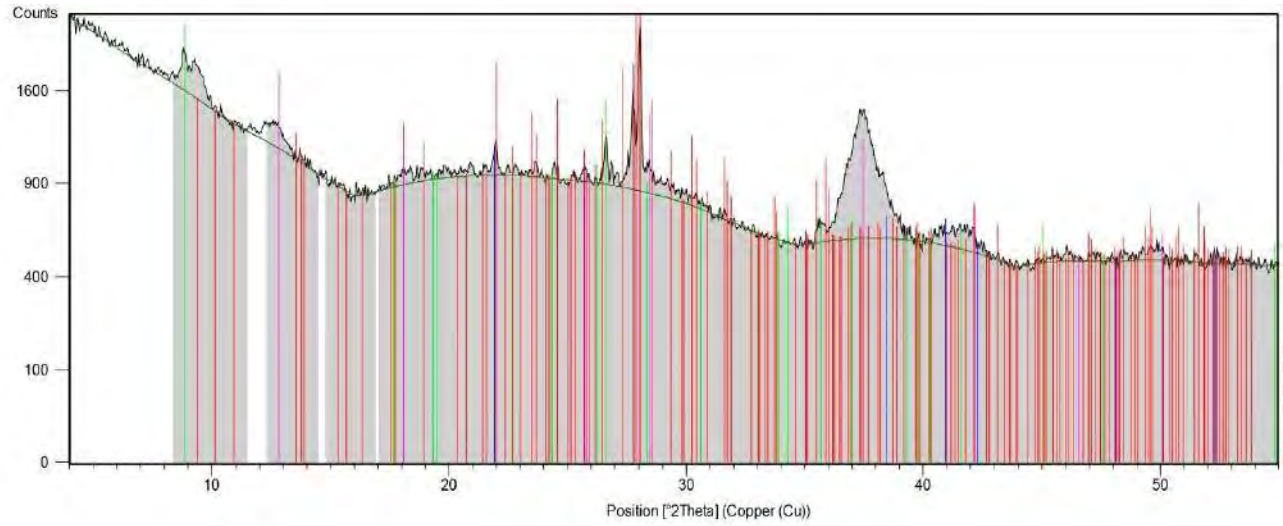
Counts
1600
900
400
100
0
10
20
30
40
50
Position [°2Theta] (Copper (Cu))

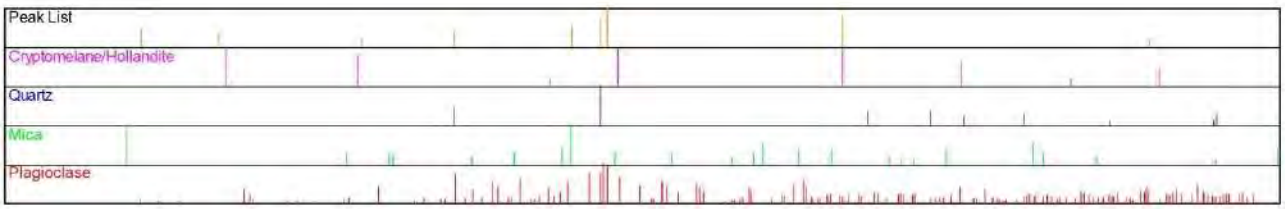
Peak List
Cryptomelane/Hollandite
Quartz
Mica
Plagioclase


3 cm

2023-PAL-37

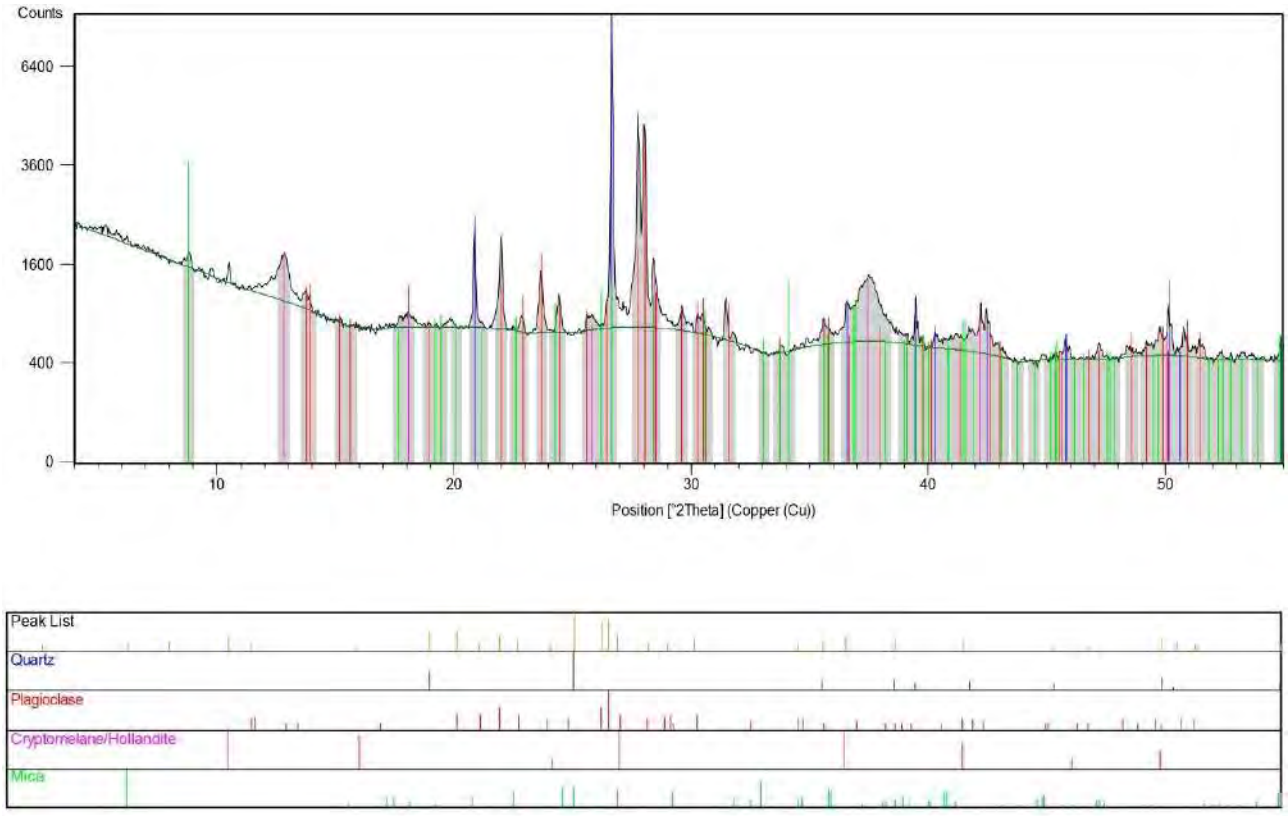
Counts
6400
3600
1600
400
0
10
20
30
40
50
Position [°2Theta] (Copper (Cu))
Peak List
Quartz
Plagioclase
Cryptomelane/Hollandite
Micas


3 cm

2023-PAL-38

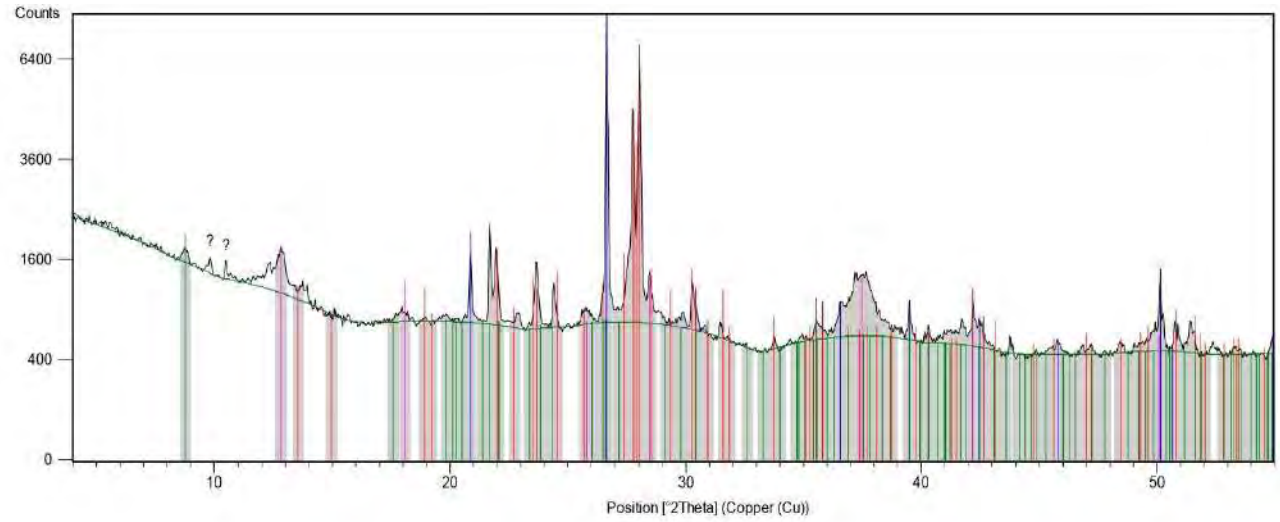
Counts
6400
3600
1600
400
0
? ?
10
20
30
40
50
Position [°2Theta] (Copper (Cu))
Peak List
Quartz
Plagioclase
Cryptomelane/Hollandite
Clay


3 cm

2023-PAL-40

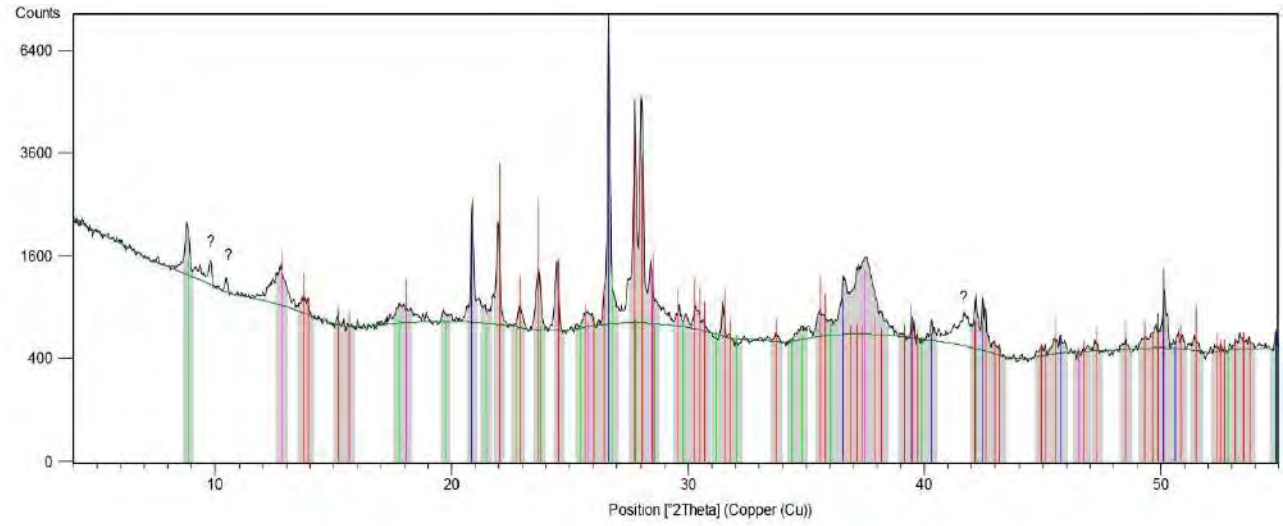
Counts
6400
3600
1600
400
0
10
20
30
40
50
Position [°2Theta] (Copper (Cu))
?
?
?

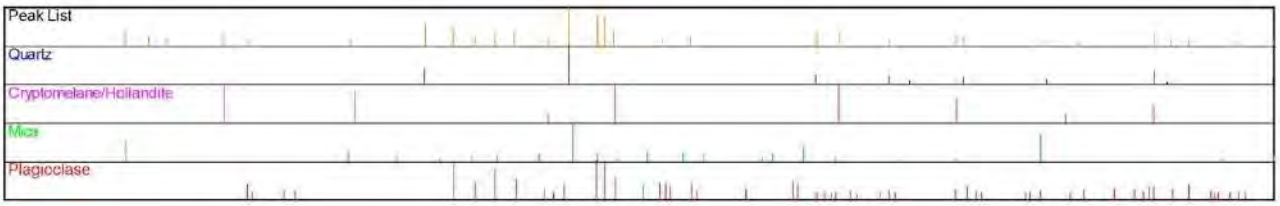
Peak List
Quartz
Cryptomelane/Hollandite
Mica
Plagioclase


5 cm

2023-PAL-43

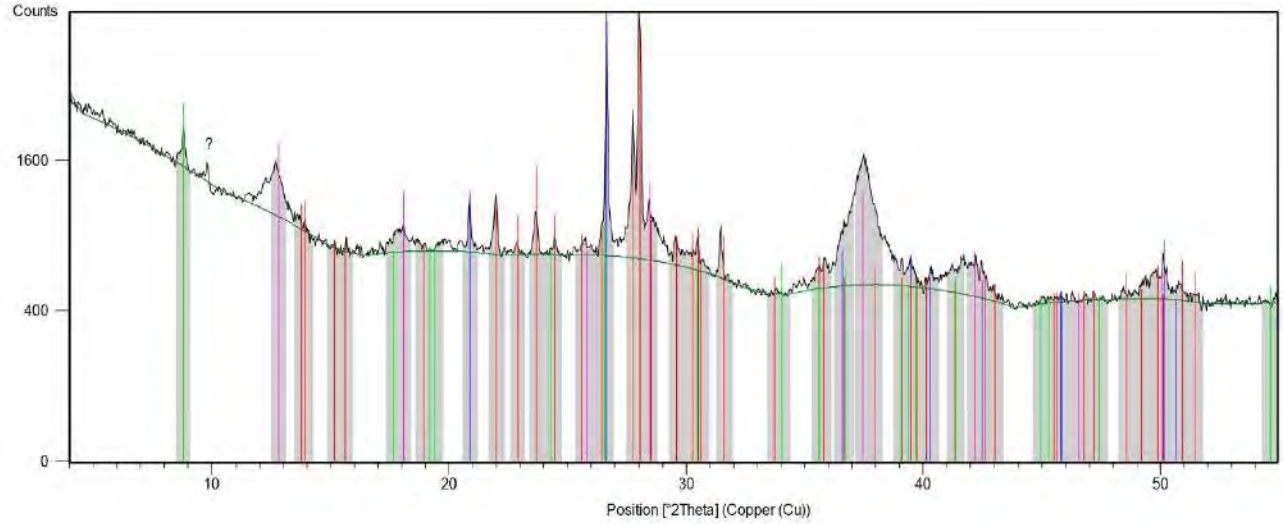
Counts
1600
400
0
?
10
20
30
40
50
Position [°2Theta] (Copper (Cu))

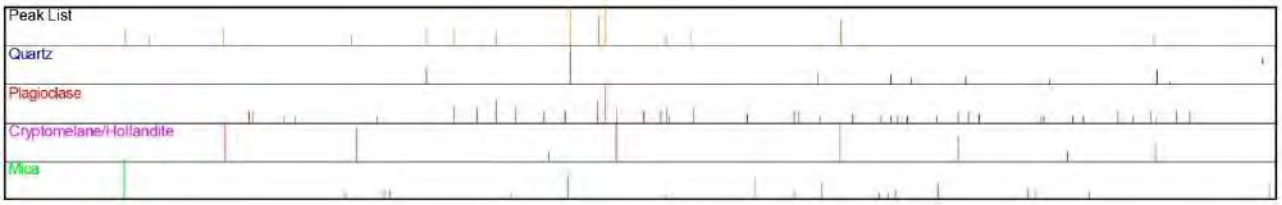
Peak List
Quartz
Plagioclase
Cryptomelane/Hollandite
Mica


2 cm

2023-PAL-44

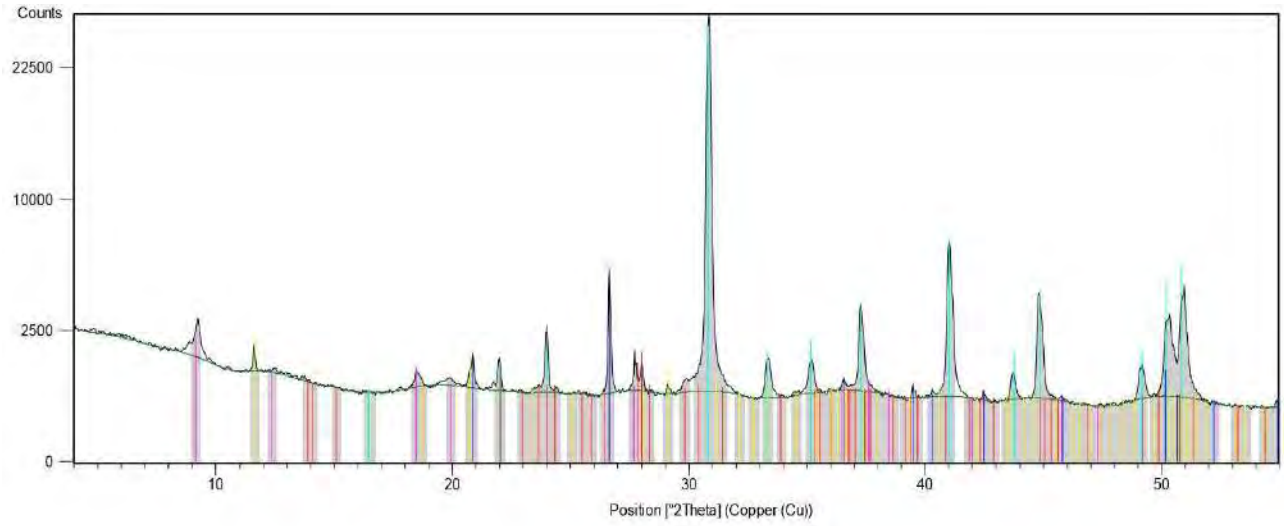
Counts
22500
10000
2500
0
10
20
30
40
50
Position [°2Theta] (Copper (Cu))

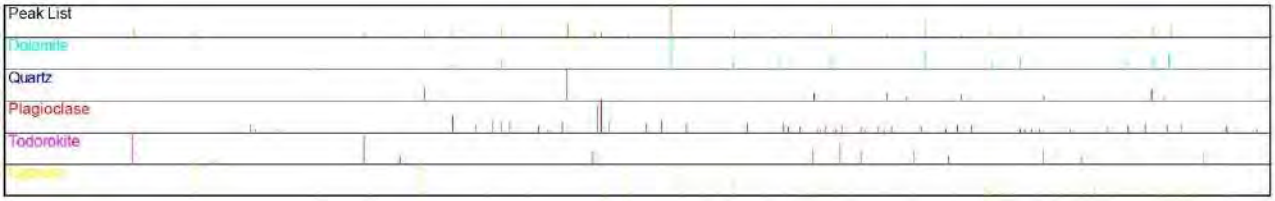
Peak List
Dolomite
Quartz
Plagioclase
Todorokite


3 cm

2023-PAL-45

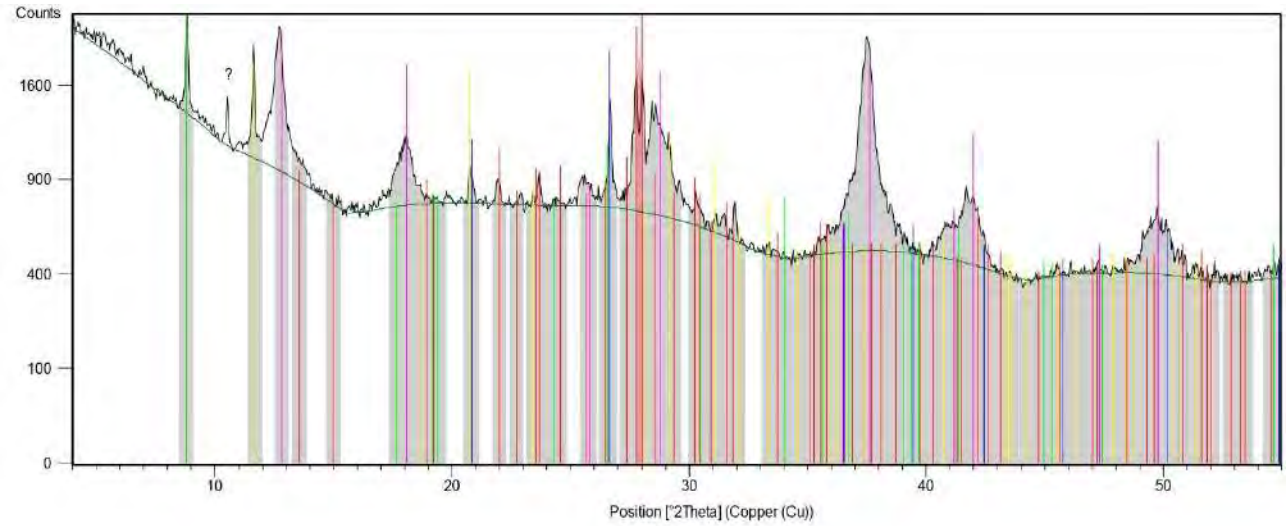
Counts
1600
900
400
100
0
?
10
20
30
40
50
Position [°2Theta] (Copper (Cu))

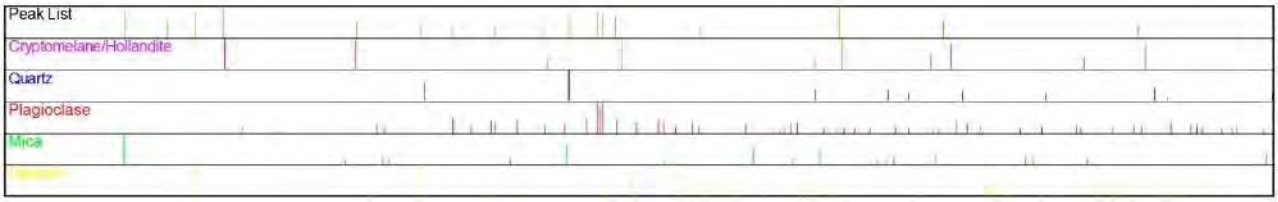
Peak List
Cryptomelane/Hollandite
Quartz
Plagioclase
Mica


3 cm

2023-PAL-46

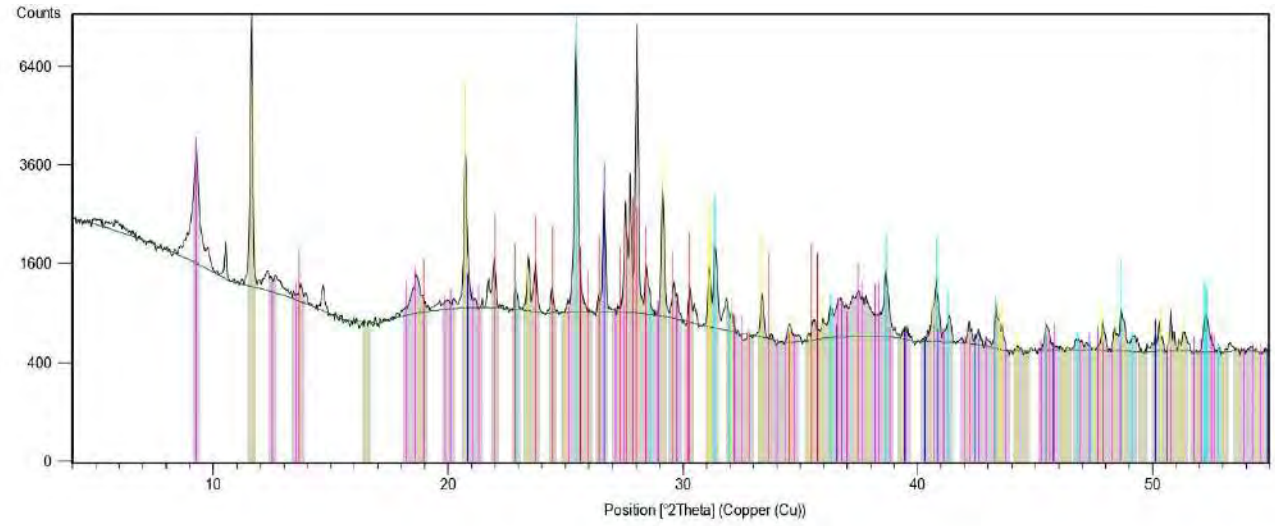
Counts
6400
3600
1600
400
0
10
20
30
40
50
Position [°2Theta] (Copper (Cu))

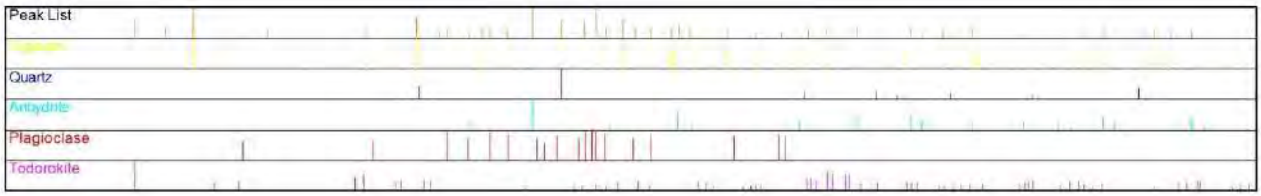
Peak List
Quartz
Anhydrite
Plagioclase
Todorokite


5 cm

2023-PAL-47A

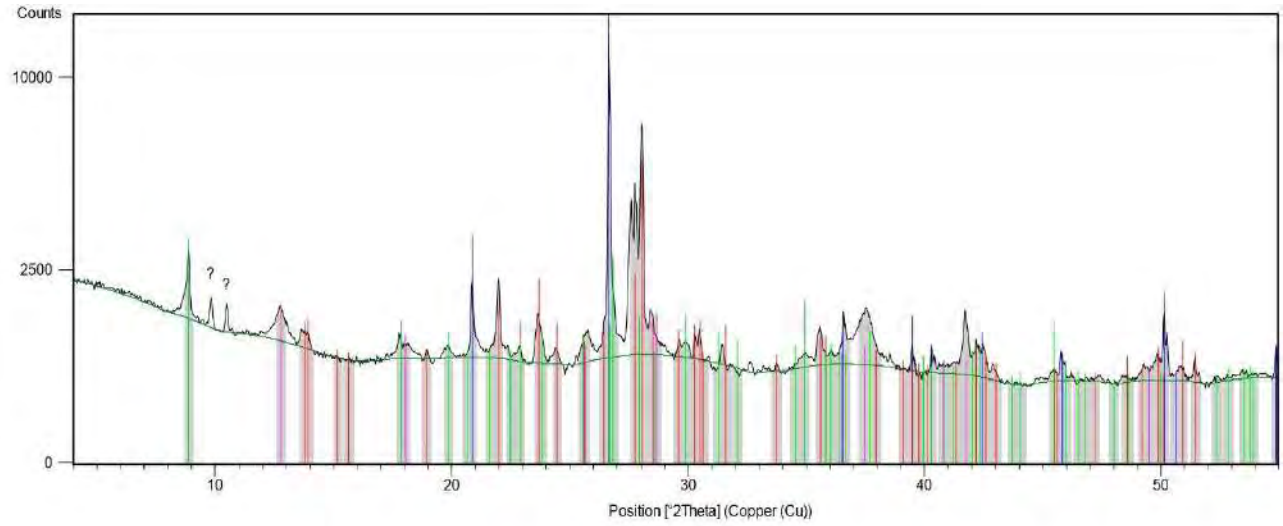
Counts
10000
2500
0
? ?
10
20
30
40
50
Position [°2Theta] (Copper (Cu))

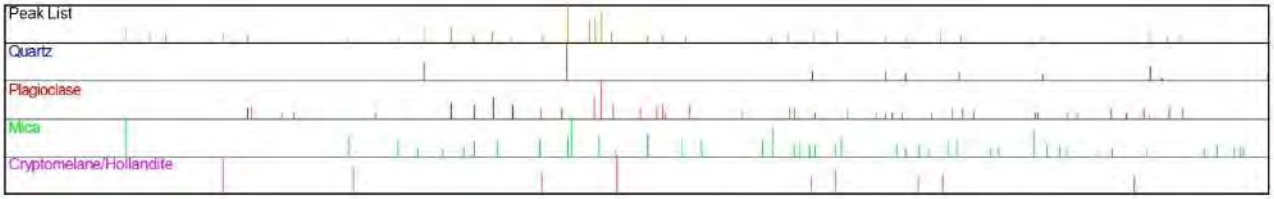
Peak List
Quartz
Plagioclase
Mica
Cryptomelane/Hollandite

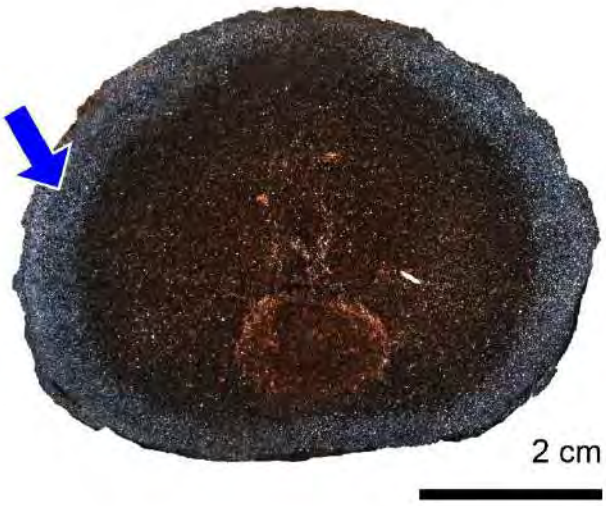
2 cm

2023-PAL-47B

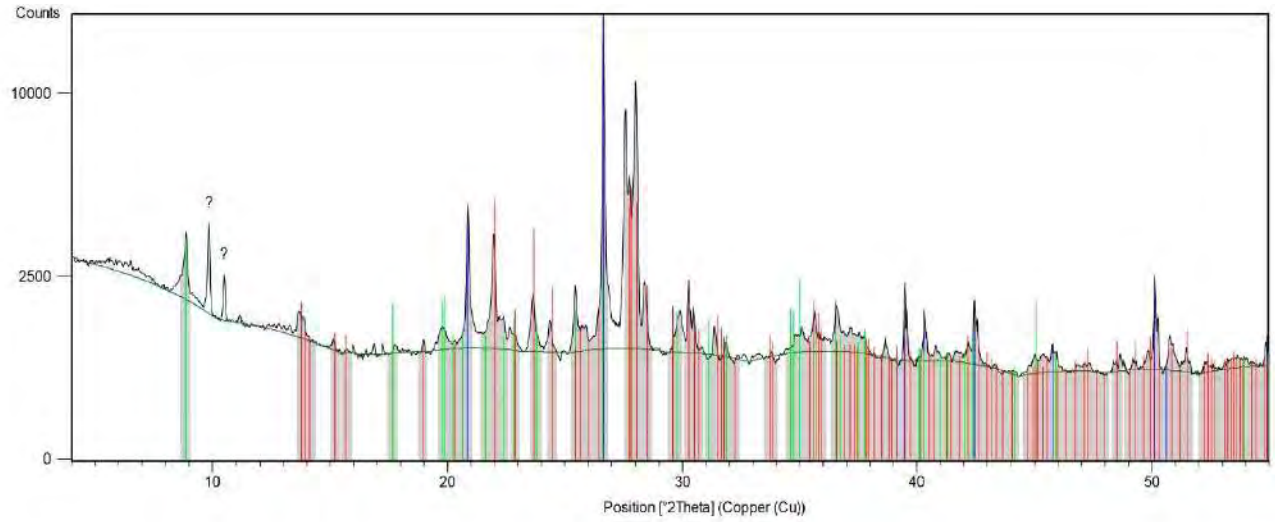
Counts
10000
2500
0
?
?
10
20
30
40
50
Position [°2Theta] (Copper (Cu))

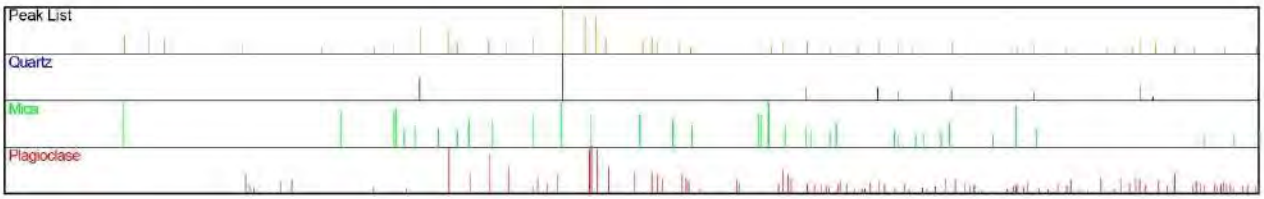
Peak List
Quartz
Mica
Plagioclase

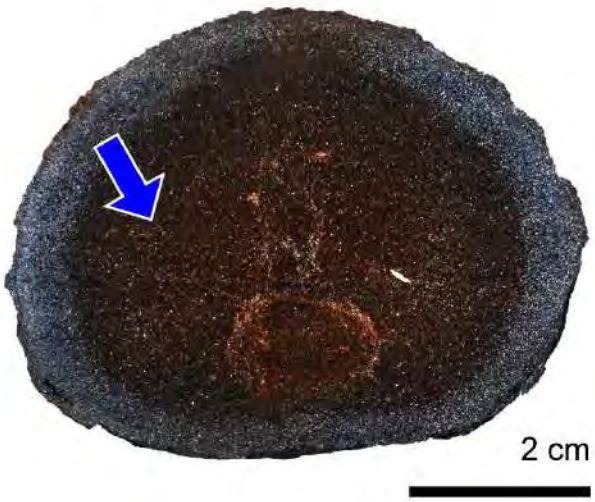
2 cm

2023-PAL-48A

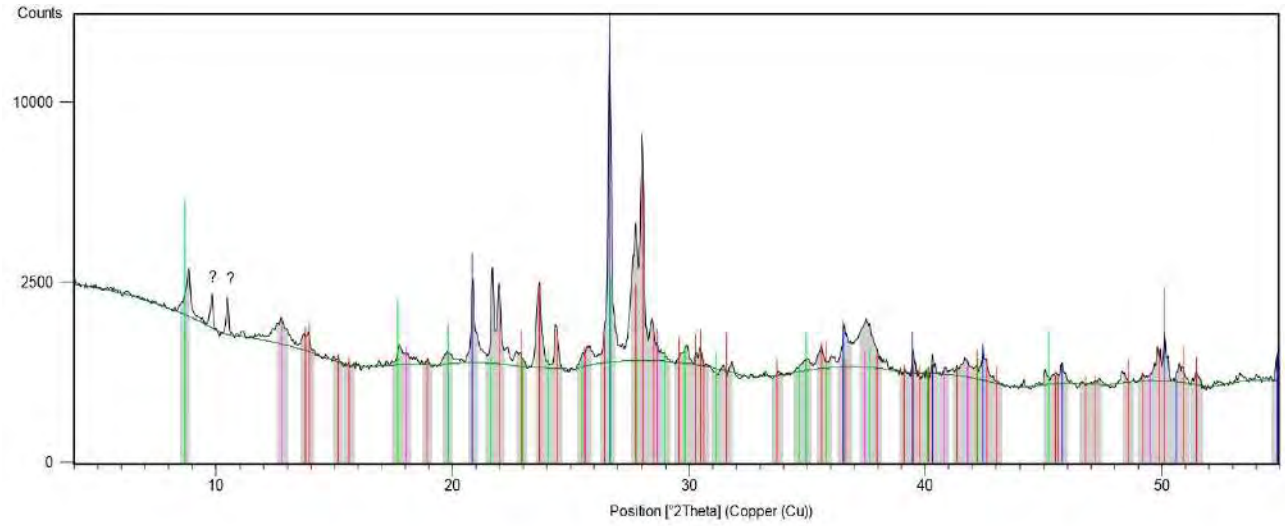
Counts
10000
2500
0
? ?
10
20
30
40
50
Position [°2Theta] (Copper (Cu))

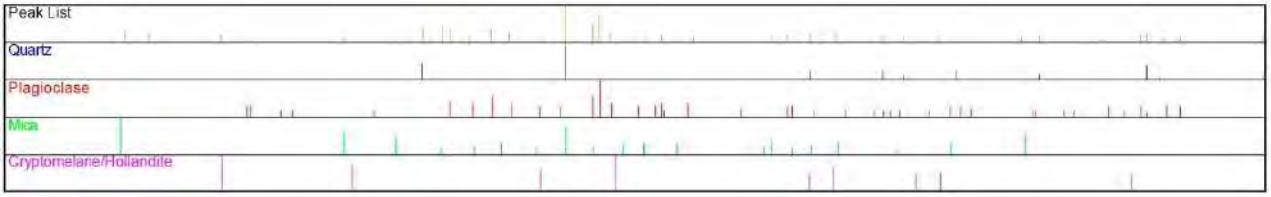
Peak List
Quartz
Plagioclase
Mica
Cryptomelane/Hollandite

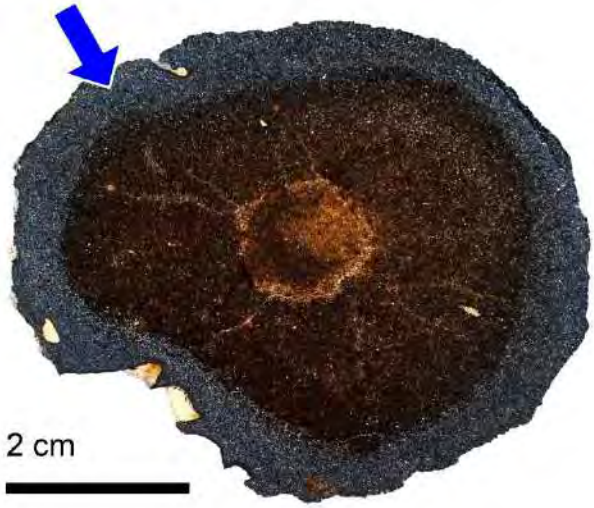
2 cm

2023-PAL-48B

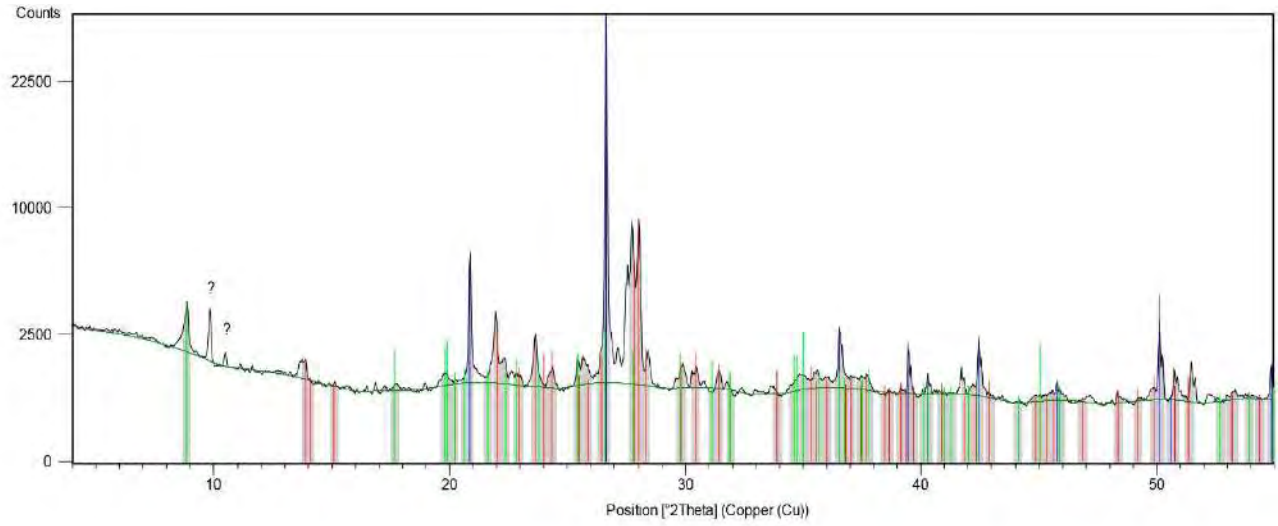
Counts
22500
10000
2500
0
?
?
10
20
30
40
50
Position [°2Theta] (Copper (Cu))

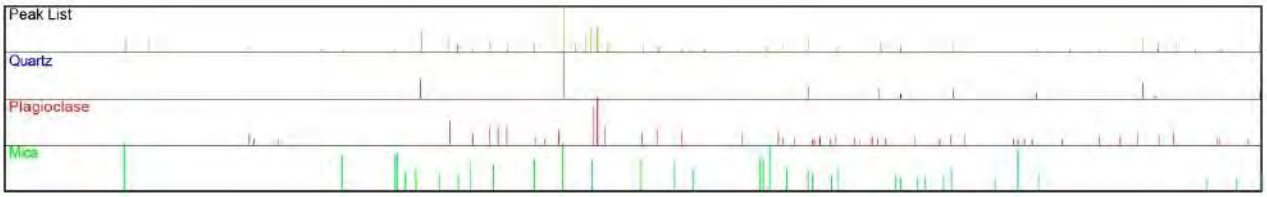
Peak List
Quartz
Plagioclase
Mica

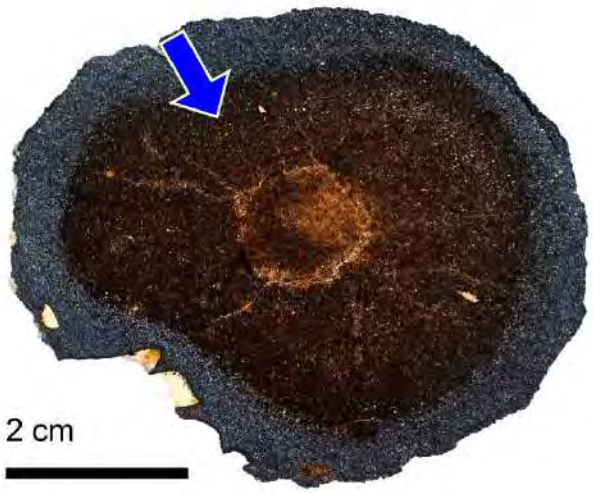
2 cm

Appendix D: EPMA results (wt%)

EPMA Label	SiO_2	Al_2O_3	CaO	K_2O	PbO	SO_3	P_2O_5	MgO	Na_2O	MnO	FeO	CoO	ZnO	CuO	NiO	TiO_2	BaO	Total
2023-PAL-19-Cercle-A-1	<d.l.	<d.l.	0.12	5.27	<d.l.	<d.l.	1.68	0.15	0.41	72.64	<d.l.	0.12	<d.l.	<d.l.	<d.l.	<d.l.	<d.l.	80.38
2023-PAL-19-Cercle-A-2	<d.l.	<d.l.	0.27	5.15	<d.l.	<d.l.	1.52	0.27	0.54	74.31	<d.l.	0.20	<d.l.	<d.l.	<d.l.	<d.l.	<d.l.	82.26
2023-PAL-19-Cercle-A-3	<d.l.	0.47	1.29	3.94	<d.l.	1.54	1.61	0.53	0.62	65.73	<d.l.	0.48	<d.l.	<d.l.	<d.l.	<d.l.	<d.l.	76.20
2023-PAL-19-Cercle-B-1	<d.l.	<d.l.	0.47	5.16	<d.l.	0.56	1.70	0.23	0.54	71.78	<d.l.	<d.l.	<d.l.	<d.l.	<d.l.	<d.l.	<d.l.	80.44
2023-PAL-19-Cercle-B-2	<d.l.	0.66	0.10	4.78	<d.l.	<d.l.	1.96	0.33	0.62	70.41	<d.l.	0.30	<d.l.	<d.l.	<d.l.	<d.l.	0.24	79.39
2023-PAL-19-Cercle-B-3	<d.l.	<d.l.	0.15	5.15	<d.l.	<d.l.	1.46	0.16	0.40	72.65	<d.l.	0.20	<d.l.	<d.l.	<d.l.	<d.l.	<d.l.	80.17
2023-PAL-19-Cercle-C-1	0.73	0.59	1.29	1.80	0.22	<d.l.	1.52	0.70	0.76	62.87	2.09	0.75	<d.l.	<d.l.	<d.l.	<d.l.	0.59	73.90
2023-PAL-19-Cercle-C-2	<d.l.	<d.l.	0.25	2.34	<d.l.	<d.l.	1.03	1.04	1.52	69.31	<d.l.	<d.l.	<d.l.	<d.l.	<d.l.	<d.l.	0.17	75.67
2023-PAL-19-Cercle-C-3	<d.l.	<d.l.	0.29	1.88	<d.l.	<d.l.	0.71	1.22	1.57	69.12	<d.l.	<d.l.	<d.l.	<d.l.	<d.l.	<d.l.	<d.l.	74.79
2023-PAL-40-Cercle-A-1	0.13	0.19	0.22	1.69	<d.l.	<d.l.	0.81	1.84	2.11	68.74	<d.l.	0.44	<d.l.	<d.l.	<d.l.	<d.l.	<d.l.	76.16
2023-PAL-40-Cercle-A-2	1.85	0.88	0.09	4.92	<d.l.	<d.l.	0.58	0.63	0.90	71.14	<d.l.	0.14	<d.l.	<d.l.	<d.l.	<d.l.	0.21	81.34
2023-PAL-40-Cercle-A-6	1.31	0.56	0.09	4.73	<d.l.	<d.l.	0.40	0.43	0.63	72.19	<d.l.	0.15	<d.l.	<d.l.	<d.l.	0.17	0.83	81.49
2023-PAL-40-Cercle-A-7	<d.l.	0.17	0.18	1.65	<d.l.	<d.l.	0.82	1.80	2.11	68.83	<d.l.	0.44	<d.l.	<d.l.	<d.l.	<d.l.	<d.l.	75.99
2023-PAL-40-Cercle-B-2	0.13	0.49	0.11	3.41	<d.l.	<d.l.	0.99	0.62	1.36	71.10	<d.l.	0.48	<d.l.	<d.l.	<d.l.	<d.l.	0.18	78.87
2023-PAL-40-Cercle-B-4	0.14	0.50	0.13	3.38	<d.l.	<d.l.	1.04	0.66	1.31	71.49	<d.l.	0.42	<d.l.	<d.l.	<d.l.	<d.l.	0.52	79.59
2023-PAL-40-Cercle-B-5	0.18	0.52	0.14	3.31	<d.l.	<d.l.	1.08	0.66	1.55	72.14	<d.l.	0.26	<d.l.	<d.l.	<d.l.	<d.l.	0.41	80.25
2023-PAL-40-Cercle-C-1	0.21	0.33	0.23	2.20	<d.l.	<d.l.	0.88	1.49	1.75	68.63	<d.l.	0.25	<d.l.	<d.l.	<d.l.	<d.l.	0.27	76.23
2023-PAL-40-Cercle-C-2	0.49	0.37	0.17	1.96	<d.l.	0.23	0.89	1.92	1.39	64.32	<d.l.	0.39	<d.l.	<d.l.	<d.l.	<d.l.	0.71	72.84
2023-PAL-35-Cercle-A-1	0.16	1.07	0.14	3.80	<d.l.	<d.l.	2.03	0.44	1.83	70.84	<d.l.	0.45	<d.l.	<d.l.	<d.l.	<d.l.	<d.l.	80.77
2023-PAL-35-Cercle-A-2	<d.l.	0.30	<d.l.	2.67	<d.l.	<d.l.	1.33	0.37	1.87	66.00	<d.l.	0.32	<d.l.	<d.l.	<d.l.	<d.l.	<d.l.	72.87
2023-PAL-35-Cercle-A-3	0.14	1.04	0.21	3.20	<d.l.	<d.l.	1.53	0.63	2.27	70.65	<d.l.	0.54	<d.l.	<d.l.	<d.l.	<d.l.	<d.l.	80.20
2023-PAL-35-Cercle-B-1	<d.l.	<d.l.	0.09	5.66	<d.l.	<d.l.	0.81	0.14	0.62	76.78	<d.l.	0.12	<d.l.	<d.l.	<d.l.	<d.l.	<d.l.	84.22
2023-PAL-35-Cercle-B-2	0.18	<d.l.	0.20	1.82	<d.l.	<d.l.	0.80	1.23	2.53	71.29	<d.l.	0.28	<d.l.	0.13	<d.l.	<d.l.	<d.l.	78.45
2023-PAL-35-Cercle-B-3	0.15	<d.l.	<d.l.	5.63	<d.l.	<d.l.	0.50	<d.l.	0.52	77.65	<d.l.	<d.l.	<d.l.	<d.l.	<d.l.	<d.l.	<d.l.	84.45
2023-PAL-35-Cercle-B-4	5.26	1.81	0.14	2.13	<d.l.	0.27	1.10	1.34	1.49	61.84	3.74	0.30	<d.l.	<d.l.	<d.l.	<d.l.	<d.l.	79.42
2023-PAL-35-Cercle-B-5	<d.l.	1.00	0.22	2.09	<d.l.	0.28	1.20	1.04	2.18	68.52	<d.l.	1.21	<d.l.	<d.l.	<d.l.	<d.l.	<d.l.	77.74
2023-PAL-35-Cercle-B-6	0.62	1.07	0.13	3.75	<d.l.	0.23	1.66	0.47	1.60	70.45	<d.l.	0.37	<d.l.	<d.l.	<d.l.	<d.l.	<d.l.	80.37
2023-PAL-35-Cercle-B-7	1.12	1.32	0.13	3.55	<d.l.	<d.l.	1.40	0.81	1.61	69.62	<d.l.	0.44	<d.l.	<d.l.	0.09	<d.l.	<d.l.	80.09

EPMA Label	SiO_2	Al_2O_3	CaO	K_2O	PbO	SO_3	P_2O_5	MgO	Na_2O	MnO	FeO	CoO	ZnO	CuO	NiO	TiO_2	BaO	Total
2023-PAL-35-Cercle-C-1	0.16	<d.l.	0.09	5.75	<d.l.	<d.l.	0.68	<d.l.	0.59	76.87	<d.l.	0.18	<d.l.	<d.l.	<d.l.	<d.l.	<d.l.	84.31
2023-PAL-35-Cercle-C-2	0.26	0.09	0.20	1.66	<d.l.	<d.l.	0.94	1.43	2.57	71.05	<d.l.	0.30	<d.l.	<d.l.	<d.l.	<d.l.	0.38	78.88
2023-PAL-35-Cercle-C-3	<d.l.	<d.l.	<d.l.	5.84	<d.l.	<d.l.	0.70	0.09	0.53	77.27	<d.l.	0.17	<d.l.	<d.l.	<d.l.	<d.l.	<d.l.	84.60
2023-PAL-35-Cercle-C-4	0.56	0.29	<d.l.	4.28	<d.l.	<d.l.	0.35	0.54	0.99	71.48	<d.l.	0.20	<d.l.	<d.l.	<d.l.	0.17	<d.l.	78.86
2023-PAL-35-Cercle-C-5	0.30	0.15	<d.l.	3.52	<d.l.	<d.l.	0.24	0.33	0.51	69.34	<d.l.	0.18	<d.l.	<d.l.	<d.l.	0.16	<d.l.	74.72
2023-PAL-35-Cercle-C-6	0.11	<d.l.	0.17	2.85	<d.l.	0.25	0.73	0.77	1.72	71.82	<d.l.	1.26	<d.l.	<d.l.	<d.l.	<d.l.	<d.l.	79.66
2023-PAL-35-Cercle-C-7	1.82	0.67	<d.l.	4.27	<d.l.	<d.l.	0.35	0.75	0.87	73.36	<d.l.	0.18	<d.l.	<d.l.	<d.l.	0.19	<d.l.	82.45
2023-PAL-34-Cercle-A-2	0.13	0.11	0.12	2.84	<d.l.	<d.l.	0.37	0.78	1.98	73.41	<d.l.	0.10	<d.l.	<d.l.	<d.l.	<d.l.	<d.l.	79.84
2022-PAL-03-Cercle-A-1	<d.l.	<d.l.	<d.l.	5.61	<d.l.	<d.l.	0.57	0.18	0.46	74.21	0.13	<d.l.	<d.l.	<d.l.	<d.l.	<d.l.	<d.l.	81.16
2022-PAL-03-Cercle-A-2	0.97	0.40	0.10	4.47	<d.l.	<d.l.	0.77	0.65	0.69	71.58	0.54	0.16	<d.l.	<d.l.	<d.l.	<d.l.	<d.l.	80.33
2022-PAL-03-Cercle-A-3	0.17	0.13	0.19	2.13	<d.l.	0.26	0.42	1.36	1.83	69.50	0.16	0.11	<d.l.	<d.l.	0.11	<d.l.	<d.l.	76.36
2022-PAL-03-Cercle-A-4	2.93	1.05	0.17	1.62	<d.l.	0.33	1.53	1.40	1.00	55.19	9.60	0.38	<d.l.	<d.l.	<d.l.	<d.l.	<d.l.	75.19
2022-PAL-03-Cercle-A-5	0.14	1.04	0.14	4.38	<d.l.	<d.l.	1.72	0.33	0.99	70.31	0.19	0.29	<d.l.	<d.l.	<d.l.	<d.l.	<d.l.	79.54
2022-PAL-03-Cercle-A-6	0.16	0.12	0.14	4.93	<d.l.	<d.l.	0.82	0.18	0.91	73.41	0.14	0.18	<d.l.	0.13	<d.l.	<d.l.	<d.l.	81.11
2022-PAL-03-Cercle-A-7	11.44	6.10	<d.l.	2.78	<d.l.	<d.l.	0.64	0.79	0.49	58.68	2.61	0.10	<d.l.	<d.l.	<d.l.	<d.l.	0.19	83.81
2022-PAL-03-Cercle-A-10	0.14	<d.l.	<d.l.	5.67	<d.l.	<d.l.	0.61	<d.l.	0.38	74.84	0.19	<d.l.	<d.l.	<d.l.	<d.l.	<d.l.	<d.l.	81.82
2022-PAL-03-Cercle-A-11	4.23	1.26	0.16	2.21	<d.l.	<d.l.	0.81	1.29	1.08	65.63	2.46	0.37	<d.l.	<d.l.	<d.l.	<d.l.	<d.l.	79.51
2022-PAL-03-Cercle-A-12	<d.l.	<d.l.	0.21	2.10	<d.l.	0.23	0.76	1.39	1.60	70.41	0.15	<d.l.	<d.l.	<d.l.	<d.l.	<d.l.	<d.l.	76.84
2022-PAL-03-Cercle-A-13	0.11	<d.l.	0.16	2.57	<d.l.	<d.l.	0.38	1.20	1.66	70.60	0.14	<d.l.	<d.l.	<d.l.	<d.l.	<d.l.	<d.l.	76.83
2022-PAL-03-Cercle-A-14	1.82	0.53	0.15	1.99	<d.l.	0.24	0.83	1.65	1.28	67.33	0.98	0.32	<d.l.	<d.l.	<d.l.	<d.l.	<d.l.	77.13
2022-PAL-03-Cercle-A-15	0.12	<d.l.	<d.l.	5.69	<d.l.	<d.l.	0.68	<d.l.	0.42	74.28	0.16	<d.l.	<d.l.	<d.l.	<d.l.	<d.l.	<d.l.	81.35
2022-PAL-03-Cercle-B-1	0.11	1.04	<d.l.	4.18	0.17	0.27	1.90	0.59	0.87	68.52	0.16	0.32	<d.l.	<d.l.	<d.l.	<d.l.	<d.l.	78.14
2022-PAL-03-Cercle-B-2	<d.l.	<d.l.	0.17	2.26	<d.l.	<d.l.	0.50	1.20	1.76	68.99	0.10	<d.l.	<d.l.	<d.l.	<d.l.	<d.l.	<d.l.	74.98
2022-PAL-03-Cercle-B-3	3.63	1.44	0.09	2.20	<d.l.	0.24	1.09	1.53	1.01	70.04	2.80	0.33	<d.l.	<d.l.	<d.l.	<d.l.	0.22	84.63
2022-PAL-03-Cercle-B-4	0.15	0.19	0.14	2.36	<d.l.	<d.l.	0.49	1.35	1.62	69.61	0.14	<d.l.	<d.l.	<d.l.	<d.l.	<d.l.	<d.l.	76.04
2022-PAL-03-Cercle-B-5	0.13	0.26	0.16	2.55	<d.l.	<d.l.	0.48	1.04	1.67	69.56	0.10	<d.l.	<d.l.	<d.l.	<d.l.	<d.l.	<d.l.	75.95
2022-PAL-03-Cercle-B-6	4.98	3.16	<d.l.	4.36	<d.l.	<d.l.	2.08	0.50	0.63	61.02	5.37	0.10	<d.l.	<d.l.	<d.l.	0.16	<d.l.	82.37
2022-PAL-03-Cercle-B-7	7.13	2.30	0.12	2.90	<d.l.	0.25	0.87	1.09	0.95	60.09	4.66	0.22	<d.l.	<d.l.	<d.l.	<d.l.	<d.l.	80.58
2022-PAL-03-Cercle-B-8	6.97	3.33	0.13	4.24	0.20	<d.l.	1.83	0.62	0.57	56.99	5.62	<d.l.	<d.l.	<d.l.	<d.l.	0.17	<d.l.	80.68
2022-PAL-03-Cercle-B-9	4.48	2.18	0.18	3.39	<d.l.	<d.l.	1.44	1.19	0.88	60.29	5.13	0.17	<d.l.	<d.l.	<d.l.	0.25	<d.l.	79.58

EPMA Label	SiO_2	Al_2O_3	CaO	K_2O	PbO	SO_3	P_2O_5	MgO	Na_2O	MnO	FeO	CoO	ZnO	CuO	NiO	TiO_2	BaO	Total
2022-PAL-03-Cercle-B-10	0.11	<d.l.	0.17	2.16	<d.l.	<d.l.	0.44	1.35	1.90	69.22	0.14	<d.l.	<d.l.	<d.l.	<d.l.	<d.l.	<d.l.	75.49
2022-PAL-03-Cercle-B-11	<d.l.	<d.l.	<d.l.	5.90	<d.l.	<d.l.	0.72	0.08	0.35	79.46	0.19	<d.l.	<d.l.	<d.l.	<d.l.	<d.l.	<d.l.	86.70
2022-PAL-03-Cercle-B-12	13.30	4.04	0.11	3.41	<d.l.	<d.l.	0.88	0.68	0.52	59.46	3.79	<d.l.	<d.l.	<d.l.	<d.l.	<d.l.	<d.l.	86.19
2022-PAL-03-Cercle-B-13	0.17	0.08	0.14	2.74	<d.l.	<d.l.	0.32	1.11	1.70	70.40	0.21	<d.l.	<d.l.	<d.l.	<d.l.	<d.l.	<d.l.	76.86
2022-PAL-03-Cercle-C-2	3.13	1.29	0.14	5.34	<d.l.	<d.l.	0.63	0.35	0.53	70.24	1.28	<d.l.	<d.l.	<d.l.	<d.l.	<d.l.	<d.l.	82.93
2022-PAL-03-Cercle-C-3	6.63	2.44	0.10	2.87	<d.l.	0.38	1.10	1.22	0.76	60.39	3.43	0.23	<d.l.	<d.l.	<d.l.	<d.l.	<d.l.	79.55
2022-PAL-03-Cercle-C-4	0.18	0.24	0.17	2.56	<d.l.	<d.l.	<d.l.	1.20	1.85	71.15	0.14	<d.l.	<d.l.	<d.l.	<d.l.	<d.l.	<d.l.	77.50
2022-PAL-03-Cercle-C-5	0.17	1.60	0.26	4.68	<d.l.	<d.l.	2.21	0.34	0.94	69.73	0.13	0.26	<d.l.	<d.l.	<d.l.	<d.l.	<d.l.	80.32
2022-PAL-03-Cercle-C-8	<d.l.	0.93	0.11	4.17	<d.l.	<d.l.	1.66	0.67	0.87	69.61	0.16	0.33	<d.l.	<d.l.	<d.l.	<d.l.	<d.l.	78.51
2022-PAL-03-Cercle-C-9	1.17	0.55	0.13	2.21	<d.l.	0.25	0.89	1.45	1.34	65.76	3.80	0.33	<d.l.	<d.l.	<d.l.	<d.l.	<d.l.	77.88
2022-PAL-03-Cercle-C-10	0.18	0.10	0.12	2.33	<d.l.	<d.l.	<d.l.	1.27	1.86	71.31	0.18	<d.l.	<d.l.	<d.l.	0.10	<d.l.	<d.l.	77.44
2022-PAL-03-Cercle-C-11	1.77	0.89	0.11	2.54	<d.l.	0.23	0.91	1.46	1.17	65.77	2.80	0.19	<d.l.	<d.l.	<d.l.	<d.l.	<d.l.	77.83
2022-PAL-03-Cercle-D-1	0.11	0.85	0.41	4.70	<d.l.	0.64	1.78	0.55	0.72	68.28	0.12	0.29	<d.l.	<d.l.	<d.l.	<d.l.	<d.l.	78.45
2022-PAL-03-Cercle-D-2	0.16	0.11	0.12	3.65	<d.l.	<d.l.	0.63	0.68	0.82	70.37	0.31	0.16	<d.l.	<d.l.	<d.l.	<d.l.	<d.l.	77.01
2022-PAL-03-Cercle-D-3	1.04	0.46	0.16	1.96	<d.l.	<d.l.	0.63	1.73	1.56	66.42	1.66	0.24	<d.l.	<d.l.	<d.l.	<d.l.	<d.l.	75.85
2022-PAL-03-Cercle-D-6	0.13	0.18	0.12	4.05	<d.l.	<d.l.	0.73	0.50	1.23	72.32	0.13	<d.l.	0.19	<d.l.	<d.l.	<d.l.	<d.l.	79.59
2022-PAL-03-Cercle-D-7	0.16	0.40	0.12	3.86	<d.l.	<d.l.	0.98	0.66	1.23	71.57	0.16	<d.l.	<d.l.	<d.l.	<d.l.	<d.l.	<d.l.	79.14
2022-PAL-03-Cercle-D-8	1.17	1.52	<d.l.	4.39	<d.l.	<d.l.	2.50	0.27	0.71	62.89	5.53	0.17	<d.l.	<d.l.	<d.l.	<d.l.	<d.l.	79.15
2023-PAL-27-Cercle-A-1	8.41	5.46	0.18	3.25	<d.l.	<d.l.	1.20	0.91	1.17	60.95	1.31	0.32	<d.l.	0.16	<d.l.	<d.l.	0.57	83.89
2023-PAL-27-Cercle-A-2	0.25	0.67	0.19	2.27	<d.l.	<d.l.	1.16	0.89	1.54	71.25	0.35	0.48	<d.l.	0.14	<d.l.	<d.l.	0.50	79.70
2023-PAL-27-Cercle-A-3	<d.l.	0.79	0.25	2.33	<d.l.	<d.l.	1.65	0.89	1.87	70.75	0.20	0.34	<d.l.	0.14	<d.l.	<d.l.	0.64	79.85
2023-PAL-27-Cercle-A-4	0.11	0.60	0.19	2.11	<d.l.	<d.l.	1.10	1.01	1.95	70.81	0.25	0.55	<d.l.	<d.l.	<d.l.	<d.l.	0.57	79.23
2023-PAL-27-Cercle-A-5	<d.l.	<d.l.	0.11	5.55	<d.l.	<d.l.	1.25	0.11	0.61	76.44	0.17	<d.l.	<d.l.	0.12	<d.l.	<d.l.	0.22	84.59
2023-PAL-27-Cercle-A-6	1.80	1.25	0.20	3.01	<d.l.	<d.l.	1.18	1.09	1.68	68.52	1.14	0.45	<d.l.	0.15	<d.l.	0.22	0.63	81.33
2023-PAL-27-Cercle-A-7	<d.l.	0.68	0.22	2.21	0.18	<d.l.	1.43	0.99	1.86	69.49	0.32	0.57	<d.l.	0.14	<d.l.	<d.l.	0.72	78.80
2023-PAL-27-Cercle-A-8	<d.l.	0.47	0.18	2.15	<d.l.	<d.l.	1.13	0.93	1.91	70.97	0.18	0.71	<d.l.	<d.l.	<d.l.	<d.l.	0.61	79.24
2023-PAL-27-Cercle-A-9	2.74	0.51	0.20	1.90	<d.l.	<d.l.	1.11	0.98	1.78	69.56	0.21	0.69	<d.l.	0.14	<d.l.	<d.l.	0.64	80.46
2023-PAL-27-Cercle-A-10	<d.l.	0.61	0.18	2.18	<d.l.	0.24	1.34	1.00	1.83	69.73	0.28	0.67	<d.l.	<d.l.	<d.l.	<d.l.	0.84	78.91
2023-PAL-27-Cercle-A-11	0.12	0.18	0.14	4.09	<d.l.	<d.l.	1.11	0.50	1.30	75.19	0.12	0.28	<d.l.	0.15	<d.l.	<d.l.	0.27	83.47
2023-PAL-27-Cercle-A-12	0.12	<d.l.	0.09	5.71	<d.l.	<d.l.	0.57	<d.l.	0.34	78.03	0.13	<d.l.	<d.l.	<d.l.	<d.l.	<d.l.	<d.l.	85.00

EPMA Label	SiO_2	Al_2O_3	CaO	K_2O	PbO	SO_3	P_2O_5	MgO	Na_2O	MnO	FeO	CoO	ZnO	CuO	NiO	TiO_2	BaO	Total
2023-PAL-27-Cercle-A-13	5.21	2.65	0.19	2.81	<d.l.	<d.l.	1.25	0.97	1.64	65.15	1.38	0.31	<d.l.	<d.l.	<d.l.	<d.l.	0.48	82.04
2023-PAL-27-Cercle-A-14	<d.l.	0.74	0.19	2.33	<d.l.	<d.l.	1.57	0.91	1.81	70.50	0.10	0.53	<d.l.	0.13	<d.l.	<d.l.	0.49	79.30
2023-PAL-27-Cercle-A-15	<d.l.	0.86	0.24	2.44	<d.l.	<d.l.	1.51	0.91	1.88	70.41	0.18	0.43	<d.l.	0.17	<d.l.	<d.l.	0.47	79.50
2023-PAL-27-Cercle-B-1	<d.l.	0.72	0.23	1.99	<d.l.	<d.l.	1.58	1.02	2.46	70.14	0.13	0.49	<d.l.	<d.l.	<d.l.	<d.l.	0.23	78.99
2023-PAL-27-Cercle-B-2	0.22	1.34	0.16	3.77	<d.l.	<d.l.	2.02	0.44	1.65	73.81	0.17	0.34	<d.l.	<d.l.	<d.l.	<d.l.	0.35	84.27
2023-PAL-27-Cercle-B-3	6.79	3.50	0.33	3.49	<d.l.	<d.l.	1.28	0.65	1.16	63.91	1.49	0.24	<d.l.	<d.l.	<d.l.	<d.l.	0.79	83.63
2023-PAL-27-Cercle-B-4	3.77	2.38	0.10	3.11	<d.l.	<d.l.	1.49	0.73	1.37	65.84	1.42	0.27	<d.l.	<d.l.	<d.l.	<d.l.	0.66	81.13
2023-PAL-27-Cercle-B-5	<d.l.	0.21	0.21	2.13	<d.l.	0.26	0.89	0.95	1.91	70.47	0.13	0.87	<d.l.	<d.l.	<d.l.	<d.l.	1.09	79.12
2023-PAL-27-Cercle-B-6	<d.l.	0.26	0.24	1.92	<d.l.	0.26	0.81	0.97	2.10	70.35	0.12	0.91	<d.l.	0.12	<d.l.	<d.l.	0.91	78.97
2023-PAL-27-Cercle-B-7	<d.l.	0.55	0.15	4.31	<d.l.	<d.l.	1.71	0.41	1.33	73.44	0.13	0.23	<d.l.	<d.l.	<d.l.	<d.l.	0.33	82.58
2023-PAL-27-Cercle-B-8	<d.l.	0.36	0.22	2.13	<d.l.	<d.l.	0.89	0.98	2.11	70.70	0.12	0.83	<d.l.	<d.l.	<d.l.	<d.l.	1.06	79.39
2023-PAL-27-Cercle-B-9	0.40	0.89	0.17	4.15	<d.l.	<d.l.	1.65	0.36	1.23	73.19	0.19	0.21	<d.l.	0.14	<d.l.	<d.l.	0.51	83.09
2023-PAL-27-Cercle-B-10	11.33	2.88	0.22	2.85	<d.l.	<d.l.	1.01	0.61	2.54	61.84	0.76	0.44	<d.l.	<d.l.	<d.l.	<d.l.	0.98	85.45
2023-PAL-27-Cercle-B-12	0.56	0.60	0.17	2.32	<d.l.	<d.l.	0.97	0.82	1.55	71.04	0.56	0.73	<d.l.	<d.l.	<d.l.	<d.l.	0.94	80.27
2023-PAL-27-Cercle-C-1	<d.l.	0.76	0.19	2.13	<d.l.	0.25	1.54	1.04	2.26	70.29	0.37	0.48	<d.l.	<d.l.	<d.l.	<d.l.	0.31	79.63
2023-PAL-27-Cercle-C-2	<d.l.	0.80	0.27	2.36	<d.l.	0.26	1.72	0.91	2.14	69.21	0.19	0.36	<d.l.	<d.l.	<d.l.	<d.l.	0.45	78.68
2023-PAL-27-Cercle-C-3	<d.l.	0.61	0.19	2.11	<d.l.	<d.l.	1.36	1.04	2.28	71.27	0.09	0.61	0.21	0.16	<d.l.	<d.l.	0.46	80.39
2023-PAL-27-Cercle-C-4	8.67	3.71	0.27	3.43	<d.l.	<d.l.	1.81	0.81	0.98	60.79	3.23	0.16	<d.l.	<d.l.	<d.l.	<d.l.	0.49	84.34
2023-PAL-27-Cercle-C-5	2.66	1.91	0.12	4.01	<d.l.	<d.l.	1.44	1.02	1.44	68.06	1.78	0.32	<d.l.	<d.l.	<d.l.	0.51	0.43	83.70
2023-PAL-27-Cercle-C-6	<d.l.	1.15	0.17	3.27	<d.l.	<d.l.	1.90	0.62	1.56	71.26	0.27	0.49	<d.l.	<d.l.	<d.l.	<d.l.	0.33	81.01
2023-PAL-27-Cercle-C-7	6.20	3.30	0.10	4.30	<d.l.	<d.l.	1.67	0.71	0.71	62.23	0.92	0.09	<d.l.	<d.l.	<d.l.	<d.l.	<d.l.	80.23
2023-PAL-27-Cercle-C-8	<d.l.	0.84	0.21	2.43	<d.l.	<d.l.	1.71	0.98	2.14	71.76	1.37	0.46	<d.l.	<d.l.	<d.l.	<d.l.	0.53	82.43
2023-PAL-27-Cercle-C-9	<d.l.	1.10	0.30	3.03	<d.l.	0.25	1.78	0.88	2.09	73.37	0.16	0.81	<d.l.	<d.l.	<d.l.	<d.l.	0.30	84.07
2023-PAL-27-Cercle-D-1	<d.l.	<d.l.	0.24	1.83	<d.l.	0.24	0.61	1.12	2.05	70.96	0.13	0.27	<d.l.	<d.l.	<d.l.	<d.l.	0.27	77.72
2023-PAL-27-Cercle-D-2	<d.l.	0.45	0.21	2.02	<d.l.	<d.l.	1.21	1.05	1.85	69.95	0.12	0.74	<d.l.	0.14	<d.l.	<d.l.	0.82	78.56
2023-PAL-27-Cercle-D-3	0.11	0.42	0.23	1.97	<d.l.	<d.l.	1.20	1.06	2.04	70.34	0.17	0.77	<d.l.	<d.l.	<d.l.	<d.l.	0.82	79.13
2023-PAL-27-Cercle-D-4	<d.l.	0.29	0.28	1.86	<d.l.	<d.l.	0.84	0.97	2.03	70.46	0.11	0.84	<d.l.	<d.l.	<d.l.	<d.l.	0.86	78.53
2023-PAL-27-Cercle-D-5	0.37	0.69	0.15	3.87	<d.l.	<d.l.	1.38	0.37	1.49	73.51	0.17	0.34	<d.l.	<d.l.	<d.l.	<d.l.	0.54	82.88
2023-PAL-27-Cercle-D-6	7.98	3.27	0.23	3.49	<d.l.	<d.l.	1.06	0.88	0.80	63.22	2.29	0.15	<d.l.	<d.l.	<d.l.	<d.l.	1.17	84.54
2023-PAL-27-Cercle-D-7	17.67	1.85	0.15	2.26	<d.l.	<d.l.	0.68	0.81	1.29	56.41	1.09	0.32	<d.l.	<d.l.	<d.l.	<d.l.	0.96	83.49

EPMA Label	SiO_2	Al_2O_3	CaO	K_2O	PbO	SO_3	P_2O_5	MgO	Na_2O	MnO	FeO	CoO	ZnO	CuO	NiO	TiO_2	BaO	Total
2023-PAL-27-Cercle-D-8	<d.l.	0.62	0.13	4.79	<d.l.	<d.l.	1.61	0.22	0.94	74.30	0.16	0.16	<d.l.	<d.l.	<d.l.	<d.l.	0.23	83.16
2023-PAL-27-Cercle-D-9	<d.l.	0.10	0.21	2.36	<d.l.	<d.l.	0.75	0.85	1.79	72.58	0.12	0.81	<d.l.	0.14	<d.l.	<d.l.	0.72	80.41
2023-PAL-27-Cercle-D-10	<d.l.	0.18	0.26	2.01	<d.l.	<d.l.	0.66	0.96	1.92	71.07	0.12	0.86	<d.l.	<d.l.	<d.l.	<d.l.	0.81	78.86
2023-PAL-27-Cercle-D-11	<d.l.	0.29	0.21	2.23	<d.l.	<d.l.	0.84	0.81	1.93	71.46	0.10	0.90	<d.l.	<d.l.	<d.l.	<d.l.	1.10	79.87
2023-PAL-27-Cercle-D-12	0.27	0.31	0.24	2.06	0.25	<d.l.	0.88	0.98	1.88	70.56	0.33	0.82	<d.l.	<d.l.	<d.l.	<d.l.	1.02	79.60
2023-PAL-09-Cercle-A-1	<d.l.	<d.l.	1.29	0.90	<d.l.	<d.l.	<d.l.	4.33	1.49	65.47	0.20	0.15	0.18	<d.l.	0.18	<d.l.	0.46	74.65
2023-PAL-09-Cercle-A-2	11.43	3.23	1.49	0.82	<d.l.	<d.l.	<d.l.	3.97	0.91	51.72	1.88	0.94	<d.l.	<d.l.	0.16	0.41	1.29	78.25
2023-PAL-09-Cercle-A-3	<d.l.	<d.l.	1.26	0.89	<d.l.	<d.l.	<d.l.	4.54	1.46	65.47	0.14	0.10	0.25	<d.l.	0.18	<d.l.	0.56	74.85
2023-PAL-09-Cercle-A-5	0.35	0.08	1.18	0.82	<d.l.	<d.l.	<d.l.	5.01	1.27	64.46	0.17	<d.l.	<d.l.	<d.l.	<d.l.	<d.l.	0.44	73.77
2023-PAL-09-Cercle-B-1	7.11	2.04	1.57	1.07	<d.l.	<d.l.	0.27	3.86	1.19	58.26	0.85	<d.l.	<d.l.	<d.l.	<d.l.	<d.l.	0.78	77.00
2023-PAL-09-Cercle-C-1	19.61	3.38	1.45	0.81	<d.l.	<d.l.	<d.l.	3.48	0.78	45.77	1.82	<d.l.	<d.l.	<d.l.	0.12	<d.l.	0.76	77.99
2023-PAL-09-Cercle-C-3	1.52	0.48	1.49	0.87	<d.l.	<d.l.	<d.l.	4.18	1.33	62.73	0.42	<d.l.	0.17	<d.l.	0.14	<d.l.	0.44	73.78
2023-PAL-09-Cercle-C-4	10.98	3.32	1.53	1.00	<d.l.	<d.l.	0.23	3.72	1.09	54.40	1.12	0.17	0.24	<d.l.	<d.l.	0.17	0.99	78.97
2023-PAL-09-Cercle-D-1	0.30	0.07	1.70	0.86	<d.l.	<d.l.	<d.l.	4.40	1.47	63.13	0.21	0.26	<d.l.	<d.l.	0.21	<d.l.	0.34	72.96
2023-PAL-09-Cercle-D-2	11.59	3.90	1.24	0.99	<d.l.	<d.l.	<d.l.	4.83	0.98	52.48	1.54	2.64	0.22	<d.l.	0.17	0.14	1.37	82.10
2023-PAL-48A-Cercle-B-3	0.32	1.41	0.44	2.19	<d.l.	<d.l.	0.41	1.71	1.85	66.46	1.73	0.24	<d.l.	<d.l.	0.11	<d.l.	0.58	77.46
2023-PAL-48A-Cercle-C-3	0.28	3.94	0.43	2.47	<d.l.	<d.l.	0.37	1.54	1.49	65.85	1.57	0.25	0.23	<d.l.	0.21	<d.l.	0.57	79.20
2023-PAL-48A-Cercle-C-4	0.35	3.68	0.44	2.55	<d.l.	<d.l.	0.43	1.42	1.93	65.33	1.82	0.26	<d.l.	<d.l.	0.20	<d.l.	0.62	79.03
2023-PAL-48A-Cercle-D-5	0.32	8.50	0.44	1.77	<d.l.	<d.l.	0.28	1.74	1.40	61.06	1.71	0.36	0.39	<d.l.	0.51	<d.l.	0.39	78.87
2023-PAL-48A-Cercle-E-2	0.26	4.97	0.33	2.46	<d.l.	<d.l.	0.30	1.35	1.50	65.97	0.38	0.36	0.27	<d.l.	0.16	<d.l.	0.63	78.95
2023-PAL-48A-Cercle-E-4	5.33	8.35	0.43	1.60	<d.l.	<d.l.	0.39	1.51	0.94	53.14	7.47	0.31	0.23	<d.l.	0.68	0.20	0.58	81.16
2023-PAL-48A-Cercle-E-6	0.31	1.54	0.29	4.55	<d.l.	<d.l.	0.78	0.50	1.27	71.60	0.31	0.16	0.22	<d.l.	0.09	<d.l.	0.37	81.99
2023-PAL-48A-Cercle-E-8	0.50	0.49	0.63	1.65	<d.l.	<d.l.	0.48	1.98	2.30	63.93	3.86	0.30	<d.l.	<d.l.	<d.l.	0.57	0.68	77.37
2023-PAL-48A-Cercle-E-9	0.87	0.98	0.32	2.96	<d.l.	<d.l.	0.33	1.19	1.95	68.83	1.77	0.22	<d.l.	<d.l.	<d.l.	0.20	0.64	80.26
2023-PAL-29-Cercle-A-1	2.48	1.17	0.13	3.10	<d.l.	0.29	0.81	1.36	1.64	65.43	1.27	0.59	<d.l.	<d.l.	<d.l.	0.36	<d.l.	78.62
2023-PAL-29-Cercle-A-2	<d.l.	0.25	0.20	2.42	<d.l.	<d.l.	0.75	0.82	2.33	70.71	<d.l.	0.62	<d.l.	<d.l.	<d.l.	<d.l.	<d.l.	78.10
2023-PAL-29-Cercle-A-3	<d.l.	0.12	0.20	3.66	<d.l.	0.25	1.03	0.52	1.37	72.19	0.11	0.38	<d.l.	<d.l.	<d.l.	<d.l.	<d.l.	79.83
2023-PAL-29-Cercle-A-4	<d.l.	0.25	0.23	2.44	<d.l.	0.37	0.67	0.97	2.19	70.06	0.14	0.63	<d.l.	<d.l.	<d.l.	<d.l.	<d.l.	77.95
2023-PAL-29-Cercle-A-5	<d.l.	0.07	0.19	2.81	<d.l.	0.24	0.50	0.73	2.18	71.01	0.13	0.47	<d.l.	<d.l.	<d.l.	<d.l.	<d.l.	78.33
2023-PAL-29-Cercle-A-6	<d.l.	0.28	0.25	2.40	<d.l.	0.23	0.73	0.84	2.21	70.18	0.10	0.69	<d.l.	<d.l.	<d.l.	<d.l.	<d.l.	77.91

EPMA Label	SiO_2	Al_2O_3	CaO	K_2O	PbO	SO_3	P_2O_5	MgO	Na_2O	MnO	FeO	CoO	ZnO	CuO	NiO	TiO_2	BaO	Total
2023-PAL-29-Cercle-A-8	0.50	0.51	0.30	2.37	<d.l.	0.26	0.72	0.70	2.14	69.67	0.56	0.70	<d.l.	<d.l.	<d.l.	<d.l.	<d.l.	78.43
2023-PAL-29-Cercle-A-9	<d.l.	0.29	0.18	2.56	<d.l.	0.44	0.80	0.94	2.06	69.88	0.10	0.64	<d.l.	<d.l.	<d.l.	<d.l.	<d.l.	77.89
2023-PAL-29-Cercle-B-1	0.11	0.28	0.12	3.20	<d.l.	0.40	0.96	0.75	1.65	69.93	0.10	0.45	<d.l.	<d.l.	<d.l.	<d.l.	<d.l.	77.94
2023-PAL-29-Cercle-B-2	<d.l.	0.14	0.13	2.97	<d.l.	0.30	0.74	0.80	1.74	70.13	<d.l.	0.40	<d.l.	<d.l.	<d.l.	<d.l.	<d.l.	77.34
2023-PAL-29-Cercle-B-3	0.86	0.63	0.11	2.75	<d.l.	0.27	0.85	1.05	1.96	67.98	0.56	0.59	<d.l.	<d.l.	<d.l.	<d.l.	<d.l.	77.63
2023-PAL-29-Cercle-B-4	<d.l.	0.29	0.11	2.44	<d.l.	0.38	0.71	0.99	2.41	69.57	0.30	0.69	<d.l.	<d.l.	<d.l.	<d.l.	<d.l.	77.89
2023-PAL-29-Cercle-B-5	<d.l.	0.28	0.10	2.49	<d.l.	0.37	0.80	1.08	2.03	69.15	0.14	0.63	<d.l.	<d.l.	<d.l.	<d.l.	<d.l.	77.08
2023-PAL-29-Cercle-B-6	<d.l.	0.11	0.09	6.07	<d.l.	<d.l.	0.50	<d.l.	0.43	75.14	0.14	<d.l.	<d.l.	<d.l.	<d.l.	<d.l.	<d.l.	82.49
2023-PAL-29-Cercle-B-7	7.70	2.55	0.39	4.76	<d.l.	<d.l.	1.01	0.24	1.58	63.14	0.78	0.10	<d.l.	<d.l.	<d.l.	<d.l.	<d.l.	82.26
2023-PAL-29-Cercle-B-8	0.14	0.26	<d.l.	5.41	<d.l.	<d.l.	0.73	0.16	0.92	73.96	0.14	<d.l.	<d.l.	<d.l.	<d.l.	<d.l.	<d.l.	81.73
2023-PAL-29-Cercle-C-1	0.14	0.08	<d.l.	5.58	<d.l.	<d.l.	0.49	<d.l.	0.60	73.71	0.11	0.11	<d.l.	<d.l.	<d.l.	<d.l.	<d.l.	80.82
2023-PAL-29-Cercle-C-2	<d.l.	0.14	<d.l.	5.87	<d.l.	<d.l.	0.35	<d.l.	0.23	74.59	0.14	<d.l.	<d.l.	<d.l.	<d.l.	<d.l.	<d.l.	81.32
2023-PAL-29-Cercle-C-4	0.13	0.20	0.16	2.65	<d.l.	0.38	0.76	1.19	2.42	73.65	0.13	0.91	<d.l.	<d.l.	<d.l.	<d.l.	<d.l.	82.56
2023-PAL-29-Cercle-C-5	<d.l.	0.25	0.17	2.47	<d.l.	0.40	0.69	1.09	2.08	74.93	0.15	0.81	<d.l.	<d.l.	<d.l.	<d.l.	<d.l.	83.04
2023-PAL-29-Cercle-C-6	1.54	0.77	0.21	2.68	<d.l.	0.37	0.81	0.96	2.22	72.61	0.66	0.73	<d.l.	<d.l.	<d.l.	<d.l.	<d.l.	83.54
2023-PAL-29-Cercle-C-7	<d.l.	0.25	0.15	2.27	<d.l.	0.40	0.70	1.08	1.94	67.83	0.13	0.69	<d.l.	<d.l.	<d.l.	<d.l.	<d.l.	75.43
2023-PAL-29-Cercle-C-8	<d.l.	0.23	0.17	2.38	<d.l.	0.33	0.79	1.02	1.88	68.04	0.13	0.68	<d.l.	<d.l.	<d.l.	<d.l.	<d.l.	75.65
2023-PAL-29-Cercle-C-10	<d.l.	0.10	0.19	2.81	<d.l.	0.36	0.88	1.10	1.92	75.37	<d.l.	0.44	<d.l.	<d.l.	<d.l.	<d.l.	<d.l.	83.18
2023-PAL-29-Cercle-C-11	<d.l.	0.15	0.34	2.74	<d.l.	0.28	0.72	1.22	1.74	75.69	0.17	0.77	<d.l.	<d.l.	<d.l.	<d.l.	<d.l.	83.82
2023-PAL-29-Cercle-D-1	<d.l.	<d.l.	<d.l.	1.11	<d.l.	<d.l.	0.35	0.54	2.20	63.47	0.15	0.83	<d.l.	<d.l.	<d.l.	<d.l.	<d.l.	68.65
2023-PAL-29-Cercle-D-2	1.12	0.59	0.10	1.59	<d.l.	<d.l.	0.42	0.64	1.65	57.04	1.98	0.78	<d.l.	<d.l.	<d.l.	0.51	<d.l.	66.43
2023-PAL-29-Cercle-D-4	2.60	1.20	<d.l.	5.16	<d.l.	<d.l.	0.73	0.70	0.53	67.28	1.41	0.47	<d.l.	<d.l.	<d.l.	0.28	<d.l.	80.36
2023-PAL-29-Cercle-D-5	0.11	0.16	0.18	2.58	<d.l.	0.33	0.53	0.91	2.40	70.46	0.14	0.68	<d.l.	<d.l.	<d.l.	<d.l.	<d.l.	78.48
2023-PAL-29-Cercle-D-5B	0.12	0.17	0.22	2.66	<d.l.	0.46	0.62	1.10	2.19	75.82	0.12	0.78	<d.l.	<d.l.	<d.l.	<d.l.	<d.l.	84.26
2023-PAL-29-Cercle-D-6	0.37	0.35	<d.l.	6.16	<d.l.	<d.l.	0.55	0.13	0.40	78.23	0.35	0.47	<d.l.	<d.l.	<d.l.	<d.l.	<d.l.	87.00
2023-PAL-29-Cercle-D-7	<d.l.	0.09	0.15	2.93	<d.l.	0.38	0.53	1.00	2.07	74.54	0.16	1.16	<d.l.	<d.l.	<d.l.	<d.l.	<d.l.	83.00
2023-PAL-29-Cercle-E-1	<d.l.	0.22	0.14	2.53	<d.l.	0.28	0.92	0.93	2.11	68.73	0.11	0.64	<d.l.	<d.l.	<d.l.	<d.l.	<d.l.	76.62
2023-PAL-29-Cercle-E-2	<d.l.	<d.l.	0.12	2.62	<d.l.	0.32	0.68	0.97	1.95	69.41	0.11	0.35	<d.l.	<d.l.	<d.l.	<d.l.	<d.l.	76.53
2023-PAL-29-Cercle-E-3	<d.l.	<d.l.	0.14	2.53	<d.l.	0.26	0.77	1.17	2.21	76.32	0.16	0.48	<d.l.	<d.l.	<d.l.	<d.l.	<d.l.	84.03
2023-PAL-29-Cercle-E-4	<d.l.	0.26	0.16	2.15	<d.l.	0.48	0.62	0.87	2.31	67.94	0.23	0.78	<d.l.	<d.l.	<d.l.	<d.l.	<d.l.	75.81

EPMA Label	SiO_2	Al_2O_3	CaO	K_2O	PbO	SO_3	P_2O_5	MgO	Na_2O	MnO	FeO	CoO	ZnO	CuO	NiO	TiO_2	BaO	Total
2023-PAL-29-Cercle-E-5	0.12	0.23	0.24	2.26	<d.l.	0.37	0.54	1.06	2.49	74.91	0.13	0.87	<d.l.	<d.l.	<d.l.	<d.l.	<d.l.	83.21
2023-PAL-43-Cercle-A-1	0.12	0.57	0.10	6.19	<d.l.	<d.l.	1.39	0.15	0.75	74.21	0.13	0.32	<d.l.	<d.l.	<d.l.	<d.l.	<d.l.	83.93
2023-PAL-43-Cercle-A-2	0.15	0.38	0.10	6.09	<d.l.	<d.l.	1.27	0.18	0.77	74.75	0.14	0.33	<d.l.	<d.l.	<d.l.	<d.l.	<d.l.	84.16
2023-PAL-43-Cercle-A-3	11.55	2.69	0.22	4.70	<d.l.	<d.l.	0.97	0.59	1.08	65.69	0.54	0.57	<d.l.	<d.l.	<d.l.	<d.l.	<d.l.	88.60
2023-PAL-43-Cercle-A-4	0.14	0.19	0.26	2.40	<d.l.	0.27	0.69	1.73	1.87	70.72	0.13	1.14	<d.l.	<d.l.	<d.l.	<d.l.	<d.l.	79.54
2023-PAL-43-Cercle-A-5	<d.l.	0.20	0.33	2.41	<d.l.	0.23	0.70	1.43	2.16	69.86	0.13	1.10	<d.l.	<d.l.	<d.l.	<d.l.	0.28	78.83
2023-PAL-43-Cercle-A-6	0.11	0.18	0.36	2.47	<d.l.	0.30	0.64	1.42	2.12	70.13	0.16	1.14	<d.l.	<d.l.	<d.l.	<d.l.	<d.l.	79.04
2023-PAL-43-Cercle-A-7	0.13	0.19	0.24	2.38	<d.l.	0.36	0.75	1.39	2.30	69.84	0.12	1.22	<d.l.	<d.l.	<d.l.	<d.l.	<d.l.	78.93
2023-PAL-43-Cercle-A-8	0.79	0.20	0.22	2.26	<d.l.	0.34	0.68	1.77	1.72	69.84	0.23	1.23	<d.l.	<d.l.	<d.l.	<d.l.	<d.l.	79.28
2023-PAL-43-Cercle-A-9	<d.l.	0.17	0.29	2.34	<d.l.	0.30	0.69	1.64	2.11	69.24	0.11	1.34	<d.l.	<d.l.	<d.l.	<d.l.	<d.l.	78.24
2023-PAL-43-Cercle-A-10	0.15	0.15	0.29	2.28	<d.l.	0.40	0.65	1.61	2.13	69.58	0.15	1.38	<d.l.	0.13	<d.l.	<d.l.	0.17	79.08
2023-PAL-43-Cercle-A-11	<d.l.	0.15	0.27	2.38	<d.l.	0.29	0.72	1.38	1.99	69.27	0.17	1.26	<d.l.	<d.l.	<d.l.	<d.l.	<d.l.	77.89
2023-PAL-43-Cercle-A-12	11.14	4.34	0.11	6.31	<d.l.	<d.l.	1.09	0.48	0.92	65.86	0.42	0.45	<d.l.	<d.l.	<d.l.	<d.l.	<d.l.	91.12
2023-PAL-43-Cercle-B-1	<d.l.	0.17	0.30	2.66	<d.l.	0.35	0.68	1.16	2.46	69.44	0.11	1.10	<d.l.	<d.l.	<d.l.	<d.l.	<d.l.	78.44
2023-PAL-43-Cercle-B-2	<d.l.	0.16	0.28	2.42	<d.l.	0.34	0.76	1.21	2.42	69.08	0.22	1.28	<d.l.	<d.l.	<d.l.	<d.l.	<d.l.	78.18
2023-PAL-43-Cercle-B-3	<d.l.	0.17	0.24	2.41	<d.l.	0.37	0.77	1.29	2.52	69.68	0.10	1.26	<d.l.	<d.l.	<d.l.	<d.l.	<d.l.	78.81
2023-PAL-43-Cercle-B-4	<d.l.	0.16	0.28	2.47	<d.l.	0.43	0.70	1.26	2.38	69.07	0.12	1.35	<d.l.	<d.l.	<d.l.	<d.l.	<d.l.	78.21
2023-PAL-43-Cercle-C-1	0.11	0.33	0.14	6.12	<d.l.	<d.l.	1.33	0.13	0.79	73.76	<d.l.	0.70	<d.l.	<d.l.	<d.l.	<d.l.	<d.l.	83.41
2023-PAL-43-Cercle-C-2	0.20	0.66	0.11	5.75	<d.l.	<d.l.	1.43	0.29	0.91	72.88	0.38	0.57	<d.l.	<d.l.	<d.l.	<d.l.	0.21	83.39
2023-PAL-43-Cercle-C-3	<d.l.	0.08	<d.l.	6.36	<d.l.	<d.l.	0.83	0.11	0.47	76.54	0.12	0.18	<d.l.	<d.l.	<d.l.	<d.l.	<d.l.	84.69
2023-PAL-43-Cercle-C-4	0.13	0.16	0.26	2.80	<d.l.	0.29	0.75	1.37	1.89	69.77	0.10	0.84	<d.l.	<d.l.	<d.l.	<d.l.	0.46	78.80
2023-PAL-43-Cercle-C-6	0.14	<d.l.	0.09	5.69	<d.l.	<d.l.	0.45	0.12	0.73	76.65	0.13	0.13	<d.l.	<d.l.	<d.l.	<d.l.	<d.l.	84.13
2023-PAL-43-Cercle-C-7	0.54	<d.l.	0.12	5.56	<d.l.	<d.l.	0.43	0.13	0.91	76.04	0.16	0.16	<d.l.	<d.l.	<d.l.	<d.l.	0.18	84.25
2023-PAL-43-Cercle-C-9	<d.l.	0.42	0.13	6.03	<d.l.	<d.l.	1.26	0.15	0.68	74.30	0.14	0.35	<d.l.	<d.l.	<d.l.	<d.l.	<d.l.	83.45
2023-PAL-38-Cercle-A-1	2.61	0.93	0.13	5.13	<d.l.	<d.l.	0.61	0.30	0.72	70.61	1.70	0.93	<d.l.	<d.l.	<d.l.	<d.l.	0.24	83.92
2023-PAL-38-Cercle-A-2	0.23	0.23	<d.l.	5.35	<d.l.	<d.l.	0.45	<d.l.	0.81	75.22	0.17	0.11	<d.l.	<d.l.	<d.l.	<d.l.	<d.l.	82.57
2023-PAL-38-Cercle-A-3	15.18	7.62	0.35	2.20	<d.l.	<d.l.	0.84	0.78	0.77	48.95	5.27	0.81	<d.l.	<d.l.	<d.l.	<d.l.	0.56	83.33
2023-PAL-38-Cercle-A-4	1.02	0.34	0.17	4.63	<d.l.	<d.l.	0.58	0.50	0.92	71.68	0.56	1.17	0.17	<d.l.	<d.l.	<d.l.	<d.l.	81.74
2023-PAL-38-Cercle-A-5	11.90	2.69	0.19	3.05	<d.l.	<d.l.	0.80	1.00	1.26	54.55	6.59	1.15	<d.l.	<d.l.	0.11	<d.l.	0.57	83.84
2023-PAL-38-Cercle-A-6	0.13	<d.l.	0.09	5.06	<d.l.	<d.l.	0.43	0.17	0.76	73.46	0.23	0.96	<d.l.	<d.l.	<d.l.	<d.l.	<d.l.	81.29

EPMA Label	SiO_2	Al_2O_3	CaO	K_2O	PbO	SO_3	P_2O_5	MgO	Na_2O	MnO	FeO	CoO	ZnO	CuO	NiO	TiO_2	BaO	Total
2023-PAL-38-Cercle-A-7	0.12	<d.l.	<d.l.	6.07	<d.l.	<d.l.	0.56	<d.l.	0.36	75.24	0.16	0.74	<d.l.	<d.l.	<d.l.	<d.l.	<d.l.	83.24
2023-PAL-38-Cercle-A-8	0.12	0.17	0.18	2.78	<d.l.	<d.l.	0.53	0.86	1.88	70.45	0.14	1.45	<d.l.	<d.l.	<d.l.	<d.l.	0.33	78.89
2023-PAL-38-Cercle-A-9	0.20	0.17	0.15	3.62	<d.l.	<d.l.	0.80	0.46	1.94	72.80	0.22	0.17	<d.l.	<d.l.	<d.l.	<d.l.	<d.l.	80.54
2023-PAL-38-Cercle-A-10	<d.l.	0.09	0.19	2.49	<d.l.	0.31	0.51	0.88	1.95	70.07	0.14	1.43	<d.l.	<d.l.	<d.l.	<d.l.	0.25	78.31
2023-PAL-38-Cercle-A-12	2.61	1.00	0.37	1.91	<d.l.	<d.l.	1.74	0.84	1.27	54.33	13.19	0.51	<d.l.	<d.l.	<d.l.	2.30	0.69	80.75
2023-PAL-38-Cercle-A-13	10.13	1.92	0.21	2.55	<d.l.	<d.l.	1.03	0.84	1.04	57.67	7.58	0.92	<d.l.	<d.l.	<d.l.	<d.l.	0.67	84.55
2023-PAL-38-Cercle-A-14	0.11	<d.l.	0.10	4.89	<d.l.	<d.l.	0.53	0.27	0.86	74.17	0.17	0.98	0.17	<d.l.	<d.l.	<d.l.	0.20	82.46
2023-PAL-38-Cercle-B-1	0.16	0.11	<d.l.	5.47	<d.l.	<d.l.	0.38	<d.l.	0.57	76.57	0.15	0.09	<d.l.	<d.l.	<d.l.	<d.l.	<d.l.	83.49
2023-PAL-38-Cercle-B-2	<d.l.	<d.l.	0.11	5.83	<d.l.	<d.l.	0.65	0.09	0.44	75.11	0.27	0.65	<d.l.	<d.l.	<d.l.	<d.l.	<d.l.	83.15
2023-PAL-38-Cercle-B-3	11.85	2.08	0.12	2.62	<d.l.	<d.l.	0.93	1.05	0.92	52.72	7.89	0.68	<d.l.	<d.l.	<d.l.	<d.l.	0.52	81.38
2023-PAL-38-Cercle-B-4	0.13	0.07	0.16	2.50	<d.l.	0.23	0.50	0.82	1.54	65.92	0.25	1.34	<d.l.	<d.l.	<d.l.	<d.l.	0.28	73.73
2023-PAL-38-Cercle-B-5	<d.l.	0.11	0.20	2.21	<d.l.	0.27	0.67	0.87	1.82	70.36	0.16	1.43	<d.l.	<d.l.	<d.l.	<d.l.	0.23	78.34
2023-PAL-38-Cercle-B-6	0.11	<d.l.	0.19	2.41	<d.l.	0.24	0.59	0.89	1.69	70.28	0.19	1.29	<d.l.	<d.l.	<d.l.	<d.l.	<d.l.	77.88
2023-PAL-38-Cercle-B-7	0.54	0.22	<d.l.	5.40	<d.l.	<d.l.	0.53	0.12	0.55	74.74	0.52	0.54	<d.l.	<d.l.	<d.l.	<d.l.	0.24	83.39
2023-PAL-38-Cercle-B-8	0.13	0.10	<d.l.	5.09	<d.l.	<d.l.	0.71	0.19	0.70	74.01	0.25	1.00	<d.l.	<d.l.	<d.l.	<d.l.	<d.l.	82.18
2023-PAL-38-Cercle-B-9	<d.l.	0.13	0.22	2.06	<d.l.	0.23	0.63	1.10	2.03	69.41	0.30	1.44	<d.l.	<d.l.	<d.l.	<d.l.	<d.l.	77.56
2023-PAL-38-Cercle-B-10	0.70	0.28	<d.l.	5.82	<d.l.	<d.l.	0.55	0.30	0.55	74.17	0.40	0.64	<d.l.	<d.l.	<d.l.	<d.l.	<d.l.	83.41
2023-PAL-38-Cercle-B-11	<d.l.	0.14	0.20	2.00	<d.l.	0.35	0.65	1.07	2.14	69.77	0.14	1.38	<d.l.	<d.l.	<d.l.	<d.l.	0.22	78.06
2023-PAL-38-Cercle-B-12	<d.l.	0.15	0.21	2.14	<d.l.	0.27	0.76	1.00	2.16	69.38	<d.l.	1.56	<d.l.	<d.l.	<d.l.	<d.l.	<d.l.	77.62
2022-PAL-04-Cercle-B-1	0.15	0.45	<d.l.	6.33	<d.l.	<d.l.	1.33	0.26	0.67	70.96	0.14	0.77	<d.l.	<d.l.	<d.l.	<d.l.	<d.l.	81.07
2022-PAL-04-Cercle-B-2	0.18	0.22	0.21	2.70	<d.l.	0.33	0.73	1.47	1.12	67.18	0.14	0.94	<d.l.	<d.l.	<d.l.	<d.l.	0.38	75.60
2022-PAL-04-Cercle-B-3	<d.l.	0.47	0.19	5.32	<d.l.	<d.l.	1.67	0.37	1.08	70.49	0.15	0.20	<d.l.	<d.l.	<d.l.	<d.l.	0.23	80.18
2022-PAL-04-Cercle-B-4	0.26	0.96	0.12	5.94	<d.l.	<d.l.	1.28	0.13	0.85	70.62	0.13	0.63	<d.l.	<d.l.	<d.l.	<d.l.	<d.l.	80.92
2022-PAL-04-Cercle-B-5	0.16	0.23	0.21	2.47	<d.l.	0.32	0.58	1.39	1.30	66.90	0.13	1.11	<d.l.	<d.l.	<d.l.	<d.l.	0.22	75.03
2022-PAL-04-Cercle-B-6	0.12	0.42	0.13	6.30	<d.l.	<d.l.	1.26	0.20	0.73	70.98	0.15	0.67	<d.l.	<d.l.	<d.l.	<d.l.	<d.l.	80.96
2022-PAL-04-Cercle-B-7	0.16	0.46	0.12	6.49	<d.l.	<d.l.	1.38	0.18	0.74	75.11	0.17	0.52	<d.l.	<d.l.	<d.l.	<d.l.	<d.l.	85.33
2022-PAL-04-Cercle-B-8	0.15	0.41	0.16	2.90	<d.l.	0.28	1.11	1.66	1.50	65.81	1.05	0.69	<d.l.	<d.l.	<d.l.	<d.l.	0.65	76.36
2022-PAL-04-Cercle-B-9	0.15	0.48	0.13	6.35	<d.l.	<d.l.	1.23	0.14	0.65	72.16	0.11	0.32	<d.l.	<d.l.	<d.l.	<d.l.	<d.l.	81.71
2022-PAL-04-Cercle-B-12	0.13	0.20	0.27	2.86	<d.l.	0.29	0.46	1.58	2.22	70.01	<d.l.	1.04	<d.l.	<d.l.	<d.l.	<d.l.	0.28	79.34
2022-PAL-04-Cercle-B-13	0.13	<d.l.	<d.l.	6.62	<d.l.	<d.l.	0.33	<d.l.	0.44	78.30	0.15	0.08	<d.l.	<d.l.	<d.l.	<d.l.	<d.l.	86.05

EPMA Label	SiO_2	Al_2O_3	CaO	K_2O	PbO	SO_3	P_2O_5	MgO	Na_2O	MnO	FeO	CoO	ZnO	CuO	NiO	TiO_2	BaO	Total
2022-PAL-04-Cercle-B-14	<d.l.	<d.l.	0.17	4.35	<d.l.	<d.l.	0.73	0.74	1.85	74.39	0.10	0.50	<d.l.	<d.l.	<d.l.	<d.l.	<d.l.	82.83
2022-PAL-10-Cercle-A-1	0.20	0.51	<d.l.	5.47	<d.l.	<d.l.	1.02	0.09	0.76	75.39	0.18	0.45	0.23	0.13	<d.l.	<d.l.	<d.l.	84.43
2022-PAL-10-Cercle-A-2	0.11	0.17	0.26	2.40	<d.l.	0.27	0.59	1.08	1.74	70.78	0.11	1.76	<d.l.	<d.l.	<d.l.	<d.l.	0.20	79.49
2022-PAL-10-Cercle-A-4	0.24	0.52	<d.l.	5.52	<d.l.	<d.l.	0.83	0.11	0.58	75.11	0.17	0.47	<d.l.	0.13	<d.l.	<d.l.	<d.l.	83.68
2022-PAL-10-Cercle-A-5	0.17	0.43	<d.l.	5.07	<d.l.	<d.l.	1.12	0.15	0.91	74.07	0.13	0.55	<d.l.	<d.l.	<d.l.	<d.l.	<d.l.	82.61
2022-PAL-10-Cercle-A-6	0.29	0.70	<d.l.	5.45	<d.l.	<d.l.	0.88	0.10	0.66	74.76	0.27	0.51	<d.l.	<d.l.	<d.l.	<d.l.	<d.l.	83.64
2022-PAL-10-Cercle-A-7	0.11	0.26	0.15	2.09	<d.l.	0.25	0.69	1.00	1.69	70.98	0.22	1.67	<d.l.	<d.l.	<d.l.	<d.l.	0.18	79.30
2022-PAL-10-Cercle-A-8	11.31	4.17	0.17	3.49	<d.l.	<d.l.	0.67	0.71	1.00	59.29	2.36	1.01	<d.l.	<d.l.	<d.l.	0.22	0.47	84.87
2022-PAL-10-Cercle-A-11	<d.l.	0.19	0.14	2.12	<d.l.	0.30	0.89	1.10	1.54	69.16	0.11	1.42	<d.l.	<d.l.	<d.l.	<d.l.	0.26	77.23
2022-PAL-10-Cercle-A-12	0.14	0.47	<d.l.	5.05	<d.l.	<d.l.	1.08	0.24	0.85	74.77	0.13	0.43	<d.l.	0.15	<d.l.	<d.l.	<d.l.	83.31
2022-PAL-10-Cercle-A-13	10.05	0.51	0.09	5.23	<d.l.	<d.l.	0.32	0.27	0.41	67.34	0.48	1.23	<d.l.	<d.l.	<d.l.	<d.l.	<d.l.	85.93
2022-PAL-10-Cercle-A-14	0.29	0.81	0.10	4.80	<d.l.	<d.l.	0.93	0.17	1.03	74.30	0.13	0.59	<d.l.	0.14	<d.l.	<d.l.	<d.l.	83.29
2022-PAL-10-Cercle-A-15	<d.l.	0.28	0.14	1.96	<d.l.	0.32	0.65	1.08	2.21	68.95	0.16	2.14	<d.l.	<d.l.	<d.l.	<d.l.	<d.l.	77.89

<d.l. = below detection limit

Appendix E: Bulk geochemistry results

Analytical method	Unit	Detection limit	Analyte \ Sample	2022-PAL-02	2022-PAL-03	2022-PAL-04	2022-PAL-06	2022-PAL-11	2022-PAL-14	2023-PAL-02	2023-PAL-04	2023-PAL-08	2023-PAL-13	2023-PAL-16	2023-PAL-22	2023-PAL-25	2023-PAL-29	2023-PAL-32	2023-PAL-34	2023-PAL-35	2023-PAL-36	2023-PAL-38	2023-PAL-40	2023-PAL-45	2023-PAL-46	2023-PAL-47A
XRF	%	0.01	**Al_2O_3**	6.05	3.95	5.75	1.31	5.34	4.25	7.95	4.89	5.04	12.94	7.81	5.44	5.75	7.00	5.02	7.84	7.14	5.49	7.40	7.02	5.48	6.66	8.50
XRF	%	0.01	**BaO**	0.19	0.04	0.23	0.03	0.28	0.11	0.16	0.10	0.33	0.16	0.99	0.71	0.22	0.06	0.08	0.03	0.09	0.16	0.24	0.20	0.54	0.05	0.31
XRF	%	0.01	**CaO**	0.70	0.53	0.71	13.23	0.95	13.30	7.02	1.68	1.04	2.64	1.45	0.86	0.93	1.25	0.76	2.39	2.24	0.69	1.29	1.27	1.34	7.58	1.60
XRF	%	0.01	**Cr_2O_3**	0.005	0.005	0.01	0.02	0.005	0.005	0.005	0.005	0.005	0.005	0.005	0.005	0.005	0.005	0.01	0.005	0.005	0.01	0.005	0.005	0.005	0.005	0.005
XRF	%	0.01	**Fe_2O_3**	2.19	1.54	1.14	4.45	1.41	2.50	1.83	2.53	1.39	8.68	1.69	4.51	2.01	1.30	3.51	2.19	2.27	0.90	2.47	9.73	1.01	1.52	7.51
XRF	%	0.01	**K_2O**	3.25	3.52	4.12	0.44	4.13	0.92	2.77	2.09	3.14	2.45	2.55	3.06	3.35	3.02	3.39	3.26	3.26	3.66	2.75	2.79	3.87	1.93	2.72
XRF	%	0.01	**MgO**	0.82	0.86	0.95	15.47	0.84	10.68	0.93	1.72	1.03	1.60	1.33	1.37	1.04	0.86	0.71	0.84	0.99	1.40	0.88	0.95	1.03	1.52	1.05
XRF	%	0.01	**MnO**	48.54	55.69	47.50	20.33	52.23	19.56	25.01	43.38	45.72	4.85	34.52	46.92	49.62	38.48	48.79	39.24	39.85	40.56	37.84	34.31	45.82	25.70	28.68
XRF	%	0.01	**Na_2O**	1.72	1.42	1.78	1.10	1.41	1.46	2.44	1.99	1.98	3.21	2.54	1.76	1.91	2.81	1.74	2.16	2.14	2.24	2.49	2.21	2.15	2.45	2.00
XRF	%	0.01	**P_2O_5**	0.58	0.88	0.83	0.59	0.63	0.48	0.69	0.82	1.19	0.16	0.30	0.93	0.95	0.55	0.86	0.53	0.90	0.78	0.61	0.76	0.49	0.38	0.30
XRF	%	0.01	**SO_3**	0.11	0.21	0.40	0.92	0.99	0.20	7.18	1.27	0.36	1.28	0.10	0.30	0.39	0.51	0.24	1.41	1.57	0.35	0.15	0.16	0.70	9.62	0.24
XRF	%	0.05	**SiO_2**	21.15	14.68	21.21	10.54	16.28	19.46	34.72	24.17	24.12	56.45	33.85	17.98	17.95	31.12	20.08	27.09	25.44	28.00	29.77	27.37	22.35	30.95	35.38
XRF	%	0.01	**TiO_2**	0.24	0.13	0.23	0.07	0.21	0.22	0.23	0.17	0.19	0.50	0.24	0.20	0.24	0.24	0.21	0.26	0.23	0.10	0.28	0.31	0.20	0.17	0.38
WST-SEQ	%	0.01	**LOI 1000**	9.91	11.19	10.02	28.83	10.39	24.65	10.02	11.67	9.92	5.28	9.18	10.79	10.29	9.55	10.42	9.41	9.97	11.14	9.15	9.58	9.94	14.03	8.02
ICP-AES	%	0.01	**SiO_2**	21.40	15.00	21.90	10.35	16.40	18.95	34.00	23.80	23.80	55.70	32.90	17.80	17.70	30.60	19.75	26.80	25.30	27.60	29.60	27.30	22.40	0.00	34.50
ICP-AES	%	0.01	**Al_2O_3**	5.92	3.95	5.71	1.29	5.23	4.17	7.85	4.83	4.97	12.45	7.67	5.40	5.67	6.87	4.97	7.79	7.08	5.44	7.40	7.00	5.49	0.00	8.49
ICP-AES	%	0.01	**Fe_2O_3**	2.07	1.46	1.10	4.28	1.33	2.41	1.78	2.48	1.32	7.90	1.64	4.39	1.94	1.22	3.41	2.13	2.23	0.85	2.42	9.68	0.98	0.00	7.43
ICP-AES	%	0.01	**CaO**	0.69	0.54	0.71	13.10	0.94	13.25	6.87	1.68	1.03	2.48	1.45	0.86	0.93	1.23	0.76	2.43	2.27	0.70	1.32	1.26	1.36	0.00	1.62
ICP-AES	%	0.01	**MgO**	0.83	0.93	0.97	15.40	0.86	10.70	0.85	1.70	1.02	1.35	1.28	1.32	1.06	0.82	0.73	0.84	0.96	1.28	0.86	0.89	0.99	0.00	1.01
ICP-AES	%	0.01	**Na_2O**	1.74	1.46	1.72	1.05	1.43	1.46	2.45	2.00	1.89	3.20	2.55	1.78	1.92	2.82	1.76	2.17	2.20	2.27	2.54	2.26	2.18	0.00	1.98
ICP-AES	%	0.01	**K_2O**	3.20	3.43	3.98	0.41	4.07	0.90	2.59	1.96	2.92	2.43	2.42	2.89	3.14	2.82	3.17	3.08	3.11	3.43	2.60	2.66	3.71	0.00	2.65
ICP-AES	%	0.002	**Cr_2O_3**	0.004	0.005	0.005	0.002	0.005	0.003	0.001	0.002	0.002	0.001	0.002	0.001	0.001	0.002	0.002	0.001	0.002	0.001	0.001	0.004	0.002	0.000	0.003
ICP-AES	%	0.01	**TiO_2**	0.21	0.12	0.21	0.07	0.19	0.20	0.20	0.15	0.17	0.42	0.22	0.18	0.22	0.22	0.19	0.24	0.21	0.10	0.26	0.29	0.20	0.00	0.36

Analytical method	Unit	Detection limit	Analyte \ Sample	2022-PAL-02	2022-PAL-03	2022-PAL-04	2022-PAL-06	2022-PAL-11	2022-PAL-14	2023-PAL-02	2023-PAL-04	2023-PAL-08	2023-PAL-13	2023-PAL-16	2023-PAL-22	2023-PAL-25	2023-PAL-29	2023-PAL-32	2023-PAL-34	2023-PAL-35	2023-PAL-36	2023-PAL-38	2023-PAL-40	2023-PAL-45	2023-PAL-46	2023-PAL-47A
ICP-AES	%	0.01	**MnO**	44.90	52.40	45.20	19.45	48.60	18.85	23.80	41.70	43.80	4.29	33.30	45.10	47.70	36.50	46.60	37.90	38.50	39.00	36.60	33.30	45.10	0.00	26.60
ICP-AES	%	0.01	**P_2O_5**	0.55	0.86	0.81	0.59	0.60	0.48	0.66	0.79	1.13	0.15	0.27	0.90	0.92	0.51	0.81	0.51	0.86	0.75	0.59	0.73	0.47	0.00	0.31
ICP-AES	%	0.01	**SrO**	0.02	0.05	0.02	0.06	0.01	0.09	0.07	0.12	0.08	0.04	0.10	0.09	0.02	0.02	0.02	0.04	0.04	0.06	0.03	0.03	0.21	0.00	0.13
ICP-AES	%	0.01	**BaO**	0.17	0.03	0.21	0.02	0.26	0.10	0.14	0.09	0.31	0.14	0.95	0.67	0.20	0.04	0.07	0.03	0.08	0.15	0.23	0.19	0.52	0.00	0.29
WST-SEQ	%	0.01	**LOI**	12.35	13.25	11.85	32.10	12.55	27.00	12.40	13.90	12.15	7.63	10.85	13.70	12.75	11.30	11.95	11.75	12.35	12.65	10.80	11.15	11.30	16.35	10.10
LECO	%	0.01	**C**	0.04	0.05	0.06	5.29	0.04	4.92	0.06	0.02	0.04	0.03	0.03	0.03	0.03	0.15	0.06	0.11	0.06	0.05	0.04	0.05	0.03	0.02	0.11
LECO	%	0.01	**S**	0.06	0.07	0.13	0.31	0.37	0.08	2.86	0.45	0.13	0.50	0.04	0.11	0.15	0.19	0.09	0.54	0.59	0.11	0.05	0.06	0.25	3.75	0.10
ICP-MS	ppm	0.5	**Ba**	1530.0	294.0	1920.0	210.0	2350.0	847.0	1315.0	850.0	2830.0	1325.0	8870.0	6310.0	1850.0	407.0	663.0	294.0	724.0	1335.0	2140.0	1750.0	4910.0	0.0	2660.0
ICP-MS	ppm	0.1	**Ce**	173.0	26.9	29.3	4.4	89.5	18.8	43.6	31.8	51.3	46.2	42.3	57.7	120.0	25.9	40.7	24.5	28.3	37.7	96.1	48.7	41.9	0.0	52.2
ICP-MS	ppm	5	**Cr**	5	6	10	17	2.5	24	6	6	8	9	10	2.5	5	16	7	5	2.5	2.5	9	26	2.5	0	12
ICP-MS	ppm	0.01	**Cs**	2.92	2.05	3.73	0.81	2.79	2.12	2.63	1.76	2.08	7.62	4.56	2.11	2.53	2.98	2.83	2.10	2.18	3.49	3.45	2.92	2.69	0.00	3.42
ICP-MS	ppm	0.05	**Dy**	7.05	4.92	6.34	1.18	3.98	1.20	3.19	1.85	3.67	3.28	2.86	7.71	7.34	6.39	9.83	1.94	2.16	1.92	7.67	10.65	2.44	0.00	6.45
ICP-MS	ppm	0.03	**Er**	4.96	3.13	4.05	0.87	2.78	0.76	2.78	1.34	3.56	2.08	1.93	6.81	4.29	3.79	6.29	1.38	1.68	1.52	4.69	7.42	1.56	0.00	4.52
ICP-MS	ppm	0.02	**Eu**	0.84	0.76	0.74	0.15	0.55	0.35	0.56	0.32	0.44	0.93	0.59	0.88	1.10	0.62	1.44	0.54	0.48	0.37	1.20	1.54	0.65	0.00	1.20
ICP-MS	ppm	0.1	**Ga**	26.9	26.5	32.1	17.0	32.9	22.4	13.8	16.5	18.8	18.9	19.2	20.3	23.7	22.3	22.9	24.3	24.0	23.1	24.8	23.4	25.9	0.0	18.0
ICP-MS	ppm	0.05	**Gd**	5.36	5.05	5.11	1.02	3.60	1.42	2.69	1.62	3.24	3.47	2.45	5.36	5.83	3.95	9.29	2.00	1.92	1.72	6.03	8.40	2.68	0.00	6.31
ICP-MS	ppm	0.5	**Ge**	0.5	0.3	0.5	0.3	0.3	0.6	0.7	0.5	0.5	1.0	1.0	0.3	0.3	0.7	0.6	0.6	0.5	0.6	0.6	0.6	0.6	0.0	0.8
ICP-MS	ppm	0.05	**Hf**	1.85	1.48	2.05	0.44	1.49	1.63	2.52	1.61	1.59	4.14	2.29	1.18	1.49	2.60	1.66	2.03	1.57	1.62	2.58	3.28	3.21	0.00	3.75
ICP-MS	ppm	0.01	**Ho**	1.51	1.04	1.33	0.27	0.87	0.26	0.84	0.46	1.08	0.71	0.66	1.99	1.50	1.37	2.14	0.50	0.48	0.47	1.62	2.48	0.56	0.00	1.47
ICP-MS	ppm	0.1	**La**	12.4	12.1	11.6	2.3	10.1	9.4	15.6	10.3	23.9	27.5	17.8	13.0	10.1	11.9	11.9	11.9	10.9	14.1	14.7	15.6	22.1	0.0	25.7
ICP-MS	ppm	0.01	**Lu**	0.79	0.49	0.66	0.14	0.46	0.12	0.44	0.26	0.63	0.41	0.36	1.34	0.66	0.53	0.98	0.28	0.30	0.35	0.78	1.27	0.26	0.00	0.62
ICP-MS	ppm	0.05	**Nb**	3.87	3.19	4.75	1.03	3.51	3.04	5.20	3.63	3.57	6.99	5.25	2.41	3.02	4.95	3.78	4.11	3.64	4.42	4.56	4.37	7.04	0.00	5.13
ICP-MS	ppm	0.1	**Nd**	16.8	10.6	9.8	2.2	11.7	7.7	13.0	9.6	12.7	21.1	13.9	14.7	17.5	9.9	18.1	10.6	9.5	10.4	21.9	23.0	18.5	0.0	27.6
ICP-MS	ppm	0.02	**Pr**	4.15	2.89	2.70	0.55	2.92	2.12	3.64	2.62	3.53	5.69	3.76	3.56	3.68	2.76	3.93	2.90	2.60	3.11	5.24	5.28	4.72	0.00	6.93
ICP-MS	ppm	0.2	**Rb**	38.4	32.0	48.9	14.5	38.1	30.6	55.8	34.6	38.2	92.6	66.3	30.1	31.4	57.3	41.3	40.6	41.5	65.6	50.7	44.7	53.1	0.0	74.2

Analytical method	Unit	Detection limit	Analyte / Sample	2022-PAL-02	2022-PAL-03	2022-PAL-04	2022-PAL-06	2022-PAL-11	2022-PAL-14	2023-PAL-02	2023-PAL-04	2023-PAL-08	2023-PAL-13	2023-PAL-16	2023-PAL-22	2023-PAL-25	2023-PAL-29	2023-PAL-32	2023-PAL-34	2023-PAL-35	2023-PAL-36	2023-PAL-38	2023-PAL-40	2023-PAL-45	2023-PAL-46	2023-PAL-47A
ICP-MS	ppm	0.03	**Sm**	4.29	2.95	2.52	0.64	3.04	1.59	2.59	2.00	2.40	4.19	2.95	4.08	5.66	2.37	6.56	2.39	2.11	2.01	6.57	7.03	3.45	0.00	5.48
ICP-MS	ppm	0.5	**Sn**	0.7	0.5	0.8	0.3	0.6	0.3	0.7	0.6	0.6	1.4	0.7	0.6	0.7	0.6	0.6	0.6	0.7	0.7	0.7	0.8	1.0	0.0	0.6
ICP-MS	ppm	0.1	**Sr**	141.0	379.0	230.0	562.0	141.0	783.0	626.0	1035.0	725.0	390.0	907.0	796.0	164.5	141.0	157.5	382.0	352.0	564.0	236.0	309.0	1915.0	0.0	1220.0
ICP-MS	ppm	0.1	**Ta**	0.2	0.1	0.3	0.05	0.1	0.1	0.4	0.3	0.3	0.5	0.4	0.2	0.2	0.4	0.3	0.3	0.3	0.4	0.3	0.3	0.4	0.0	0.3
ICP-MS	ppm	0.01	**Tb**	0.98	0.79	0.94	0.15	0.58	0.19	0.46	0.28	0.49	0.53	0.39	1.02	1.10	0.95	1.53	0.32	0.33	0.29	1.10	1.58	0.39	0.00	1.01
ICP-MS	ppm	0.05	**Th**	4.26	3.71	5.67	0.91	3.66	3.01	6.19	4.20	4.08	8.05	5.08	3.02	3.26	6.21	4.40	4.13	4.13	7.23	5.41	5.38	5.33	0.00	5.90
ICP-MS	ppm	0.01	**Tm**	0.76	0.44	0.64	0.12	0.43	0.10	0.41	0.24	0.55	0.36	0.34	1.13	0.70	0.62	0.95	0.23	0.25	0.25	0.78	1.16	0.23	0.00	0.61
ICP-MS	ppm	0.05	**U**	11.75	4.84	11.50	1.92	8.76	3.42	3.93	3.79	11.05	6.44	6.22	8.56	11.10	10.20	4.86	2.08	1.97	5.13	4.05	3.66	6.21	0.00	4.31
ICP-MS	ppm	5	**V**	374	32	377	123	636	156	99	172	280	131	649	216	281	124	55	39	46	175	522	449	736	0	86
ICP-MS	ppm	0.5	**W**	1.2	0.7	1.3	2.0	0.9	2.6	0.8	1.2	1.6	1.7	2.4	1.0	1.1	1.2	1.6	1.3	1.3	1.8	1.4	1.3	1.5	0.0	1.2
ICP-MS	ppm	0.1	**Y**	29.4	33.6	26.5	12.2	19.5	7.3	37.7	15.8	49.5	20.8	16.4	66.6	28.1	25.2	59.1	14.5	15.1	12.9	33.2	59.3	16.7	0.0	47.1
ICP-MS	ppm	0.03	**Yb**	5.28	2.80	4.34	0.78	2.89	0.75	2.65	1.60	3.26	2.51	2.19	7.87	4.57	3.85	6.24	1.48	1.72	2.05	5.02	7.85	1.61	0.00	3.70
ICP-MS	ppm	1	**Zr**	64	50	76	23	52	63	94	59	57	152	87	45	57	106	66	75	58	56	100	145	141	0	152
ICP-MS	ppm	0.1	**As**	152.5	124.5	0.05	47.4	167.5	86.2	66.5	0.05	146.0	105.0	0.05	0.05	0.05	117.5	82.8	0.0	213.0	0.1	243.0	236.0	0.05	0	15.5
ICP-MS	ppm	0.01	**Bi**	5.44	0.29	0.39	0.04	6.08	0.10	0.07	0.06	0.07	0.08	0.07	0.12	0.98	0.14	0.27	0.00	0.05	0.07	2.87	0.26	0.11	0	0.08
ICP-MS	ppm	0.005	**Hg**	0.020	0.016	0.007	0.387	0.0025	0.032	0.043	0.020	0.042	0.181	0.177	0.018	0.007	0.0025	0.0025	0.000	0.008	0.019	0.0025	0.018	0.112	0.000	0.289
ICP-MS	ppm	0.005	**In**	0.060	0.024	0.059	0.010	0.168	0.017	0.008	0.013	0.025	0.016	0.011	0.058	0.097	0.018	0.032	0.000	0.013	0.013	0.069	0.036	0.012	0.000	0.014
ICP-MS	ppm	0.001	**Re**	0.001	0.003	0.004	0.041	0.002	0.006	0.003	0.003	0.003	0.009	0.003	0.011	0.002	0.002	0.002	0.000	0.005	0.003	0.001	0.002	0.002	0.000	0.002
ICP-MS	ppm	0.05	**Sb**	8.18	1.15	13.65	0.60	9.24	3.81	1.29	2.71	5.93	1.51	22.90	7.75	4.91	3.92	0.98	0.00	0.92	2.35	2.63	2.50	27.20	0.00	1.28
ICP-MS	ppm	0.2	**Se**	3.5	2.4	18.2	5.2	5.7	2.8	2.5	3.7	7.7	1.0	1.3	5.7	3.1	13.4	2.8	0.0	4.2	2.1	3.5	3.5	2.0	0.0	1.2
ICP-MS	ppm	0.01	**Te**	0.13	0.07	0.16	0.01	0.72	0.07	0.06	0.08	0.37	0.04	0.09	0.10	0.12	0.01	0.03	0.00	0.02	0.07	0.06	0.06	0.33	0.00	0.05
ICP-MS	ppm	0.02	**Tl**	5.76	52.30	116.50	48.80	77.80	118.00	62.40	61.40	0.01	3.36	80.40	80.10	17.85	0.82	128.50	0.00	0.01	41.90	17.05	69.20	80.20	0.00	54.70
ICP-AES	ppm	0.5	**Ag**	0.25	0.25	0.25	1.3	0.25	0.25	0.25	0.25	0.25	0.25	0.25	0.25	0.25	0.25	0.25	0.25	0.25	0.25	0.25	0.25	0.25	0.25	0.25
ICP-AES	ppm	0.5	**Cd**	8.6	273.0	52.0	0.3	30.3	752.0	169.5	272.0	378.0	19.3	357.0	85.4	33.2	5.7	174.0	203.0	151.0	925.0	16.9	241.0	118.5	199.0	269.0
ICP-AES	ppm	1	**Co**	4420	1830	3320	1115	6290	1620	2050	2550	2960	111	1335	2830	2640	3850	1945	1145	1685	1720	4230	1555	397	428	691

Analytical method	Unit	Detection limit	Analyte \ Sample	2022-PAL-02	2022-PAL-03	2022-PAL-04	2022-PAL-06	2022-PAL-11	2022-PAL-14	2023-PAL-02	2023-PAL-04	2023-PAL-08	2023-PAL-13	2023-PAL-16	2023-PAL-22	2023-PAL-25	2023-PAL-29	2023-PAL-32	2023-PAL-34	2023-PAL-35	2023-PAL-36	2023-PAL-38	2023-PAL-40	2023-PAL-45	2023-PAL-46	2023-PAL-47A
ICP-AES	ppm	1	**Cu**	475	124	187	16	393	35	61	111	99	59	162	415	496	150	225	144	247	182	324	227	102	18	145
ICP-AES	ppm	10	**Li**	20	20	30	40	40	20	10	20	10	30	20	30	30	20	20	20	30	30	20	30	20	50	20
ICP-AES	ppm	1	**Mo**	28	0.5	432	165	208	231	26	64	198	30	125	256	48	49	0.5	0.5	9	368	20	44	203	4	21
ICP-AES	ppm	1	**Ni**	140	147	57	833	149	1405	127	443	198	40	398	72	104	49	90	65	48	55	88	119	98	516	221
ICP-AES	ppm	2	**Pb**	202	70	70	23	784	71	44	49	59	15	58	94	200	51	66	45	56	62	269	55	74	37	40
ICP-AES	ppm	1	**Sc**	6	2	5	1	5	3	3	3	3	7	4	4	6	4	4	4	4	2	5	5	2	2	6
ICP-AES	ppm	2	**Zn**	280	356	230	1330	379	810	342	442	530	111	523	238	309	152	334	218	216	161	209	383	234	516	425